The Dissertation Committee for Jasmine Man-Chi Tam Certifies that this is the approved version of the following dissertation:

Synthesis, Stabilization, and Controlled Assembly of Organic and Inorganic Nanoparticles for Therapeutic and Imaging Applications

Committee:

Keith P. Johnston, Supervisor

Robert O. Williams, III

Konstantin V. Sokolov

Jason T. McConville

Venkat Ganesan

Thomas M. Truskett

Synthesis, Stabilization, and Controlled Assembly of Organic and Inorganic Nanoparticles for Therapeutic and Imaging Applications

by

Jasmine Man-Chi Tam, B.S.

Dissertation

Presented to the Faculty of the Graduate School of

The University of Texas at Austin

in Partial Fulfillment

of the Requirements

for the Degree of

Doctor of Philosophy

The University of Texas at Austin

December 2009

Dedication

To my family, Brandon, and Toby

Acknowledgements

A dissertation is never the work of just one person. I would have never come so far without the advice, discussions, and support I received from many people. First, I would like to sincerely thank my advisor, Dr. Keith P. Johnston, for his enthusiastic guidance throughout my Ph.D. studies. His strive for excellence in research has pushed me to always "dig deeper" into the science. Special thanks are given to Dr. Robert Williams and Dr. Jason McConville for their invaluable knowledge in the field of pharmaceutics and their support during my first years. I would like to thank Dr. Konstantin Sokolov, whose patient guidance and encouragement during the last 1.5 years have enabled me to accomplish more than I could have imagined in a new field. I also appreciate the assistance from my committee members, Dr. Venkat Ganesan and Dr. Thomas Truskett, for their encouraging words and comments, which have helped shape the scope of this dissertation.

I am especially grateful to my lab mates, including Dr. Michal Matteucci, who trained me during my first year and has become a dear friend, to Dr. Griffin Smith, whose willingness to help out a new graduate student even while he was trying to finish his own dissertation was a true encouragement, to Dr. Josh Engstrom for his collaboration that led to chapters 3 and 4, to Dr. Wei Yang for her assistance with the animal study in chapter 2, in addition to her exceptional friendship, to Leo Ma, whose creativity in the lab and his enthusiastic discussions about his research contributed to the successes in chapters 5 and 6, and to Avi Murthy, who helped collect the data for chapters 5 and 6 and spent countless hours with me to come up with a mechanism for our research – I am truly grateful. Special thanks are given to Dr. Mehul Patel for his uplifting camaraderie that helped to make our discussions about research more fun, and to Dan Slanac and Andrea Miller for their support and friendship. Thanks to Dr. Domingo Ferrer for his help in experiments and whose positive attitude and willingness to help was always an encouragement. Exceptional gratitude is given to my sister, Justina Tam, who performed all the cell studies in chapter 5, which significantly enhanced the impact of this research, as well as her ever-cheerful attitude which always made experiments more enjoyable.

Finally, I thank my family for instilling in me the greatest motivation to learn and their constant love and support, and to Brandon, who has been so supportive throughout the years, enduring my moodiness through stressful days and always treating me with love and patience. And to little Toby, you are always able to bring a smile to my face and everything always seems better when you are around.

Synthesis, Stabilization, and Controlled Assembly of Organic and Inorganic Nanoparticles for Therapeutic and Imaging Applications

Publication No._____________

Jasmine Man-Chi Tam, Ph.D.
The University of Texas at Austin, 2009

Supervisor: Keith P. Johnston

Nanoparticles have garnered much attention in pharmaceutical and biomedical fields because their small size and high surface area facilitate drug absorption, improve access to cells and organs, and enhance optical imaging. However, delivery of nanoparticles to the body is not always feasible or effective. Here, nanoparticle assemblies (flocs or clusters) for pulmonary drug delivery and biomedical imaging in cells are shown to facilitate delivery, interactions with cells, and manipulation of optical properties of inorganic/organic nanocomposites. The formation of aggregates by physical techniques and their mechanisms are described in detail.

For pulmonary delivery, particles with aerodynamic diameters between 1-5 μm deposit efficiently in the deep lungs. However, crystalline, non-porous, poorly water soluble drugs of this size require long dissolution times, limiting absorption by the body. Therefore, drug dissolution must be "decoupled" from deposition to improve absorption. To address this challenge, drug nanoparticles were dispersed within 4-μm water droplets when administered via nebulization or as micron-sized flocs using a pressurized metered dose inhaler (pMDI). Upon deposition in aqueous media, the aerosolized nanoparticle assemblies dissociated into constituent nanoparticles, raising the available surface area for dissolution and increasing dissolution rates, relative to solid particles. Poorly water soluble drug nanoparticles were prepared using a controlled precipitation (CP) or thin film freezing (TFF) process, in which stable nanoparticles (30-300 nm in diameter) with high potencies (>90 wt% drug) were produced by rapidly nucleating drug solutions in the presence of strongly adsorbing polymers or by freezing, respectively. Amorphous, nanoparticles prepared by CP produced stable aqueous dispersions with high fine particle fractions (FPF) of 77% and total emitted doses (TED) of 1.5 mg/min upon nebulization. CP and TFF also produced anisotropic particles (aspect ratios >5), which formed stable suspensions in a hydrofluoroalkane propellant. Inefficient packing of anisotropic particles formed loose, open flocs that stacked upon each other to prevent settling. Upon pMDI actuation, atomized propellant droplets shear apart and template portions of the floc to yield porous particles with high FPFs (49-64%) and TEDs (2.4 mg/actuation).

The controlled assembly of gold nanoparticles into clusters is also of great interest for biomedical imaging and therapy because clusters exhibit improved near infrared absorbance (where blood and tissue are most transparent), relative to single spherical particles, and can biodegrade into clearable particles. Gold nanoparticles (5 nm) were assembled into clusters between 30 to 100 nm in diameter with high gold loadings, resulting in strong NIR absorbance. The assembly was kinetically controlled with weakly adsorbing polymers by manipulating electrostatic, van der Waals, steric, and depletion forces. Furthermore, clusters assembled with a biodegradable polymer deaggregated back into primary particles in physiological media and within cells. This kinetic assembly platform is applicable to a wide variety of fields that require high metal loadings and small particle sizes.

Table of Contents

List of Tables

List of Figures

Chapter 1: Introduction

Nanoparticles are of great interest for pharmaceutical and biomedical applications, especially in areas such as drug delivery and biomedical imaging because of their small size, high surface area, and tunable properties[1]. Extensive research on nanoparticle formation processes has been conducted to improve drug delivery because it has been reported that 40% of drugs currently being developed by the pharmaceutical industry have poor water solubility, which can lead to low bioavailability[2, 3]. For these poorly water soluble drugs, their absorption into the body is limited by their slow dissolution rates in bodily fluids[4]. Dissolution rates may be enhanced by reducing particle size, which increases the surface area for adsorption, A, and decreases the boundary layer thickness, h, as predicted by the Noyes-Whitney equation[5]:

$$\frac{\partial \mathrm{M}}{\partial \mathrm{t}} = \frac{\mathrm{DA}}{\mathrm{h}}(\Delta \mathrm{C}) \qquad (1.1)$$

where M is the mass of undissolved drug, t is time, D is the average diffusion coefficient, and ΔC is the difference between the equilibrium concentration of the drug adjacent to the particle surface and the concentration in the bulk. Furthermore, when the sizes of nanoparticles are reduced to < 50 nm, the biological pathways in targeted cells can undergo profound changes[6-11]. Nanoparticles < 30 nm in diameter become comparable to the size of small viruses, antibodies, membrane receptors, and other biomolecules, which can penetrate cell membranes and leaky vasculature in cancerous tumors more efficiently than particles >50 nm [6-11]. Particle in this size range are of significant interest for therapeutic and imaging applications.

Common drug nanoparticle formation techniques include mechanical milling[12] and high pressure homogenization[13, 14], which often require long processing times, risk contamination with impurities, and offer little control over the morphology of the final product[15]. The formation of nanoparticles of poorly water soluble drugs by precipitation from solution, however, offers more control over the production of amorphous versus crystalline drugs, high drug loadings, as well as high process yields[16-26]. Two of the nanoparticle formation processes that were used in this research include controlled antisolvent precipitation (CP)[18-20] and thin film freezing (TFF)[23-25]. In the case of CP, high surface area particles are produced by generating large levels of drug supersaturation to induce rapid nucleation of the drug in the presence of amphiphilic polymeric stabilizers, which mitigate particle growth[19, 20](Figure 1.1). Briefly, a poorly water soluble drug, dissolved in an organic solvent that is miscible with water, is introduced to an aqueous solution containing stabilizers. Upon mixing of the two phases, supersaturation of the drug leads to nucleation and precipitation. The large interfacial area produced by the nucleating surfaces provides a strong driving force for the adsorption of the stabilizers to the newly formed particle surfaces. The hydrophilic blocks of the amphiphilic stabilizers preferentially orient towards the drug/water interface and provide steric stabilization, thus minimizing growth by condensation or coagulation. In the TFF process, a drug solution is dripped onto on a cryogenically cooled surface to form a thin film that freezes within one second[23, 26](Figure 1.2). Cooling of the feed solution as it freezes leads to the nucleation of drug particles. Particle aggregation is minimized due to the restricted mobility of particles in the frozen state. In this process, nanoparticles may be formed with or without surfactants or stabilizers, as freezing rates dictate nucleation rates. For both nanoparticle formation processes, increased nucleation rates, produced by increasing levels of supersaturation or by increasing cooling rates in CP and TFF, respectively, facilitate the formation of smaller particles.

Similar mechanisms used to produce organic pharmaceutical nanoparticles have been applied in this thesis to the synthesis of inorganic nanoparticles. For gold nanoparticles, increasing nucleation rates result in the formation of smaller nanoparticles, just as observed during the production of the drug nanoparticles. Gold nanoparticles are generally synthesized by reduction of soluble precursors[27-31]. Reactions conducted using stronger reducing agents, such as sodium borohydride compared to sodium citrate, or at elevated temperatures, ~97 compared to 25°C, resulted in the production of smaller nanoparticles, less than 5 nm in diameter, due to increased reaction rates and thus nucleation rates[28, 30, 32]. Gold nanoparticles synthesized in aqueous media at room temperature or using citrate as the only reducing agent are generally greater than >25 nm in diameter[29-31].

For nanoparticles with various morphologies, strategies may be designed to efficiently deliver them to the appropriate location in the body and to maximize their therapeutic function. Although nanoparticles possess many desirable properties that have been reported to enhance therapeutic and imaging applications, efficient delivery of these nanoparticles to a specific location in the body is not trivial due to their extremely small size. Furthermore, in some situations, nanoparticle assemblies possess more desirable properties compared to single, isolated nanoparticles. Two such cases will be discussed, where clusters of nanoparticles are used to improve pulmonary drug delivery as well as facilitate efficient imaging/photothermal therapy of cells and tissues. In the case of pulmonary delivery, nanoparticles may be efficiently delivered to the deep lungs within micron-sized aggregates[33-35]. These nanoparticle assemblies were achieved by spray drying nanoparticle dispersions and carefully controlling the time for the spray dried droplet to evaporate and the time for particles within the droplet to diffuse to the air-water interface. The time was varied by manipulating spray drying conditions (temperature, concentration of particles in the feed, solvent, etc ….) to control the cluster's porosity, and thus aerosol properties. Upon deposition in aqueous media, the assemblies were shown to deaggregate into its constituent particles, which would facilitate drug dissolution.

For bimedical applications, clusters of gold nanoparticles possess more desirable optical properties for imaging of cells and photothermal therapy than single, isolated gold nanoparticles[36-39]. Gold nanoparticles conjugated with anti-EGFR monoclonal antibodies have been shown to form clusters during cell uptake. When the targeted gold binds to the EGFR receptors on cells, they are taken up by the cell, into endosomes, which clusters them together[36-38]. Upon cluster formation, the surface plasmon resonance (SPR) of the gold shifts into the near infrared region (NIR), where blood, water, and tissues absorb minimally, which facilitates efficient imaging and photothermal therapy of targeted cells and leaves untargeted cells unharmed. Therefore, the development of robust, broadly applicable assembly methods for nanocluster assembly of organic and inorganic nanoparticles is of interest to improve the efficiency of nanoparticle delivery to the body as well as to take advantage of improved optical properties of clusters of metal nanoparticles.

1.1 PULMONARY DELIVERY

Pulmonary delivery is an attractive route of drug administration because it is non-invasive and offers advantages of an enormous absorptive surface area (140 m^2), thin absorptive membrane (0.1 – 0.5 μm), highly vascularized epithelium, and avoidance of first pass metabolism[40]. Effective treatment of respiratory diseases, such as asthma and chronic bronchitis, by pulmonary drug delivery methods has been well established.[40, 41] More recently, research on the aerosol delivery of systemic drugs has resulted in several pulmonary insulin products[42-46]. Thus, pulmonary drug delivery is versatile in its ability to treat diseases both locally and systemically. Furthermore, aerosol drug delivery provides a promising alternative to conventional oral treatments (where drug doses may be 5-10 times higher than pulmonary doses, due to extensive drug metabolism in the stomach/intestines[40, 47]) and parenteral treatment (which is more invasive and thus, less patient compliant).

Drug particles may be delivered to the lungs by nebulization, pressurized metered dose inhaler (pMDI), or dry powder inhaler (DPI). Nebulization, in which a drug solution or suspension is aerosolized into droplets for inhalation using a vibrating mesh screen or piezoelectric device, is easy to use and is the most capable method of delivering large drug doses[48], up to 300 mg, in one sitting due to its ease of administration[49]. However, nebulizers are expensive and not portable, and thus not ideal for treating diseases that may require sudden, immediate treatment, such as asthma[50, 51]. pMDIs and DPIs are more appropriate treatment options for these types of diseases because they are portable. pMDIs remain the most popular form of pulmonary drug delivery because they are the least expensive of the three options, reliable, and provide effort-independent dosing [52, 53].

To achieve high deposition of drug particles in the alveoli of the lungs, where drug absorption is most efficient as a consequence of extremely thin membranes (0.1 – 0.2 μm)[40], aerosolized particles must possess an aerodynamic diameter (d_a) between 1-5 μm. Particles larger than 5 μm tend to deposit in the throat or upper airways whereas smaller, sub-micron particles are often exhaled during expiration without appreciable deposition[54, 55]. Crystalline, non-porous, poorly water soluble drugs of the appropriate size for efficient alveoli deposition require long dissolution times, limiting absorption by the body. Furthermore, these slow-dissolving particles are readily cleared by alveolar macrophages, the lung's primary defense mechanism against foreign matter, within several hours after deposition[40, 56, 57]. Clearly, there exists a conflict between particles with optimal size for deep lung deposition and optimal size for efficient drug absorption (Figure 1.3). To address this challenge, drug nanoparticles may be "packaged" into micron-sized assemblies that, upon deposition in aqueous media, are able to dissociate to undergo rapid dissolution, as will be described in chapters 2-4.

1.1.1 Delivery of nanoparticles to the lungs by nebulization

Aerosolized droplets emitted from nebulizers may be tuned to 1-5 µm in diameter, the ideal size range for deep lung delivery [58]. Therefore, in order to efficiently delivery nanoparticles to the lungs, they may be delivered within the nebulized droplets, which are already optimized for deep lung deposition. Nebulization of poorly water soluble drugs dissolved in organic solvents, such as ethanol or propylene glycol, has been shown to efficiently deliver large drug doses directly to the lungs, on the order of 300 mg/dose[40, 49, 59, 60]. However, the prolonged and consistent exposure of organic solvents to the lungs often caused severe lung irritation during clinical trials, limiting its long-term viability[61]. To avoid the use of potentially irritating organic solvents, aqueous nanoparticle dispersions may be prepared for nebulization. In addition to the previously mentioned advantages of nanoparticles versus microparticles regarding enhanced dissolution rates and reduced macrophage clearance, the delivery of nanoparticles is further advantageous for nebulization compositions because smaller nanoparticles are more stable against flocculation and settling, relative to microparticle dispersions. Furthermore, nanoparticles may be distributed more uniformly throughout the 1-5 µm carrier droplets than microparticles, as shown in Figure 1.4, which facilitates the delivery of larger doses, as well as more uniform drug distribution throughout the alveoli, which can enhance absorption rates[62, 63].

Previous studies have demonstrated the advantages of pulmonary delivery of nanoparticle dispersions[63-66]. Nebulization of nanoparticle dispersions of milled budesonide[63] as well as itraconazole, formed by spray freezing into liquid (SFL)[64, 65] and TFF[66], yielded optimal aerosol properties for deep lung deposition by utilizing the aerosolized micron-sized water droplet as a vehicle to efficiently deliver the nanoparticles to the lungs. Furthermore, nebulization of itraconazole nanoparticles, produced using SFL and TFF, to a mouse model yielded high lung tissue to serum ratios, demonstrating superior local therapy in the lungs while minimizing systemic levels, relative to oral or parenteral delivery [65, 66], which is highly desirable to reduce toxicity concerns. However, these previous studies required at least 40 wt % of excipient to effectively stabilize the drug nanoparticles in an aqueous dispersion. Chapter 2 will examine an alternative particle formation technique to produce stable poorly water soluble drug nanoparticles with higher drug potencies.

1.1.2 Delivery of nanoparticles to the lungs using a pressurized metered dose inhaler (pMDI)

pMDIs are commonly formulated as suspensions due to the low solubilities of many drugs and proteins in hydrofluoroalkane (HFA) propellants[67]. The traditional methods used to stabilize colloidal particles in water have not been successful in HFA because of the lack of efficient electrostatic and steric repulsive forces. Electrostatic stabilization in HFA is negligible compared to the van der Waals (VDW) attractive forces, due to ion pairing that results from the low dielectric constants[68, 69]. Steric stabilization is also severely limited because the hydrogenated tails of FDA-approved surfactants are poorly solvated by HFA, due to its low polarizability[52, 67, 70-72]. Therefore, drug loadings in pMDI formulations have been restricted to 1-5 wt% to minimize flocculation and settling that may lead to irreversible particle aggregation[67]. Despite the low drug loadings, suspensions of milled or spray dried particles, which are most commonly delivered using pMDIs, often flocculate and settle within minutes[67, 73, 74]. This rapid particle settling often results in an increase in d_a and inconsistent dosing between actuations, as evidenced by the low fine particle fractions (percentage of delivered particles estimated to deposit in the deep lungs[40]) between 5-30% [75] and respirable doses between 30-200 µg/actuation[40, 73, 75] that are typical of pMDI compositions. The low respirable doses achieved by pMDIs limit their ability to treat systemic diseases, as required doses for drugs such as insulin and some anti-cancer agents are 1-10 mg/dose[76].

Therefore, pMDI administration has been limited to the delivery of high potency (low dose) drugs.

To improve pMDI performance, reduced particle flocculation and settling in HFAs have been demonstrated with hollow, porous particles, which possess excellent suspension stability in HFAs with no visible settling up to four hours[73]. The porous structure allows the HFA to permeate and fill the particle, minimizing the density difference between the suspended particles and the surrounding HFA, and thus reducing VDW attraction forces[77]. Additionally, the hollow, porous particles achieved high FPFs when delivered using a pMDI, ranging from 40-70% for a wide variety of drugs [73, 77-79]. However, their high porosity, as well as the high excipient levels required to produce their porous morphology, limits their drug mass/particle loading, capping their maximum respirable dose at ~300 μg/actuation[67]. Therefore, the production pMDIs capable of delivering high drug doses requires the development of a stabilization mechanism that does not rely on colloidal stabilization of particles in HFA. This concept is explored in chapters 3 and 4 using anisotropic particles.

1.2 CONTROLLED ASSEMBLY OF NANOPARTICLE CLUSTERS FOR BIOMEDICAL IMAGING AND THERAPY

Clusters of metal nanoparticles have been shown to possess different optical properties than isolated nanoparticles due to a change in their surface plasmon resonance when packed closely together[80]. For a variety of applications, robust and widely applicable synthetic strategies are needed to pack high levels of functionality (i.e. high metal loadings) into clusters with an overall size smaller than ~30 to 100 nm. Clustering of gold nanoparticles is of extreme interest for imaging and therapeutic applications, such as photothermal therapy, because the surface plasmon resonance (SPR) of gold may be shifted to the near-infrared region (NIR), where soft tissues and blood are most transparent, upon tight packing between gold particles within a cluster[81-83]. Presently available gold nanoparticles that absorb in the NIR possess hollow or non-spherical geometries and are typically larger than 50 nm[84-90], above the threshold size of approximately 5.5 nm required for efficient renal clearance from the body [91]. These nanoparticles are essentially non-biodegradable since the metallic bonds between atoms are inert, and thus concerns about their accumulation and long-term toxicity[91, 92] have restricted their translation into clinical practice. Therefore, the assembly of gold nanoparticles into clusters using a biodegradable polymer, which possess the potential to deaggregate into clearable particles, offers a significant improvement over currently available materials for imaging processes.

To regulate their size, clusters are most often formed by thermodynamic self assembly. A "bricks and mortar" technique was developed by Rotello and co-workers to template the assembly of metal nanoparticles into clusters using polymers, proteins, and DNA[80, 93] and Glotzer et al. used polymer-tethered nanoparticles to demonstrate cluster assembly [94]. Gold nanoparticles have also been assembled in the cores of block copolymer micelles[95-98] and on the surface of micelles[99, 100]. Amphiphilic gold Janus spheres, containing hydrophobic and hydrophilic domains self-assemble into clusters[101-104] upon manipulation of pH or solvent quality. For thermodynamically driven cluster assembly, high concentrations of strongly interacting templating agents are required. Therefore, a significant amount of these templating agents often remain in the final cluster, typically limiting the metal loading well below 50 wt%.

Kinetic assembly of clusters, in contrast to thermodynamic self assembly, may achieve extremely high metal loadings by manipulating electrostatic interactions between charged particles. For example, variation of pH or ionic strength of dilute dispersions of citrate-capped gold nanoparticles screens electrostatic repulsion and induces cluster growth[105, 106]. Lysine-[107-110] and cysteine-[111] capped gold nanoparticles at high loadings aggregate reversibly in response to changes in charge with pH. Despite the ability of these gold clusters to exhibit strong NIR absorbance, cluster growth and shape in each of these cases was difficult to control, due to the absence of a stabilizing agent and often produced irregularly shaped aggregates greater than several hundred nanometers in diameter. Therefore, a conflict arises in both thermodynamically- and kinetically-controlled assembly between the need for sufficient levels of stabilizers to produce small clusters <50 nm while simultaneously achieving high metal loadings for high functionality. To address this conflict, the ability to simultaneously control cluster size and optical properties by mediating VDW, electrostatic, steric, and depletion forces will be demonstrated in chapters 4 and 5.

1.3 OBJECTIVES

In many situations, nanoparticle assemblies possess more desirable properties over single, isolated nanoparticles. Assemblies of nanoparticles may be more efficiently delivered to the desired location in the body and for, inorganic metal nanoparticles, possess improved optical properties in a clustered state versus isolated nanoparticles. The primary goals of this dissertation are (1) to demonstrate enhanced pulmonary delivery of nanoparticles to the lungs by facilitating their delivery as micron-sized assemblies and (2) to demonstrate the assembly of gold nanoparticles into clusters of controlled size and optical properties for improved biomedical imaging and therapy applications. The kinetically controlled assembly of both organic and inorganic nanoparticles will be demonstrated to provide efficient delivery of nanoparticles to the body as well as improved function. Control over cluster formation and also their break-up will be discussed. The assembly of these clusters is driven by attractive van der Waals forces. The size and morphology of the clusters will be shown to influence their delivery and functional properties. In contrast to thermodynamic assembly methods, which require strong interactions between the particles and a templating agent that results in low particle loadings within the cluster, the kinetic assembly of clusters facilitates high drug or metal nanoparticles loadings to maximize functionality.

For the first goal of this dissertation, there are two key objectives. First, the stability and aerosol performance of nebulized dispersions of a poorly water soluble drug was investigated. The nanoparticles for nebulization were produced by CP. The effect of drug/surfactant levels during the formation process on particle size and crystallinity was examined in order to determine the optimal level of surfactant required to stabilize small nanoparticles (<300 nm) while maintaining high drug potencies. Furthermore, the mechanism behind drug absorption of these nanoparticle dispersions in the lungs was examined by developing a model to examine the dissolution and permeation of poorly water soluble drugs in lung tissue. For the second objective, this dissertation describes the concept of forming stable nanoparticle suspensions of both proteins and poorly water soluble drugs in HFAs by using anisotropic particles. Anisotropic particles form loose, open flocs in HFA, due to their inefficient packing relative to spherical particles, which are able to stack upon each other and prevent settling to form stable suspensions. The mechanism by which the atomized HFA droplets, formed upon pMDI actuation, template the flocs into aerosolized particles to achieve high fine particle fractions in pulmonary delivery is described. The particle morphologies for pMDI delivery, produced using CP and TFF, were rods, thin plates, and needles of varying size and aspect ratios. The effect of particle size and shape on suspension stability and aerosol properties, as well as the extension of this concept to deliver higher doses, on the order of milligrams/actuation, is also examined. Furthermore, the ability of these nanoparticle assemblies to deaggregate upon deposition in aqueous media to facilitate drug dissolution, relative to a non-porous particle of similar size, is also discussed.

For the second goal of this dissertation, the kinetic assembly of 5 nm constituent gold particles into clusters, with tunable sizes between 30 nm to 100 nm, which manifest intense NIR absorbance and strong optical contrast in live cells is described. The combination of high gold particle volume fractions during the cluster formation process and the inclusion of a weakly adsorbing polymeric stabilizer to mediate interactions between gold primary particles facilitates the production of clusters with high gold loadings and close-spacing between the gold particles in the cluster. These properties enable strong NIR absorbance. The mechanism by which the clusters nucleate and grow is described in terms of the electrostatic, van der Waals, steric and depletion forces. When a biodegradable polymeric stabilizer is used in the cluster formation process, nanoclusters deaggregate completely into the constituent 5 nm primary gold particles upon degradation of the polymer binder under physiologically relevant conditions in solution and in live cells. This general concept for the assembly of hybrid polymer/inorganic nanoclusters combines advantages of the biodegradability of a polymer binder/stabilizer with the strong imaging contrast and therapeutic capabilities afforded by the NIR-active closely-spaced metal nanoparticle assembly.

1.4 DISSERTATION OUTLINE

The first half of this dissertation focuses on the formation and stabilization of nanoparticle assemblies for pulmonary drug delivery applications. In chapter 2, stable, aqueous dispersions of a poorly water soluble drug were nebulized to demonstrate the successful delivery of nanoparticles to the lungs. Aqueous colloidal dispersions of amorphous poorly water soluble drug nanoparticles were produced by controlled antisolvent precipitation and stabilized using only 10% wt of a polymeric stabilizer. Rapid nucleation rates and efficient stabilization of the particles by adsorbed polymer minimized crystal growth within the dispersion to yield average particle sizes of ~300 nm with over 80% by volume of the particles smaller than 1 μm. The small size of the drug nanoparticles, relative to the micron-sized droplet, made them ideal for delivery via nebulization because they could uniformly disperse throughout the micron-sized aerosolized droplet, whose aerodynamic diameter was controlled by the nebulizer. The nebulized dispersion yielded a mass median aerodynamic diameter (MMAD) of 2.5 μm and a FPF of 72%, indicating that the dispersion possessed optimal aerodynamic properties for deep lung deposition. Dissolution of the amorphous nanoparticles produced supersaturation values 18 times the drug's aqueous equilibrium solubility. The nebulization of the nanoparticle dispersion to mice produced therapeutic lung levels and systemic concentrations below toxic limits. Therefore, the sizes of the aerosolized aqueous droplets were optimal to efficiently delivery the drug nanoparticles to the lungs, and, upon deposition, the amorphous drug nanoparticles could disperse and facilitate rapid dissolution. A dissolution/permeation model was developed to characterize the effects of particle size, solubility, and drug dose on the absorption half-lives of poorly water soluble drugs in the alveoli. The *in-vitro* and *in-vivo* data, as well as the dissolution/permeation model, indicate that nebulization of amorphous nanoparticle suspensions has the potential to enhance lung epithelial absorption markedly for poorly water soluble drugs, relative to respiratory delivery of crystalline, micron-sized particles.

In contrast to chapter 2, in which nanoparticles were stabilized in an aqueous dispersion for nebulization, nanoparticles are purposely flocculated to form micron-sized assemblies for delivery by a pMDI in chapter 3. A novel concept for the formation of stable protein (bovine serum albumin, BSA) suspensions in a HFA propellant for pMDI delivery, which is based on purposely forming flocs of particles, is presented. Rod-shaped BSA particles with an aspect ratio of 24, produced by TFF, formed highly open, low density, space-filling flocs, held together weakly by VDW forces, in HFA that were stable against settling for over one year at a drug concentration of 10 mg/mL. In contrast, spherical particles produced by milling formed dense aggregates in HFA at the same drug loading settled within one minute. Therefore, the pMDI suspension stability is dependent on the geometry of the suspended particles, and not on surfactants or stabilizers. Upon pMDI actuation, the atomized HFA droplets were shown to break apart and template the weakly associated, highly open, friable flocs. Evaporation of the HFA droplet produced capillary forces that compacted the templated floc to produce porous particles with optimal mass median aerodynamic diameters (MMAD) for deep lung delivery. The pMDI suspensions composed of anisotropic particles produced aerosol particles with geometric diameters on the order of 10 μm with low densities, on the order of 0.2 g/cm^3, which enabled optimal MMADs between 3-4 μm, high fine particle fractions (47%), and a delivered dose up to 0.7 mg/actuation.

The novel concept of purposely forming flocs for efficient pMDI delivery, presented in chapter 3, was extended to another drug system, as well as to the delivery of higher drug doses in chapter 4. Anisotropic particles of a poorly water soluble drug, itraconazole (Itz) were also shown to form stable suspensions in HFA as well as to yield aerosol particles possessing optimal aerodynamic sizes for deep lung deposition. The effects of particle size, shape and aspect ratio on floc formation and structure, as well as aerodynamic properties upon pMDI delivery were examined. In comparison to the BSA nanorods that possessed an aspect ratio of 24, the ability of the Itz particles of different morphologies, which include thin, rectangular plates (maximum dimension of 600 nm, aspect ratio of 10) and long, needle-shaped crystals (maximum dimension of 8 μm, aspect ratio of 5), to form stable suspensions of open flocs in HFA is examined. In addition, the ability of these lower aspect ratio particles to produce appropriately-sized aerosol particles for deep lung delivery is also discussed. This concept of floc formation for pMDIs was further explored by studying the ability of these pMDI compositions to handle higher drug loadings, up to 50 mg/mL, in terms of suspension stability and aerosol performance. Despite the factor of 5 increase in drug loading, stable suspensions in HFA, optimal MMADs between 3-4 μm, and high FPFs up to 64%, while delivering total emitted doses up to 3.5 mg/actuation, were achieved. Finally, improved dissolution rates for the aerosolized, porous flocs of the poorly water soluble drug, Itz, relative to dense aggregates of milled particles, is also described. This novel concept of forming extremely stable pMDI suspensions without stabilizers, based on the flocculation of anisotropic particles, is of practical interest because it encompasses a wide-range of drug classes, demonstrates increased deliverable doses from a pMDI, and enhances the dissolution of particles that are delivered to the lungs.

In contrast to the flocculation methods presented in chapters 3-4 where loose, open flocs were desirable, chapters 5-6 discusses the assembly of gold nanoparticles into tight, closely-spaced clusters for applications in biomedical imaging and therapy. In chapters 3-4, weak VDW interactions between anisotropic particles, in which the contact areas between particles was small, facilitated the formation of open, low density flocs. For the clusters of spherical gold nanoparticles, much more dense assemblies were formed, as expected, due to more efficient packing of spherical particles. Chapter 5 introduces a novel platform for the kinetically-controlled assembly of 5 nm gold particles into ~100 nm metal/polymer biodegradable nanoclusters with strong NIR absorbance for multimodal applications. The small size of the clusters is shown to enable efficient uptake by macrophage cells, while close-spacing between gold nanoparticles within the clusters facilitates strong NIR scattering and absorption. The nanoclusters are bound together with a biodegradable triblock copolymer of polylactic acid and polyethylene glycol, PLA(2K)-*b*-PEG(10K)-*b*-PLA(2K), enabling cluster deaggregation under physiological conditions to release the constituent clearable gold nanoparticles. The ability of the clusters to deaggregate minimizes concerns of systemic toxicity and particle accumulation. The nanocluster size and spacing between constituent gold nanoparticles are controlled by regulating particle concentration during cluster formation, as well as mediating interactions between ligand-coated gold cores and the biodegradable polymer binder. Key aspects in this chapter are to demonstrate the ability of these nanoclusters to be taken up by live macrophage cells and to deaggregate into clearable particles within the cells.

By elucidating a detailed mechanism by which these clusters are formed, nanocluster properties, such as size and interparticle spacing, may be tuned. A mechanism to describe nanocluster formation, growth, and assembly in terms of the electrostatic, VDW, steric and depletion forces is presented in chapter 6. Nanoclusters with high gold loadings are produced upon the nucleation of electrostatically stabilized gold nanoparticles at high volume fractions in the presence of a weakly adsorbing polymer. Polymer adsorption to the gold nanoparticles reduces particle charge and thus weakens electrostatic repulsion, facilitating cluster growth by VDW forces. The purposeful nucleation of clusters by polymer adsorption also enables regulation of cluster size because the adsorbed polymer provides steric stabilization to the growing cluster. Therefore, cluster growth is controlled by simultaneously increasing gold and polymer concentrations using physical processes, such as solvent evaporation or mixing. Along with high gold particle volume fractions, depletion forces, which exclude the weakly adsorbed polymer from the cluster interior, facilitate low polymer loadings and close spacing between gold particles. Exclusion of the polymer to the cluster exterior provides sufficient steric stabilization to prevent unregulated cluster growth, enabling the tuning of the cluster size down to only ~30 nm. Therefore, the key to controlling both cluster size and interparticle spacing within the cluster is the inclusion of a weakly adsorbing polymer that simultaneously facilitates cluster nucleation and provides steric stabilization to the nucleating cluster. The generality of this kinetically controlled nanocluster assembly method, capable of producing clusters with high metal loadings and sizes between 30-100 nm, demonstrates great promise , as the ability to pack high levels of functionality into small clusters is applicable for a wide range of fields, including sensors, memory devices, and optoelectronics, in addition to multimodal systems for biomedical applications.

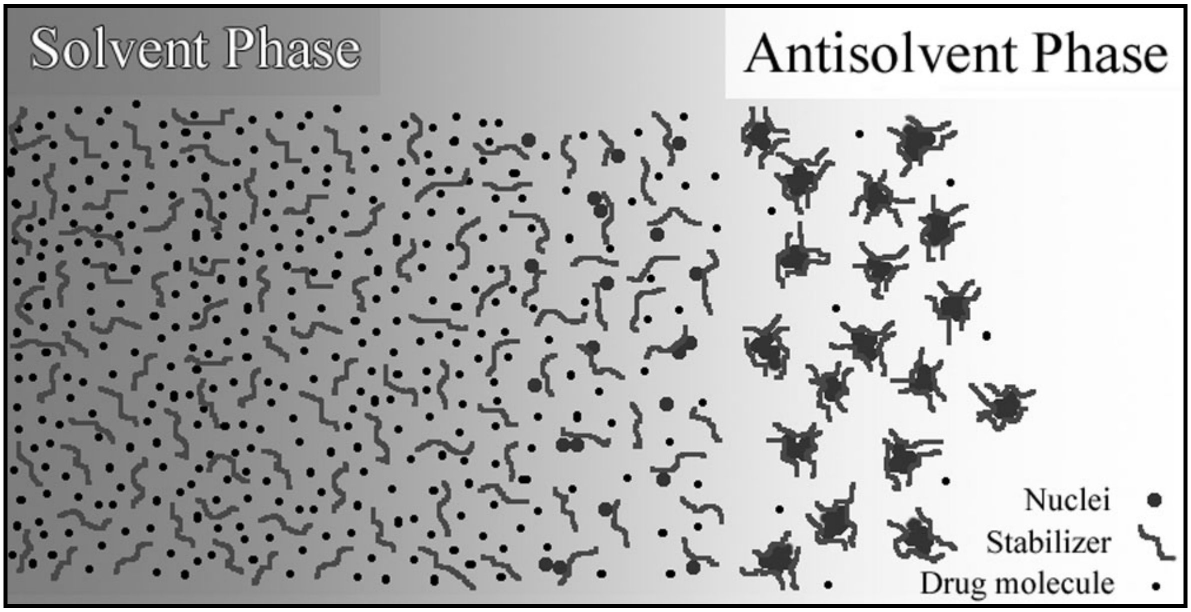

Figure 1.1 Controlled precipitation of drug particles in the presence of amphiphilic molecules[19].

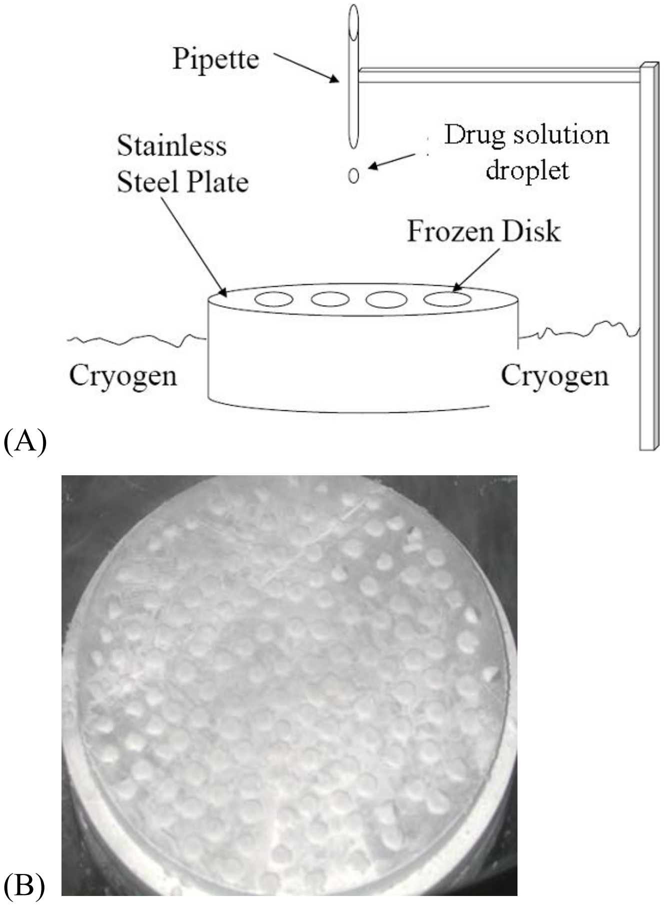

Figure 1.2 (A) Schematic of the TFF process and (B) photograph of the frozen drug droplets after impaction onto the cryogenically cooled surface.

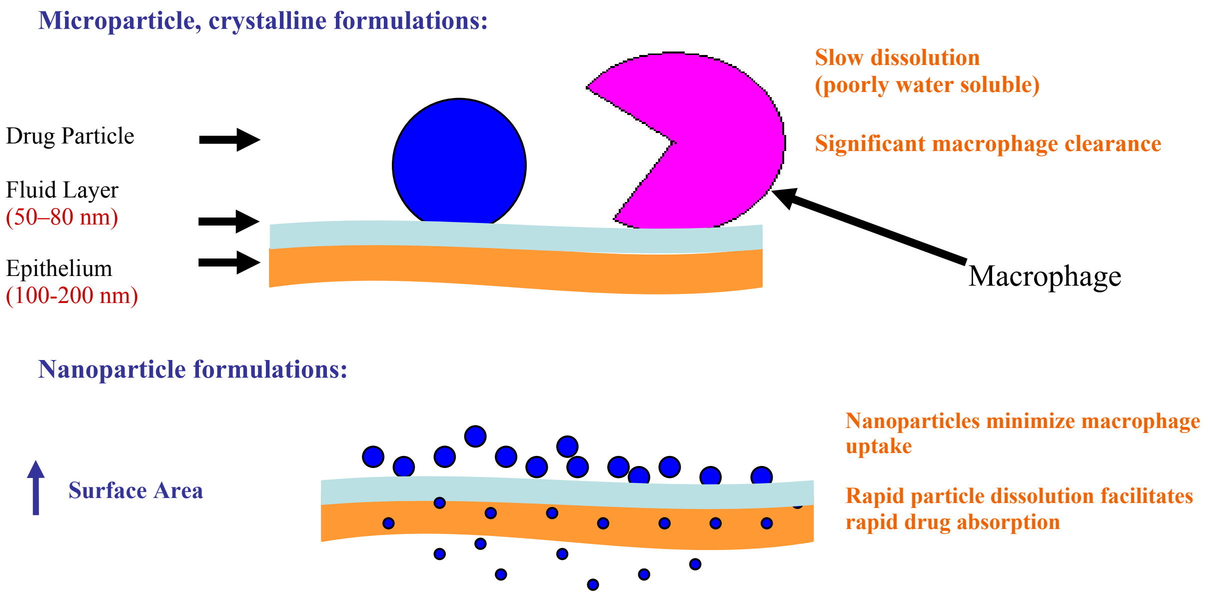

Figure 1.3 Nanoparticle formulations may enhance bioavailability by minimizing macrophage uptake and improving dissolution rates.

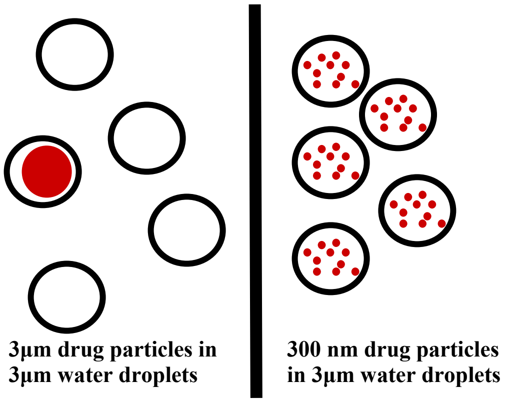

Figure 1.4 Schematic to demonstrate that nanoparticles are more evenly distributed within 1-4 µm water droplets, compared to 3 µm particles.

1.5 REFERENCES

1. Sanvicens, N.; Marco, M. P., Multifunctional nanoparticles – properties and prospects for their use in human medicine *Trends in Biotechnology* **2008,** 26, (8), 425-433.

2. Lipinski, C., Poor aqueous solubility - an industry wide problem in drug discovery. *American Pharmaceutical Review* **2002,** 5, 82-85.

3. Lipinski, C. A., Avoiding investment in doomer drugs, is poor solubility an industry wide problem? *Current Drug Discovery* **2001**, 17-19.

4. Amidon, G. L.; Lennernaes, H.; Shah, V. P.; Crison, J. R., A theoretical basis for a biopharmaceutic drug classification: the correlation of in vitro drug product dissolution and in vivo bioavailability. *Pharmaceutical Research* **1995,** 12, (3), 413-20.

5. Noyes, A. A.; Whitney, W. R., The rate of solution of solid substances in their own solutions. . *Journal of the American Chemical Society* **1897,** 19, 930-934.

6. Ferrari, M., Cancer nanotechnology: opportunities and challenges. *Nature Reviews Cancer* **2005,** 5, (3), 161-171.

7. Zhou, Y.; Jiang, K.; Chen, Y.; Liu, S., Gold nanoparticle-incorporated core and shell crosslinked micelles fabricated from thermoresponsive block copolymer of N-isopropylacrylamide and a novel primary-amine containing monomer. *Journal of Polymer Science, Part A: Polymer Chemistry* **2008,** 46, (19), 6518-6531.

8. Waters, V.; Sokol, S.; Reddy, B.; Soong, G.; Chun, J.; Prince, A., The effect of cyclosporin A on airway cell proinflammatory signaling and pneumonia. *American Journal of Respiratory Cell and Molecular Biology* **2005,** 33, (2), 138-144.

9. Wang, A. Z.; Bagalkot, V.; Vasilliou, C. C.; Gu, F.; Alexis, F.; Zhang, L.; Shaikh, M.; Yuet, K.; Cima, M. J.; Langer, R.; Kantoff, P. W.; Bander, N. H.; Jon, S.; Farokhzad, O. C., Superparamagnetic iron oxide nanoparticle-aptamer bioconjugates for combined prostate cancer imaging and therapy. *ChemMedChem* **2008,** 3, (9), 1311-1315.

10. Weissleder, R., Molecular Imaging in Cancer. *Science* **2006,** 312, (5777), 1168-1171.

11. Jiang, W.; Kim, B. Y. S.; Rutka, J. T.; Chan, W. C. W., Nanoparticle-mediated cellular response is size-dependent. *Nature Nanotechnology* **2008,** 3, (3), 145-150.

12. Liversidge, E. M.; Liversidge, G. G.; Cooper, E. R., Nanosizing: a formulation approach for poorly-water-soluble compounds. *European Journal of Pharmaceutical Sciences* **2003,** 18, 113-120.

13. Jacobs, C.; Kayser, O.; Muller, R. H., Nanosuspensions as a new approach for the formulation for the poorly soluble drug tarazepide. *Int J Pharm* **2000,** 196, 161-164.

14. Muller, R. H.; Bohm, B. H. L. In *Nanosuspensions*, Colloidal Drug Carriers Expert Meeting, Berlin, 1997; Berlin, 1997; pp 149-174.

15. Muller, R. H.; Jacobs, C.; Kayser, O., Nanosuspensions as particulate drug formulations in therapy: Rationale for development and what we can expect for the future. *Advanced Drug Delivery Reviews* **2001,** 47, 3-19.

16. Shoyele, S. A.; Cawthorne, S., Particle engineering techniques for inhaled biopharmaceuticals. *Advanced Drug Delivery Reviews* **2006,** 58, (9-10), 1009-1029.

17. Rasenack, N.; Muller, B. W., Dissolution Rate Enhancement by in Situ Micronization of Poorly Water-Soluble Drugs. *Pharmaceutical Research* **2002,** 19, (12), 1894-1900.

18. Rogers, T. L.; Gillespie, I. B.; Hitt, J. E.; Fransen, K. L.; Crowl, C. A.; Tucker, C. J.; Kupperblatt, G. B.; Becker, J. N.; Wilson, D. L.; Todd, C.; Broomall, C. F.; Evans, J. C.; Elder, E. J., Development and Characterization of a Scalable Controlled Precipitation Process to Enhance the Dissolution of Poorly Water-Soluble Drugs. *Pharmaceutical Research* **2004,** 21, (11), 2048-2057.

19. Matteucci, M. E.; Hotze, M. A.; Johnston, K. P.; Williams, R. O., III, Drug Nanoparticles by Antisolvent Precipitation: Mixing Energy versus Surfactant Stabilization. *Langmuir* **2006,** 22, (21), 8951-8959.

20. Matteucci, M. E.; Brettmann, B. K.; Rogers, T. L.; Elder, E. J.; Williams, R. O.; Johnston, K. P., Design of Potent Amorphous Drug Nanoparticles for Rapid Generation of Highly Supersaturated Media. *Molecular Pharmaceutics* **2007,** 4, (5), 782-793.

21. Young, T. J.; Mawson, S.; Johnston, K., Rapid Expansion from Supercritical to Aqueous Solution to Produce Submicron Suspensions of Water-Insoluble Drugs. *Biotechnology Progress* **2000,** 16, 402-407.

22. Vaughn, J. M.; Gao, X.; Yacaman, M.-J.; Johnston, K. P.; Williams, R. O., Comparison of powder produced by evaporative precipitation into aqueous solution (EPAS) and spray freezing into liquid (SFL) technologies using novel Z-contrast STEM and complimentary techniques. *European Journal of Pharmaceutics and Biopharmaceutics* **2005,** 60, (1), 81-89.

23. Overhoff, K. A.; Engstrom, J. D.; Chen, B.; Scherzer, B. D.; Milner, T. E.; Johnston, K. P.; Williams, R. O., Novel ultra-rapid freezing particle engineering process for enhancement of dissolution rates of poorly water-soluble drugs. *European Journal of Pharmaceutics and Biopharmaceutics* **2007,** 65, (1), 57-67.

24. Overhoff, K. A.; Moreno, A.; Miller, D. A.; Johnston, K. P.; Williams, R. O., Solid dispersions of itraconazole and enteric polymers made by ultra-rapid freezing. *International Journal of Pharmaceutics* **2007,** 336, (1), 122-132.

25. Engstrom, J. D.; Lai, E. S.; Ludher, B.; Chen, B.; Milner, T. E.; Kitto, G. B.; Williams III, R. O.; Johnston, K. P., Formation of stable submicron protein particles by thin film freezing. *Pharmaceutical Research* **2008,** 25, (6), 1334-1336.

26. Engstrom, J. D.; Simpson, D. T.; Cloonan, C.; Lai, E. S.; Williams, R. O., III; Kitto, G. B.; Johnston, K. P., Stable high surface area lactate dehydrogenase particles produced by spray freezing into liquid nitrogen. *European Journal of Pharmaceutics and Biopharmaceutics* **2007,** 65, (2), 163-174.

27. Brust, M.; Walker, M.; Bethell, D.; Schiffrin, D. J.; Whyman, R., Synthesis of thiol-derivatized gold nanoparticles in a two-phase liquid-liquid system. *Journal of the Chemical Society, Chemical Communications* **1994**, (7), 801-2.

28. Grabar, K. C.; Allison, K. J.; Baker, B. E.; Bright, R. M.; Brown, K. R.; Freeman, R. G.; Fox, A. P.; Keating, C. D.; Musick, M. D.; Natan, M. J., Two-dimensional arrays of colloidal gold particles: a flexible approach to macroscopic metal surfaces. *Langmuir* **1996,** 12, 23535-2361.

29. Qu, Y.; Lu, X., Aqueous synthesis of gold nanoparticles and their cytotoxicity in human dermal fibroblasts-fetal. *Biomedical Materials* **2009,** 4, (2), 025007/1-025007/5.

30. Turkevich, J.; Stevenson, P. C.; Hillier, J., The nucleation and growth processes in the synthesis of colloidal gold. *Discussions of the Faraday Society* **1951,** No. 11, 55-75.

31. Turkevich, J.; Stevenson, P. C.; Hillier, J., The formation of colloidal gold. *Journal of Physical Chemistry* **1953,** 57, 670-3.

32. Moon, S. Y.; Sekino, T.; Kusunose, T.; Tanaka, S.-i., Simple one-step synthesis of water and organic media soluble gold nanoparticles with various shapes and sizes. *Journal of Crystal Growth* **2009,** 311, (3), 651-656.

33. Hadinoto, K.; Phanapavudhikul, P.; Kewu, Z.; Tan, R. B. H., Dry powder aerosol delivery of large hollow nanoparticulate aggregates as prospective carriers of nanoparticulate drugs: Effects of phospholipids. *International Journal of Pharmaceutics* **2007,** 333, (1-2), 187-198.

34. Hadinoto, K.; Phanapavudhikul, P.; Zhu, K.; Tan, R. B. H., Novel Formulation of Large Hollow Nanoparticles Aggregates as Potential Carriers in Inhaled Delivery of Nanoparticulate Drugs. *Industrial & Engineering Chemistry Research* **2006,** 45, (10), 3697-3706.

35. Tsapis, N.; Bennett, D.; Jackson, B.; Weitz, D. A.; Edwards, D. A., Trojan particles: large porous carriers of nanoparticles for drug delivery. *Proceedings of the National Academy of Sciences of the United States of America* **2002,** 99, (19), 12001-12005.

36. Aaron, J.; Nitin, N.; Travis, K.; Kumar, S.; Collier, T.; Park, S. Y.; Jose-Yacaman, M.; Coghlan, L.; Follen, M.; Richards-Kortum, R.; Sokolov, K., Plasmon resonance coupling of metal nanoparticles for molecular imaging of carcinogenesis in vivo. *Journal of Biomedical Optics* **2007,** 12, (3), 034007/1-034007/11.

37. Aaron, J. S.; Oh, J.; Larson, T. A.; Kumar, S.; Milner, T. E.; Sokolov, K. V., Increased optical contrast in imaging of epidermal growth factor receptor using magnetically actuated hybrid gold/iron oxide nanoparticles. *Optics Express* **2006,** 14, (26), 12930-12943.

38. Larson, T. A.; Bankson, J.; Aaron, J.; Sokolov, K., Hybrid plasmonic magnetic nanoparticles as molecular specific agents for MRI/optical imaging and photothermal therapy of cancer cells. *Nanotechnology* **2007,** 18, (32), 325101/1-325101/8.

39. Sokolov, K. V.; Follen, M.; Aaron, J.; Pavlova, I.; Malpica, A.; Lotan, R.; Richards-Kortum, R., Real-time vital optical imaging of precancer using anti-epidermal growth factor receptor antibodies conjugated to gold nanoparticles. *Cancer Research* **2003,** 63, 1999-2004.

40. Courrier, H. M.; N. Butz; Vandamme, T. F., Pulmonary Drug Delivery Systems: Recent Developments and Prospects. *Critical Reviews in Therapeutic Drug Carrier Systems* **2002,** 19, (4 and 5), 425-498.

41. Bernstein, J. A.; Amin, H.; Smith, S., Therapeutic Uses of Lung Aerosol. In *Inhalation Aerosols: Physical and Biological Basis for Therapy*, Hickey, A. J., Ed. Informa healthcare USA, Inc.: New York, NY, 2007; Vol. 221, pp 219-252.

42. Benfait, C., Kos reports achievements of new research and development milestones. *Kos Press Release* **2004**.

43. Edwards, D.; Hanes, J.; Caponetti, G.; Mintzes, J.; Deaver, D.; Lotan, N.; Langer, R., Large Porous Particles for Pulmonary Delivery. *Science* **1997,** 276.

44. Patton, J. S., Unlocking the opportunity of tight glycaemic control: innovative delivery of insulin via the lung. *Diabetes, Obesity and Metabolism* **2005,** 7, (Suppl. 1), S5-S8.

45. Patton, J. S.; Bukar, J. G.; Eldon, M. A., Clinical pharmacokinetics and pharmacodynamics of inhaled insulin. *Clinical Pharmacokinetics* **2004,** 43, (12), 781-801.

46. White, S.; Bennett, D. B.; Cheu, S.; Conley, P. W.; Guzek, D. B.; Gray, S.; Howard, J.; Malcolmson, R.; Parker, J. M.; Roberts, P.; Sadrzadeh, N.; Schumacher, J. D.; Seshadri, S.; Sluggett, G. W.; Stevenson, C. L.; Harper, N. J., EXUBERA: Pharmaceutical Development of a Novel Product for Pulmonary Delivery of Insulin. *Diabetes Technology & Therapeutics* **2005,** 7, (6), 896-906.

47. Charnick, S. B.; Yu, Z.; Athill, L. V.; Karara, A. H.; Tse, F. L. S.; Lau, D. T. W., Pharmacokinetics of SDZ 64-412, a novel antiasthmatic agent, following intravenous, oral, and inhalation dosing in the rat. *Biopharmaceutics & Drug Disposition* **1994,** 15, (4), 317-27.

48. Watts, A. B.; McConville, J. T.; Robert O. Williams, I., Current Therapies and Technological Advances in Aqueous Aerosol Drug Delivery. *Drug Development and Industrial Pharmacy* **2008,** 34, (9), 913-922.

49. Keenan, R. J.; Iacono, A.; Dauber, J. H.; Zeevi, A.; Yousem, S. A.; Ohori, N. P.; Burckart, G. J.; Kawai, A.; Smaldone, G. C.; Griffith, B. P., Treatment of refractory acute allograft rejection with aerosolized cyclosporine in lung transplant recipients. *Journal of Thoracic and Cardiovascular Surgery* **1997,** 113, (2), 335-341.

50. Shoyele, S. A.; Slowey, A., Prospects of formulating proteins/peptides as aerosols for pulmonary drug delivery. *International Journal of Pharmaceutics* **2006,** 314, (1), 1-8.

51. Atkins, P. J.; Barker, N. P.; Mathisen, D., The design and development of inhalation drug delivery systems. In *Pharmaceutical Inhalation Aerosol Technology*, Hickey, A. J., Ed. Marcel Dekker Inc.: New York, New York, 1992; Vol. 54, pp 155-185.

52. Smyth, H. D. C., The influence of formulation variables on the performance of alternative propellant-driven metered dose inhalers. *Advanced Drug Delivery Reviews* **2003,** 55, (7), 807-828.

53. Terzano, C., Pressurized Metered Dose Inhalers and Add-on Devices. *Pulmonary Pharmacology & Therapeutics* **2001,** 14, (5), 351-366.

54. Heyder, J.; Gebhart, J.; Rudolf, G.; Schiller, C. F.; Stahlhofen, W., Deposition of particles in the human respiratory tract in the size range 0.005-15 [mu]m. *Journal of Aerosol Science* **1986,** 17, (5), 811-825.

55. Heyder, J.; Rudolf, G., Mathematical models of particle deposition in the human respiratory tract. *Journal of Aerosol Science* **1984,** 15, (6), 697-707.

56. Kreyling, W. G.; Scheuch, G., *Clearance of Particles Deposited in the Lungs* New York Marcel Dekker Inc: New York, 2000; Vol. 143.

57. Oberdoerster, G., Effects and fate of inhaled ultrafine particles. *ACS Symposium Series* **2005,** 890, (Nanotechnology and the Environment), 37-59.

58. Courrier, H. M.; Butz, N.; Vandamme, T. F., Pulmonary drug delivery systems: recent developments and prospects. *Critical Reviews in Therapeutic Drug Carrier Systems* **2002,** 19, (4 & 5), 425-498.

59. Iacono Aldo, T.; Johnson Bruce, A.; Grgurich Wayne, F.; Youssef, J. G.; Corcoran Timothy, E.; Seiler Deidre, A.; Dauber James, H.; Smaldone Gerald, C.; Zeevi, A.; Yousem Samuel, A.; Fung John, J.; Burckart Gilbert, J.; McCurry Kenneth, R.; Griffith Bartley, P., A randomized trial of inhaled cyclosporine in lung-transplant recipients. *The New England journal of medicine* **2006,** 354, (2), 141-50.

60. Burckart, G.; G. Smaldone; M. Eldon; R. Venkataramanan; J. Dauber; A. Zeevi; K. McCurry; T. McKaveney; T. Corcoran; B. Griffith; Ionoco, A., Lung Deposition and Pharacokinetics of Cyclosproine after Aeroslization in Lung Transplant Patients. *Pharmaceutical Research* **2003,** 20, (2), 252-256.

61. Klyashchitsky, B. A.; Owen, A. J., Nebulizer-compatible liquid formulations for aerosol pulmonary delivery of hydrophobic drugs: glucocorticoids and cyclosporine. *Journal of Drug Targeting* **1999,** 7, (2), 79-99.

62. Ostrander, K. D.; Bosch, H. W.; Bondanza, D. M., An in-vitro assessment of a NanoCrystal beclomethasone dipropionate colloidal dispersion via ultrasonic nebulization. *European Journal of Pharmaceutics and Biopharmaceutics* **1999,** 48, (3), 207-215.

63. Jacobs, C.; Muller, R. H., Production and characterization of a budesonide nanosuspension for pulmonary administration. *Pharmaceutical Research* **2002,** 19, (2), 189-194.

64. McConville, J. T.; Overhoff, K. A.; Sinswat, P.; Vaughn, J. M.; Frei, B. L.; Burgess, D. S.; Talbert, R. L.; Peters, J. I.; Johnston, K. P.; Williams, R. O., III, Targeted High Lung Concentrations of Itraconazole Using Nebulized Dispersions in a Murine Model. *Pharmaceutical Research* **2006,** 23, (5), 901-911.

65. Vaughn, J. M.; McConville, J. T.; Burgess, D.; Peters, J. I.; Johnston, K. P.; Talbert, R. L.; Williams, R. O., III, Single dose and multiple dose studies of itraconazole nanoparticles. *European Journal of Pharmaceutics and Biopharmaceutics* **2006,** 63, (2), 95-102.

66. Yang, W.; Tam, J.; Miller, D. A.; Zhou, J.; McConville, J. T.; Johnston, K. P.; Williams, R. O., High bioavailability from nebulized itraconazole nanoparticle dispersions with biocompatible stabilizers. *International Journal of Pharmaceutics* **2008,** 361, (1-2), 177-188.

67. Rogueda, P., Novel hydrofluoroalkane suspension formulations for respiratory drug delivery. *Expert Opinion on Drug Delivery* **2005,** 2, (4), 625-638.

68. Rogueda, P. G. A., HPFP, a model propellant for pMDIs. *Drug Development and Industrial Pharmacy* **2003,** 29, (1), 39-49.

69. Traini, D.; Rogueda, P.; Young, P.; Price, R., Surface Energy and Interparticle Forces Correlations in Model pMDI Formulations. *Pharmaceutical Research* **2005,** 22, (5), 816-825.

70. McDonald, K. J.; Martin, G. P., Transition to CFC-free metered dose inhalers - into the new millennium. *International Journal of Pharmaceutics* **2000,** 201, (1), 89-107.

71. Johnson, K. A., Interfacial phenomena and phase behavior in metered-dose inhaler formulations. *Lung Biology in Health and Disease* **1996,** 94, (Inhalation Aerosols), 385-415.

72. Selvam, P.; Peguin, R. P. S.; Chokshi, U.; da Rocha, S. R. P., Surfactant Design for the 1,1,1,2-Tetrafluoroethane-Water Interface: ab initio Calculations and in situ High-Pressure Tensiometry. *Langmuir* **2006,** 22, (21), 8675-8683.

73. Dellamary, L. A.; Tarara, T. E.; Smith, D. J.; Woelk, C. H.; Adractas, A.; Costello, M. L.; Gill, H.; Weers, J. G., Hollow porous particles in metered dose inhalers. *Pharmaceutical Research* **2000,** 17, (2), 168-174.

74. Michael, Y.; Snowden, M. J.; Chowdhry, B. Z.; Ashurst, I. C.; Davies-Cutting, C. J.; Riley, T., Characterisation of the aggregation behavior in a salmeterol and fluticasone propionate inhalation aerosol system. *International Journal of Pharmaceutics* **2001,** 221, (1-2), 165-174.

75. Keller, M., Innovations and perspectives of metered dose inhalers in pulmonary drug delivery. *International Journal of Pharmaceutics* **1999,** 186, (1), 81-90.

76. Patton, J. S., Pulmonary drug delivery comes of age: the outlook for 2005 & beyond. *Drug Delivery Technology* **2005,** 5, (4), 46-49.

77. Hirst, P. H.; Pitcairn, G. R.; Weers, J. G.; Tarara, T. E.; Clark, A. R.; Dellamary, L. A.; Hall, G.; Shorr, J.; Newman, S. P., In vivo lung deposition of hollow porous particles from a pressurized metered dose inhaler. *Pharmaceutical Research* **2002,** 19, (3), 258-264.

78. Tarara, T. E., MIchael S. Hartman, Howard Gill, Characterization of Suspension-Based Metered Dose Inhaler Formulations Composed of Spray-Dried Budesonide Microcrystals Dispersed in HFA-134a. *Pharmaceutical Research* **2004,** 21, (9), 1607-1614.

79. Weers, J. G.; Tarara, T. E.; Dellamary, L. A.; Kabalnov, A.; Schutt, E. G. Stabilized preparations for use in metered dose inhalers. 98-US20615

9916422, 19980929., 1999.

80. Ofir, Y.; Samanta, B.; Rotello, V. M., Polymer and biopolymer mediated self-assembly of gold nanoparticles. *Chemical Soceity Reviews* **2008,** 37, (9), 1814-1825.

81. Weissleder, R., A clearer vision for in vivo imaging. *Nature Biotechnology* **2001,** 19, (4), 316-317.

82. Peer, D.; Karp, J. M.; Hong, S.; Farokhzad, O. C.; Margalit, R.; Langer, R., Nanocarriers as an emerging platform for cancer therapy. *Nature Nanotechnology* **2007,** 2, (12), 751-760.

83. Jain, P. K.; El-Sayed, I. H.; El-Sayed, M. A., Gold Nanoparticles Target Cancer. *NanoToday* **2007,** 2, (1), 18-29.

84. Adler, D. C.; Huang, S.-W.; Huber, R.; Fujimoto, J. G., Photothermal detection of gold nanoparticles using phase-sensitive optical coherence tomography. *Optics Express* **2008,** 16, (7), 4376-4393.

85. Loo, C.; Lowery, A.; Halas, N.; West, J.; Drezek, R., Immunotargeted Nanoshells for Integrated Cancer Imaging and Therapy. *Nano Letters* **2005,** 5, (4), 709-711.

86. Hirsch, L. R.; Stafford, R. J.; Bankson, J. A.; Sershen, S. R.; Rivera, B.; Price, R. E.; Hazle, J. D.; Halas, N. J.; West, J. L., Nanoshell-mediated near-infrared thermal therapy of tumors under magnetic resonance guidance. *Proceedings of the National Academy of Sciences of the United States of America* **2003,** 100, (23), 13549-13554.

87. Pissuwan, D.; Valenzuela, S. M.; Killingsworth, M. C.; Xu, X.; Cortie, M. B., Targeted destruction of murine macrophage cells with bioconjugated gold nanorods. *Journal of Nanoparticle Research* **2007,** 9, (6), 1109-1124.

88. Huang, X.; El-Sayed, I. H.; Qian, W.; El-Sayed, M. A., Cancer Cell Imaging and Photothermal Therapy in the Near-Infrared Region by Using Gold Nanorods. *Journal of the American Chemical Society* **2006,** 128, (6), 2115-2120.

89. Chen, J.; Saeki, F.; Wiley, B. J.; Cang, H.; Cobb, M. J.; Li, Z.-Y.; Au, L.; Zhang, H.; Kimmey, M. B.; Li, X.; Xia, Y., Gold Nanocages: Bioconjugation and Their Potential Use as Optical Imaging Contrast Agents. *Nano Letters* **2005,** 5, (3), 473-477.

90. Skrabalak, S. E.; Chen, J.; Au, L.; Lu, X.; Li, X.; Xia, Y., Gold nanocages for biomedical applications. *Advanced Materials* **2007,** 19, (20), 3177-3184.

91. Choi, H. S.; Liu, W.; Misra, P.; Tanaka, E.; Zimmer, J. P.; Ipe, B. I.; Bawendi, M. G.; Frangioni, J. V., Renal clearance of quantum dots. *Nature Biotechnology* **2007,** 25, (10), 1165-1170.

92. Lewinski, N.; Colvin, V.; Drezek, R., Cytotoxicity of nanoparticles. *Small* **2008,** 4, (1), 26-49.

93. Srivastava, S.; Samanta, B.; Arumugam, P.; Han, G.; Rotello, V. M., DNA-mediated assembly of iron platinum (FePt) nanoparticles. *Journal of Materials Chemistry* **2007,** 17, (1), 52-55.

94. Iacovella, C. R.; Horsch, M. A.; Glotzer, S. C., Local ordering of polymer-tethered nanospheres and nanorods and the stabilization of the double gyroid phase. *The Journal of Chemical Physics* **2008,** 129, 044902-1 - 0440902-10.

95. Frankamp, B. L.; Uzun, O.; Ilhan, F.; Boal, A. K.; Rotello, V. M., Recognition-Mediated Assembly of Nanoparticles into Micellar Structures with Diblock Copolymers. *Journal of the American Chemical Society* **2002,** 124, (6), 892-893.

96. Gopidas, K. R.; Whitesell, J. K.; Fox, M. A., Nanoparticle-Cored Dendrimers: Synthesis and Characterization. *Journal of the American Chemical Society* **2003,** 125, 6491-6502.

97. Uzun, O.; Frankamp, B. L.; Sanyal, A.; Rotello, V. M., Recognition-Mediated Assembly of Nanoparticle-Diblock Copolymer Micelles with Controlled Size. *Chemistry of Materials* **2006,** 18, (23), 5404-5409.

98. Sakai, T.; Alexandridis, P., Metal nanoparticle synthesis and organization in 1D, 2D and 3D structures formed by amphiphilic block copolymers. *PMSE Preprints* **2005,** 93, 798-799.

99. Li, J.; He, W.-D.; Sun, X.-L., Preparation of poly(styrene-b-N-isopropylacrylamide) micelles surface-linked with gold nanoparticles and thermo-responsive ultraviolet-visible absorbance. *Journal of Polymer Science, Part A: Polymer Chemistry* **2007,** 45, (22), 5156-5163.

100. Bae, K. H.; Choi, S. H.; Park, S. Y.; Lee, Y.; Park, T. G., Thermosensitive Pluronic Micelles Stabilized by Shell Cross-Linking with Gold Nanoparticles. *Langmuir* **2006,** 22, (14), 6380-6384.

101. Isojima, T.; Suh, S. K.; Vander Sande, J. B.; Hatton, T. A., Controlled Assembly of Nanoparticle Structures: Spherical and Toroidal Superlattices and Nanoparticle-Coated Polymeric Beads. *Langmuir* **2009,** 25, (14), 8292-8298.

102. Harada, T.; Hatton, T. A., Formation of Highly Ordered Rectangular Nanoparticle Superlattices by the Cooperative Self-Assembly of Nanoparticles and Fatty Molecules. *Langmuir* **2009,** 25, (11), 6407-6412.

103. Isojima, T.; Lattuada, M.; Vander Sande, J. B.; Hatton, T. A., Reversible Clustering of pH- and Temperature-Responsive Janus Magnetic Nanoparticles. *ACS Nano* **2008,** 2, (9), 1799-1806.

104. Lattuada, M.; Hatton, T. A., Preparation and Controlled Self-Assembly of Janus Magnetic Nanoparticles. *Journal of the American Chemical Society* **2007,** 129, (42), 12878-12889.

105. Wilcoxon, J. P.; Martin, J. E.; Schaefer, D. W., Aggregation in colloidal gold. *Physical Review A: Atomic, Molecular, and Optical Physics* **1989,** 39, (5), 2675-88.

106. Chow, M. K.; Zukoski, C. F., Gold sol formation mechanisms: role of colloidal stability. *Journal of Colloid and Interface Science* **1994,** 165, (1), 97-109.

107. Guo, Y.; Ma, Y.; Xu, L.; Li, J.; Yang, W., Conformational Change Induced Reversible Assembly/Disassembly of Poly-L-lysine-Functionalized Gold Nanoparticles. *Journal of Physical Chemistry C* **2007,** 111, (26), 9172-9176.

108. Horovitz, O.; Mocanu, A.; Tomoaia, G.; Bobos, L.; Dubert, D.; Daian, I.; Yusanis, T.; Tomoaia-Cotisel, M., Lysine mediated assembly of gold nanoparticles. *Studia Universitatis Babes-Bolyai, Chemia* **2007,** 52, (1), 97-108.

109. Murthy, V. S.; Cha, J. N.; Stucky, G. D.; Wong, M. S., Charge-Driven Flocculation of Poly(L-lysine)-Gold Nanoparticle Assemblies Leading to Hollow Microspheres. *Journal of the American Chemical Society* **2004,** 126, (16), 5292-5299.

110. Xu, L.; Guo, Y.; Xie, R.; Zhuang, J.; Yang, W.; Li, T., Three-dimensional assembly of Au nanoparticles using dipeptides. *Nanotechnology* **2002,** 13, (6), 725-728.

111. Lim, I. I. S.; Ip, W.; Crew, E.; Njoki, P. N.; Mott, D.; Zhong, C.-J.; Pan, Y.; Zhou, S., Homocysteine-mediated reactivity and assembly of gold nanoparticles. *Langmuir* **2007,** 23, (2), 826-833.

Chapter 2: Amorphous Cyclosporin Nanodispersions for Enhanced Pulmonary Deposition and Dissolution

Aqueous colloidal dispersions of amorphous cyclosporin A (CsA) nanoparticles, intended for pulmonary delivery, were formed by controlled antisolvent precipitation and stabilized with 10% polysorbate 80. Dissolution of the dispersion of CsA nanoparticles produced supersaturation values 18 times the aqueous equilibrium solubility. Nebulization of the dispersion to mice produced therapeutic lung levels and systemic concentrations below toxic limits. The sizes of the aerosolized aqueous droplets are optimal for deep lung deposition, whereas the amorphous drug nanoparticles facilitate rapid dissolution. A dissolution/permeation model was developed to characterize the effects of particle size, solubility, and drug dose on the absorption half-lives of poorly water soluble drugs in the alveolar epithelium. For crystalline 3 μm particles with a solubility of 1 μg/mL, the half-life for absorption was estimated to be 500 minutes. The half-life may be reduced to less than 1 minute by increasing the solubility by a factor of 100 with an amorphous form as well as by decreasing the particle size ten fold. The *in-vitro* and *in-vivo* data, as well as the dissolution/permeation model, indicate that nebulization of amorphous nanoparticle suspensions has the potential to enhance lung epithelial absorption markedly for poorly water soluble drugs, relative to respiratory delivery of crystalline, micron-sized particles.

2.1 INTRODUCTION

Pulmonary drug delivery has been a popular form of therapy for asthma and has become increasingly attractive for cystic fibrosis, lung cancer, immunosuppression, tuberculosis, pulmonary hypertension, and diabetes[1-5]. The advantages of this non-invasive delivery route include: (1) an enormous absorptive surface area of 140 m^2 and vasculature that facilitate rapid delivery of large drug doses, (2) targeted lung therapy with reduced systemic side effects relative to other routes of administration, and (3) avoidance of hepatic first-pass metabolism[3]. As a result, pulmonary drug doses can be 80-90% lower than a required oral dose in some cases[3, 6].

Recently, nanoparticle formulations of poorly water soluble drugs have been developed for respiratory delivery to raise dissolution rates and thus enhance bioavailability [7, 8]. The reduced macrophage uptake of nanoparticles, relative to larger particles, also minimizes pulmonary clearance[3, 9-11]. Phagocytosis is most prevalent for particles with diameters of approximately 1 μm and is reduced for particles smaller than 500 nm and larger than 3 μm[3, 10, 11]. Alveolar macrophage uptake of 1 μm particles has been observed as early as 15 minutes after nebulization[12]. Evora et al. reported up to 65% of macrophages had phagocytosed 3 μm particles within one hour after incubation in a cell culture[13]. Furthermore, 30-60% of 1-3 μm particles have been observed to be phagocytosed 2-4 hours post aerosolization, with complete pulmonary clearance of particles within 24 hours [11, 14, 15]. Large, porous particles, with diameters of 5-20 μm, have also been delivered to the lungs because of their ability to evade macrophage clearance[16-18].

Although nanoparticles offer the benefit of enhanced dissolution, the particles are predominantly exhaled after inspiration, without appreciable deposition, as a consequence of their low inertia [19-21]. Tsapis and Edwards formed “Trojan particles” composed of polystyrene nanoparticle aggregates in the form of a hollow sphere with a favorable aerodynamic diameter to address this challenge[9]. The nanoparticles were released upon contact with a dissolution medium such as alveolar fluid, offering the potential for rapid dissolution. Nebulization of aqueous nanoparticle dispersions is an alternative approach[22-24]. The aqueous droplet diameters may be tuned to 1-5 μm, the ideal range for deep lung delivery [3]. Nanoparticle dispersions are more stable against flocculation and settling relative to microparticle dispersions, particularly for low molecular weight steric stabilizers such as polysorbate 80. Furthermore, nanoparticles have been shown to be distributed more uniformly throughout the 1-5 μm carrier droplets than microparticles [7, 25, 26]. Suppose the volume fraction, *f*, of particles in the solvent is 0.01. Then only about 1/100 of 3 μm carrier droplets will contain a 3 μm particle. In contrast each carrier droplet would contain about ten 300 nm particles according to the relationship:

$$N_{\text{particles}}/N_{\text{drops}} = f \, \frac{r_{\text{drop}}^{3}}{r_{\text{particle}}^{3}} \qquad (2.1)$$

Thus, nanoparticle colloidal dispersions, relative to microparticle colloidal dispersions, have the potential to increase the rate of drug absorption by promoting more uniform drug distribution throughout the alveoli[22, 26]. Furthermore, aerosol impactor studies show improvements in fine particle fractions (percentage of the emitted dose that deposits within the region of therapeutic benefit [26]) for nebulization of dispersions of nanoparticles relative to micron-sized particles [7, 26, 27].

Methods of forming drug nanoparticles for inhalation include encapsulation into a polymer [28-30], liposome [31], solid lipid nanoparticle (SLN) [32], or complexation into cyclodextrin [33-35]. Despite the benefits of these techniques, the drug/excipient ratio is limited in some cases and the long-term cytotoxic effects of the excipients must be considered. Ostrander et al. roller-milled beclomethasone dipropionate in an aqueous dispersion with a surfactant for approximately 4 days to produce 164 nm particles. Nebulization of aqueous dispersions of these nanoparticles delivered higher emitted doses with much higher fine particle fractions relative to the commercial microparticle product (34.8% and 56-72%, respectively)[26]. Likewise, phase I clinical trials of a nebulized crystalline nanobudesonide (75-300 nm) aqueous dispersion yielded double the maximum plasma concentrations in approximately half the time when compared to a microparticle inhalation dispersion with a mean diameter of 4.4 μm. The higher peak plasma levels were attributed to faster systemic absorption resulting from more rapid dissolution and a higher fine particle fraction [22, 36]. However, milling is not suitable for all drugs because it has been shown to produce partially amorphous drug domains complicating control of crystalline morphology, and thus the drug stability [37].

Recent studies in our laboratories have demonstrated the advantages of pulmonary delivery of both amorphous and crystalline dispersions of nanoparticles. Nebulization of nanoparticle aggregates of itraconazole, formed by spray freezing into liquid (SFL) and evaporative precipitation into aqueous solution (EPAS), yielded fine particle fractions between 71 – 85% in *in-vitro* studies and high lung concentrations in mice [23, 24]. Furthermore, high lung tissue to serum ratios demonstrated superior local therapy in the lung while minimizing systemic levels, relative to oral or parenteral delivery [24]. To further advance this delivery approach, it would be desirable to examine a variety of classes of poorly water soluble drugs and to more fully understand the effect of particle deposition in the lungs and the role of supersaturation on particle dissolution and absorption mechanisms.

CsA, a cyclic undecapeptide, is of interest for immunosuppression in patient populations that have undergone organ transplantation procedures[3, 38], treatment of autoimmune diseases[38], and the management of chronic and inflammatory conditions, such as asthma[39]. CsA is highly lyophilic and very poorly water soluble with an octanol/water partition coefficient (i.e. log P) of 4.3 [40], and a solubility of 7.3 μg/mL in water[41, 42]. The delivery of sufficient amounts of CsA to lung tissue with oral or parenteral formulations can cause severe systemic side effects as a result of renal and liver toxicity [43-45]. Furthermore, the bioavailability of oral CsA formulations has been highly variable in clinical trials [46].

Studies have been conducted to maximize drug levels in the lung and minimize systemic toxicity by nebulizing CsA solutions in ethanol to rats [47-50]. Effective immunosuppression has also been observed in human lung transplant recipients with CsA-propylene glycol solutions, which produced enhanced lung concentrations relative to oral delivery [51-54]. However, patients developed severe lung irritation even after receiving anesthesia, signifying limitations for long-term use [55]. Other studies have shown successful production and nebulization of CsA nanoparticles by liposomal [56, 57] and cyclodextrin [39] encapsulation. These methods can be limited by unknown toxicity effects[3, 31, 34], low drug loading, or drug leakage, in the case of liposomal encapsulation[31, 32, 58].

The primary objectives of the current study were (1) to nebulize stable amorphous nanoparticle dispersions of CsA to achieve high fine particle fractions and high levels of absorption into the lung epithelium, (2) to achieve higher and, thus, more favorable lung tissue to serum levels relative to oral and parenteral techniques, and (3) to more fully understand the deposition, dissolution, and absorption mechanisms for these nanodispersions. Relative to previous pulmonary studies of nanoparticle dispersions, new features of this study were to raise the drug/surfactant ratio to 10:1, examine the stability of the dispersions with respect to particle size and crystallization, investigate *in vitro* the degree of supersaturation produced in pH 7.4 dissolution media, and to examine the impact of delivering amorphous drug nanoparticles on lung absorption with a dissolution/permeation model. The amorphous nanoparticles were formed by controlled antisolvent precipitation[59] with small amounts of polysorbate 80, which adsorbed on the surface of the particles and arrested growth. The surfactant orients preferentially at the drug-water interface and not throughout the particle. Thus only a small amount of surfactant is needed to stabilize the particle, corresponding to a high drug/surfactant ratio[60, 61]. The model provides a general framework for understanding dissolution and permeation for poorly water soluble drugs with solubilities ranging from 1 to 100 μg/mL. Furthermore, this model highlights the benefits of high supersaturation levels for amorphous particles and small particle sizes. The uniform distribution of the drug particles in the aqueous droplets is shown to have the potential to influence the distribution of drug concentration in the alveoli. Finally, the model is used to estimate drug absorption half-lives as a function of supersaturation, particle size, and dose, relative to the time for the onset of macrophage uptake, which can be as little as 15 minutes after nebulization[12].

2.2 EXPERIMENTAL

2.2.1 Materials

U.S.P. grade cyclosporin A (CsA) and polysorbate 80 (T80) were purchased from Spectrum Chemical (Gardena, CA). B.P. grade itraconazole (ITZ) was acquired from Hawkins, Inc. (Minneapolis, MN). HPLC grade acetonitrile (ACN), diethyl ether, n-hexane, ACS grade hydrochloric acid (12.1 N), and methanol were used as received from Fisher Chemicals (Fairlawn, NJ). Sodium hydroxide pellets were obtained from EM Science (Gibbstown, NJ).

2.2.2 Controlled antisolvent precipitation into aqueous solution

The precipitation process used to produce nanoparticle dispersions of CsA was based on previously established methods[59, 62]. Deionized (DI) water (50 g) containing an appropriate amount of polysorbate 80 constituted the antisolvent phase into which 15 g of methanol containing 3.2% w/w CsA was injected. Vacuum distillation was used to reduce the methanol to very low residual levels in the aqueous dispersion. Nanoparticle dispersions were characterized directly after precipitation or were stored at 4°C. If dry powder was required for characterization techniques, the aqueous dispersion was frozen drop-wise into liquid nitrogen and lyophilized using a Virtis Advantage Tray Lyophilizer (Virtis Company, Gardiner, NY) with 24 hours of primary drying at -40°C followed by 36 hours of secondary drying at 25°C. Dried powders were stored in a dessicator under vacuum.

2.2.3 Particle size analysis

The size distribution of CsA particles in aqueous dispersion was measured by static light scattering with a Malvern Mastersizer-S (Malvern Instruments, Ltd., Worcestershire, UK). Approximately 4-5 mL of an 8.4 mg/mL dispersion was diluted with 500 mL of pure DI water to obtain an obscuration between 10-15%.

The size distribution of CsA particles after nebulization was measured by dynamic light scattering (DLS), as the sample size was too small for static light scattering. Approximately 5 mL of the CsA/T80 in water dispersion (8.4 mg/mL) were nebulized using an Aeroneb® Pro micropump vibrating mesh nebulizer (Aerogen Inc., Mountain View, CA) for 15 minutes. The aerosol mist was captured in a 100 mL pyrex beaker containing about 10 mL of DI water. The contents of the beaker were analyzed by a custom-built DLS apparatus [63]. The scattering angle was 90°, and the data were analyzed with a digital autocorrelator (Brookhaven BI-9000AT) with 522 real time channels and a non-negative least-squares (NNLS) method (Brookhaven 9KDLSW32). Measurements were made over a period of 2 minutes. Reported average diameters correspond to the maximum of the distribution.

2.2.4 Scanning electron microscopy (SEM)

Aqueous dispersions were diluted by approximately one-tenth using pure DI water, then flash frozen onto aluminum SEM stages pre-cooled in liquid nitrogen. In certain experiments, the aqueous dispersions were centrifuged (Sorvall, model RC-5C, Newtown, CT) for 10 minutes at 17,000 RPM at $4^{o}C$. The supernatant, containing the excess surfactant, was decanted, and the remaining particles were reconstituted with DI water to yield a concentration of approximately 1 mg/mL. The reconstituted dispersions were flash frozen onto SEM stages pre-cooled in liquid nitrogen. Subsequently, the stages were lyophilized. The remaining particles were sputter coated with gold-palladium for 30 seconds using a K575 sputter coater (Emitech Products, Inc., Houston, TX). Micrographs were taken using a Hitachi S-4500 field emission scanning electron microscope (Hitachi Ltd., Tokyo, Japan) at an accelerating voltage of 10-15 kV.

2.2.5 Brunauer-Emmett-Teller (BET) surface area measurement

Specific surface areas of powder were measured using a BET apparatus (Quantichrome Instruments, Nova 2000 version 6.11 instrument, Boynton Beach, FL) with nitrogen as the adsorbate gas. Weighed powder was added to a 9 mm Quantichrome bulb sample cell and degassed for a minimum of 8 hours. Six points were taken over a range of relative pressures from 0.05 to 0.35. The data were analyzed with the Brunauer-Emmett-Teller equation using Nova Enhanced Data Reduction Software (Version 2.13).

2.2.6 X-ray diffraction (XRD)

The crystallinity of the dried powders was determined from X-ray diffraction patterns obtained using $CuK\alpha_1$ radiation with a wavelength of 1.5404 Å at 40 kV and 20 mA from a Philips PW 1720 X-ray generator (Philips Analytical Inc., Natick, MA).

Dried powder was pressed onto a glass slide to from a level surface. A 2Θ step size of 0.05^o and a dwell time of 9 seconds were used from 5-50 2Θ degrees.

2.2.7 Temperature modulated differential scanning calorimetry (mDSC)

A 2920 modulated DSC (TA Instruments, New Castle, DE) was used to characterize drug crystallinity. The drug powders were placed in hermetically sealed aluminum pans and then purged with 150 mL/min of nitrogen. An amplitude of 1^oC, period of 1 minute, and an underlying heating rate of 5^oC/min from 25^oC to 200^oC were used. Glass transition temperatures (Tg's) were reported as the inflection point in thermograms and were determined using TA Universal Analysis 2000 software.

2.2.8 Density measurements

A Micromemeritics AccuPyc 1330 helium pycnometer (Norcross, GA) was used to determine powder density. Weighed powder was added to a 10 cm^3 sample holder. Mean values and standard deviations were obtained from three measurements.

2.2.9 Dissolution

Dissolution rates were measured by adding the nanoparticle dispersion (8.4 mg CsA/mL) to pH 7.4 phosphate buffer with 0.02% w/v SDS at 37.2^oC. The amount of the amorphous drug added was above the equilibrium solubility of the drug in its crystalline state, thus supersaturated solutions were formed. Dissolution media (50 mL) were preheated in 100 mL dissolution vessels (Varian Inc., Cary, NC) placed in a VanKel VK6010 Dissolution Tester with a Vanderkamp VK650A heater/circulator (VanKel, Cary, NC). The dispersions of the drug nanoparticles were added drop-wise to the dissolution media at a rate of approximately 10 drops/min over approximately 2.5 minutes. This slow addition technique was used to reduce the presence of excess particles, which may act as heterogeneous sites for nucleation of the supersaturated solutions and facilitate precipitation[61]. Prior to the addition of the last five drops of the dispersion, the dissolution media was clear. Subsequent addition produced slight turbidity and drug addition was terminated. At this point, the final dose was 240 µg CsA/ mL of dissolution media. In the case of bulk CsA dissolution, dispersions were produced by adding the as received drug powder to a 0.084% w/v polysorbate 80 in DI water solution and sonicating for 2-3 minutes using a Branson Sonifier 450 (Branson Ultrasonics Corporation, Danbury, CT) with a 102 converter and tip operated in pulse mode at 35 W. The dispersions were then added to the dissolution media as described above. Sample aliquots (1.5 mL) were taken at various time points and immediately filtered using a 0.02 µm syringe filter. It was assumed that drug that passed through the filter was dissolved as the filter pore size was more than 10 times smaller than the average particle diameter. The filtrate (0.8 mL) was diluted with 0.8 mL of acetonitrile. The drug concentration in all samples was quantified by HPLC.

2.2.10 Aerosol particle size analysis using a cascade impactor

An aliquot (5 mL) of the CsA/T80 in water dispersion (8.4 mg/mL) was nebulized using an Aeroneb® Pro micropump nebulizer for 10 minutes at an air flow rate of 28.3 L/min. A non-viable eight-stage cascade impactor (Thermo-Andersen, Smyrna, GA) was used to determine aerodynamic droplet size distributions and to quantify total emitted dose (TED), fine particle fraction (FPF), mass median aerodynamic diameter (MMAD), and geometric standard deviation (GSD). FPF was defined as the percentage of particles with an aerodynamic diameter less than 4.7 µm. Fiberglass filters (81 mm diameter) (ThermoFisher Scientific, Franklin, MA) were set atop each impactor plate to absorb the aerosolized suspensions and prevent overload of the plates. Each stage was rinsed with a known volume of ACN. Each filter was placed in a separate container with a known volume of ACN and allowed to soak for at least 30 minutes. Samples were filtered using a 0.2 μm syringe filter prior to quantification of drug concentrations with a high performance liquid chromatography (HPLC) method[64].

2.2.11 Pulmonary dosing to mice

Aerosols were delivered to twelve male ICR mice (Harlan Sprague Dawley Inc., Indianapolis, IN) weighing 25-30 g via nebulization with an aqueous 8.4 mg/mL CsA dispersion using a nose-only dosing chamber (Figure 2.1). The study protocol was approved by the Institutional Animal Care and Use Committee (IACUC) at the University of Texas at Austin, Austin, TX. All animals were maintained in accordance with the American Association for Accreditation of Laboratory Animal Care. Mice were acclimated in restraint tubes (Batelle, Columbus, OH) for 15 minutes/day for 2 days prior to dosing. Approximately 3 mLs of the CsA dispersion were nebulized over a 15 minute period. Two mice were sacrificed at each time point (0.5, 1, 3, 6, 12, and 24 hours after the end of aerosolization) by CO_2 narcosis. Whole blood (~ 1 mL aliquots), obtained by cardiac puncture, and lung tissue was extracted for analysis by HPLC. The amount of inhaled drug to reach the mouse was estimated to be ~3.5 mg CsA /kg body weight as calculated by the following equations: [39, 65, 66].

$$\text{Whole Body Dose(mg/kg)} = \frac{C_{\text{chamber}}\ (\text{mg/L}) * \text{RMV (L/min)} * \text{D(min)} * \text{F}}{\text{W(kg)}} \tag{2.2}$$

$$\text{RMV} = \frac{4.19 * \text{W(g)}^{0.66}}{1000} \tag{2.3}$$

$$\text{Lung Dose} = 0.05 * \text{Whole Body Dose} \tag{2.4}$$

where $C_{chamber}$ is the drug concentration in the dosing chamber, *RMV* (rate minute volume) is the volume of air inhaled in one minute, estimated by the animals' body weight, *D* is the duration of the exposure, *F* is the fine particle fraction (defined as the percentage of particles with an aerodynamic diameter less than 5.4 μm), and *W* is the animals' body weight. $C_{chamber}$ was estimated to be 30 mg/L by using average TED's from Anderson Cascade Impactor tests and the nose only dosing chamber volume to calculate the chamber concentration after each minute of nebulization and then taking the average of the concentrations over the 15 minute nebulization time. The optimal particle size for deep lung exposure in mice is approximately 3 μm[23, 67], comparable to the value of 1-3 μm for humans. Given the similarity of these values, Fukaya et al.[39] chose a FPF cut-off of 5.4 μm for mice, a typical value for humans.

2.2.12 Whole blood and lung extraction and chromatographic analysis

Calibration standards, whole blood, and homogenized lung samples were analyzed as described previously[64]. Briefly, normal saline (1 mL) was added to each harvested lung sample, which was homogenized using a rotor stator. An aliquot of a 40 μg/mL itraconazole in methanol solution (50 μL) was added to 450 μL of homogenized lung as an internal standard. A 95/5 v/v diethyl ether/methanol mixture (1.1 mL) was added to the samples. The samples were shaken on a mechanical shaker for 15 minutes and centrifuged at 6000 rpm for 5 minutes. An aliquot (900 μL) of the ether/methanol phase was pipetted to a new vial. This process was repeated. Both supernatant aliquots were added to the same vial. The sample vials were placed in an aluminum heating block (60°C) under a stream of nitrogen for ~30 minutes until dry. Methanol (450 μL), 0.025 M HCL (225 μL), and n-hexane (900 μL) were added to each sample. The samples were shaken for 5 minutes and centrifuged at 6000 rpm for 5 minutes. The n-hexane layer was discarded. Ether (450 μL) and 0.025M sodium hydroxide (450 μL) were added to each sample. The samples were shaken for 10 minutes and centrifuged as before. The ether layer was transferred to a new vial. An additional 450 μL of diethyl ether was added to each sample and the shaking and centrifugation process was repeated. The ether layer was transferred to the same vial as the ether supernatant from the previous step. The samples were evaporated to dryness under the conditions mentioned previously. The samples were reconstituted with 250 μL of mobile phase (ACN/water 70/30 v/v), vortex mixed for 1 minute, and centrifuged at 6000 rpm for 5 minutes. A 150 μL aliquot was pipetted into HPLC vials with low volume inserts. CsA was extracted from whole blood samples using the same process. Each sample was analyzed using a Shimadzu LC-10 HPLC system (Columbia, MD) equipped with a Hypersil C18 column (5 μm, 150 x 4.6mm) (Thermoelectron Corporation, Waltham, MA) protected by a C-18 guard column (5 mm, 7.5 x 4.6 mm) (Alltech Associates Inc., Deerfield, IL) heated to 75^{o}C. The CsA and Itz peak eluted at 7.8 and 4.0 minutes, respectively, at a flow rate of 1 mL/min, injection volume of 100 μL, and an absorption wavelength of 225 nm. A noncompartmental model was used to determine pharmacokinetic parameters for the lung tissue concentration profile using WinNonlin version 4.1 (Pharsight Corporation, Mountain View, CA). The whole blood concentration profile was evaluated using a one-compartmental analysis for extravascular administration.

2.3 RESULTS

2.3.1 In-vitro characterization of CsA dispersion

2.3.1.1 Morphology and size distribution for high potency nanoparticle dispersions made by controlled antisolvent precipitation

Aqueous nanodispersions of CsA intended for pulmonary delivery were formed by controlled antisolvent precipitation. Due to the lung's sensitivity to foreign material and to limit disruption of the molecular monolayer of lung surfactant, minimal amounts of excipient are desired [68]. Thus, the mass of polysorbate 80 added to the aqueous phase during precipitation was varied to determine the smallest amount of surfactant required to stabilize nanoparticles[59]. Static light scattering results (Figure 2.2) show that a CsA to polysorbate 80 ratio of 1 to 0.1 produced particles with an average diameter of 300 nm, despite the very small amount of surfactant. Drug loading was kept constant at ~8.4 mg CsA/mL. Although a small secondary peak between 2-3 μm was observed (accounting for about 20% of the particles by volume), over 80% of the particles had a diameter of 1 μm or less. For smaller amounts of surfactant extensive growth was present. Therefore, all further results in this paper refer to an 8.4 mg CsA/mL dispersion with a CsA/T80 ratio of 1/0.1.

To confirm the static light scattering results, SEM images of the 1/0.1 CsA/T80 powder were taken. Primary nanoparticles on the order of 300 nm with bridging between the particles were observed (Figure 2.3A). However, upon removal of excess polysorbate 80 from the formulation by centrifugation, the lyophilized drug particles appeared to be relatively spherical in shape without the bridges between particles (Figure 2.3B). Thus, the presence of polysorbate 80, a liquid at room temperature, during drying most likely facilitated the formation of the interconnecting bridges between the primary particles. The particle sizes in Figure 2.3B are representative of the upper end of the size distribution, as the centrifugation process for removal of excess surfactant also removed the majority of the smaller nanoparticles. To further verify that the bridging observed between nanoparticles resulted from the drying process, DLS was used to determine the hydrodynamic diameter of the CsA/T80 particles. The average diameter of 311 nm (Figure 2.4), corresponded with sizes given by static light scattering. Thus, the DLS results and the SEMs in Figure 2.3B indicate that the interconnecting bridges between the particles in Figure 2.3A appear to be an artifact of polysorbate 80's presence during drying and are not indicative of the drug particle morphology while in aqueous suspension. In contrast to the spherical nanoparticles produced by controlled antisolvent precipitation, large high aspect ratio plates were observed for the bulk drug particles with lengths greater than 15 μm and a large polydispersity (Figure 2.3C).

The particle sizes obtained from SEM and measured by static and dynamic light scattering may be compared with values inferred from BET surface area measurements.

The BET surface area of the CsA/T80 powder was ~9.5 m^2/g, which corresponds to an effective particle diameter of ~490 nm, assuming monodisperse particles. This calculated diameter is modestly higher than the results from light scattering. The difference in size could result from aggregation of the particles during drying as indicated in the bridging between primary particles in the SEMs. Overall, the difference between the sizes determined by SEM, light scattering, and BET are relatively small. The small size of the primary particles formed by the controlled antisolvent precipitation process is within the desired range for the pulmonary experiments.

To further complement the particle sizing techniques mentioned above, Stokes' settling rates were calculated for the primary particles as follows:

$$V_{\text{settling}} = \frac{2gr^2(\rho_p - \rho_{\text{medium}})}{9\eta} \qquad (2.5)$$

where r is the particle radius, ρ_p is the particle density, ρ_{medium} is the medium density, and η is the medium viscosity. For the particle concentration of 1% w/v delivered to animals, a settling front was not observed over 48 hours. Therefore, the dispersions were diluted to 0.1 % w/v to reduce turbidity in order to discern a settling front. At this low concentration, modifications to Stokes' settling rate to account for particle interactions were not needed. The calculated Stokes' settling rate for a particle with an r of 150 nm, ρ_p of 1.3 g/cm^3 (as determined by helium pycnometry) in water (ρ_{medium} of 1 g/cm^3, and η of 0.89 mPa·s) was 0.006 cm/hr (0.1 cm/day). The observed settling rate was 0.005 cm/hr. The similarity between Stokes' and experimental settling rates infer that the CsA/T80 particles are approximately 300 nm in diameter, further supporting the particle size results reported above and also indicate minimal aggregation of nanoparticles while in dispersion.

To understand the fate of particles in the droplets during nebulization, the size distribution of the sample emitted from the nebulizer was measured by DLS. The size distribution, by volume, of the nebulizer output was very similar to that of the original suspension (Figure 2.4). Thus, the nebulization process did not cause aggregation of nanoparticles in the aerosolized droplets and was capable of delivering nanoparticles to the lungs.

In addition to characterizing the particle size of the CsA/T80 formulation, the morphology was determined by XRD. The XRD pattern for the received bulk powder did not show the characteristic peaks of crystalline CsA as reported by Chen et al[60] (Figure 2.5), indicating that the starting material was predominantly amorphous. The amorphous nature of the "as received" bulk CsA was confirmed by DSC (Figure 2.6), which did not show a melting point even upon heating to 200°C. The reported CsA melting point is 150°C [69]. However, a T_g at 120°C was observed, which matches values reported in the literature[70]. An absence of crystalline peaks was also observed in the XRD pattern of 1/0.1 CsA/T80 powder (Figure 2.5), inferring a primarily amorphous morphology.

2.3.1.2 Supersaturation of aqueous media with amorphous CsA dispersion

Particle size reduction of crystalline materials raises the surface area, A, while high energy polymorphs including the amorphous state increase the solubility, C_{sat}, leading to faster dissolution rates as predicted by the Noyes-Whitney equation:

$$\frac{dM}{dt} = \frac{DA}{h}(C_{sat} - C) \qquad (2.6)$$

where M is the mass of undissolved drug, D is the diffusion coefficient, h is the boundary layer thickness, and C is the concentration in solution. Dissolution of the CsA/T80 dispersion in pH 7.4 phosphate buffer at 37°C was conducted under supersaturated conditions. In Figure 2.7, the drug concentration reached 113 μg/mL in four hours, 15.5 times the equilibrium solubility of crystalline CsA in pure water at 37°C, which was reported as 7.3 μg/mL [41, 42]. After 4 hours, the supersaturation reached a plateau and showed no sign of precipitation for up to 4 days, at which the drug concentration reached 128 μg/mL (data not shown). Dissolution of bulk powder with polysorbate 80 in the same drug to surfactant ratio of 1/0.1 was measured under supersaturation conditions. After four hours, the drug concentration was 79 μg/mL (~10.8 times the equilibrium solubility) and reached a plateau at 81 μg/mL in 4 days. Figure 2.7 also illustrates that the nanoparticle formulation dissolved much more rapidly than the bulk formulation. After 10 minutes, the nanoparticle and bulk particle concentrations were 96 and 13 μg/mL, respectively. The high levels of supersaturation maintained after 4 days indicate the presence of metastable equilibrium between the slight excess of amorphous particles and the dissolved drug.

2.3.1.3 Fine particle fraction determined by Anderson cascade impactor

The Anderson cascade impactor was used to determine the aerodynamic particle size distribution. The Aeroneb Pro micropump nebulizer produced an aqueous mist of fine droplets with sizes ranging between 1 – 4 μm [23], which falls within the optimal size range for effective aerosol delivery (i.e. between 1 and 5 μm)[3]. Upon nebulizing an aqueous nanodispersion, the physical properties of water dictate the carrier droplet size, offering the potential of high fine particle fractions and uniform drug delivery. An MMAD of 2.02 μm with a GSD of 1.83 and a FPF of 77.4% (Table 2.1) were observed.

To examine storage stability of the dispersion, the cascade impactor experiment was repeated after three weeks of storage at 4°C. The MMAD increased slightly to 2.52 μm with a GSD of 1.85 and a FPF of 73.9%. The similar TEDs of about 1450 μg/min and high fine particle fractions after three weeks of storage indicate that the particles in the dispersions still have the potential for reaching the deep lung. The relatively uniform data seen in the cascade impactor results for three weeks is consistent with the observation of slow settling fronts.

2.3.1.4 Stability of amorphous nanoparticle dispersion after 10 months

Nebulized dispersions must be stable against particle aggregation and settling to achieve uniform drug delivery. As shown in Figure 2.8, particle size distributions by volume (and also by number, not shown) for the CsA/T80 aqueous dispersion did not change significantly for up to ten months. The percentage of particles, by volume, under 1 μm remained between 85-89%, while the D_{50} (diameter at which the cumulative sample volume was under 50%) was maintained at 300 nm. Thus, despite the enhanced solubility of the amorphous nanoparticles, the mass of drug in the continuous phase is trivial when compared to the drug loading in the suspension (<1.5%, based on maximum dissolved concentrations achieved in the supersaturation experiments). The extremely low Ostwald ripening may indicate slow addition of the cyclic peptide to the surfactant coated particles[71].

In addition to particle size stability, the ability of the CsA/T80 particles to maintain an amorphous morphology while in an aqueous dispersion was also investigated. To examine storage stability, the CsA/T80 dispersion was stored for 10 months at 4°C and was then frozen and lyophilized. The resultant XRD pattern showed that the CsA/T80 nanoparticles remained amorphous over the ten month period (Figure 2.5). Furthermore, the DSC scan of the lyophilized nanoparticles did not show a melting peak, further indicating that the powder was still amorphous (Figure 2.6).

2.3.2 In-vivo characterization of CsA dispersion

The deposition of CsA/T80 nanoparticles into the deep lungs via nebulization was tested in mice. Lung tissue and blood concentration profiles following a single inhalation dose are shown in Figure 2.9, while the corresponding pharmacokinetic parameters are summarized in Table 2.2. Averaged lung levels peaked at 10.5 μg/g of wet lung tissue at 1 hour, maintaining an average concentration of at least 1.7 μg/g for 24 hours. Average blood levels peaked at 372 ng/mL at 3 hours and slowly declined to 174 ng/mL at 24 hours. Areas under the curve (AUCs) were two orders of magnitude higher in the lungs than in the blood. The systemic concentrations were desirable for therapeutic immunosuppression levels (100-250 ng/mL [72]) in humans, but were well below renal and hepatotoxic levels of 800 ng/mL[46]. Hence, nebulization of this CsA/T80 formulation has the potential to provide local lung therapy and beneficial systemic levels with minimal toxicity concerns.

2.4 DISCUSSION

2.4.1 Role of surfactant in arresting particle growth during controlled antisolvent precipitation

The controlled antisolvent precipitation process produced particles in the 300-500 nm size range, which was desirable for achieving stable nanodispersions and high fine particle fractions in the cascade impactor. As the aqueous and organic phases mixed, supersaturation was created, promoting rapid nucleation[59]. The high hydrophilicity of polysorbate 80 (HLB of 15) and hydrogen bonding interactions of the ethylene oxide groups with water caused polysorbate 80 to favor the interface between the drug particle surface and water, relative to the hydrophobic particle interior[61]. The passivation of the particle surface by polysorbate 80 hinders particle growth by condensation of molecules into the solid phase and by particle coagulation.

Polysorbate 80 was chosen as the stabilizer as it has been shown to stabilize CsA nanoparticles at concentrations of 1.0% and 5.0% w/w in aqueous media [60, 73]. Previous pulmonary formulations containing higher concentrations of polysorbate 80 nebulized to mice did not show damage, inflammation, or cell mitigation in lung cells based on histology analyses in mice [74] . Additionally, a similar product, polysorbate 20, is utilized in a pulmonary recombinant human interferon alpha-2b product developed by Aradigm[75]. However, this is simply a model system to illustrate the benefits of pulmonary nanoparticle delivery.

As shown in Figure 2.2, a CsA to polysorbate 80 ratio of 1 to 0.1 produced particles with an average diameter of 300 nm. Below this drug to surfactant ratio, particle growth was excessive, indicating limited steric stabilization and passivation. Above this ratio, the surface coverage on the growing particles became sufficient to produce the desired particle size of 300 nm, as described by the Damkoler number or ratio of mixing time to overall precipitation time. Additional amounts of polysorbate 80 did not significantly reduce the particles size, as can be noted in the particle size distribution of the 1/0.5 CsA/T80 formulation. This type of plateau region in particle size has also been observed for itraconazole and naproxen[61, 76, 77]. High drug loadings have also been achieved for CsA particles produced by evaporative precipitation into aqueous solution [60] and rapid expansion from supercritical to aqueous solution[73].

In contrast, CsA to surfactant ratios were on the order of only 1/8 for liposomes formulations in which the drug was dissolved in the relatively small volume of the bilayers [56, 78]. In liposomal and SLN encapsulations, it is challenging to produce high enough drug/lipid ratios for practical use. The concentrations of aqueous drug-liposomal dispersions may be increased to ameliorate this problem. However, the high viscosities of the concentrated dispersions [78], may result in plugging of the nebulizer jets [58]. The integrity of lipid formulations during nebulization is also a concern, as there have been numerous reports of drug leakage[31, 32, 58, 79]. Polymer and cyclodextrin complexed CsA formulations have also been investigated. The consequences of polymer or cyclodextrin internalization by macrophages and subsequent degradation within cells have not been determined. There is also concern about the effects of polymer or cyclodextrin accumulation in the lungs and how quickly these agents must degrade to minimize tissue irritation [3, 31, 34].

2.4.2 Supersaturation and particle curvature

The higher solubility of the CsA/T80 nanoparticles (r = 150 nm) relative to the solid dispersion of the large bulk particles (r = 2.5 -7.5 μm) can be analyzed by the Kelvin equation

$$\frac{x_a}{x_b} = \exp\left[\frac{2\gamma V_m}{RT}\left(\frac{1}{r_a} - \frac{1}{r_b}\right)\right] \qquad (2.7)$$

where x is the solubility of dissolved solid, γ is the interfacial tension between the particle and the solvent, V_m is the molar volume of the solute, and r is the particle radius. The greater LaPlace pressure for the smaller particles raises the chemical potential and solubility. For a V_m of 0.001 m^3/mol and a typical γ of 50 mJ/m^2 [80] between water and a hydrophobic drug, the predicted solubility ratio is 1.3. The experimentally observed value was 1.6. Thus, it is likely that curvature played a significant role in the supersaturation.

2.4.3 Modeling of dissolution and permeation rates of drugs in the lung

CsA must dissolve in the alveoli and permeate through the epithelial layer into lung tissue, before being cleared by macrophages, in order to elicit a therapeutic response[44, 45, 81]. To better understand drug absorption in the lungs, a transport model has been developed to examine the effects of solubility and particle size on drug dissolution in lung fluid and subsequent permeation through the epithelial membrane. The model will be used to determine the time for half of the drug to be absorbed, i.e. dissolve in lung fluid and permeate the epithelial layer. For simplicity, the model assumes a monodisperse particle size distribution and that the drug is either completely amorphous or completely crystalline with a single equilibrium solubility.

The dissolution rate of CsA spherical nanoparticles was determined by the Noyes-Whitney equation.

$$\frac{\partial M}{\partial t} = -\frac{D}{2r} 4\pi r^2 (C_{sat} - C) \qquad (2.8)$$

where the boundary layer thickness was approximated by the particle diameter. For spherical geometry, $M = (4/3)\pi r^3 \rho$ and

$$\frac{\partial r}{\partial t} = -\frac{D}{2r\rho}(C_{sat} - C) \qquad (2.9)$$

The flux of drug through a membrane is given by J = PΔC = P(C-0) where *P* is the permeability. The permeate drug concentration for the epithelium was assumed to be zero. A material balance on the dissolved drug in the fluid of a single alveolus includes an inlet flow for dissolution of the particles and an outlet flow for permeability through the epithelium

$$\frac{\partial C}{\partial t} = N_p D \frac{2\pi r}{V}(C_{sat} - C) - \frac{AP}{V} C \qquad (2.10)$$

where N_p is the number of drug particles deposited in an alveolus, and *V* and *A* are the volume of lung fluid and surface area for a single alveolus, respectively. The flux across the lung epithelium may be assumed to be constant since the thickness of the mouse lung epithelium (0.1-0.4 μm) is small compared to the diameter of a mouse alveolus (31 μm)[82, 83]. Therefore, a planar geometry was used for the permeation in eq. 2.10. It was assumed that the absorption of drug from each alveolus into the lung tissue was independent of absorption from other alveoli.

Equations (2.9) and (2.10) were solved simultaneously using Matlab's (Natick, MA) ode15s solver with the initial conditions of t=0, $r=r_0$ and C=0. The diffusion coefficient was estimated to be 3.8 x 10^{-6} cm^2/s using the Wilke-Chang equation[84] based upon the properties of CsA. A value of 1.0 x 10^{-5} cm/s was used for the permeability based on typical measured permeabilities of similar poorly soluble drugs in lung cell cultures, which range from 10^{-6}-10^{-4} cm/s[85]. The total number of drug particles deposited in the lungs was calculated from an estimated total mass of deposited drug and the volume of a single particle. The value for total drug mass deposited into the lungs was approximated from the lung tissue C_{max} (1.9 μg) and the corresponding blood concentration (750 ng) from the mouse study. The number of alveoli in a mouse was estimated to be ~2.25 $x10^7$ based on a reported alveolar surface area of 680 cm^2 [82] and alveolus diameter of 31 μm[83]. Total alveolar fluid volume was estimated to be 8.3 μL, on the basis of a human alveolar surface fluid volume of 15 mL [68, 86] and the ratio of human lung to mouse lung weight. The mass of permeated drug, $M_{permeated}$, or drug theoretically absorbed by lung tissue from a single alveolus, was determined from the mass of deposited drug M_o, and the masses of undissolved and dissolved drug via the material balance

$$M_0 = N_p \frac{4}{3}\pi r^3 \rho + CV + M_{permeated} \qquad (2.11)$$

Figure 2.10 illustrates predicted lung tissue absorption times for dissolution and permeation for two particle sizes and two drug dosages, M_0. In addition, three solubilities were considered (1, 10, and 100 μg/mL) to capture aqueous solubilities for typical poorly water soluble drugs including budesonide[87], CsA[41], and triamcinolone acetonide[87]. For a 12.5 μg drug/g lung dose in Figure 2.10a (chosen based on the CsA C_{max} recovered from lung tissue at t=1 hr and the corresponding blood concentration given in Figure 2.9) and 3 μm drug particles, only 1 in 192 alveoli are estimated to receive a particle, assuming uniform drug distribution throughout the mice's lungs. However, approximately 5 drug particles are deposited in each alveolus for 300 nm drug particles. Thus, values of 1 and 5 were input for N_p to estimate absorption times for 3 μm and 300 nm particles, respectively. The time required for 50% drug absorption is predicted to reach almost 10 hours for 3μm crystalline very poorly water soluble drugs (aqueous solubility = 1 μg/mL), such as the anti-asthmatics beclomethasone dipropionate[88] and fluticasone propionate[87]. With an increase in the solubility by a factor of 10, the absorption time decreases by an order of magnitude. Additionally, the combined reduction of particle size to 300 nm along with an increase in solubility to 10 μg/mL, reduces the absorption time by 3 orders of magnitude.

Figure 2.10b shows predicted absorption half lives for drug particles at a drug loading of 125 μg drug/g lung, which is comparable to lung levels achieved in clinical pulmonary CsA trials[54]. At this higher drug loading, 1 in 19 alveoli were estimated to receive a 3 μm drug particle, while each alveolus would receive 52 drug particles with 300 nm diameters. Thus, for 3 μm particles, increasing the drug loading would increase the number of alveoli that receive a drug particle, but the number of particles deposited per alveolus, N_p, is still unity for the determination of the absorption time. Therefore, predicted absorption times did not change for the 3 μm particles with dosage. Long times are required for large concentrations of drug to permeate in a small fraction of the alveoli when $N_p = 1$. Additionally, dissolution of microparticles is slower than that of nanoparticles due to the smaller particle surface area per unit volume. The absorption time increased for the 300 nm particles as the dosage was raised to 125 μg/g since N_p and the concentration of drug in each alveolus increased, but remained an order of magnitude less than the case of microparticles. For a given mass of deposited drug, the nanoparticles are distributed more uniformly throughout the alveoli leading to a much larger surface area available for absorption. For 3 μm particles, a larger mass must dissolve and permeate in a localized area, slowing the absorption process.

To focus on the dissolution resistance independently of the permeability, the half-lives were predicted for an essentially infinite permeability of 10^{10} cm/s as shown in Figure 2.10c. Here, the results were the same for both dosages of 12.5 and 125 μg/g. Since 300 nm particles undergo rapid dissolution, absorption half lives were not significantly affected by the different drug loadings. Each half life was about an order of magnitude shorter than in Figure 2.10a ($P=10^{-5}$ cm/s), indicating that the absorption was limited significantly by permeability.

Amorphous nanoparticles with solubilities of 100 μg/mL are predicted by the model to dissolve and permeate the epithelial tissue on the order of minutes. These predicted results are in agreement with experimental pulmonary absorption data conducted by Schanker and colleagues, which reported absorption half lives for a variety of lipophilic drugs (administered as a very dilute solution in phosphate buffer) to be on the order of 1 minute[89-91]. For CsA, the absorption was substantially lower than for typical lipophilic drugs, as was evident in the blood levels in Figure 2.9. It is probable, based on *in vitro* dissolution results, that CsA dissolved quite rapidly. However, CsA's high affinity to bind with the intended protein target, cyclophilin, in the lung tissue reduced further permeation into the bloodstream. Handschumacher et al. reported that 0.96 moles of CsA bound per mole of cyclophilin, indicating a high binding affinity[92]. Observations of prolonged CsA retention in lung tissue in previous studies have also been attributed to CsA binding to phospholipids in lung surfactant [54, 93]. For example, upon intra-arterial administration, CsA concentrations in the lung were an order of magnitude higher than in any of the other organs[94]. The lipophilicity of CsA promotes interactions with lung surfactant phospholipids leading to avidity for CsA by lung tissue. High binding affinities to proteins in lung tissue have also been attributed to extended drug retention in pulmonary tissues for drugs such as fluticasone propionate and amphotericin B [95-97].

2.4.4 Comparison of in vivo formulations

The present CsA/T80 dispersion offers advantages over previously reported CsA formulations as shown in Table 2.3 for reducing variability in bioavailability and systemic toxicity. Lung levels in our formulation were similar to those produced by a similar intramuscular CsA dose. However, the blood levels were five times lower[49]. An oral dose of the commercial CsA product, Neoral, dosed to mice at 10 mg/kg also yielded high blood levels, well above the toxic limit for more than 12 hours after dosing[98]. In general, doses which produce blood levels below the toxic limit have not been shown to provide sufficient absorption into lung tissue [44]. CsA is believed to bind to cyclophilin, a cytosolic protein found in lung tissue, to form a complex that inhibits calcineurin. The inhibition of calcineurin blocks T-cell activation, which is responsible for a myriad of immune and regulatory responses[99, 100]. Thus, for CsA to elicit a therapeutic response, sufficient drug levels must be absorbed into the lung tissue.

Aerosolized formulations of CsA solutions in ethanol yielded extremely high lung concentrations in a rat model[49, 50], but with extremely high systemic levels [49]. The high concentrations of ethanol exposed to the lung could have opened up tight junctions, leading to enhanced particle passage into the blood stream[101]. A solution formulation with propylene glycol, currently in clinical trials, produced lung levels as high as 112 μg/g by gamma scintigraphy, while maintaining acceptable blood levels [54]. In solution formulations, drug particles of unknown size may nucleate and grow upon mixing ethanol with lung fluids. The polydispersity in particle size will influence the dissolution rate, absorption, and thus the therapeutic effectiveness, since CsA must dissolve and be absorbed before it is cleared[44, 45, 81]. Thus, the delivery of amorphous CsA nanoparticles have the potential to enhance therapeutic effectiveness over current solution formulations by facilitating rapid absorption into the lung tissue without yielding high systemic levels. Despite rapid dissolution of the aerosolized CsA nanoparticles, localized therapy was still achieved most likely due to CsA's known affinities for constituents found in pulmonary tissue. Additionally, the large amounts of solvent required for solution formulations may not only open up tight junctions and augment CsA levels in the blood, but can in some cases cause severe lung irritation.

2.5 CONCLUSIONS

CsA amorphous nanoparticle dispersions nebulized to mice produced efficacious drug concentrations in both the lung tissue and blood stream, within the therapeutic window. This accomplishment may be particularly useful for lung transplant recipients or for those patients requiring non-steroid asthma treatment, where the effectiveness of CsA has been limited due to a narrow therapeutic window. Furthermore, nebulization of the CsA nanodispersions with high drug loadings circumvents problems in solution-based pulmonary formulations including irritation of lung tissues by organic solvents or large amounts of excipients. It also generates much higher lung tissue concentrations (10.5 μg drug/g lung) than oral and parenteral delivery, while maintaining lower systemic toxicity levels (370 ng/mL). Thus, the development of an aerosolized nanoparticle formulation to target the deep lungs will not only make CsA a more viable option for treatment of lung diseases, but this methodology can also be applied to other drugs that have narrow therapeutic windows.

In nebulization of nanoparticle dispersions, the vast difference in length scales of the drug particles and water droplets optimizes, simultaneously, both deposition and dissolution in the lung tissue. The water droplets provide high fine particle fractions (77%), whereas the size of the drug particles favors enhanced dissolution. For amorphous CsA, *in-vitro* supersaturation levels reached up to 18 times the equilibrium solubility. To better understand the drug absorption in the lungs, a dissolution/permeation model was developed to characterize the effects of particle size, morphology, solubility, and drug dose on absorption half-lives of poorly water soluble drugs in the alveolar epithelium. For a 3 μm drug particle with a solubility of 1 μg/mL, the half-life is predicted to decrease from 500 to 5 minutes with an increase in supersaturation to 100, which can be achieved by the formation of an amorphous form[61], or particle size reduction to 300 nm. Thus, the model indicates that modification of drug properties to enhance drug dissolution can affect drug absorption times markedly. Due to the flexibility of the model, it can also be applied in the development of other pulmonary poorly water soluble drug formulations to predict if absorption rates will be sufficient to avoid clearance by macrophages. For CsA, the model predicts rapid absorption into lung tissue, where interactions with the lung surfactant and/or the intended protein target cyclophilin, inhibited further permeation to the bloodstream. As a result, favorably high lung levels were maintained for 24 hours.

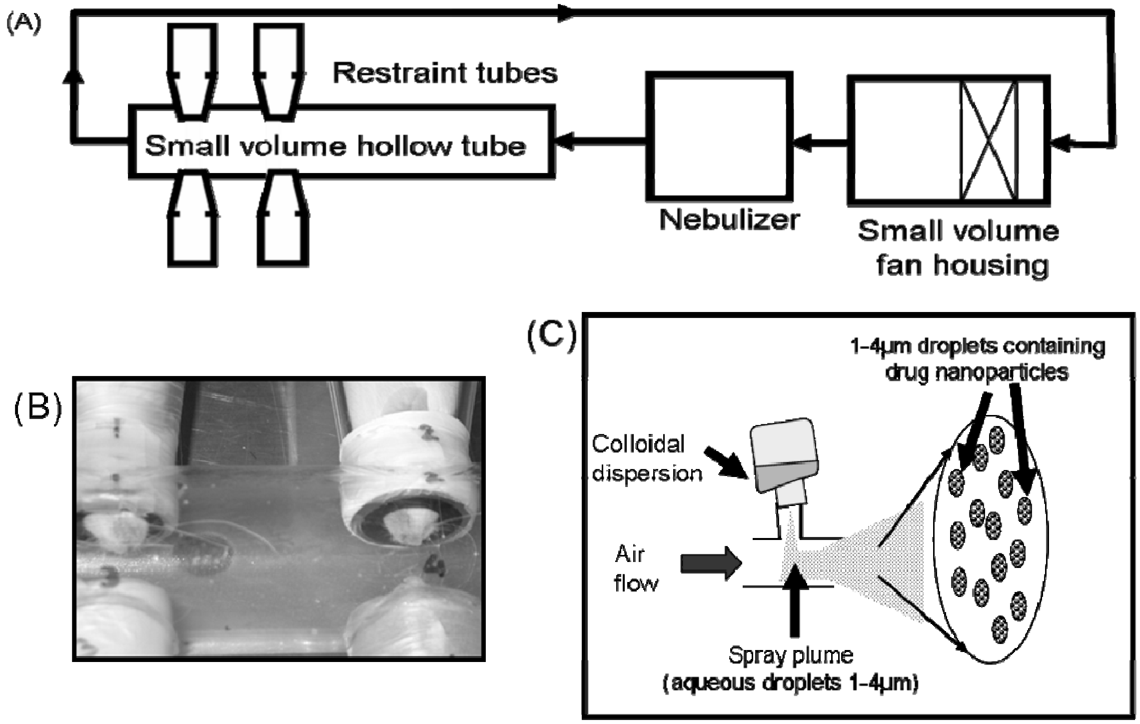

Figure 2.1 Schematic of small animal nose-only dosing apparatus: (A) Sketch of dosing apparatus, (B) Close-up image of animals' noses positioned in dosing chamber, (C) Illustration of nebulized drug dispersion, in which nanoparticles are evenly distributed within 1-4 µm water droplets.

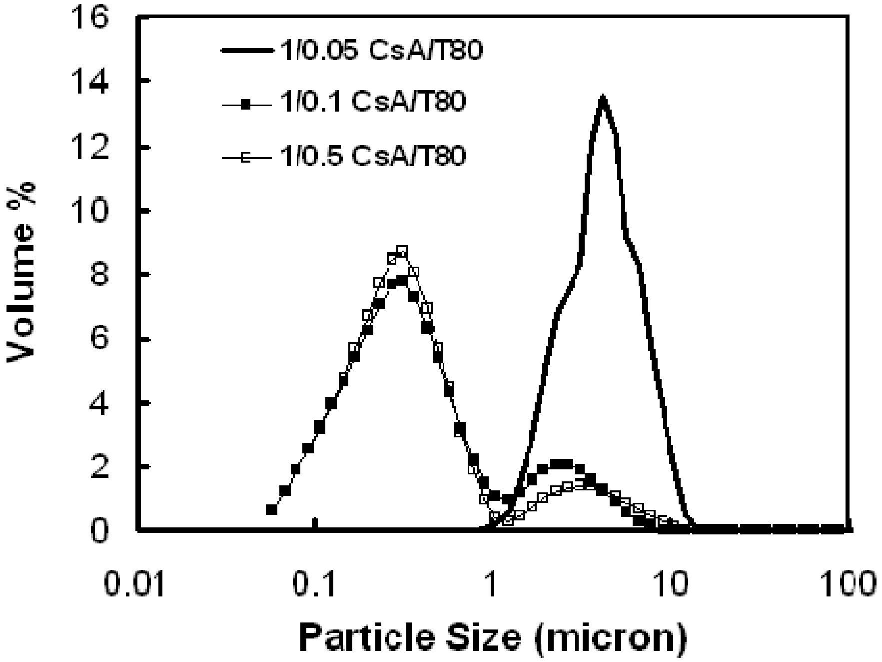

Figure 2.2 Effect of polysorbate 80 concentration on CsA particle size distribution in an aqueous dispersion.

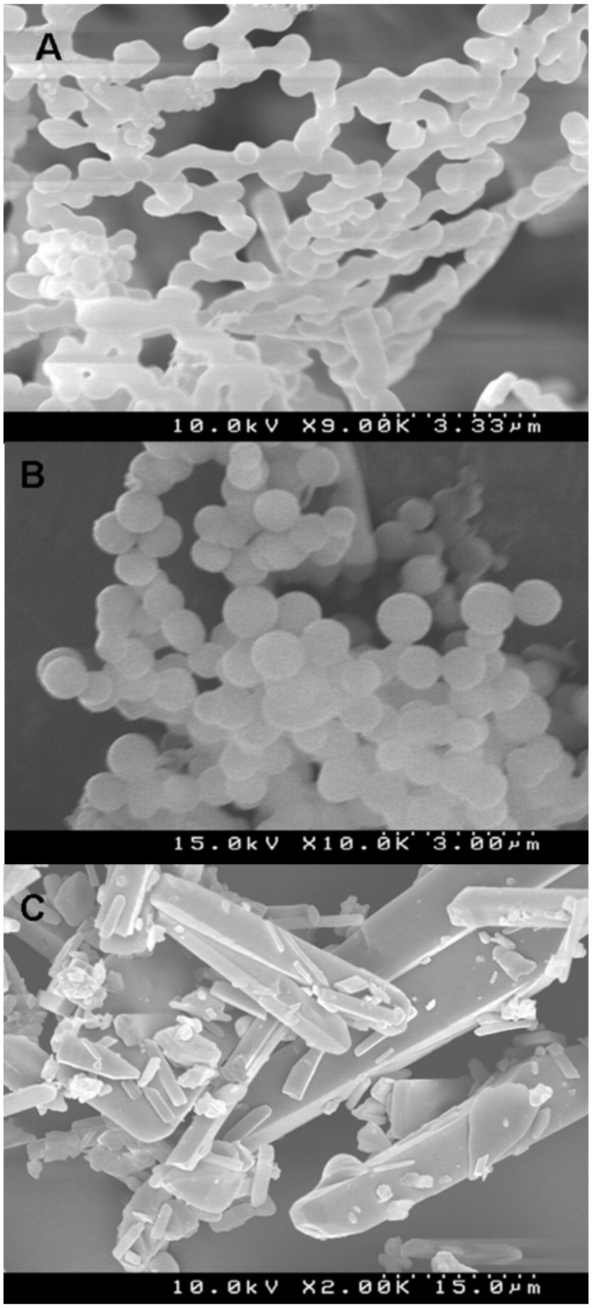

Figure 2.3 SEM images of (A) CsA:T80 (1:0.1) powder obtained by lyophilization of the nanodispersion produced by controlled antisolvent precipitation, (B) the same formulation but after removing excess polysorbate 80 prior to lyophilization, and (C) bulk CsA as received.

(A)

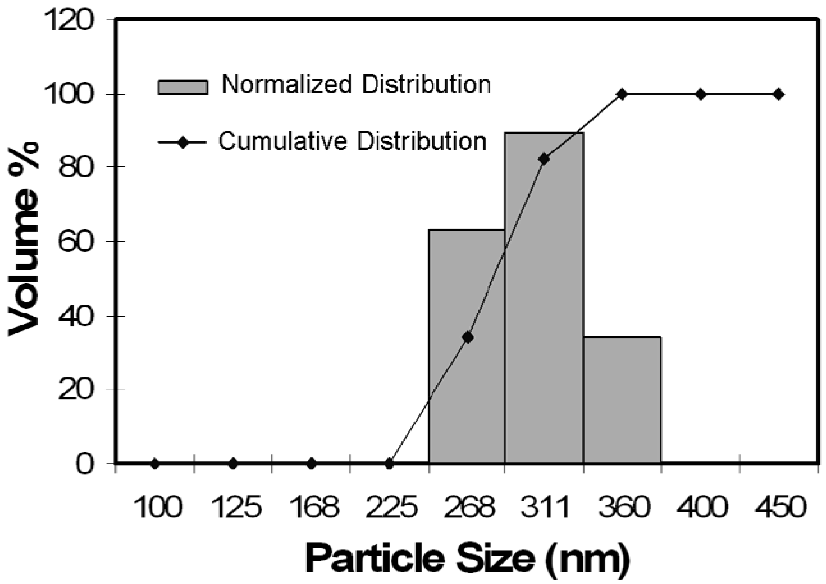

(B)

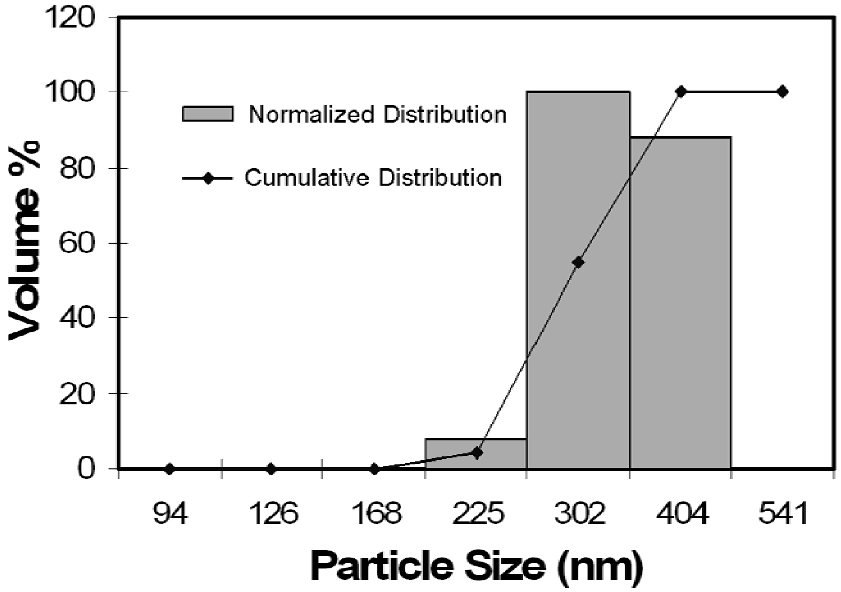

Figure 2.4 Particle size measurements of the CsA nanodispersion before (A) and after (B) nebulization. In (A), 48% of the particles, by volume, had a diameter of 296 nm or less. In (B), 55% of the particles, by volume, had a diameter of 302 nm or less.

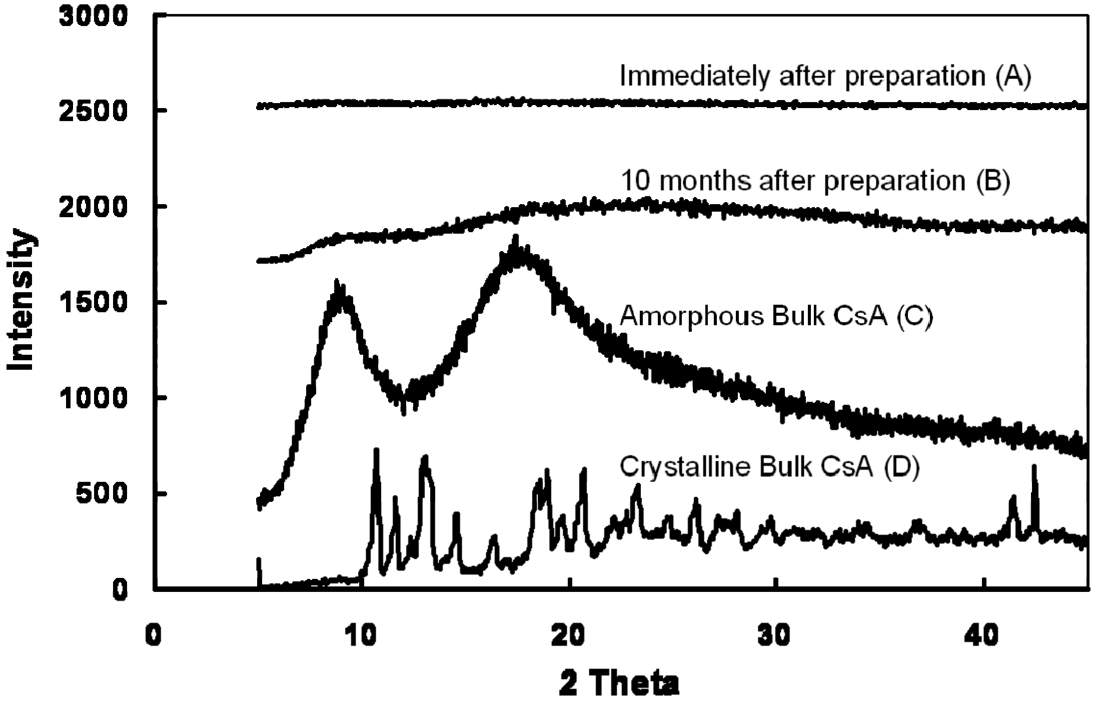

Figure 2.5 X-ray diffraction (XRD) of CsA:T80 (1:0.1) powders (A-B) and bulk CsA (C-D). Results in (D) were obtained from Chen et al.[60]. The dispersion was frozen and lyophilized immediately after precipitation in in (A) and after storage in dispersion for over 10 months at 4°C in (B).

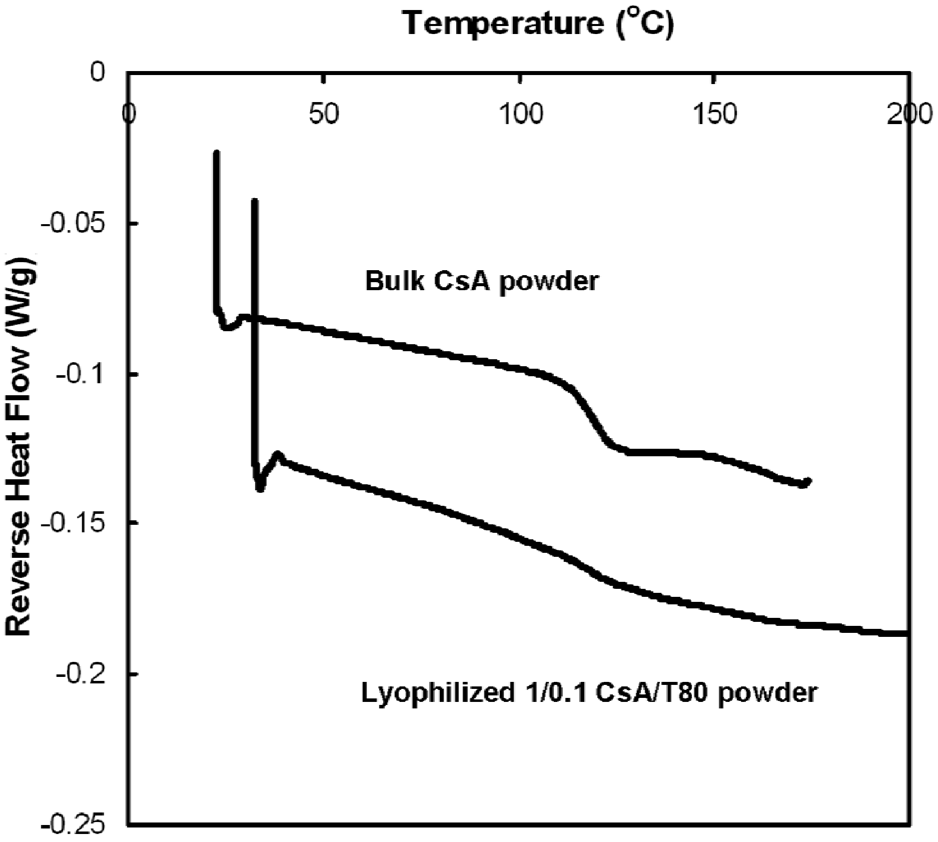

Figure 2.6 mDSC thermograms of bulk CsA powder and lyophilized 1/0.1 CsA/T80 particle dispersions that were stored for 10 months at 4° C. No melting peak was observed for either powder. A T_g at ~ 120°C was observed.

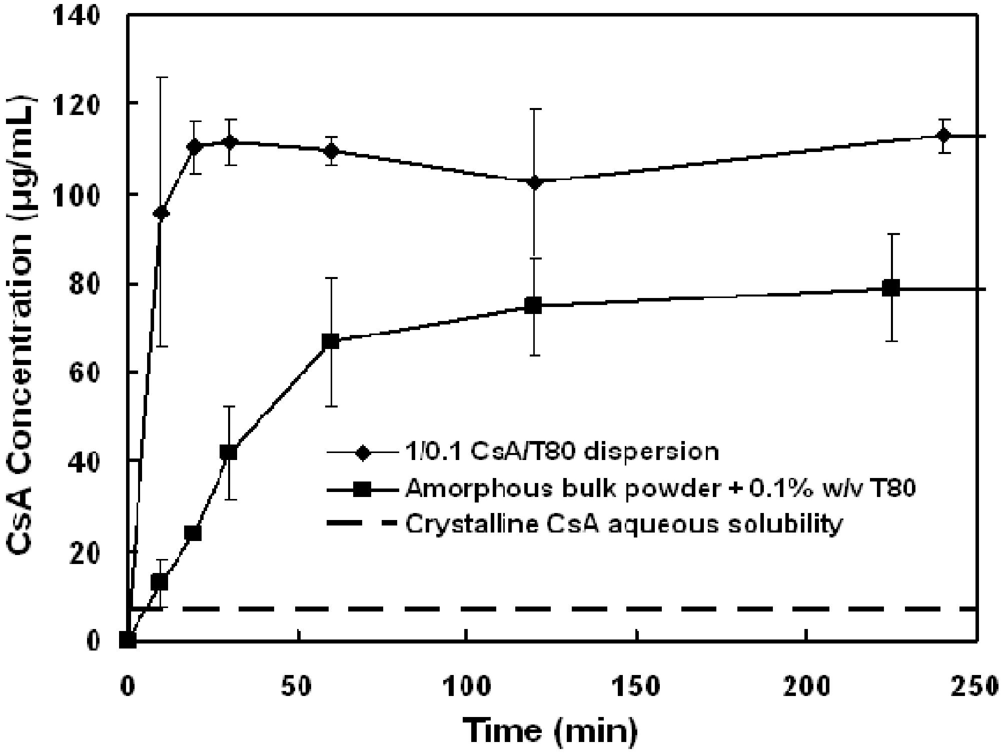

Figure 2.7 Supersaturation concentrations of CsA nanoparticle dispersions after dropwise addition to pH 7.4 phosphate buffer. All samples were filtered with 0.02µm filters. The dashed line represents the reported aqueous solubility (7.3 µg/mL) of crystalline CsA[41,42].

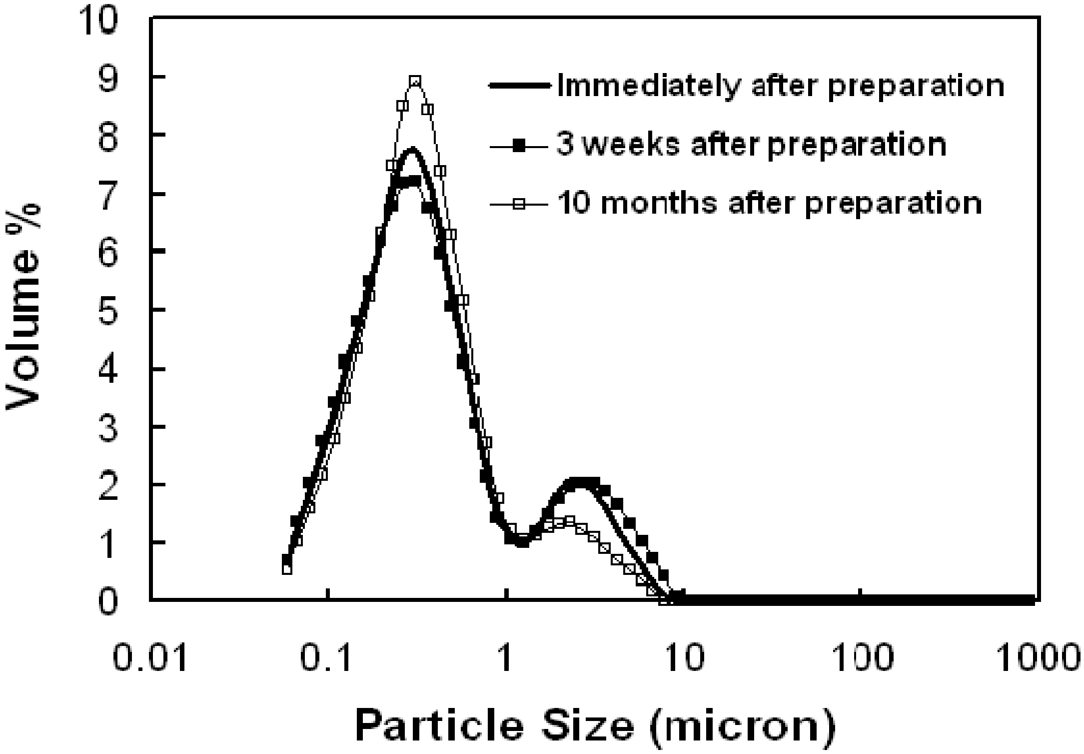

Figure 2.8 Effect of storage time on CsA particle size distribution in an aqueous dispersion. Dispersions were stored at 4°C and sonicated for 5 minutes with a probe sonicator prior to measurement.

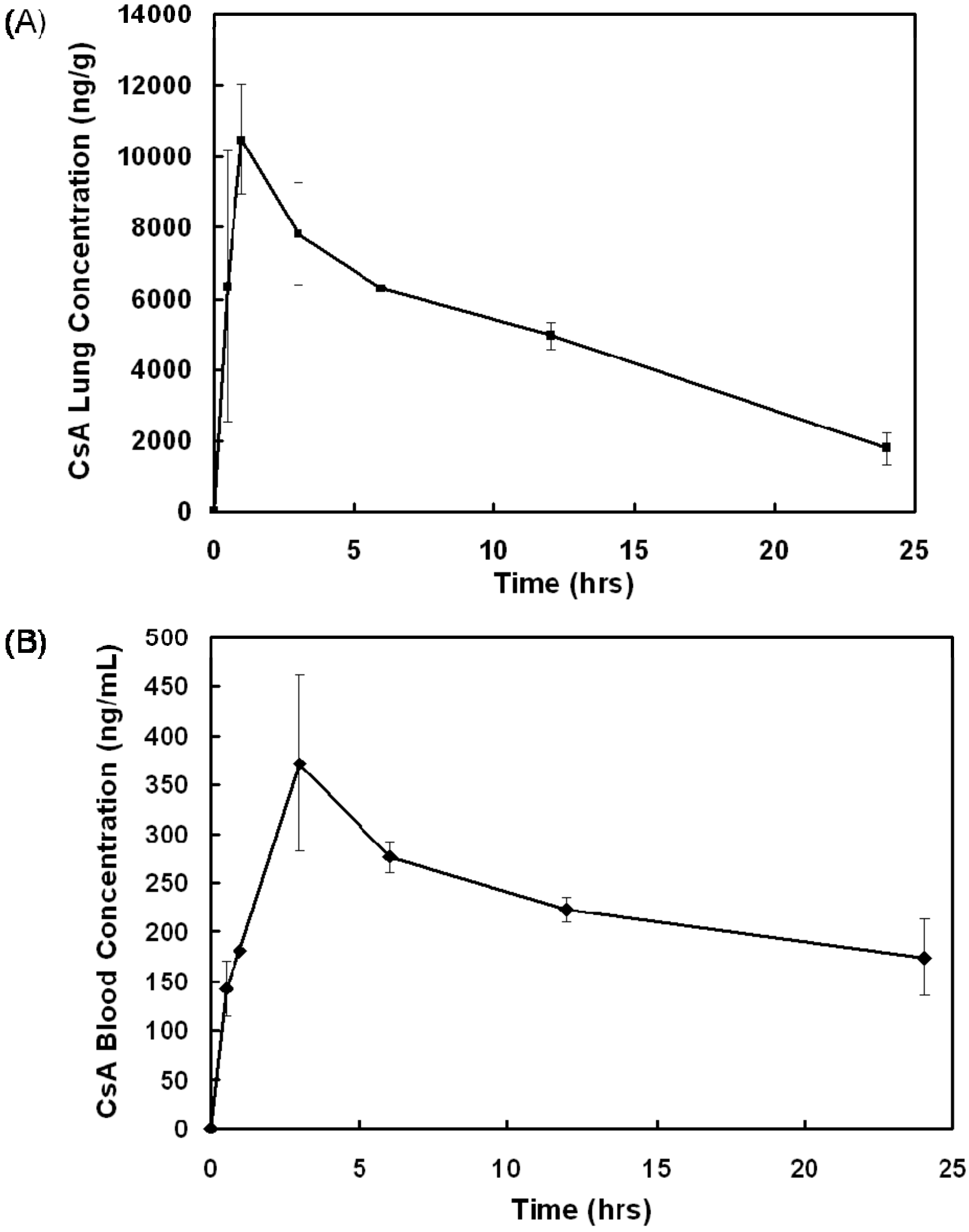

Figure 2.9 (A) Mean lung concentrations (ng CsA/g wet lung tissue) and (B) mean whole blood concentrations (ng CsA/mL) over 24 hours for mice dosed with CsA:T80 (1:0.1). n=2 mice per time point.

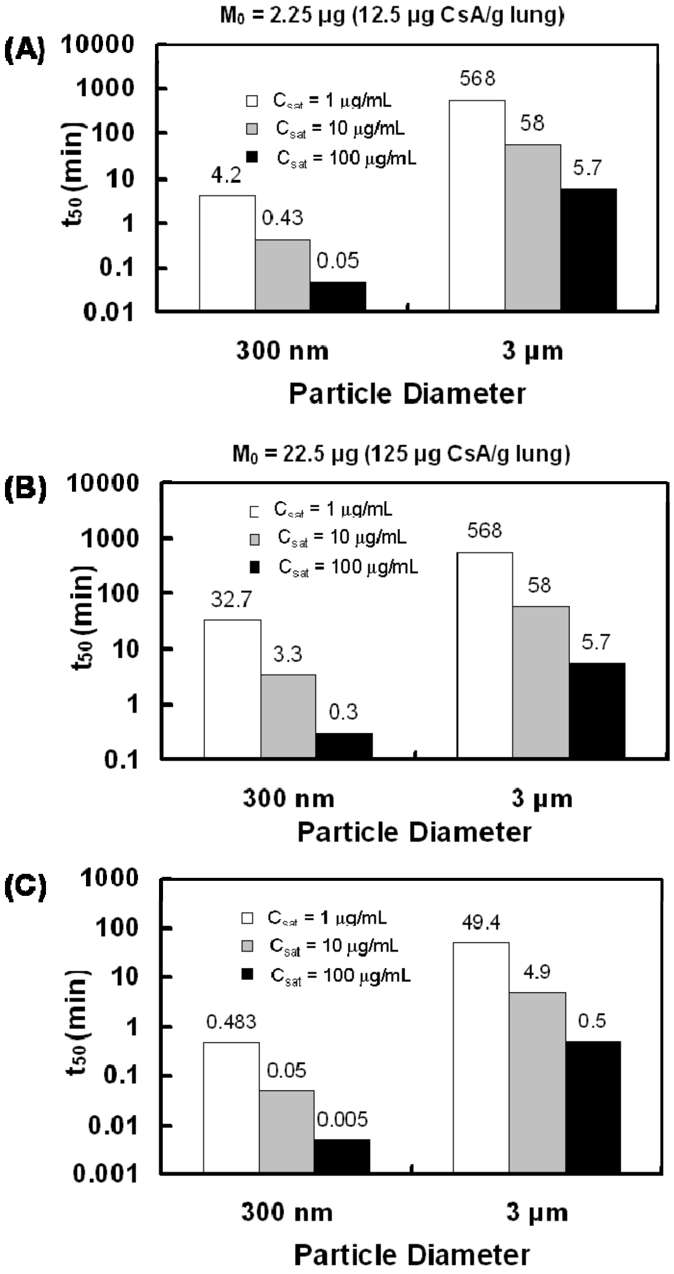

Figure 2.10 Predicted absorption half lives (time for 50% of drug to dissolve and permeate though lung epithelium) for drug particles of two different sizes and two different drug loadings over a range of solubilities (A-B). In (C), absorption half lives are predicted when permeability, P, is very high (P=1010 cm/s). Absorption half-lives were the same for both 12.5 µg/g and 125 µg/g drug loadings for this high permeability.

Table 2.1 Andersen cascade impactor data for a 1/0.1 CsA/T80 dispersion in water (8.4 mg/mL) aerosolized using an Aeroneb® Pro micropump nebulizer with an airflow rate of 28.3 L/min.

	Initial	3 Weeks Storage
TED (µg/min)	1452.5	1448.0
FPF (%)	77.4	73.9
MMAD (µm)	2.02	2.52
GSD	1.83	1.85

Table 2.2 Pharmacokinetic parameters for lung and whole blood concentrations for mice dosed with a 1/0.1 CsA/T80 dispersion (8.4 mg/mL) for 15 minutes.

Pharmacokinetic Parameter	Lung[a]	Whole Blood[b]
C_{max}(ng/mL)	10,500	372.2
t_{max} (hr)	1.0	3.7
$t_{1/2}$ (hr)	9.6	18.2
K_{01} absorption (1/hr)	------	0.890
K_{10} elimination (1/hr)	0.0724	0.038
AUC_{inf} (ng-hr/mL)	144,400	9665.4

[a] Based on non-compartmental analysis of lung tissue concentration versus time
[b] Based on one-compartmental analysis of whole blood concentrations versus time for extravascular administration

Table 2.3 Comparison of CsA lung and blood levels from several in-vivo studies

	Subject	**Lung C_{max} (ng/g)**	**Blood C_{max} (ng/mL)**	**Lung AUC (ng-hr/g)**	**Blood AUC (ng-hr/mL)**	**Dose (mg/kg)**
Nebulized dispersion (aqueous)**	Mouse	10,500	372	144,400	9,665	3.5
Nebulized solution (ethanol)[50]	Rat	46,000-89,000	---	---	---	3.6
Nebulized solution (ethanol) [49]	Rat	175,000	3,500	477,964	27,449	5.0
Nebulized solution (propylene glycol)[54]	Human	46,000-112,000	119-402	---	715-1565	~ 4.3
Intramuscular solution (ethanol) [49]	Rat	12,500	1600	157,706	17,965	5.0
Oral (Neoral microemulsion) [98]	Mouse	---	2557	---	41,021	10.0

** results from this study

2.6 REFERENCES

1. Adjei, A.; Gupta, P., Pulmonary delivery of therapeutic peptides and proteins. *Journal of Controlled Release* **1994,** 29, (3), 361-73.

2. Adjei, A. L.; Gupta, P. K., *Inhalation Delivery of Therapeutic Peptides and Proteins*. New York, 1997; Vol. 107, p 913 pp.

3. Courrier, H. M.; Butz, N.; Vandamme, T. F., Pulmonary drug delivery systems: recent developments and prospects. *Critical Reviews in Therapeutic Drug Carrier Systems* **2002,** 19, (4 & 5), 425-498.

4. Garcia-Contreras, L.; Hickey, A. J., Aerosol treatment of cystic fibrosis. *Critical Reviews in Therapeutic Drug Carrier Systems* **2003,** 20, (5), 317-356.

5. Hickey, A. J., Aerosol delivery and asthma therapy. *Advanced Drug Delivery Reviews* **2003,** 55, (7), 777.

6. Charnick, S. B.; Yu, Z.; Athill, L. V.; Karara, A. H.; Tse, F. L. S.; Lau, D. T. W., Pharmacokinetics of SDZ 64-412, a novel antiasthmatic agent, following intravenous, oral, and inhalation dosing in the rat. *Biopharmaceutics & Drug Disposition* **1994,** 15, (4), 317-27.

7. Rabinow, B. E., Nanosuspensions in drug delivery. *Nature Reviews Drug Discovery* **2004,** 3, (9), 785-796.

8. Muller, R. H.; Jacobs, C.; Kayser, O., Nanosuspensions as particulate drug formulations in therapy. Rationale for development and what we can expect for the future. *Advanced Drug Delivery Reviews* **2001,** 47, (1), 3-19.

9. Tsapis, N.; Bennett, D.; Jackson, B.; Weitz, D. A.; Edwards, D. A., Trojan particles: large porous carriers of nanoparticles for drug delivery. *Proceedings of the National Academy of Sciences of the United States of America* **2002,** 99, (19), 12001-12005.

10. Kreyling, W. G.; Scheuch, G., *Clearance of Particles Deposited in the Lungs* New York Marcel Dekker Inc: New York, 2000; Vol. 143.

11. Oberdoerster, G., Effects and fate of inhaled ultrafine particles. *ACS Symposium Series* **2005,** 890, (Nanotechnology and the Environment), 37-59.

12. Forsgren, P.; Modig, J.; Gerdin, B.; Axelsson, B.; Dahlback, M., Intrapulmonary deposition of aerosolized Evans blue dye and liposomes in an experimental porcine model of early ARDS. *Upsala Journal of Medical Sciences* **1990,** 95, (2), 117-36.

13. Evora, C.; Soriano, I.; Rogers, R. A.; Shakesheff, K. M.; Hanes, J.; Langer, R., Relating the phagocytosis of microparticles by alveolar macrophages to surface chemistry: the effect of 1,2-dipalmitoylphosphatidylcholine. *Journal of Controlled Release* **1998,** 51, (2,3), 143-152.

14. Zhou, H.; Zhang, Y.; Biggs, D. L.; Manning, M. C.; Randolph, T. W.; Christians, U.; Hybertson, B. M.; Ng, K.-y., Microparticle-based lung delivery of INH decreases INH metabolism and targets alveolar macrophages. *Journal of Controlled Release* **2005,** 107, (2), 288-299.

15. Lehnert, B. E.; Morrow, P. E., Association of 59iron oxide with alveolar macrophages during alveolar clearance. *Experimental Lung Research* **1985,** 9, (1-2), 1-16.

16. Edwards, D.; Hanes, J.; Caponetti, G.; Mintzes, J.; Deaver, D.; Lotan, N.; Langer, R., Large Porous Particles for Pulmonary Delivery. *Science* **1997,** 276.

17. Fiegel, J.; Fu, J.; Hanes, J., Poly(ether-anhydride) dry powder aerosols for sustained drug delivery in the lungs. *Journal of Controlled Release* **2004,** 96, (3), 411-423.

18. Hanes, J.; Dawson, M.; Har-el, Y.-e.; Suh, J.; Fiegel, J., Gene delivery to the lung. *Drugs and the Pharmaceutical Sciences* **2004,** 134, (Pharmaceutical Inhalation Aerosol Technology (2nd Edition)), 489-539.

19. Heyder, J.; Rudolf, G., Mathematical models of particle deposition in the human respiratory tract. *Journal of Aerosol Science* **1984,** 15, (6), 697-707.

20. Heyder, J.; Gebhart, J.; Rudolf, G.; Schiller, C. F.; Stahlhofen, W., Deposition of particles in the human respiratory tract in the size range 0.005-15 [mu]m. *Journal of Aerosol Science* **1986,** 17, (5), 811-825.

21. Hadinoto, K.; Phanapavudhikul, P.; Zhu, K.; Tan, R. B. H., Novel Formulation of Large Hollow Nanoparticles Aggregates as Potential Carriers in Inhaled Delivery of Nanoparticulate Drugs. *Industrial & Engineering Chemistry Research* **2006,** 45, (10), 3697-3706.

22. Jacobs, C.; Muller, R. H., Production and characterization of a budesonide nanosuspension for pulmonary administration. *Pharmaceutical Research* **2002,** 19, (2), 189-194.

23. McConville, J. T.; Overhoff, K. A.; Sinswat, P.; Vaughn, J. M.; Frei, B. L.; Burgess, D. S.; Talbert, R. L.; Peters, J. I.; Johnston, K. P.; Williams, R. O., III, Targeted High Lung Concentrations of Itraconazole Using Nebulized Dispersions in a Murine Model. *Pharmaceutical Research* **2006,** 23, (5), 901-911.

24. Vaughn, J. M.; McConville, J. T.; Burgess, D.; Peters, J. I.; Johnston, K. P.; Talbert, R. L.; Williams, R. O., III, Single dose and multiple dose studies of

itraconazole nanoparticles. *European Journal of Pharmaceutics and Biopharmaceutics* **2006,** 63, (2), 95-102.

25. Chan, H. K.; Gonda, I., Development of a systematic theory of suspension inhalation aerosols. II. Aggregates of monodisperse particles nebulized in polydisperse droplets. *International Journal of Pharmaceutics* **1988,** 41, (1-2), 147-57.

26. Ostrander, K. D.; Bosch, H. W.; Bondanza, D. M., An in-vitro assessment of a NanoCrystal beclomethasone dipropionate colloidal dispersion via ultrasonic nebulization. *European Journal of Pharmaceutics and Biopharmaceutics* **1999,** 48, (3), 207-215.

27. Pandey, R.; Khuller, G. K., Antitubercular inhaled therapy: opportunities, progress and challenges. *Journal of Antimicrobial Chemotherapy* **2005,** 55, (4), 430-435.

28. Kawashima, Y.; Yamamoto, H.; Takeuchi, H.; Fujioka, S.; Hino, T., Pulmonary delivery of insulin with nebulized dl-lactide/glycolide copolymer (PLGA) nanospheres to prolong hypoglycemic effect. *Journal of Controlled Release* **1999,** 62, (1-2), 279-287.

29. Zhang, Q.; Shen, Z.; Nagai, T., Prolonged hypoglycemic effect of insulin-loaded polybutylcyanoacrylate nanoparticles after pulmonary administration to normal rats. *International journal of pharmaceutics* **2001,** 218, (1-2), 75-80.

30. Feng, S.-S.; Li, M.; Chen, B.-H.; Pack, D., Polymeric nanospheres fabricated with natural emulsifiers for clinical administration of an anticancer drug paclitaxel (Taxol). *Materials Science & Engineering, C: Biomimetic and Supramolecular Systems* **2002,** C20, (1-2), 85-92.

31. Bhavane, R.; Karathanasis, E.; Annapragada Ananth, V., Agglomerated vesicle technology: a new class of particles for controlled and modulated pulmonary drug delivery. *Journal of controlled release : official journal of the Controlled Release Society* **2003,** 93, (1), 15-28.

32. Muller, R. H.; Mader, K.; Gohla, S., Solid lipid nanoparticles (SLN) for controlled drug delivery - a review of the state of the art. *European Journal of Pharmaceutics and Biopharmaceutics* **2000,** 50, (1), 161-177.

33. Chetty, D. J.; Chien, Y. W., Novel methods of insulin delivery: an update. *Critical Reviews in Therapeutic Drug Carrier Systems* **1998,** 15, (6), 629-670.

34. Evrard, B.; Bertholet, P.; Gueders, M.; Flament, M. P.; Piel, G.; Delattre, L.; Gayot, A.; Leterme, P.; Foidart, J. M.; Cataldo, D., Cyclodextrins as a potential carrier in drug nebulization. *Journal of Controlled Release* **2004,** 96, (3), 403-410.

35. Cabral Marques, H. M.; Hadgraft, J.; Kellaway, I. W.; Taylor, G., Studies of cyclodextrin inclusion complexes. IV. The pulmonary absorption of salbutamol

from a complex with 2-hydroxypropyl-b-cyclodextrin in rabbits. *International Journal of Pharmaceutics* **1991,** 77, (2-3), 303-7.

36. Kraft, W. K.; Steiger, B.; Beussink, D.; Quiring, J. N.; Fitzgerald, N.; Greenberg, H. E.; Waldman, S. A., The pharmacokinetics of nebulized nanocrystal budesonide suspension in healthy volunteers. *Journal of Clinical Pharmacology* **2004,** 44, (1), 67-72.

37. Chan, H.-K.; Chew, N. Y. K., Novel alternative methods for the delivery of drugs for the treatment of asthma. *Advanced Drug Delivery Reviews* **2003,** 55, (7), 793-805.

38. Thomas, K.; Koelwel, C.; Machei, U.; Farber, L.; Gopferich, A., Three generations of cyclosporine a formulations: an in vitro comparison. *Drug development and industrial pharmacy* **2005,** 31, (4-5), 357-66.

39. Fukaya, H.; Limura, A.; Hoshiko, K.; Fuyumuro, T.; Noji, S.; Nabeshima, T., A cyclosporin A/maltosyl-a-cyclodextrin complex for inhalation therapy of asthma. *European Respiratory Journal* **2003,** 22, (2), 213-219.

40. Cheng, W. P.; Gray, A. I.; Tetley, L.; Hang, T. L. B.; Schaetzlein, A. G.; Uchegbu, I. F., Polyelectrolyte Nanoparticles with High Drug Loading Enhance the Oral Uptake of Hydrophobic Compounds. *Biomacromolecules* **2006,** 7, (5), 1509-1520.

41. Zhou, Y. Cyclosporin A: Solubilization, solid dispersion, and solid state transformation. Purdue University, 2000.

42. Ismailos, G.; Reppas, C.; Dressman, J. B.; Macheras, P., Unusual solubility behaviour of cyclosporin A in aqueous media. *The Journal of Pharmacy and Pharmacology* **1991,** 43, (4), 287-9.

43. Martinet, Y.; Pinkston, P.; Saltini, C.; Spurzem, J.; Mueller-Quernheim, J.; Crystal, R. G., Evaluation of the in vitro and in vivo effects of cyclosporine on the lung T-lymphocyte alveolitis of active pulmonary sarcoidosis. *American Review of Respiratory Disease* **1988,** 138, (5), 1242-8.

44. Letsou, G. V.; Safi, H. J.; Reardon, M. J.; Ergenoglu, M.; Li, Z.; Klonaris, C. N.; Baldwin, J. C.; Gilbert, B. E.; Waldrep, J. C., Pharmacokinetics of liposomal aerosolized cyclosporine A for pulmonary immunosuppression. *The Annals of thoracic surgery* **1999,** 68, (6), 2044-8.

45. Iacono, A. T.; Burckart, G. J.; Zeevi, A.; Kunter, E.; Griffith, B. P., Local immunosuppression: The lung. *Immunology and Medicine Series* **2001,** 29, (Therapeutic Immunosuppression), 333-356.

46. Fahr, A., Cyclosporin clinical pharmacokinetics. *Clinical pharmacokinetics* **1993,** 24, (6), 472-95.

47. Blot, F.; Faurisson, F.; Bernard, N.; Sellam, S.; Friard, S.; Tavakoli, R.; Carbon, C.; Stern, M.; Bisson, A.; Pocidalo, J. J.; Caubarrere, I., Nebulized cyclosporine in the rat: assessment of regional lung and extrapulmonary deposition. *Transplantation* **1999,** 68, (2), 191-5.

48. Mitruka, S. N.; Pham, S. M.; Zeevi, A.; Li, S.; Cai, J.; Burckart, G. J.; Yousem, S. A.; Keenan, R. J.; Griffith, B. P., Aerosol cyclosporine prevents acute allograft rejection in experimental lung transplantation. *Journal of Thoracic and Cardiovascular Surgery* **1998,** 115, (1), 28-37.

49. Mitruka, S. N.; Won, A.; McCurry, K. R.; Zeevi, A.; McKaveney, T.; Venkataramanan, R.; Iacono, A.; Griffith, B. P.; Burckart, G. J., In the lung aerosol cyclosporine provides a regional concentration advantage over intramuscular cyclosporine. *Journal of heart and lung transplantation : official publication of the International Society for Heart Transplantation* **2000,** 19, (10), 969-75.

50. Keenan, R. J.; Duncan, A. J.; Yousem, S. A.; Zenati, M.; Schaper, M.; Dowling, R. D.; Alarie, Y.; Burckart, G. J.; Griffith, B. P., Improved immunosuppression with aerosolized cyclosporine in experimental pulmonary transplantation. *Transplantation* **1992,** 53, (1), 20-5.

51. Keenan, R. J.; Iacono, A.; Dauber, J. H.; Zeevi, A.; Yousem, S. A.; Ohori, N. P.; Burckart, G. J.; Kawai, A.; Smaldone, G. C.; Griffith, B. P., Treatment of refractory acute allograft rejection with aerosolized cyclosporine in lung transplant recipients. *Journal of Thoracic and Cardiovascular Surgery* **1997,** 113, (2), 335-341.

52. Iacono, A. T.; Corcoran, T. E.; Griffith, B. P.; Grgurich, W. F.; Smith, D. A.; Zeevi, A.; Smaldone, G. C.; McCurry, K. R.; Johnson, B. A.; Dauber, J. H., Aerosol cyclosporin therapy in lung transplant recipients with bronchiolitis obliterans. *European Respiratory Journal* **2004,** 23, (3), 384-390.

53. Iacono Aldo, T.; Johnson Bruce, A.; Grgurich Wayne, F.; Youssef, J. G.; Corcoran Timothy, E.; Seiler Deidre, A.; Dauber James, H.; Smaldone Gerald, C.; Zeevi, A.; Yousem Samuel, A.; Fung John, J.; Burckart Gilbert, J.; McCurry Kenneth, R.; Griffith Bartley, P., A randomized trial of inhaled cyclosporine in lung-transplant recipients. *The New England journal of medicine* **2006,** 354, (2), 141-50.

54. Burckart, G. J.; Smaldone, G. C.; Eldon, M. A.; Venkataramanan, R.; Dauber, J.; Zeevi, A.; McCurry, K.; McKaveney, T. P.; Corcoran, T. E.; Griffith, B. P.; Iacono, A. T., Lung Deposition and Pharmacokinetics of Cyclosporine After Aerosolization in Lung Transplant Patients. *Pharmaceutical Research* **2003,** 20, (2), 252-256.

55. Klyashchitsky, B. A.; Owen, A. J., Nebulizer-compatible liquid formulations for aerosol pulmonary delivery of hydrophobic drugs: glucocorticoids and cyclosporine. *Journal of Drug Targeting* **1999,** 7, (2), 79-99.

56. Gilbert, B. E.; Wilson, S. Z.; Garcon, N. M.; Wyde, P. R.; Knight, V., Characterization and administration of cyclosporine liposomes as a small-particle aerosol. *Transplantation* **1993,** 56, (4), 974-7.

57. Waldrep, J. C.; Arppe, J.; Jansa, K. A.; Vidgren, M., Experimental pulmonary delivery of cyclosporin A by liposome aerosol. *International Journal of Pharmaceutics* **1998,** 160, (2), 239-250.

58. Taylor, K. M. G.; Taylor, G.; Kellaway, I. W.; Stevens, J., The stability of liposomes to nebulisation. *International Journal of Pharmaceutics* **1990,** 58, (1), 57-61.

59. Matteucci, M. E.; Hotze, M. A.; Johnston, K. P.; Williams, R. O., III, Drug Nanoparticles by Antisolvent Precipitation: Mixing Energy versus Surfactant Stabilization. *Langmuir* **2006,** 22, (21), 8951-8959.

60. Chen, X.; Young, T. J.; Sarkari, M.; Williams, R. O.; Johnston, K. P., Preparation of cyclosporine A nanoparticles by evaporative precipitation into aqueous solution. *International Journal of Pharmaceutics* **2002,** 242, (1-2), 3-14.

61. Matteucci, M. E.; Brettmann, B. K.; Rogers, T. L.; Elder, E. J.; Williams, R. O.; Johnston, K. P., Design of Potent Amorphous Drug Nanoparticles for Rapid Generation of Highly Supersaturated Media. *Molecular Pharmaceutics* **2007,** 4, (5), 782-793.

62. Rogers, T. L.; Gillespie, I. B.; Hitt, J. E.; Fransen, K. L.; Crowl, C. A.; Tucker, C. J.; Kupperblatt, G. B.; Becker, J. N.; Wilson, D. L.; Todd, C.; Broomall, C. F.; Evans, J. C.; Elder, E. J., Development and Characterization of a Scalable Controlled Precipitation Process to Enhance the Dissolution of Poorly Water-Soluble Drugs. *Pharmaceutical Research* **2004,** 21, (11), 2048-2057.

63. Smith, P. G., Jr.; Ryoo, W.; Johnston, K. P., Electrostatically Stabilized Metal Oxide Particle Dispersions in Carbon Dioxide. *Journal of Physical Chemistry B* **2005,** 109, (43), 20155-20165.

64. Sawchuk, R. J.; Cartier, L. L., Liquid-chromatographic determination of cyclosporin A in blood and plasma. *Clinical Chemistry (Washington, DC, United States)* **1981,** 27, (8), 1368-71.

65. McMahon, T. A.; Brain, J. D.; Lemott, S., Species differences in aerosol deposition. *Inhaled Part. 4, Int. Symp., 4th* **1977,** 1, 23-33.

66. Gazeley, M. J. S.; Lees, I. W.; Payne, A. N.; Webbon, P. M.; Woolley, G. E., Anatomical deposition and early distribution of an inhaled radioaerosol in conscious and anaesthetized rats. *British Journal of Pharmacology* **1986,** 87, 122.

67. Miller, F. J.; Mercer, R. R.; Crapo, J. D., Lower respiratory tract structure of laboratory animals and humans: dosimetry implications. *Aerosol Science and Technology* **1993,** 18, (3), 257-71.

68. Patton, J. S., Mechanisms of macromolecule absorption by the lungs. *Advanced Drug Delivery Reviews* **1996,** 19, (1), 3-36.

69. Tandya, A.; Dehghani, F.; Foster, N. R., Micronization of cyclosporine using dense gas techniques. *Journal of Supercritical Fluids* **2006,** 37, (3), 272-278.

70. Bunjes, H.; Rades, T., Thermotropic liquid crystalline drugs. *Journal of Pharmacy and Pharmacology* **2005,** 57, (7), 807-816.

71. Liu, Y.; Kathan, K.; Saad, W.; Prud'homme, R. K., Ostwald Ripening of b-Carotene Nanoparticles. *Physical Review Letters* **2007,** 98, (3), 036102/1-036102/4.

72. Eckstein Jens, W.; Fung, J., A new class of cyclosporin analogues for the treatment of asthma. *Expert opinion on investigational drugs* **2003,** 12, (4), 647-53.

73. Young, T. J.; Mawson, S.; Johnston, K. P.; Henriksen, I. B.; Pace, G. W.; Mishra, A. K., Rapid Expansion from Supercritical to Aqueous Solution to Produce Submicron Suspensions of Water-Insoluble Drugs. *Biotechnology Progress* **2000,** 16, (3), 402-407.

74. Vaughn, J. M.; Wiederhold, N. P.; McConville, J. T.; Coalson, J. J.; Talbert, R. L.; Burgess, D. S.; Johnston, K. P.; Williams, R. O.; Peters, J. I., Murine airway histology and intracellular uptake of inhaled amorphous itraconazole. *International Journal of Pharmaceutics* **2007,** 338, (1-2), 219-224.

75. Balwani, G.; Boyd, B.; Whatley, J. Compositions methods and systems for pulmonary delivery of recombinant human interferon alpha-2b. 2002-159083 2003223936, 20020531., 2003.

76. Johnson, B. K. Flash nanoprecipitation of organic actives via confined micromixing and block copolymer stabilization. Princeton University, 2003.

77. Matteucci, M. E.; Crisp, M. T.; Johnston, K. P.; Rogers, T. L.; Hitt, J. E.; Williams, R. O. In *Controlled Precipitation of Naproxen Nanoparticles*, American Association of Pharmaceutical Sciences, Annual Meeting, 2004; 2004.

78. Waldrep, J. C.; Arppe, J.; Jansa, K. A.; Knight, V., High dose cyclosporin A and budesonide-liposome aerosols. *International Journal of Pharmaceutics* **1997,** 152, (1), 27-36.

79. Bridges, P. A.; Taylor, K. M. G., An investigation of some of the factors influencing the jet nebulization of liposomes. *International Journal of Pharmaceutics* **2000,** 204, (1-2), 69-79.

80. Israelachvili, J., *Intermolecular and Surface Forces*. 2 ed.; Academic Press, Inc.: San Diego, 1992.

81. Burckart, G. J.; Keenan, R. J.; Iacono, A. T.; Griffith, B. P., Cyclosporine aerosol in lung transplantation. *Local Immunosuppression of Organ Transplants* **1996**, 131-139.

82. Geelhaar, A.; Weibel, E. R., Morphometric estimation of pulmonary diffusion capacity. 3. The effect of increased oxygen consumption in Japanese Waltzing mice. *Respiration Physiology* **1971,** 11, (3), 354-66.

83. Lum, H.; Mitzner, W., A species comparison of alveolar size and surface forces. *Journal of applied physiology* **1987,** 62, (5), 1865-71.

84. McCabe, W. L.; Smith, J. C.; Harriott, P., *Unit Operations of Chemical Engineering*. 6th ed.; McGraw Hill Inc.: Boston, MA, 2001.

85. Forbes, B.; Ehrhardt, C., Human respiratory epithelial cell culture for drug delivery applications. *European Journal of Pharmaceutics and Biopharmaceutics* **2005,** 60, (2), 193-205.

86. Niven, R. W., *Pharmaceutical Inhalation Aerosol Technology*. Marcel Dekker, Inc.: New York, New York, 1992; Vol. 54, p 340.

87. Davies, N. M.; Feddah, M. R., A novel method for assessing dissolution of aerosol inhaler products. *International Journal of Pharmaceutics* **2003,** 255, (1-2), 175-187.

88. Sakagami, M.; Sakon, K.; Kinoshita, W.; Makino, Y., Enhanced pulmonary absorption following aerosol administration of mucoadhesive powder microspheres. *Journal of Controlled Release* **2001,** 77, (1-2), 117-129.

89. Brown, R. A., Jr.; Schanker, L. S., Absorption of aerosolized drugs from the rat lung. *Drug metabolism and disposition: the biological fate of chemicals* **1983,** 11, (4), 355-60.

90. Enna, S. J.; Schanker, L. S., Absorption of drugs from the rat lung. *American Journal of Physiology* **1972,** 223, (5), 1227-31.

91. Schanker, L. S.; Mitchell, E. W.; Brown, R. A., Jr., Species comparison of drug absorption from the lung after aerosol inhalation or intratracheal injection. *Drug Metabolism and Disposition* **1986,** 14, (1), 79-88.

92. Handschumacher, R. E.; Harding, M. W.; Rice, J.; Drugge, R. J.; Speicher, D. W., Cyclophilin: a specific cytosolic binding protein for cyclosporin A. *Science (Washington, DC, United States)* **1984,** 226, (4674), 544-7.

93. McAllister, S. M.; Alpar, H. O.; Teitelbaum, Z.; Bennett, D. B., Do interactions with phospholipids contribute to the prolonged retention of polypeptides within the lung? *Advanced Drug Delivery Reviews* **1996,** 19, (1), 89-110.

94. Stepkowski, S. M.; Goto, S.; Ito, T.; Reynolds, K.; Didlake, R.; Kim, E. K.; Kahan, B. D., Prolongation of heterotopic heart allograft survival by local

delivery of continuous low-dose cyclosporine therapy. *Transplantation* **1989,** 47, (1), 17-23.

95. Thorsson, L.; Edsbacker, S.; Kallen, A.; Lofdahl, C.-G., Pharmacokinetics and systemic activity of fluticasone via Diskus and pMDI, and of budesonide via Turbuhaler. *British Journal of Clinical Pharmacology* **2001,** 52, (5), 529-538.

96. Esmailpour, N.; Hoegger, P.; Rabe, K. F.; Heitmann, U.; Nakashima, M.; Rohdewald, P., Distribution of inhaled fluticasone propionate between human lung tissue and serum in vivo. *European Respiratory Journal* **1997,** 10, (7), 1496-1499.

97. Patton, J. S.; C.S. Fishburn; Weers, J. G., The Lungs as a Portal of Entry for Systemic Drug Delivery. *Proceedigns of the American Thoracic Society* **2004,** 1, 338-344.

98. Liu, C.; Wu, J.; Shi, B.; Zhang, Y.; Gao, T.; Pei, Y., Enhancing the Bioavailability of Cyclosporine A Using Solid Dispersion Containing Polyoxyethylene (40) Stearate. *Drug Development and Industrial Pharmacy* **2006,** 32, (1), 115-123.

99. Ho, S.; Clipstone, N.; Timmermann, L.; Northrop, J.; Graef, I.; Fiorentino, D.; Nourse, J.; Crabtree, G. R., The mechanism of action of cyclosporin A and FK506. *Clinical Immunology and Immunopathology* **1996,** 80, (3, Pt. 2), S40-S45.

100. Kahan, B. D., Cyclosporine. *New England Journal of Medicine* **1989,** 321, (25), 1725-38.

101. Casarett, L. J.; Milley, P. S., Alveolar Reactivity Following Inhalation of Particles. *Health Physics* **1964,** 10, 1003-11.

Chapter 3: Templated Open Flocs of Nanorods for Enhanced Pulmonary Delivery with Pressurized Metered Dose Inhalers

A novel concept is presented for the formation of stable suspensions composed of very low density flocs of rod-shaped drugs in hydrofluoroalkane propellants for pressurized meter dose inhalers (pMDI), and for templating the flocs to achieve high fine particle fractions in pulmonary delivery. The flocculated suspensions in HFA 227 are stable against settling for one year. Bovine serum albumin (BSA) nanorods, ~100 nm in diameter and 2.4 μm in length, produced by thin film freezing (TFF), are shown by theory and experiment to form space filling flocs with protein particle volume fractions of only 0.0020, which are one order of magnitude lower than for flocs composed of spheres. The rods are flocculated reversibly, as they were found to break up into individual submicron primary rod particles in a polar solvent acetonitrile. Actuation of the HFA suspension with a pMDI produces high fine particle fractions (38-48%) with an emitted dose of 0.7 mg for particles with 3-4 μm aerodynamic diameters (d_a), as determined with an Andersen cascade impactor (ACI). The atomized 25 μm HFA droplets break apart and template the highly open flocs, which are held together by extremely weak van der Waals forces. Upon evaporation of the HFA, capillary forces shrink the ~25 μm templated flocs resulting in porous particles with optimal d_a = 3-4 μm for deep lung delivery. The corresponding geometric diameters d_g are on the order of 10 μm, as shown by SEM and static light scattering measurements. This novel concept for forming extremely stable suspensions of open flocs of rod shaped particles, and templating and shrinking the flocs to produce particles for efficient pMDI deep lung delivery is applicable to a wide variety of drugs without the need for surfactants or cosolvents to stabilize the primary particles.

3.1 INTRODUCTION

Until recently, the delivery of protein therapeutics has been largely limited to parenteral delivery due to the chemical and physical instabilities of proteins and challenges in permeating biological membranes [1]. Among the non-invasive routes, pulmonary delivery offers advantages of large alveolar surface area (~100 m^2), rapid absorption across the thin alveolar epithelium (0.1-0.5 μm), avoidance of first pass metabolism, and sufficient bioavailabilities [1-8]. For pulmonary delivery pressurized metered dose inhalers (pMDI) remain the most popular delivery device, relative to dry powder inhalers (DPI) and nebulizers, because of low cost, portability, and disposability [4, 9]. Because most drugs, including proteins, are insoluble in hydrofluoroalkane (HFA) propellants, most effort has focused on the design of stable suspensions [10-13], despite limited fundamental understanding [4, 11, 14]. Although certain proteins in suspensions may potentially be denatured by HFAs [4], the low degree of contact in the solid state with the solvent, relative to solutions, is highly beneficial. For example, suspension-based pMDI formulations of insulin, lysozyme, catalase and rhDNase I have been shown to be stable [15-17].

To achieve high deposition of aerosolized particles in the deep lung, the aerodynamic diameter (d_a) should range between 1-5 μm [18]. This size range may be produced by milling[11, 17], spray drying [3, 19-21], and spray freeze-drying (SFD) [22, 23]. Two recent particle engineering processes, spray freezing into liquids (SFL) [24-28], and thin film freezing (TFF) [29], were shown to produce high surface area, stable rod-like particles with 50-100 nm diameters and high aspect ratios, despite slower cooling rates than in SFD. The stability of lactate dehydrogenase, based on enzymatic activity, was increased in these processes relative to SFD, as a result of a reduction in the surface area of [26, 29] the destabilizing gas-liquid interface[26, 30]. Limited process yields, in terms of weight of protein, for spray drying (50-70%) [22, 31] and SFD (~80%) [22, 31, 32] are a major concern for highly valuable proteins.

To date, relatively few examples have been given of suspensions with 1-5% (w/w) mass loadings in HFAs that are stable against settling on time scales of over 60 s [11]. To achieve high deposition of aerosolized particles in the deep lung, the aerodynamic diameter (d_a) should range between 1-5 μm [18]. As the mass loading increases up to and above 5% (w/w), particles often aggregate within aerosolized droplets leading to unacceptably large d_a's. [11, 33]. Suspensions of cubic or spherical particles formed by milling or spray drying often flocculate irreversibly and settle in less than 60 s as illustrated in Figure 3.1A [21]. Settling can cause variable dosing between actuations [21, 34]. As a consequence of these limitations for pMDI suspensions, typical fine particle fractions (FPFs) only reach 5-30% [35]. Although surfactants and cosolvents, such as ethanol, may stabilize the suspension, surfactants currently approved by the FDA for inhalation are insoluble in HFAs [36, 37]. Surfactant tails are often not solvated well enough by HFAs, which have low polarizabilities and van der Waals forces, to provide steric stabilization [38, 39]. Thus, a key goal has been to design new surfactant structures by achieving a fundamental understanding of the molecular interactions with atomic force microscopy and theory [11, 38, 39].

An alternative approach is to modify the particle morphology to enhance the colloidal stability of the primary particles [11, 21, 40]. Large porous particles [40, 41] or hollow particles with porous or nonporous shells [21] formed by spray drying were stable against settling for at least 4 hours when suspended in HFAs. Respirable fractions were as high as 68%. Here, the presence of pores filled with HFA decreases the density difference of the particle with the surrounding HFA media and reduces van der Waals attractive forces between particles [21, 40, 41]. Recently, large porous nanoparticle (LPNP) aggregates, with d_a optimized for dry powder inhaler (DPI) delivery [20, 33], have been formed by spray drying aqueous suspensions of submicron particles. Upon contact with lung tissue, these

"Trojan particles" break up into nanoparticles to facilitate dissolution and absorption [20]. To extend this approach to a pMDI, each LPNP could be stabilized as an individual entity in a colloidal dispersion. Efficient nanoparticle delivery to the deep lung has also been achieved with nebulization of nanoparticle dispersions in aqueous media [42]. In all of the pMDI methods discussed so far, the goal has been to stabilize a colloidal dispersion of primary particles, or of individual LPNP particles in a HFA [11, 14], in many cases with surfactant stabilizers.

The primary objective of this study was to produce aggregates of high aspect ratio particles, in this case nanorods, to achieve high fine particle fractions in pMDI delivery by: (1) forming stable (against settling) flocculated suspensions of bovine serum albumin (BSA) particles, (2) subdividing (templating) the friable flocs upon formation of HFA droplets, and (3) shrinking the flocs upon HFA droplet evaporation (Figure 3.1). Here we purposely flocculate asymmetric high-aspect ratio particles without the use of surfactants or cosolvents in the HFA to prevent settling. Thus, this approach is fundamentally the opposite of most previous studies where pre-formed primary colloidal particles are stabilized in order to prevent flocculation. [11]

The suspension stability and aerosol performance upon actuation from a pMDI was evaluated for BSA particles produced by TFF, wet milling and spray drying. The addition of cubes or spheres, produced by wet milling or spray drying, to HFA 227 produced dense flocs that settled rapidly (Figure 3.1A). In contrast, high aspect ratio particles, such as nanorods with 50-100 nm diameters produced by TFF, may be expected to pack less efficiently and form much lower density flocs with greater free volume [43-47] than spheres (Figure 3.1B). These open flocs stack upon each other and occupy the entire vial to prevent settling for months, as illustrated in Figure 3.1B. The morphology was determined by scanning electron microscopy (SEM) of the original particles and after solvent removal of particles suspended in HFA 227. Upon actuation of the pMDI, the emitted HFA droplets were on the order of 25 μm. These 25 μm droplets subdivide and break apart the highly friable open flocs. We will define this process as "templating" of the flocs. Upon evaporation of the HFA droplet, the compression of the templated flocs from capillary forces will be shown to shrink the particles to produce a desirable d_a (Figure 3.1B). The d_a values after actuation of the pMDI were determined with an Anderson cascade impactor (ACI) and aerodynamic particle sizer (APS) and geometric diameters of the aerosol particles (d_g) with SLS (static light scattering) and SEM micrographs.

In the discussion section, the mechanism of the particle formation is explored in detail. Experimental and calculated settling rates are utilized to characterize particle volume fractions and fractal dimensions for flocs composed of either cylindrical (rods) or spherical primary particles. Calculations of van der Waals energies between suspended particles are presented to explain floc formation and break up into subdomains upon templating the flocs with the HFA droplets. The calculated particle shrinkage during HFA evaporation from a material balance will be shown to agree with experiment.

3.2 THEORY

The formation of stable suspensions of purposely flocculated rods depends upon the ability of the open flocs to fill large volumes in the vial. Experimental and theoretical studies indicate that rods create extremely low density flocs and thus fill much greater space compared to spheres as illustrated in Figure 3.1A [44, 46, 47]. For spheres, the volume fraction of primary particles within a floc ϕ_f is related to the floc diameter d^{floc}, primary particle diameter d_p, and fractal dimension D_f, which characterizes the floc structure, by [48]

$$\phi_f \approx \left(\frac{d^{floc}}{d_p} \right)^{D_f - 3} \qquad (3.1)$$

Philipse et al. modified eq. 3.1 to account for the packing physics of cylindrical rods of length L and diameter D with the result [46]

$$\phi_f \approx \frac{1}{r} \cdot \left(\frac{d^{floc}}{V_p^{1/3}} \right)^{D_f - 3} \qquad (3.2)$$

where $r = L/D$ is the aspect ratio [46]. A comparison of eqs. 1 and 2 indicates that ϕ_f may be much smaller for particles with large aspect ratios as shown in Figure 3.1 leading to flocs that fill a greater volume. Furthermore, if the attractive contact points of the rods prevent close packing during flocculation, the lower D_f for the rods will further reduce ϕ_f. These theoretical predictions will be demonstrated experimentally from microscopy, settling rates, and the aerodynamic and geometric diameters.

3.3 MATERIALS AND METHODS

3.3.1 Materials

Bovine serum albumin (BSA) was purchased from Sigma (St. Louis, MO). The propellant 1,1,1,2,3,3,3-heptafluoroprane (HFA 227) was purchased from Hoechst (Frankfurt, Germany) and 2H,3H-Perfluoropentane (HPFP) was purchased from SynQuest Labs Inc. (Alachua, FL). The Micro BCA Protein Assay Reagent Kit was obtained from Pierce (Rockford, IL). The water was deionized by flowing distilled water through a series of 2x7 L mixed bed vessels (Water and Power Technologies, Salt Lake City, UT) containing 60:40 anionic:cationic resin blends.

3.3.2 Powder preparation

3.3.2.1 Thin film freezing (TFF)

BSA powders were prepared by the thin film freezing (TFF) process described previously [29]. Briefly, 5 mg/mL feed solution of BSA in 10 mM pH = 7.4 potassium phosphate buffer was passed at a flow rate of 4 mL/min through a 17 gauge (1.1 mm ID, 1.5 mm OD) stainless steel syringe needle. The droplets fell from a height of 10 cm above a rotating stainless steel drum (12 rpm) 17 cm long and 12 cm in diameter. The hollow stainless steel drum was filled with dry ice to maintain a drum surface temperature of 223 K. On impact, the droplets deformed into thin films and froze. The frozen thin films were removed from the drum by a stainless steel blade and transferred to a 400 mL Pyrex® beaker filled with liquid nitrogen. The excess liquid nitrogen was evaporated in a -80 °C freezer.

A Virtis Advantage Lyophilizer (The Virtis Company, Inc., Gardiner, NY) was used to dry the frozen slurries. Primary drying was carried out at -40ºC for 36 hrs at 300 mTorr and secondary drying at 25ºC for 24 hrs at 100 mTorr. A 12 hour linear ramp of the shelf temperature from -40°C to +25°C was used at 100 mTorr.

3.3.2.2 Spray Drying

Spray drying was performed with a Buchi Model 190 mini spray dryer (Brinkmann, Westbury, NY). A 10 mg/mL BSA feed solution in 10 mM potassium phosphate buffer (pH = 7.4) was atomized using a 0.5 mm ID two fluid nozzle with an atomizing air flow rate of 200 mL/s. The liquid protein formulation was pumped through the nozzle by a peristaltic pump (VWR, Bridgeport, NJ) at a flow rate of 5 mL/min using 5 mm ID silicone tubing. The inlet temperature for the heated aspirator air was set to

150ºC at a flow rate of 1000 L/hr. The resulting outlet temperature from the above conditions was 80ºC.

3.3.2.3 Wet Milling

Bulk BSA powder as received was suspended at 5 mg/mL in acetonitrile. The BSA suspension was placed in a mill filled with 50 ceramic balls approximately 1 cm in diameter and milled on a mechanical roller for 24 hours. The milled BSA suspension was dried in the Virtis Advantage Lyophilizer at a shelf temperature of 30ºC for 12 hrs at 1000 mTorr.

3.3.3 Tapped Density

Approximately 100-300 mg of protein powder was loaded into a 100 mL graduated cylinder. The tapped density of the protein particles was measured with a Vankel tap density meter (Varian, Palo Alto, CA)

3.3.4 Scanning electron microscopy

SEM images were collected on a Hitachi Model S-4500 scanning electron microscope (Hitachi Ltd, Tokyo, Japan). The samples were prepared in a dry-box. Aluminum stages fitted with double adhesive carbon conducting tape were gently dipped into sample vials until covered by powder. Stages were then placed in septum capped vials and purged with nitrogen for transfer. To minimize the time samples were exposed to atmospheric moisture the stages were rapidly transferred to a Pelco Model 3 sputter-coater. A conductive gold layer was applied and the samples were then quickly transferred to the SEM. Total exposure to the atmosphere was less than 1 minute.

3.3.5 Preparation of HFA suspensions

The various dried BSA powders were placed in 60 mL glass bottles (Qorpak, Bridgeville, PA) and pre-cooled in a -80ºC freezer. HFA 227 was also pre-cooled in a -80ºC freezer and poured into the bottles containing the protein powders to form 0.7% (w/w) suspensions. The bottles were packed in dry ice and the suspensions were then sonicated for 2 min. using a Branson Sonifier 450 (Branson Ultrasonics Corporation, Danbury, CT) with a 102 converter and tip operated in pulse mode at 35 W. Next, 10 mL of the cooled protein formulations were dispensed into 17 mL glass pMDI aerosol vials (SGD, Paris, France) and fitted with metering valves containing 100 µL metering chambers (DF10 RC 150, Valois of America, Inc., Congers, NY). The vials were then allowed to warm up to room temperature.

3.3.6 Microscope images of protein suspended in HPFP

The various particles were initially dispersed by pipette mixing in HPFP (~ 5mg/mL) and were observed for 2 min. with a Nikon OPTIPHOT 2-POL optical microscope with an attached MTI CCD-72X camera (Nikon, Tokyo, Japan). Pictures were taken 30 and 60 seconds after initial dispersion in HPFP.

3.3.7 Particle size analysis

Particle sizes for the wet milled, spray dried and TFF particles were measured by static light scattering (SLS) with a Malvern Mastersizer-S (Malvern Instruments, Ltd.,Worcestershire, UK). Typical obscuration values ranged from 11 to 13%, corresponding to a BSA concentration of ~ 1mg/mL.

3.3.7.1 Particle size analysis of dried BSA particles

The dried powders were first suspended in HPFP at a concentration of 5 mg/mL and sonicated for 2-3 min. Approximately 5 drops of the sonicated suspension were dispensed into a 15 mL vessel containing HPFP and a magnetic stir bar and the particle sizes were analyzed by SLS. The dried powders were also suspended in acetonitrile at a concentration of 5 mg/mL and sonicated for 2-3 min. Approximately 2 mL of the sonicated suspension was dispersed into a 500 mL acetonitrile bath and the particle sizes were analyzed by SLS.

3.3.7.2 Particle size analysis of TFF particles suspended in HFA

Vials containing TFF particles suspended in HFA 227 were cooled in a -80ºC freezer. The metering valve was then removed from the vial and approximately 5 mL aliquots of the suspension were then dispensed into a 500 mL acetonitrile bath for particle size analysis.

3.3.8 Dynamic light scattering

Particles of BSA suspended in acetonitrile were analyzed by a custom-built dynamic light scattering (DLS) apparatus [49]. The scattering angle was set to 90º and the data were analyzed using a digital autocorrelator (Brookhaven BI-9000AT) and a non-negative least-squares (NNLS) routine (Brookhaven 9KDLSW32). The suspension concentration was 0.5 mg/mL which gave a measured count rate of approximately 150 kcps. Measurements were made over a period of 2 min.

3.3.9 Moisture content in pressurized metered dose inhalers

Moisture contents in the vials of each formulation were tested with an Aquatest 8 Karl-Fischer Titrator (Photovolt Instruments, Indianapolis, IN) according to the method described by Kim et al. [50]. A 19 gauge needle was inserted through the septum of the titration cell with the needle tip placed below the reagent, and each formulation was measured in triplicate. For all formulations tested the moisture content was approximately 500 ppm. The pure HFA was found to have a moisture content of 250 ppm. The total amount of moisture to the amount of protein particles was 7% (w/w).

3.3.10 Optical density measurements of protein

The μQuant spectrophotometer was used to measure turbidity at 350 nm to characterize BSA aggregation. Dry powders of BSA were reconstituted in 10 mM KPO_4 buffer (pH 7.5) to 1 mg/mL and 3 x 300 uL aliquots of each formulation were placed in a 96 well Falcon plate which was set in the spectrophotometer.

3.3.11 Quantitation of BSA

The amount of BSA was measured using the Micro BCA Protein Assay following protocols provided by Pierce (Rockford, IL). Each sample was measured in triplicate with relative standard deviations (%RSD) < 2%. The absorbance of the solutions was measured at 562 nm in a 96 well plate spectrophotometer (μQuant Model MQX200; Biotek Instruments Inc., Winooski, VT). Untreated BSA was used to prepare the protein standards at concentrations between 2 and 30 μg/mL.

3.3.12 Dose delivered through the valve (DDV) determination

The protein suspensions in HFA were actuated once through the firing adaptor of a dosage unit sample tube (26.6 mm ID x 37.7 mm OD x 103.2 mm length; 50 mL volume; Jade Corporation, Huntingdon, PA) [51]. The firing adaptor was removed, and 40 mL of DI water was added to dissolve the protein. The sampling tube was shaken and allowed to sit for at least 30 min. to assure that the protein was dissolved in water. The protein concentration was determined using the Micro BCA protein assay in conjunction with the μQuant spectrophotometer. The glass vial containing the HFA protein suspension was weighed before and after each actuation to assure that the proper dose had been released. The measurement was repeated 3 times to get an average dose delivered through the valve (DDV) for each formulation.

3.3.13 Aerodynamic diameter characterization of protein aerosol

To characterize the aerodynamic properties of the particles, an eight-stage Anderson cascade impactor (ACI) (Thermo-Anderson, Smyrna, GA) with an attached 15 cm spacer and an air flow-rate of 28.3 L/min was used to quantify mass median aerodynamic diameter (MMAD), geometric standard deviation (GSD), fine particle fraction (FPF), and emitted dose (ED). Initially 3 shots were sent to waste, and the next 5 shots were made into the ACI. The interval between shots was between 15-30 s to prevent cooling of the metering chamber and subsequent moisture condensation. After the last dose was discharged, the glass vial was removed from the impactor and the valve stem and actuator were rinsed separately with a known volume of DI water. Each plate of the impactor was placed in a separate container with a known volume of DI water and soaked for 30 min. to assure complete dissolution. The protein concentrations were then measured with the Micro BCA Protein Assay.

The d_a of the protein particles were also determined in triplicate with an Aerodynamic Particle Sizer (APS) 3321 (TSI, Shoreview, MN). The throat and spacer from the ACI were placed over the inlet of the APS and the airflow rate through the inlet was 5 L/min. Each formulation was shot once through the spacer and throat. The particle size range by mass was determined with the Aerosol Instrument Manager (AIM) software provided by TSI.

3.3.14 Geometric diameter characterization of protein aerosol

To obtain aerosolized particles for SEM (Hitachi Model S-4500, Hitachi Ltd, Tokyo, Japan) analysis, double carbon adhesive tape was applied to stage 3 of the ACI. Each formulation was actuated once through the ACI with an air flow rate of 28.3 L/min. The carbon tape was removed from stage 3 and applied to an aluminum SEM stage, which was transferred rapidly to a Pelco Model 3 sputter-coater to minimize exposure to moisture. Total exposure to the atmosphere was less than 1 minute. The SEM micrographs were then characterized with imaging software (Scion, Frederick, MD) to determine the particle size distribution of at least 100 particles.

The aerosolized particles were also characterized by SLS. Each formulation was actuated once through the ACI spacer and throat. The aerosol exited the outlet of the throat downwards 5 cm directly above the laser beam of the Malvern Mastersizer S. For each formulation 100 measurements of the aerosolized spray were made every 5 ms. The recorded measurements were then averaged to give the final profile of the aerosolized particles on a volume basis.

3.4 RESULTS

3.4.1 Suspension stability of the BSA particles in HFA

Prior to forming suspensions of BSA in HFA 227, the morphologies of the dried BSA particles prepared by TFF, wet milling and spray drying were observed by SEM (Figure 3.2). For BSA prepared by TFF, interconnected rods ~50 - 100 nm in diameter were observed with a web structure (Figure 3.2A and B). Similar morphologies were observed previously for lysozyme produced by TFF at 223 K [29]. The BSA particles prepared by wet milling (Figure 3.2C) were in the form of cubes with 400-800 nm dimensions. Lastly, spray dried BSA at a feed concentration of 10 mg/mL produced spheres 3-6 μm in diameter with corrugated surfaces (Figure 3.2D). Additionally, the bulk powder of the TFF particles before adding HFA had a low tapped density of 0.0064 g/cm^3 and required a mass of only ~100 mg to fill the entire volume of the vial (Figure 3.2E). Alternatively, the same mass of dried wet milled and spray dried particles formed a thin layer at the bottom of the vial (data not shown).

The various dried BSA particles were suspended in HFA 227 at 0.70% (w/w) corresponding to a volume fraction in the vial ϕ_v of 0.0077 (Figure 3.3), as determined from the true density of BSA ρ_p = 1.3 g/cm^3 [52]. For the TFF powder, the particles filled the entire volume of the vial immediately upon adding HFA (Figure 3.3A) and did not settle even after 1 year in storage. For a control with an extremely low ϕ_v of only 0.070% (w/w) (Figure 3.3B) the TFF particles still filled approximately half the HFA volume. For the wet milled BSA particles, the suspension initially appeared to be uniform (like Figure 3.3A), but the particles settled to the bottom after only 5 min. (Figure 3.3C). The spray dried particles dispersed well with shaking, but creamed after only 2 min. (Figure 3.3D).

Since the wet-milled particles settled in HFA 227 (1.41 g/cm^3) [53], the wet milling raised ρ to above 1.3 g/cm^3. On the contrary, the wet milled particles creamed in HPFP (1.59 g/cm^3) [53]. Thus, it was estimated that ρ_p ~ 1.50 g/cm^3, the average of the two solvent densities. Therefore, the true density reported for BSA appeared to be a skeletal density that did not account for internal pores. Upon wet milling removal of the pores raised ρ.

3.4.2 Characterization of the flocs in a surrogate solvent HPFP at ambient pressure

Because the vapor pressure of HFA 227 is above ambient at 25°C (~500 kPa) [53], the flocs were not studied *in situ* by light scattering and microscopy. Instead, the particles were characterized at ambient pressure in HPFP, a surrogate nonvolatile solvent, with a similar polarity and polarizability as HFA 227[53-55]. According to light microscopy, the TFF particles in HPFP were in the form of loosely packed flocs of rods (Figure 3.4A and B). The rods formed 200-300 µm flocs with subdomains on the order of 25 µm within 5-30 s. after dispersing the particles by pipette mixing (Figure 3.4A and B). The SLS measurements were consistent with the microscopy images in HPFP with d(v,50) values between 215-259 µm (Figure 3.5). For wet milled (Figure 3.4C) and the spray dried (Figure 3.4D) particles, 100 µm flocs formed in 30 seconds and grew to over 200 µm in 60 seconds. These flocs were more densely packed and composed of larger primary particles than those formed from TFF particles. About 50% of the wet milled particles by volume were between 1-10 µm with a secondary peak between 30-200 µm (Figure 3.5). For the spray dried particles a single peak centered at 10 µm was observed (Figure 3.5). The smaller sizes for light scattering versus microscopy may have been produced by shear from stirring.

3.4.3 Characterization of particles suspended in acetonitrile

The various dried BSA particles were also suspended in a more polarizable solvent acetonitrile to gain fundamental knowledge about the dispersibility, primary particle size and flocculation properties. Upon suspending the particles in acetonitrile a milky uniform dispersion formed (Figure 3.3E), but the particles settled after 3 days (Figure 3.3F). The dispersion/settling behavior shown in Figure 3.3E and F was also observed for wet milled and spray dried particles in acetonitrile (data not shown) with settling in ~3 days and ~30 min., respectively.

The BSA particles suspended in acetonitrile were also characterized by SLS after sonication for 2 min. As shown in Figure 3.6 the d(v,50) values were 330 nm, 410 nm and 6.3 µm for the TFF, wet milled and spray dried BSA particles, respectively, consistent with the original sizes in the SEMs in Figure 3.2. Even without sonication, significant dispersion of the TFF particles was observed with peaks at 330 nm and 20 μm, with approximately 50% of the particles by volume below 1 μm (Figure 3.6). In SLS particle sizing results are based on the equivalent volume of a sphere. In the case of the TFF nanorods a measured particle diameter of 330 nm would have an equivalent volume of 0.019 μm^3. In the case of the nanorods with 100 nm diameters, the length of the rod would be 2.4 μm which is consistent with the SEMs in Figure 3.2A and B. These experiments in acetonitrile demonstrated that the particles may be dispersed with little aggregation over 1 hr. to determine the primary particle size

To determine if exposure of the TFF particles to acetonitrile caused morphological changes, the dispersions in ACN were frozen by drip freezing into liquid nitrogen. The acetonitrile was then removed by lyophilization leaving fluffy particles with an approximate tapped density of 0.012 g/cm^3 (Figure 3.7A). When the particles were redispersed in acetonitrile the measured particle size profile was d(v,50) = 330 nm which was similar to the profile in Figure 3.6 of the original TFF dispersion, indicating the particles did not aggregate irreversibly. As observed by SEM, the morphology in Figure 3.7B was 50-100 nm diameter rods, similar to the interconnected rods of the original TFF powder in Figure 3.2A, and consistent with the sizes from light scattering results in Figure 3.6. Thus exposure to acetonitrile does not alter the morphology significantly.

3.4.4 TFF particle characterization after recovery from HFA

To further understand the flocs of TFF particles in the HFA, the particles were characterized after HFA evaporation. Isolation of the particles from HFA by lyophilization could not be achieved since the freezing point (-131ºC) of HFA 227 is too low to for conventional shelf lyophilizers [53, 56]. Alternatively, the HFA was cooled to -80ºC, well below its boiling point of -16ºC [53], and completely evaporated at atmospheric pressure. The TFF particle residue only occupied approximately 1 mL (tapped density of 0.10 g/cm^3, Figure 3.8A), an order of magnitude less than that of the starting TFF bulk powder (Figure 3.2E). The particle morphology after HFA exposure resembled rods with 100 nm diameters (Figure 3.8B), similar to the original TFF particles in Figure 3.2A. Therefore, exposure to HFA 227 followed by sonication did not significantly alter the primary nanorod particle morphology. However, the densified aggregates of the nanorods formed by capillary forces upon evaporation (Figure 3.8A) of HFA were not redispersible when reintroduced into HFA or into acetonitrile.

A second approach was used to harvest the TFF particles from HFA for further characterization at ambient pressure. A 2 mL aliquot of the cold TFF suspension was mixed directly with 500 mL of acetonitrile at 25^{o}C. The suspensions were sonicated and analyzed by SLS. The flocs deaggregated nearly completely to individual primary particles with over 80% of the volume distribution between 100 nm and 1 μm. (Figure 3.9). The distributions nearly matched those of the original TFF particles in acetonitrile (Figure 3.6).

In a third approach to analyze the TFF particle suspensions, the valve of the pMDI was submerged into acetonitrile and actuated. Submerging the actuator prevented the mixture of HFA droplets and particles from being exposed to ambient moisture and prevented HFA evaporation from effectively compacting the aerosolized particles. A slightly turbid dispersion was formed with an approximate particle concentration of 0.5 mg/mL, too low for detection by SLS, but not for DLS. From DLS, the particle size was 1-2 μm (Figure 3.10) much smaller than the 250 μm floc size in HFA. Therefore, both the second and third approach indicate the loosely flocculated nanorods in HFA may be broken up into primary nanorods, which will be shown to be beneficial for lung delivery.

3.4.5 Molecular stability of BSA exposed to HFA 227 as determined by optical density

As a means to determine the molecular stability of BSA against forming aggregates in the HFA 227, the optical density (OD) of the BSA exposed to HFA 227 was measured. The HFA 227 was removed by cooling the HFA suspension to -80ºC and allowing the HFA 227 to completely evaporate at atmospheric pressure. Aggregates of protein molecules did not appear to form according to OD measurements at 350 nm of 1 mg/mL BSA [27, 57]. The OD was the same at 0.042 for aqueous solutions in 10 mM phosphate pH = 7.4 buffer prepared from bulk and TFF powder, both before and after storage in HFA 227 for 1 week. In the glassy state, BSA is less susceptible to aggregation [56, 58]. The total moisture to BSA content was 7% (w/w) for the suspended BSA particles in HFA 227 as determined by Karl-Fischer titration. Even at particle moisture contents of 8% (w/w), BSA glass transition temperatures T_g range between 80-100ºC [59]. Thus the temperature was well below T_g, assuming the HFA 227 did not contribute to plasticization.

3.4.6 Particle characterization after actuation through the pMDI

The suspension must be stable for consistent dosing with a pMDI, which is commonly characterized by the dose (mass) delivered through the valve (DDV) (Table 3.1). The concentration was 10 mg/mL or 0.7% (w/w) in each HFA suspension. Therefore, the theoretically delivered dose per actuation would be 1 mg with the 100 µL valve. For the BSA TFF particles, the DDV values were 92% and 63% of the theoretical delivery dose for the sonicated and unsonicated TFF particles, respectively (Table 3.1). For the milled and spray dried suspensions with rapid settling, the DDV was only 30-31% of the theoretical loading. Here, the formulation was actuated less than 5 seconds after vigorous shaking. Therefore, these suspensions were not tested further for aerosol properties.

As shown in Table 3.2 and Figure 3.11A and B, the d_a determined from the Anderson cascade impactor (ACI) and the Aerodynamic Particle Sizer (APS) were in good agreement and ranged from 3 to 4 µm, within the optimal 1-5 µm range for pulmonary delivery. As determined by the ACI, the fine particle fraction (FPF) (particles less than 4.7 μm) was unusually high [35] for an HFA suspension, ranging from 38 to 47%, compared to 5 to 30% for typical suspensions [35], producing a fine particle dose/actuation of approximately 300 μg (Table 3.1). The emitted dose (ED) (amount of drug that exited the actuator) was approximately 70% of the DDV upon actuation (Table 3.1 and Figure 3.11A).

The particles were recovered from the ACI for SEM analysis. The peak drug mass in the ACI was deposited on stages 3 and 4, with d_a between 2.0-4.7 μm (Figure 3.11A). Therefore, particles were collected on stage 3 (d_a = 3-4 μm). The particles were porous and composed of rods with diameters less than 500 nm (Figure 3.12A and B), similar in morphology to the original nanorods in Figure 3.2A.

The SEMs were analyzed by Scion software to determine the volume average diameter [60, 61]

$$D_{Vol} = \frac{\sum d^4}{\sum d^3} \quad (3.3)$$

where d is the measured diameter of the particle. Approximately 200 of the BSA particles which consisted of aggregated nanorods were measured in 5 different images. The diameter of each particle was determined by averaging the longest and shortest diameter of each particle. The D_{vol} for BSA was approximately 9 μm (Table 3.2). The d_g of the aerosolized particles were also measured by SLS. An effective refractive index n_e was calculated according to the Bruggeman mixing rule [62] based on the volume fraction of BSA in the aerosolized particle ϕ_g (Appendix A). From the d_g and the d_a (Table 3.2), the particle density ρ_g can be defined by [41]

$$d_a = d_g\sqrt{\rho_g} \quad (3.4)$$

where ρ_g = 0.19 g/cm^3. The resulting $\phi_g = \rho_g / \rho_p$ = 0.14. With n = 1.45 and 1.00 for pure BSA and air, respectively, n_e = 1.1. As shown in Table 3.2 the volume average d(v,50) particle sizes varied by less than 1 μm from the values determined from the SEM micrographs. The consistent d_g values measured by SLS and SEM, and likewise for d_a, indicate that TFF particles form large porous particles, and with the optimal size range for pulmonary delivery upon aerosolization.

When the TFF particles were actuated above 10 mM phosphate buffer (pH = 7.4) the particles were visually observed to dissolve in less than 5 seconds. The high surface area favors rapid dissolution, which could be advantageous for rapid dissolution rates of proteins that have low solubilities in water [6].

3.5 DISCUSSION

The attractive van der Waals forces play a key role in the floc formation, as depicted in the summary in Figure 3.1 [14, 45, 63]. According to the Derjaguin-Landau-Verwey-Overbeek (DLVO) theory, particle stability depends on counteracting the attractive van der Waals forces by electrostatic and/or steric repulsion [14, 45, 63]. If attractive van der Waals (VdW) forces are dominant at all separation distances, particles flocculate and may then settle [14]. Currently, electrostatic stabilization in HFAs is not well understood [11], but atomic force microscopy (AFM) measurements indicate that electrostatic forces may be negligible compared to attractive VdW forces [11, 64]. The understanding of steric stabilization in HFAs is in its infancy [36, 39]. While novel surfactants are being discovered, developed and approved [38, 39], alternative means to form stable suspensions in HFAs without surfactants would be useful [11].

3.5.1 Suspension Stability for Porous or Hollow sphere Particles

The destabilizing van der Waals attractive forces between suspended particles are weaker for porous particles or hollow particles with thin solid shells [21, 40]. These particles can be stable for hours in HFAs, compared to non-porous 1-5 micron particles, which often flocculate and settle rapidly in less than 1 minute [21, 40] (see Figure 3.2). Dellamary et al. [21] suggested that the increased suspension stability resulted from a weaker attractive VdW energy potential Φ_{vdw} between the particles, but quantitative calculations were not presented [11].

As shown in Appendix A, the van der Waals energy Φ_{vdw} is directly proportional to the Hamaker constant A_{121}. In order to compare values of Φ_{vdw} it is necessary to choose a separation distance, h, between particles. Table 3.3 gives the h where Φ_{vdw} becomes equivalent to the thermal energy 3/2 k_BT at 298K. An increase in h required to overcome thermal energy indicates stronger attraction between particles. In Table 3.3, the porous particles with ϕ = 0.5 had a calculated A_{121} (Eq. A.3 in Appendix A) that was nearly a factor of 4 lower than for the non-porous particles. Consequently, h was a factor of 3 smaller. The hollow spheres from TEM images [21] were estimated to have 2-5 μm diameters and ~100 nm thick shells. Although the A_{121} for the hollow sphere particles with solid shells was the same as for the non-porous particles, the calculated h was still lower by a factor of 2 as a consequence of the differences in the geometries (Eq. A.6 in Appendix A). Therefore, the Φ_{vdw} calculations quantify the benefits of weaker attraction for porous particles or for particles with hollow cores. A reduction in Φ_{vdw} or in h to overcome thermal energy can reduce the rate of flocculation over orders of magnitude as described by the stability ratio [45, 63, 65].

Although, the porous or hollow sphere particles can effectively prevent flocculation, the particles are still subject to settling by gravity [11, 21]. If porous or hollow sphere BSA particles were suspended at ϕ_v = 0.0077, the particles would occupy ~ 10% of the suspension and could potentially settle into a dense sediment. As shown in Table

3.4, the calculated settling rate for a single hollow sphere particle with a solid shell is 6.4 x 10^{-4} mm/s indicating that the particles would settle a distance of 2 cm in ~ 9 hrs. The settled particles would then potentially aggregate irreversibly leading to decreased FPFs upon aerosolization [34].

3.5.2 Flocculation of TFF rods

To understand the space filling nature of the flocs composed of TFF rods, the volume fraction of the particles in the floc, ϕ_f, was calculated with Eq. 3.2. The volume of a TFF cylindrical rod, V_p = 0.019 μm^3, was calculated from the equivalent volume of a sphere with particle diameter d(v,50) = 0.33 μm, which was measured by SLS (Figure 3.6) in acetonitrile. For a rod with volume $V_p = \pi \cdot D^2 L / 4$ and D = 0.10 μm (Figure 3.2A and B), L is determined as 2.4 μm and thus r = 24. For r ~ 20, the predicted ϕ_f in Eq. 3.2 is ~1 order of magnitude lower than for spherical particles with equivalent d^{floc}, D_f, and where d_p for spheres scales as $V_p^{1/3}$ for rods.

To determine the effect of D_f on ϕ_f, the density of a floc ρ_f and ϕ_f were also determined experimentally from the visually observed floc settling rate, U_f, according to Stoke's law [66, 67]

$$U_f = \frac{d^{floc^2} \cdot (\rho_f - \rho_L) \cdot g}{18 \cdot \mu} \qquad (3.5)$$

where ρ_L and μ are the liquid density and viscosity, respectively, and d^{floc} = 250 μm for TFF flocs and 100 μm for spray dried and milled flocs (Figure 3.6). After solving for ρ_f in Eq. 3.5, ϕ_f may be determined by the straightforward material balance $\rho_f = \rho_L + \phi_f \cdot (\rho_p - \rho_L)$ [66, 67]. As seen in Table 3.4, ϕ_f for the TFF particles is 1-2 orders of magnitude lower than for the cube and spherical wet milled and spray dried particles. From Eq. 3.1 and 3.2 the calculated D_f values are in a narrow range from 2.5

to 2.6 in each case. Although the milled and TFF particles have nearly equivalent d^{floc} and D_f values (Table 3.4), the $1/r$ scaling in Eq. 3.2 for rods accounts for the 1 order of magnitude decrease in ϕ_f, for a given V_p, which is consistent with the theoretical prediction above.

As illustrated in Figure 3.1B, the open nanorod flocs with low ϕ_f filled large amounts of space in HFA and stacked upon each other like tumbleweeds to prevent settling. The volume fraction of flocs in the HFA suspension, ϕ^{flocs}, is given by $\phi^{flocs} = \phi_v / \phi_f$ (derivation given in Appendix A) where ϕ^{flocs} determines the space filling capability of the flocs. As ϕ^{flocs} approaches 1 the flocs occupy the entire volume of HFA (Figure 3.1B). For the dilute ϕ_v = 0.00077 suspension (Figure 3.3B), the calculated ϕ^{flocs} was 0.38 (Table 3.4) in good agreement with Figure 3.3B. At a loading 10 fold higher, ϕ_v = 0.0077, the entire vial was white without the appearance of spaces between flocs (Figure 3.3A), as expected from the low ϕ_f. Here it was not possible to observe a settling rate as the visual appearance did not change for 1 year, the maximum time tested, as the ϕ^{flocs} of essentially unity prevented settling. In order for the cubic or spherical particles to produce ϕ^{flocs} = 1 the required mass loadings for the milled and spray dried particles would be 6.7% (w/w) and 33% (w/w), respectively, compared to <0.7% (w/w) for the TFF rods. In contrast to the TFF rods, the hollow sphere particles would settle the length of the vial (~2 cm) by gravity in ~9 hours according to Stoke's law [21] for a particle diameter of 5 μm and shell thickness of 100 μm. In the settled state with a high particle volume fraction and contact between protein chains they are more likely to form irreversible particle aggregates by interparticle diffusion and sintering [68].

The open flocs in HFA 227, that gave the stable suspensions, may be shown to be favored by the relatively strong attractive forces between the primary particles [45, 63]. At first, this may seem counterintuitive to the normal goal of lowering attractive forces to stabilize colloidal dispersions. Upon addition of the HFA, the relatively strong attractive forces between the primary rods, Φ_{vdw}, cause sticky collisions to "lock in" the open structure rapidly to inhibit collapse of the flocs [45, 69]. For weaker attractive forces between primary particles, collapse has been shown to be more prevalent as particles sample a greater number of energetically favorable locations to reduce the interfacial surface area [45, 69]. Therefore, rapid flocculation from sticky collisions facilitates the formation of low density flocs that fill the entire vial and prevent settling.

In contrast to the flocs in HFA 227, colloidal dispersions of primary TFF rods in acetonitrile settled in 3 days (Figure 3.3F). This settling rate agreed with the predicted settling rate of individual effective spheres with a diameter of 330 nm from light scattering given in Table 3.4. From Table 3.3, the calculated A_{121} values for BSA in acetonitrile are 1 order of magnitude lower than in HFA 227 (Table 3.3). Therefore, the stronger attractive forces between particles in HFA relative to ACN, favors formation of open flocs, resulting in more stable suspensions against settling.

3.5.3 Aerosol formation from stable suspensions

Although the 250 μm flocs form stable suspensions, they are too large to produce optimal d_a. The shear forces in the actuator are needed to break apart the flocs. The calculation of these shear forces is rarely reported because the turbulence from the immediate onset of HFA evaporation produces complex cavitation events [61, 70]. According to empirical models, aerosolized HFA droplets are typically 10-30 μm in diameter [70]. Thus we choose an HFA droplet diameter of 25 μm. Our hypothesis is that the attractive van der Waals interactions between primary particles within a floc are very weak such that the HFA droplets may template the 250 μm flocs into 25 μm subdomains with the same ϕ_f = 0.0020 as illustrated schematically in Figure 3.1.

To separate the subdomain from the floc, the attractive forces between the interacting particles within (r_1) and outside (r_2) the subdomain surface (r_3) must be overcome (Figure 3.13). The particle density within the floc was assumed to be uniform at 1.1 x 10^{17} m^{-3} as determined from the ϕ_f = 0.0020 of the floc and V_p = 0.019 μm^3 of the rod primary particle. The total number of interacting particles was assumed to occupy a 25 nm thick shell between r_1 = 12.488 μm and r_2 = 12.513 μm (Figure 3.13). As shown in Table 3.4, at separation distances greater than 25 nm the attractive energy between particles is similar to the thermal energy. This indicates that particles at separation distances > 25 nm would not significantly contribute to the force necessary to separate the subdomain. The total number of particles in the shell was ~6, and therefore 3 particle-particle interactions had to be separated. The force to separate the interacting particles is dependent on the distance of separation of the particles (Eq. A.5). An average separation distance between the interacting particles was determined as the difference of the geometric means determined by $< r_{13} >= (r_1 \cdot r_3)^{1/2}$ and $< r_{23} >= (r_2 \cdot r_3)^{1/2}$ as shown in Figure 3.13 giving an average separation distance h between particles in the shell of 12.5 nm. From Eq. A.5 the total force necessary to separate the subdomain from the floc is ~10^{-12} N (Eq. A.5) assuming that the primary particle radius is 0.165 μm. The attractive force to separate the subdomain is very weak compared to the calculated shear force of ~10^{-4} N indicating that the subdomains can be easily templated by HFA droplets. The shear force, F_{shear}, on a 25 μm floc adhered to another floc was estimated by [71]

$$F_{shear} = \pi \cdot d^{floc^2} \cdot \tau = \frac{4 \cdot \pi \cdot d^{floc^2} \cdot \mu \cdot v^{\frac{7}{4}}}{\upsilon^{\frac{3}{4}} \cdot L_e^{\frac{1}{4}}} \qquad (3.6)$$

where d^{floc} is the floc diameter, τ is the viscous stress, μ and υ are the viscosity and kinematic viscosity of HFA 227 in the liquid state at 25°C, respectively, v is the HFA droplet velocity during atomization, and L_e is the dimension of the largest eddy generated during pMDI atomization (approximated as the dimension of the turbulent flow cavity). The floc subdomains were estimated to be 25 μm in diameter, the size of an HFA 227 droplet. The viscosity and kinematic viscosity of HFA 227 were 2.44 x 10^{-4} Pa•s and

1.76×10^{-7} m^2/s, respectively [14]. The velocity of the HFA droplets during atomization was estimated to be 30 m/s [61], and L_e was 0.7 mm, the pMDI valve diameter.

The concept of templating of the 25 μm subdomains is supported by a material balance on the protein between the volume of the HFA droplet, V_{HFA}, and the volume of the dry aerosolized particle, V_g, (Figure 3.1B) given by

$$V_g \cdot \rho_g = V_{HFA} \cdot \rho_{HFA} \quad (3.7)$$

where BSA concentrations are given by $\rho_{HFA} = \phi_v \cdot \rho_p$, and $\rho_g = \phi_g \cdot \rho_p$. It is assumed that the volume fraction of particles in a HFA droplet is approximately equal to ϕ_v as a result of the break up of the flocs. Because of the high ϕ^{flocs} (Figure 3.1B and 3.3A), it is expected that most of the HFA droplets are likely to be filled with a subdomain. From the measured d_g and d_a in Table 3.2 and ρ_g = 0.19 g/cm^3 (Eq. 3.4), ϕ_g = 0.14. The ϕ_g is nearly 20 times greater than ϕ_v in the vial. Therefore, the capillary forces in the shrinking HFA droplets during evaporation collapse the flocs [33]. Eq. 3.7 is refined to relate ϕ_g to ϕ_v as

$$\phi_g \cdot d_g{}^3 = \frac{f_{BSA}}{f_{HFA}} \cdot \phi_v \cdot d_{HFA}{}^3 \qquad (3.8)$$

where d is a diameter, f_{BSA} = 0.7 accounts for the mass fraction of drug that is emitted from the actuator, and f_{HFA} = 0.5 accounts for the mass fraction of HFA that exits the actuator orifice to form aerosolized liquid droplets (relative to vapor) [61].

From Eq. 3.8 with d_g = 9.3 μm (Table 3.2), d_{HFA} = 25 μm [70], and ϕ_v = 0.0077 , the calculated ϕ_g = 0.21, which compares reasonably well to the experimentally determined ϕ_g = 0.14. Also the polydispersity in the aerodynamic properties was small.

It would be unlikely that any other factor besides templating of the flocs with relatively uniform HFA droplets could explain these low polydispersities.

The control experiment in Figure 3.8A supports this argument since the TFF particles remained below the meniscus of the evaporating HFA 227. The tapped density of the particles was approximately 0.10 g/cm^3 (Figure 3.8A) which is within a factor of 2 of the calculated density (0.19 g/cm^3) of the aerosolized particle. Therefore, the capillary forces acting on the TFF particles during HFA evaporation compacted the particles into denser aggregates with a highly desirable value of the d_a. If needed, the d_a may be manipulated further by varying the valve volume and geometry and the HFA droplet generation. If the particles had not collapsed partially, they would have been too large and light for pulmonary delivery. Even after this collapse, the porosity and surface area were still relatively high and favorable for high dissolution rates of small molecules and proteins with limited solubilities, relative to nonporous particles [6].

3.6 CONCLUSIONS

High (38-47%) fine particle fractions in HFA 227 pMDI delivery were achieved with flocculated BSA nanorods stable against settling for up to 1 year, without the use of surfactants and cosolvents. Analysis of experimental settling rates of dilute suspensions indicated that the volume fraction, ϕ_f, of the nanorods in the flocs was an order of magnitude lower than for flocs of spherical particles produced by wet milling or spray drying. The rapid and sticky attractive collisions of nanorods facilitates the formation of low density flocs (250 μm) which stack upon each other to fill the entire solvent volume to prevent settling (Figure 3.1B). In contrast, denser flocs of spherical particles filled much less space and rapidly settled within 60 s (Figure 3.1A). The novel concept of purposely flocculating nanorods to prevent settling is fundamentally opposite the conventional approach of stabilizing colloidal dispersions of pre-formed primary particles with surfactants. The reversibility of the nanorod flocs in HFA 227 was demonstrated by break-up of the flocs into individual 330 nm primary rod particles upon transfer to the more polar solvent acetonitrile. A material balance on a shrinking HFA droplet containing a 25 μm floc subdomain predicts a final volume fraction of BSA in the aerosolized particle in agreement with experiment. Therefore, the attractive van der Waals interactions between primary particles within the floc are sufficiently weak such that the atomized HFA droplets initially template the 250 μm flocs into 25 μm subdomains. The aerosolized particles with a d_a of 3-4 μm and d_g of ~10 μm are optimal for high fine particle fractions via a pMDI. The concept of forming open flocs composed of aymmetric particles, for example nanorods, that are stable against settling without surfactants, and templating the flocs to achieve optimal d_as and high FPFs is of practical interest for wide classes of low and high molecular weight pharmaceuticals and biopharmaceuticals [29, 72, 73].

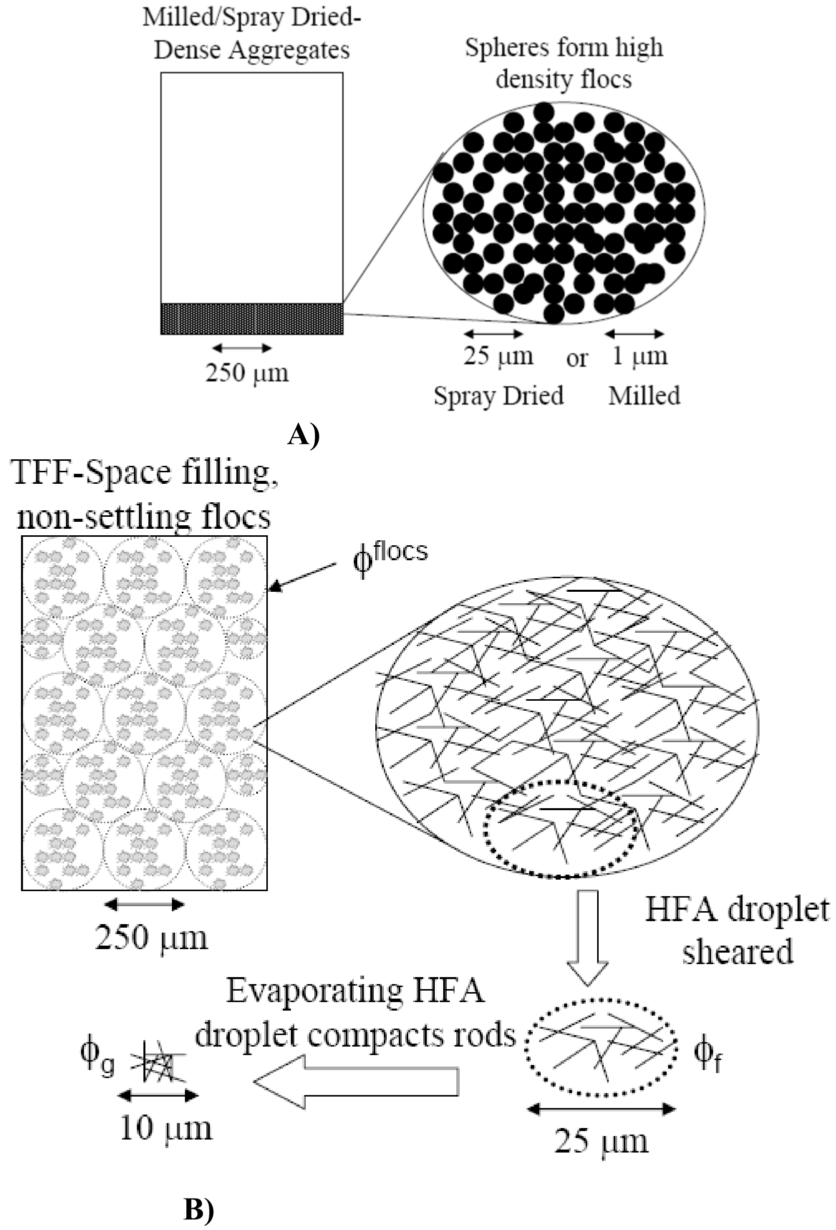

Figure 3.1 Particle suspensions of milled or spray dried particles (A) and TFF rod particles (B).

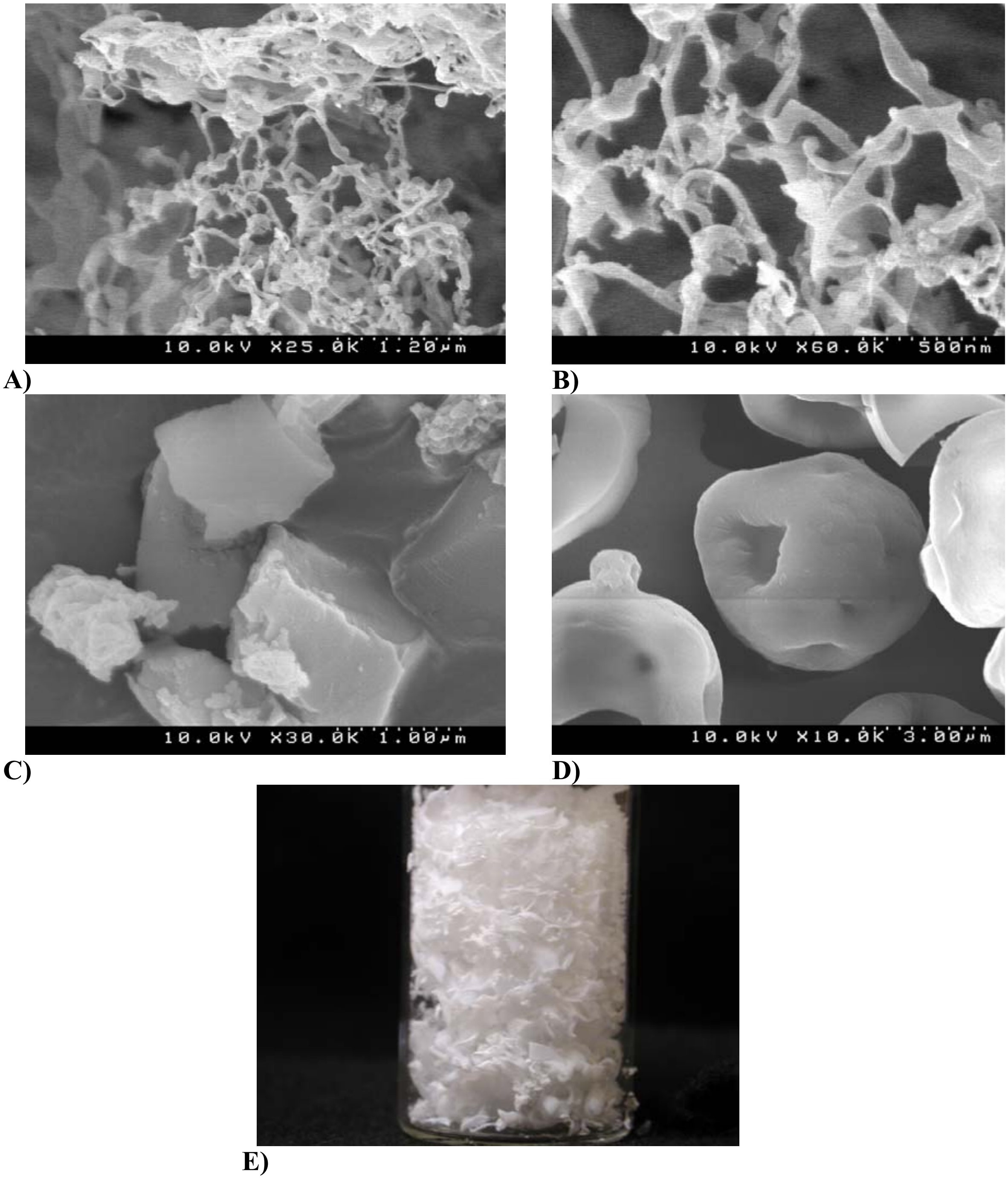

Figure 3.2 TFF particles of BSA (A, B and E), milled BSA particles (C) and spray dried BSA particles (D).

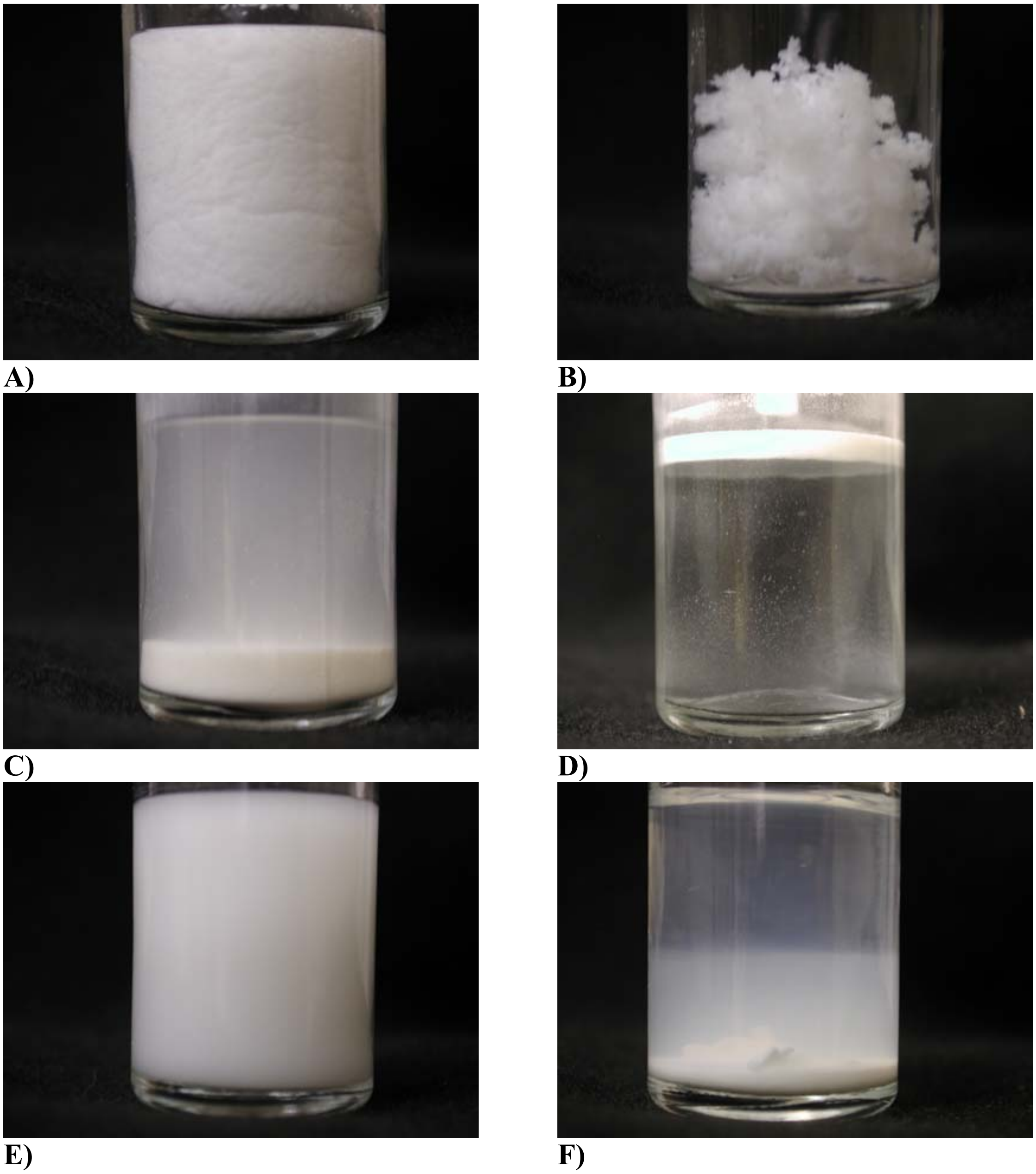

Figure 3.3 Suspensions in HFA 227 of TFF particles at $\phi_V = 0.0077$ (A) and $\phi_V = 0.00077$ (B), wet milled particles 5 minutes after shaking (C) and spray dried particles at 2 minutes after shaking (D) at $\phi_V = 0.0077$, and TFF particles in acetonitrile at $\phi_V = 0.0077$ immediately after shaking (E) and 3 days after shaking (F).

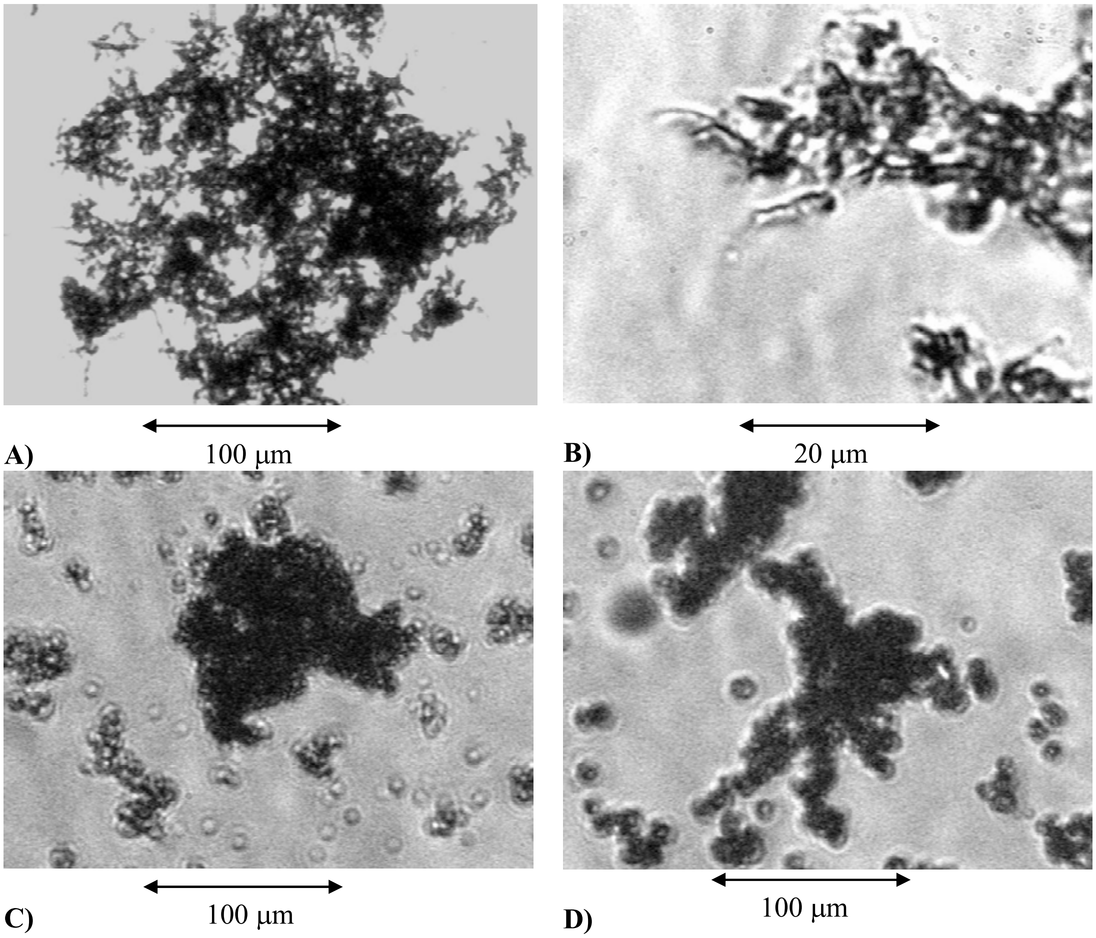

Figure 3.4 Optical microscopy images of BSA particles suspended in HPFP with TFF particles magnified 10x (A) and 60x (B) after 30 seconds, wet milled BSA particles after 30 seconds at 10x (C) and spray dried BSA particles after 30 seconds at 10x (D) The flocs from TFF particles are more open than for wet milled and spray dried particles.

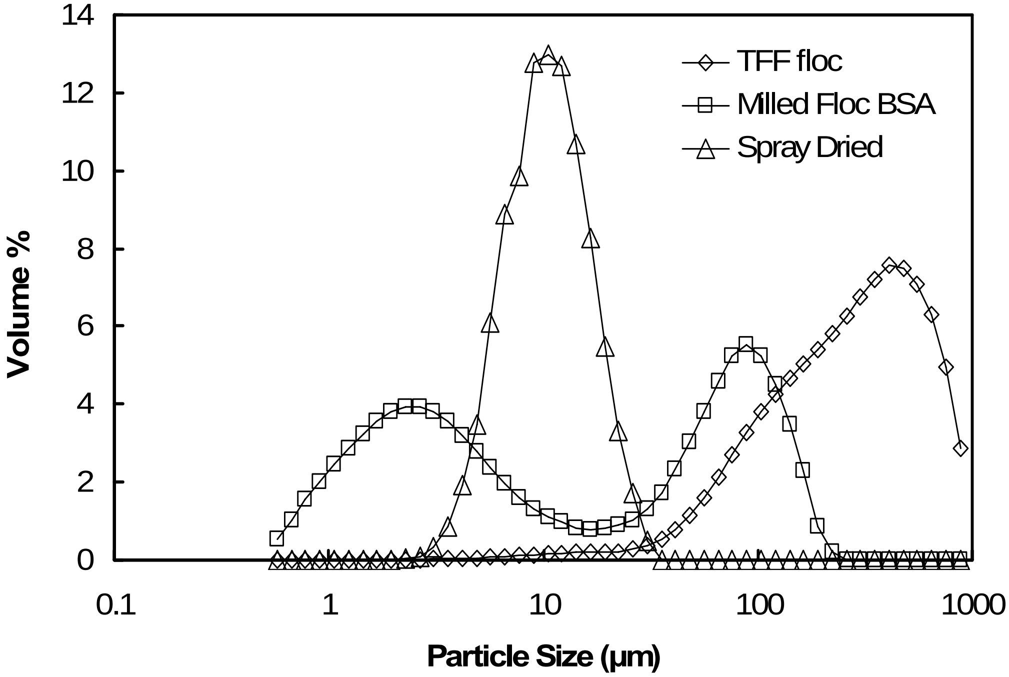

Figure 3.5 Particle sizes in HPFP measured by static light scattering for BSA nanorods formed by TFF, cubes formed by wet milling and spheres by spray drying. The large particle size for TFF nanorods indicates flocculation, consistent with the microscopy results in Figure 3.4.

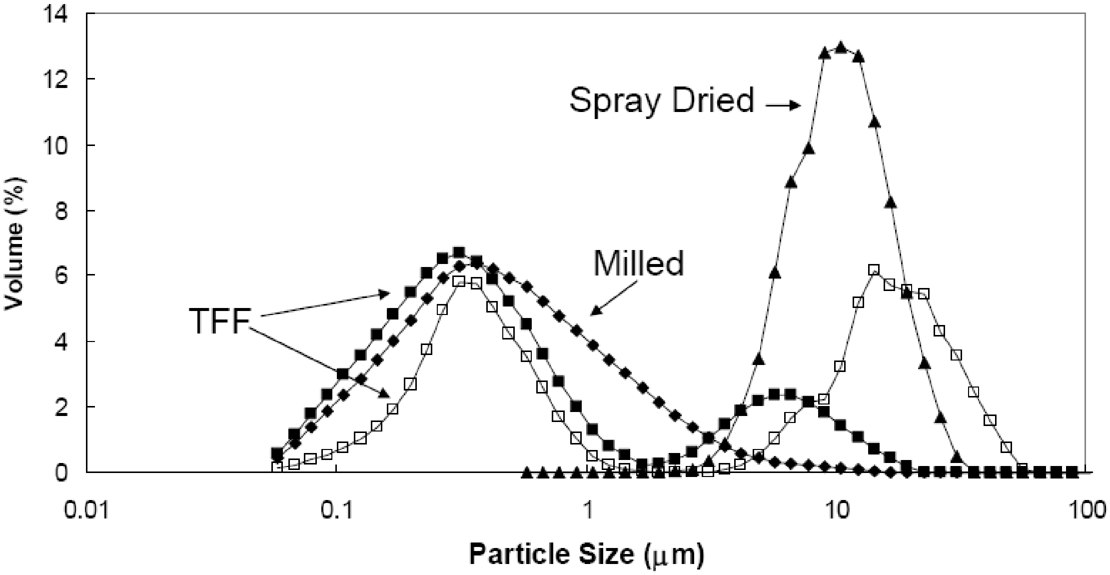

Figure 3.6 Particle sizes in acetonitrile measured by static light scattering for BSA nanorods formed by thin film freezing (TFF), cubes formed by wet milling and spheres by spray drying. Closed symbols indicate sonicated powder and open symbols indicate unsonicated powder.

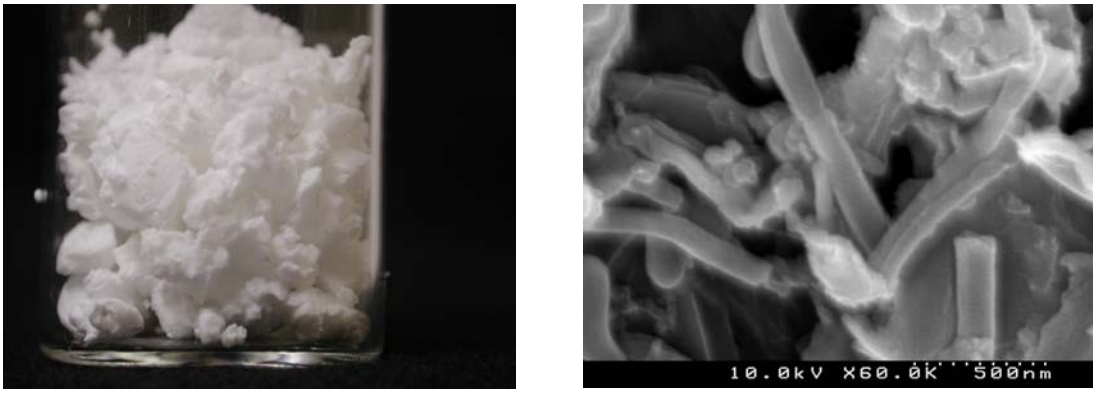

A) B)

Figure 3.7 TFF particles after suspension in ACN and lyophilization: photograph (A) and SEM (B).

A) **B)**

Figure 3.8 Photograph (A) and SEM (B) of TFF particles after HFA 227 evaporation.

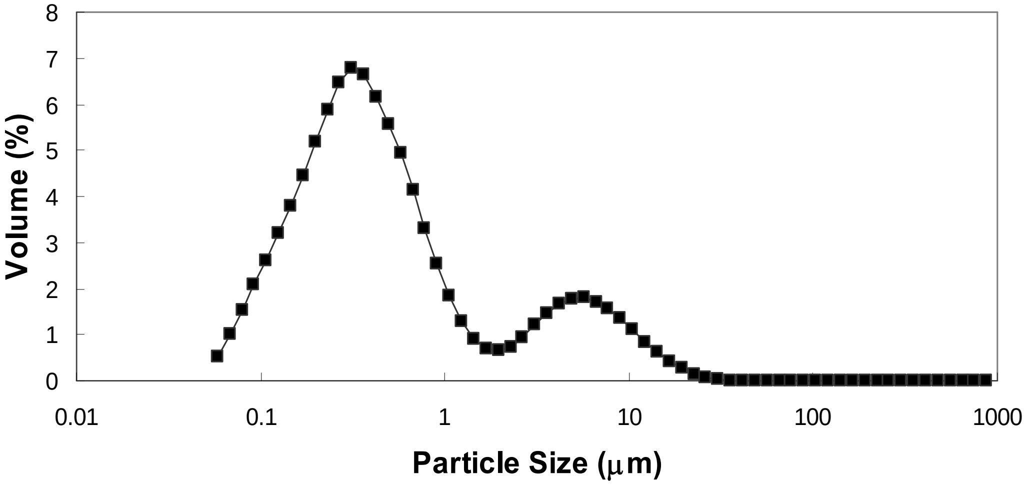

Figure 3.9 Particle size distribution measured by static light scattering for BSA nanorods suspended in HFA 227 and transferred to acetonitrile and sonicated.

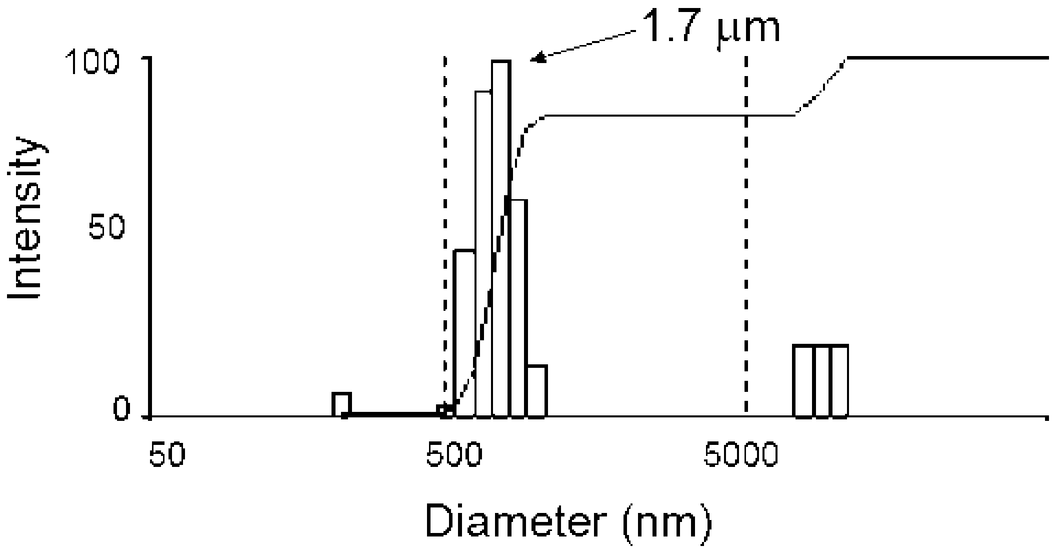

Figure 3.10 DLS of TFF particles actuated through the pMDI valve submerged beneath acetonitrile

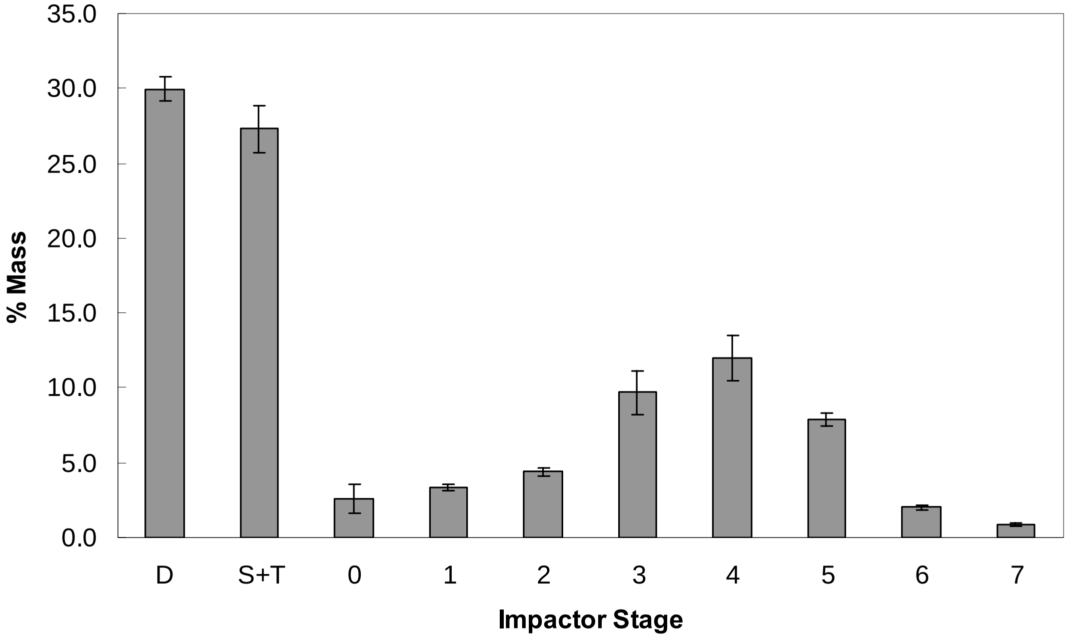

A)

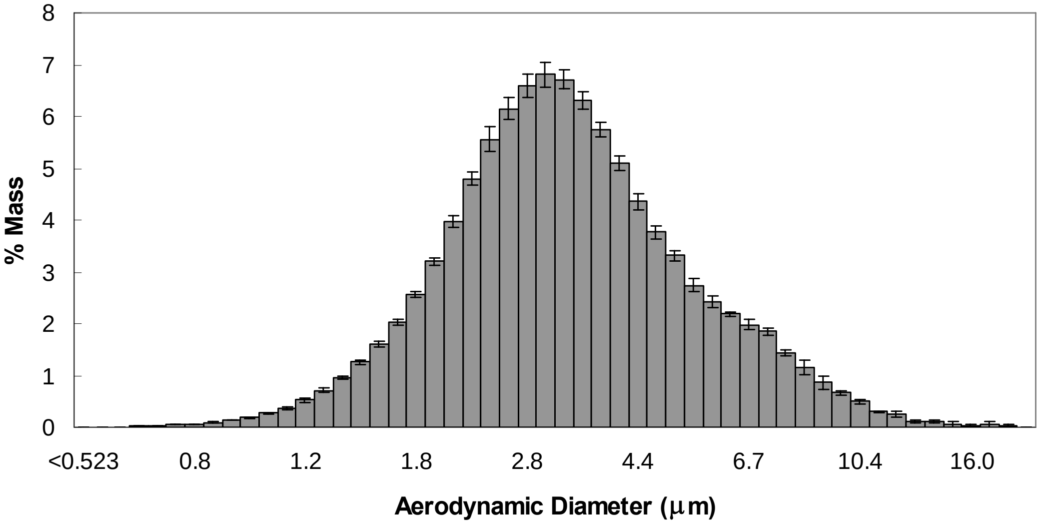

B)

Figure 3.11 ACI mass deposition profiles for device (D) and spacer and throat (S+T) and stages 0-7 (A), and APS mass distribution (B) for TFF BSA.

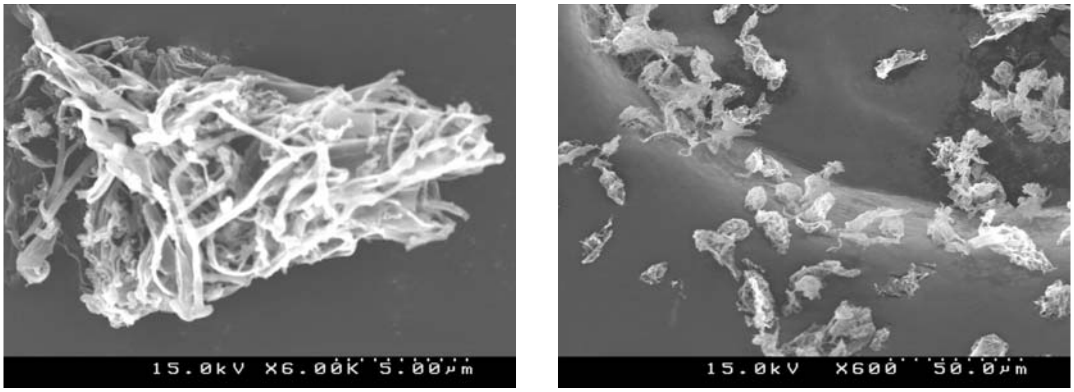

A) **B)**

Figure 3.12 BSA aerosol particles consisting of aggregates of nanorods collected from stage 3 of Anderson cascade impactor for BSA observed under high (A) and low magnification (B).

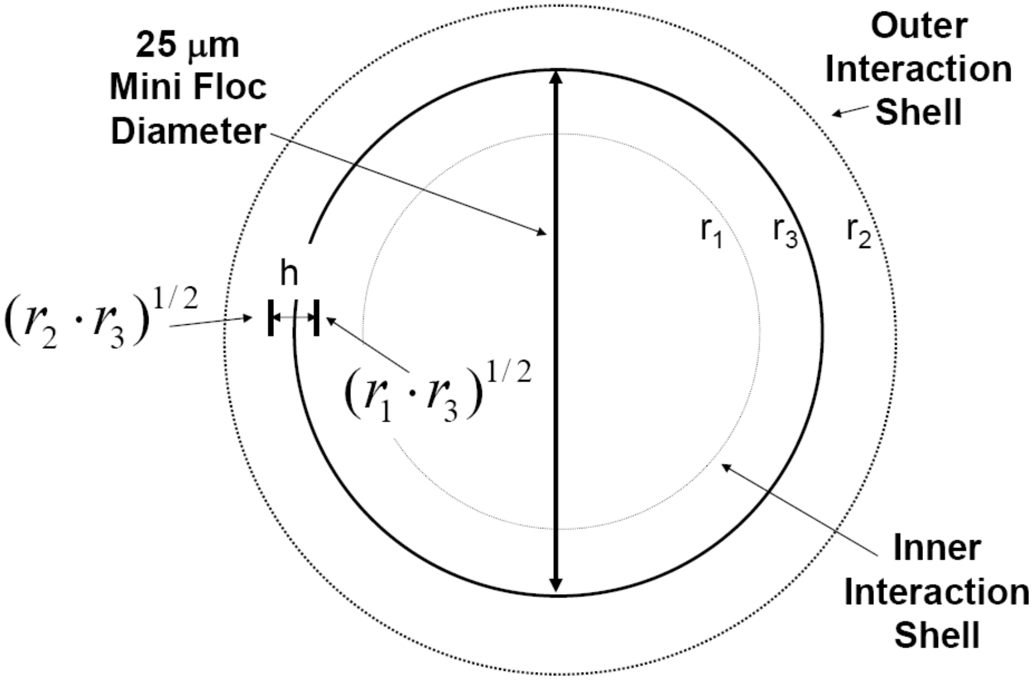

Figure 3.13 Diagram of subdomain with radius r_3 held within a floc by particles interacting within shells of radius r_1 and r_2.

Table 3.1 Dosage and aerodynamic properties of TFF, wet milled, and spray dried particle suspensions in HFA 227

Formulation	**DDV (μg)**	**%Theoretical DDV**	**FPF (%)**	**Fine Particle Dose/Actuation (μg)**	**ED (μg)**
TFF BSA	915 ± 21	92	47 ± 4.0	318 ± 31	695 ± 133
TFF BSA unsonicated	625 ± 95	63	--	--	--
Milled BSA	295 ± 17	30	--	--	--
Spray Dried BSA	308± 38	31	--	--	--

Table 3.2 Aerodynamic particle sizes determined by ACI and APS and geometric particle sizes determined by laser diffraction and SEM for TFF particles of BSA

ACI MMAD (μm)	**ACI GSD**	**APS MMAD (μm)**	**APS GSD**	**d(v,50) Particle Diameter (μm)**	**SEM Particle Diameter (μm)**	**ρ_g (g/cm^3)**
3.1 ± 0.1	1.9 ± 0.1	3.2 ± 0.03	1.6 ± 0.01	9.1 ± 0.9	9.4	0.19

Table 3.3 Calculation of the van der Waals (VdW) interaction potential Φ_{vdw} of BSA particles in HFA 227

Particle Type	**Particle Diameter (μm)**	**Hamaker Constant $10^{21} \times A_{121}$ (J)**	**Separation Distance (nm) at $\Phi_{vdw} = 3/2k_BT$**
Spray Dried-Non-Porous	5.0	14	270
Spray Dried-Porous $\phi = 0.50$	5.0	3.8	100
Spray Dried-Hollow Sphere[a] **$\phi_{shell} = 1.0$**	5.0	14	120
Spray Dried-Hollow Sphere[a] **$\phi_{shell} = 0.50$**	5.0	3.8	60
TFF Nanorods	0.33	14	23
TFF Nanorods[b]	0.33	2.6	6.9

[a] Shell thickness 100 nm

[b] TFF nanorods were in acetonitrile

Table 3.4 Settling behavior of BSA particles prepared by TFF, wet milling, and spray drying and calculations for porous shell particles prepared by spray drying.

Particle Type	**d_p (μm)**	**d^{floc} (μm)**	**$(\rho_L-\rho_f)$ (g/cm^3)**	**U_f (mm/s)**	**U_p (mm/s)**	**ϕ_v**	**ϕ^{flocs}**	**ϕ_f**	**D_f**
TFF	0.33[a]	250	0.00022	0.023	2.4×10^{-5}	0.00077	0.38	0.0020	2.5
Milled	0.41	100	0.0080[b]	0.13	3.7×10^{-5}	0.0067	0.11	0.073	2.5
Spray Dried	6.3	100	0.040	0.80	8.8×10^{-3}	0.0077	0.021	0.36	2.6
Spray Dried-Hollow Sphere	5.0[c]	--	0.013[d]	--	6.4×10^{-4}	--	--	--	--

[a] Value determined from the equivalent volume of a sphere measured from laser light scattering

[b] The density difference was determined by $\rho_f-\rho_L$ with $\rho_p = 1.5$ g/cm^3

[c] Determined from dimensions given by Dellamary et al.[21]

[d] Calculated for primary particle with 100 nm thick shell

3.7 REFERENCES

1. Agu, R. U.; Ugwoke, M. I.; Armand, M.; Kinget, R.; Verbeke, N., The lung as a route for systemic delivery of therapeutic proteins and peptides. *Respiratory Research* **2001,** 2, (4), 198-209.

2. Adjei, A. L.; Gupta, P. K., *Inhalation Delivery of Therapeutic Peptides and Proteins*. 1997; p 913.

3. White, S.; Bennett, D. B.; Cheu, S.; Conley, P. W.; Guzek, D. B.; Gray, S.; Howard, J.; Malcolmson, R.; Parker, J. M.; Roberts, P.; Sadrzadeh, N.; Schumacher, J. D.; Seshadri, S.; Sluggett, G. W.; Stevenson, C. L.; Harper, N. J., EXUBERA: Pharmaceutical Development of a Novel Product for Pulmonary Delivery of Insulin. *Diabetes Technology & Therapeutics* **2005,** 7, (6), 896-906.

4. Shoyele, S. A.; Slowey, A., Prospects of formulating proteins/peptides as aerosols for pulmonary drug delivery. *International Journal of Pharmaceutics* **2006,** 314, (1), 1-8.

5. Courrier, H. M.; Butz, N.; Vandamme, T. F., Pulmonary drug delivery systems: recent developments and prospects. *Critical Reviews in Therapeutic Drug Carrier Systems* **2002,** 19, (4 & 5), 425-498.

6. Kwon, M. J.; Bae, J. H.; Kim, J. J.; Na, K.; Lee, E. S., Long acting porous microparticle for pulmonary protein delivery. *International Journal of Pharmaceutics* **2007,** 333, (1-2), 5-9.

7. Patton, J. S.; Byron, P. R., Inhaling medicines: delivering drugs to the body through the lungs. *Nature Reviews Drug Discovery* **2007,** 6, (1), 67-74.

8. Codrons, V.; Vanderbist, F.; Verbeeck, R. K.; Arras, M.; Lison, D.; Preat, V.; Vanbever, R., Systemic delivery of parathyroid hormone (1-34) using inhalation dry powders in rats. *Journal of Pharmaceutical Sciences* **2003,** 92, (5), 938-950.

9. Garcia-Contreras, L.; Smyth, H. D. C., Liquid-spray or dry-powder systems for inhaled delivery of peptide and proteins? *American Journal of Drug Delivery* **2005,** 3, (1), 29-45.

10. Traini, D.; Young, P.; Rogueda, P.; Price, R., The Use of AFM and Surface Energy Measurements to Investigate Drug-Canister Material Interactions in a Model Pressurized Metered Dose Inhaler Formulation. *Aerosol Science and Technology* **2006,** 40, (4), 227-236.

11. Rogueda, P., Novel hydrofluoroalkane suspension formulations for respiratory drug delivery. *Expert Opinion on Drug Delivery* **2005,** 2, (4), 625-638.

12. Williams, R. O., III; Liu, J., Formulation of a protein with propellant HFA 134a for aerosol delivery. *European Journal of Pharmaceutical Sciences* **1999,** 7, (2), 137-144.

13. Williams, R. O., III; Repka, M.; Liu, J., Influence of propellant composition on drug delivery from a pressurized metered-dose inhaler. *Drug Development and Industrial Pharmacy* **1998,** 24, (8), 763-770.

14. Johnson, K. A., Interfacial phenomena and phase behavior in metered dose inhaler formulations. In *Inhalation Aerosols: Physical and biological basis for therapy*, 2 ed.; Hickey, A. J., Ed. 2007; Vol. 221.

15. Quinn, E. A.; Forbes, R. T.; Williams, A. C.; Oliver, M. J.; McKenzie, L.; Purewal, T. S., Protein conformational stability in the hydrofluoroalkane propellants tetrafluoroethane and heptafluoropropane analyzed by Fourier transform Raman spectroscopy. *International Journal of Pharmaceutics* **1999,** 186, (1), 31-41.

16. Oliver, M. J.; McKenzie, L.; Graffiths, W. D.; Morgan, G. R.; O'Kelly, N. In *Initial assessment of a protein formulated in pressurized mdis for pulmonary delivery*, RDD VII, 2000; 2000.

17. Benfait, C., Kos reports achievement of new research and development milestones. *Kos Press Release* **2004**.

18. Heyder, J.; Gebhart, J.; Rudolf, G.; Schiller, C. F.; Stahlhofen, W., Deposition of particles in the human respiratory tract in the size range 0.005-15 μm. *Journal of Aerosol Science* **1986,** 17, 811-825.

19. Ben-Jebria, A.; Chen, D.; Eskew, M. L.; Vanbever, R.; Langer, R.; Edwards, D. A., Large porous particles for sustained protection from carbachol-induced bronchoconstriction in guinea pigs. *Pharmaceutical Research* **1999,** 16, (4), 555-561.

20. Tsapis, N.; Bennett, D.; Jackson, B.; Weitz, D. A.; Edwards, D. A., Trojan particles: large porous carriers of nanoparticles for drug delivery. *Proceedings of the National Academy of Sciences of the United States of America* **2002,** 99, (19), 12001-12005.

21. Dellamary, L. A.; Tarara, T. E.; Smith, D. J.; Woelk, C. H.; Adractas, A.; Costello, M. L.; Gill, H.; Weers, J. G., Hollow porous particles in metered dose inhalers. *Pharmaceutical Research* **2000,** 17, (2), 168-174.

22. Maa, Y.-F.; Nguyen, P.-A.; Sweeney, T.; Shire, S. J.; Hsu, C. C., Protein inhalation powders: spray drying vs spray freeze drying. *Pharmaceutical Research* **1999,** 16, (2), 249-254.

23. Maa, Y.-F.; Costantino, H. R., Spray freeze-drying of biopharmaceuticals: applications and stability considerations. In *Biotechnology: Pharmaceutical*

Aspects. 2. Lyophilization of Biopharmaceuticals, Costantino, H. R.; Pikal, M. J., Eds. American Association of Pharmaceutical Scientists: Arlington, 2004; Vol. 2, pp 519-561.

24. Yu, Z.; Garcia, A. S.; Johnston, K. P.; Williams III, R. O., Spray freezing into liquid nitrogen for highly stable protein nanostructured microparticles. *European Journal of Pharmaceutics and Biopharmaceutics* **2004,** 58, (3), 529-537.

25. Engstrom, J. D.; Simpson, D. T.; Lai, E.; Williams III, R. O.; Johnston, K. P., Morphology of protein particles produced by spray freezing of concentrated solutions. *European Journal of Pharmaceutics and Biopharmaceutics* **2007,** 65, (2), 149-162.

26. Engstrom, J. D.; Simpson, D. T.; Cloonan, C.; Lai, E.; Williams III, R. O.; Kitto, G. B.; Johnston, K. P., Stable high surface area lactate dehydrogenase particles produced by spray freezing into liquid nitrogen. *European Journal of Pharmaceutics and Biopharmaceutics* **2007,** 65, (2), 163-174.

27. Yu, Z.; Johnston, K. P.; Williams III, R. O., Spray freezing into liquid versus spray-freeze drying: Influence of atomization on protein aggregation and biological activity. *European Journal of Pharmaceutical Sciences* **2006,** 27, (1), 9-18.

28. Yu, Z.; Rogers, T. L.; Hu, J.; Johnston, K. P.; Williams III, R. O., Preparation and characterization of microparticles containing peptide produced by a novel process: spray freezing into liquid. *European journal of pharmaceutics and biopharmaceutics* **2002,** 54, (2), 221-228.

29. Engstrom, J. D.; Lai, E. S.; Ludher, B.; Chen, B.; Milner, T. E.; Kitto, G. B.; Williams III, R. O.; Johnston, K. P., Formation of stable submicron protein particles by thin film freezing. *Pharmaceutical Research* **2008,** 25, (6), 1334-1346.

30. Webb, S. D.; Golledge, S. L.; Cleland, J. L.; Carpenter, J. F.; Randolph, T. W., Surface adsorption of recombinant human interferon-γ in lyophilized and spray-lyophilized formulations. *Journal of Pharmaceutical Sciences* **2002,** 91, (6), 1474-1487.

31. Nguyen, X. C.; Herberger, J. D.; Burke, P. A., Protein powders for encapsulation: a comparison of spray-freeze drying and spray drying of darbepoetin alfa. *Pharmaceutical Research* **2004,** 21, (3), 507-514.

32. Maa, Y.-F.; Prestrelski, S. J., Biopharmaceutical powders: particle formation and formulation considerations. *Current Pharmaceutical Biotechnology* **2000,** 1, (3), 283-302.

33. Gonda, I., Development of a systematic theory of suspension inhalation aerosols. I. A framework to study the effects of aggregation on the aerodynamic behavior of drug particles. *International Journal of Pharmaceutics* **1985,** 27, (1), 99-116.

34. Liao, Y.-H.; Brown, M. B.; Jones, S. A.; Nazir, T.; Martin, G. P., The effects of polyvinyl alcohol on the in vitro stability and delivery of spray-dried protein particles from surfactant-free HFA 134a-based pressurised metered dose inhalers. *International Journal of Pharmaceutics* **2005,** 304, (1-2), 29-39.

35. Keller, M., Innovations and perspectives of metered dose inhalers in pulmonary drug delivery. *International Journal of Pharmaceutics* **1999,** 186, (1), 81-90.

36. Vervaet, C.; Byron, P. R., Drug-surfactant-propellant interactions in HFA-formulations. *International Journal of Pharmaceutics* **1999,** 186, (1), 13-30.

37. Blondino, F. E.; Byron, P. R., Surfactant dissolution and water solubilization in chlorine-free liquified gas propellants. *Drug Development and Industrial Pharmacy* **1998,** 24, (10), 935-945.

38. Peguin, R. P. S.; Selvam, P.; da Rocha, S. R. P., Microscopic and Thermodynamic Properties of the HFA134a-Water Interface: Atomistic Computer Simulations and Tensiometry under Pressure. *Langmuir* **2006,** 22, (21), 8826-8830.

39. Wu, L.; Peguin, R. P. S.; Selvam, P.; Chokshi, U.; da Rocha, S. R. P., Molecular scale behavior in alternative propellant-based inhaler formulations. In *Inhalation Aerosols: Physical and biological basis for therapy*, Hickey, A. J., Ed. 2007; Vol. 221.

40. Vanbever, R.; Mintzes, J. D.; Wang, J.; Nice, J.; Chen, D.; Batycky, R.; Langer, R.; Edwards, D. A., Formulation and physical characterization of large porous particles for inhalation. *Pharmaceutical Research* **1999,** 16, (11), 1735-1742.

41. Edwards, D. A.; Hanes, J.; Caponetti, G.; Hrkach, J.; Ben-Jebria, A.; Eskew, M. L.; Mintzes, J.; Deaver, D.; Lotan, N.; Langer, R., Large porous particles for pulmonary drug delivery. *Science* **1997,** 276, (5320), 1868-1871.

42. Tam, J.; McConville, J. T.; Williams III, R. O.; Johnston, K. P., Amorphous cyclosporin A nanodispersions for enhanced pulmonary deposition and dissolution. ASAP. *Journal of Pharmaceutical Sciences* **2007**.

43. Jiang, Z.; Guan, Y., Flocculation morphology: effect of particulate shape and coagulant species on flocculation. *Water Science and Technology* **2006,** 53, (7, Particle Separation 2005: Waste Water Treatment), 9-16.

44. Goodarz-Nia, I.; Sutherland, D. N., Floc simulation. Effects of particle size and shape. *Chemical Engineering Science* **1975,** 30, (4), 407-12.

45. Hiemenz, P. C.; Rajagopalan, R., *Principles of colloid and surface chemistry*. 1997.

46. Philipse, A. P.; Wierenga, A. M., On the Density and Structure Formation in Gels and Clusters of Colloidal Rods and Fibers. *Langmuir* **1998,** 14, (1), 49-54.

47. Philipse, A. P., The Random Contact Equation and Its Implications for (Colloidal) Rods in Packings, Suspensions, and Anisotropic Powders. *Langmuir* **1996,** 12, (24), 5971.

48. Larson, R. G., *The Structure and Rheology of Complex Fluids*. Oxford University Press Inc.: New York, 1999.

49. Smith, P. G., Jr.; Ryoo, W.; Johnston, K. P., Electrostatically Stabilized Metal Oxide Particle Dispersions in Carbon Dioxide. *Journal of Physical Chemistry B* **2005,** 109, (43), 20155-20165.

50. Kim, Y.; Atwell, S. H.; Bell, R. G., Determination of water in pressurized pharmaceutical metered dose aerosol products. *Drug Development and Industrial Pharmacy* **1992,** 18, (20), 2185-95.

51. Williams, R. O., III; Liu, J.; Koleng, J. J., Influence of metering chamber volume and water level on the emitted dose of a suspension-based pMDI containing propellant 134a. *Pharmaceutical Research* **1997,** 14, (4), 438-443.

52. Berlin, E.; Pallansch, M. J., Densities of several proteins and L-amino acids in the dry state. *Journal of Physical Chemistry* **1968,** 72, (6), 1887-9.

53. Rogueda, P. G. A., HPFP, a model propellant for pMDIs. *Drug Development and Industrial Pharmacy* **2003,** 29, (1), 39-49.

54. Ashayer, R.; Luckham, P. F.; Manimaaran, S.; Rogueda, P., Investigation of the molecular interactions in a pMDI formulation by atomic force microscopy. *European Journal of Pharmaceutical Sciences* **2004,** 21, (4), 533-543.

55. Traini, D.; Young Paul, M.; Rogueda, P.; Price, R., In vitro investigation of drug particulates interactions and aerosol performance of pressurised metered dose inhalers. *Pharmaceutical Research* **2007,** 24, (1), 125-135.

56. Nail, S. L.; Jiang, S.; Chongprasert, S.; Knopp, S. A., Fundamentals of freeze-drying. In *Pharmaceutical Biotechnology. 14. Development and Manufacture of Protein Pharmaceuticals*, Nail, S. L.; Akers, M. J., Eds. Kluwer Academic/Plenum Publishers: New York, 2002; Vol. 14, pp 281-360.

57. Webb, S. D.; Cleland, J. L.; Carpenter, J. F.; Randolph, T. W., A new mechanism for decreasing aggregation of recombinant human interferon-g by a surfactant: slowed dissolution of lyophilized formulations in a solution containing 0.03% polysorbate 20. *Journal of Pharmaceutical Sciences* **2002,** 91, (2), 543-558.

58. Carpenter, J. F.; Chang, B. S.; Garzon-Rodriguez, W.; Randolph, T. W., Rational design of stable lyophilized protein formulations: theory and practice. In *Pharmaceutical Biotechnology. 13. Rational Design of Stable Protein Formulations*, Carpenter, J. F.; Manning, M. C., Eds. Kluwer Academic/Plenum Press: New York, 2002; Vol. 13, pp 109-133.

59. Farahnaky, A.; Badii, F.; Farhat, I. A.; Mitchell, J. R.; Hill, S. E., Enthalpy relaxation of bovine serum albumin and implications for its storage in the glassy state. *Biopolymers* **2005,** 78, (2), 69-77.

60. Shekunov, B. Y.; Chattopadhyay, P.; Tong, H. H. Y.; Chow, A. H. L., Particle Size Analysis in Pharmaceutics: Principles, Methods and Applications. *Pharmaceutical Research* **2007,** 24, (2), 203-227.

61. Finlay, W. H., *The mechanics of inhaled pharmaceutical aerosols*. New York, 2001.

62. Sihvola, A., *Electromagnetic mixing formulas and applications*. 1999; Vol. 47.

63. Russel, W. B.; Saville, D. A.; Schowalter, W. R., *Colloidal dispersions*. 1989.

64. Traini, D.; Rogueda, P.; Young, P.; Price, R., Surface Energy and Interparticle Forces Correlations in Model pMDI Formulations. *Pharmaceutical Research* **2005,** 22, (5), 816-825.

65. Bevan, M. A. Effect of Adsorbed Polymer on the Interparticle Potential. PhD Dissertation, Carnegie Mellon University, Pittsburgh, 1999.

66. Tang, P.; Greenwood, J.; Raper, J. A., A model to describe the settling behavior of fractal aggregates. *Journal of Colloid and Interface Science* **2002,** 247, (1), 210-219.

67. Fargues, C.; Turchiuli, C., Structural characterization of flocs in relation to their settling performances. *Chemical Engineering Research and Design* **2004,** 82, (A11), 1517.

68. Abramowitz, H.; Shah, P. S.; Green, P. F.; Johnston, K. P., Welding Colloidal Crystals with Carbon Dioxide. *Macromolecules* **2004,** 37, (19), 7316-7324.

69. Ulrich, D. R., Chemical processing of ceramics. *Chemical & Engineering News* **1990,** 68, (1), 28-40.

70. Smyth, H. D. C.; Hickey, A. J.; Evans, R. M., Aerosol generation from propellant-driven metered dose inhalers. In *Inhalation Aerosols: Physical and Biological Basis for Therapy*, Hickey Anthony, J., Ed. 2007; Vol. 221, pp 399-416.

71. French, D. L.; Edwards, D. A.; Niven, R. W., The influence of formulation on emission, deaggregation and deposition of dry powders for inhalation. *Journal of Aerosol Science* **1996,** 27, (5), 769-783.

72. Rogers, T. L.; Nelsen, A. C.; Hu, J.; Brown, J. N.; Sarkari, M.; Young, T. J.; Johnston, K. P.; Williams III, R. O., A novel particle engineering technology to enhance dissolution of poorly water soluble drugs: spray-freezing into liquid. *European journal of pharmaceutics and biopharmaceutics* **2002,** 54, (3), 271-280.

73. Rogers, T. L.; Overhoff, K. A.; Shah, P.; Santiago, P.; Yacaman, M. J.; Johnston, K. P.; Williams III, R. O., Micronized powders of a poorly water soluble drug produced by a spray-freezing into liquid-emulsion process. *European journal of pharmaceutics and biopharmaceutics* **2003,** 55, (2), 161-72.

Chapter 4: Templated Open Flocs of Anisotropic Particles for Pulmonary Delivery with Pressurized Metered Dose Inhalers

The challenges in forming uniform and stable drug suspensions in hydrofluoroalkane (HFA) propellants have limited drug dosages and efficiency of delivery with pressurized metered dose inhalers (pMDI). Herein, stable suspensions of weakly flocculated particles, in the shape of thin plates or needles, of a poorly water soluble drug, itraconazole (Itz), in HFA 227 are delivered efficiently with high doses, up to 2.4 mg/actuation. These anisotropic particles, with aspect ratios from 5-10, pack inefficiently and form low density flocs that stack upon each other to prevent settling, with no visible settling for over two years. In contrast, spherical particles produced by milling formed dense aggregates that settled within one minute. Upon actuation of the pMDI, the atomized propellant droplets shear apart and thus template portions of the highly friable flocs. Evaporation of the HFA droplets compacts the flocs to yield porous particles that possess optimal aerodynamic properties. Thus, the respirable particles are formed *in situ* in the airways, in contrast with conventional particles which are pre-formed to possess desired aerodynamic diameters before being suspended in the propellant. High fine particle fractions (49-64%) were achieved with the stable uniform suspensions, even at high drug loadings up to 50 mg/mL. This approach produces micron-sized particles, ideal for deep lung delivery, which are composed of nanoparticles that facilitate rapid dissolution to enhance the systemic absorption of poorly water soluble drugs. Pulmonary delivery of stable suspensions of templated, open flocs is broadly applicable to a range of anisotropic particle morphologies, including plates, needles, and rods of poorly water soluble drugs, as well as proteins, to deliver high doses, up to several milligrams, using minimal amounts of excipients.

4.1 INTRODUCTION

Pulmonary delivery is an attractive route of drug administration because it is non-invasive and offers advantages of an enormous absorptive surface area (140 m^2), thin absorptive membrane (0.1 – 0.5 μm), highly vascularized epithelium, and avoidance of first pass metabolism[1]. Effective treatment of respiratory diseases, such as asthma and chronic bronchitis, by pulmonary drug delivery methods has been well established[1, 2]. More recently, aerosol delivery of systemic drugs has resulted in several pulmonary insulin products[3-7]. To achieve high deposition of particles in the alveoli, where drug absorption is most efficient as a consequence of extremely thin membranes (0.1 – 0.2 μm)[1], aerosolized particles must possess an aerodynamic diameter (d_a) between 1-5 μm. Particles larger than 5 μm tend to deposit in the throat or upper airways whereas smaller, sub-micron particles are often exhaled during expiration without appreciable deposition[8, 9].

The most widely used delivery option for aerosolized particles is the pressurized metered dose inhaler (pMDI) because it is convenient, reliable, affordable , and provides effort-independent dosing [10, 11]. Formulations for use in pMDIs are commonly developed as suspensions due to the low solubilities of many drugs in hydrofluoroalkane (HFA) propellants[12]. Drug particles within the appropriate size range for pMDI delivery are most commonly produced by milling[12-15] and spray drying[7, 16-18]. However, at typical drug loadings of 1-5% w/w[12], suspensions of milled or spray dried particles in the HFA propellant often flocculate and settle within minutes, due to a lack of repulsive interactions between particles[12, 17, 19]. Thus, pMDI formulations often contain additives such as surfactants and co-solvents to aid in suspension stability[12, 20, 21]. However, hydrogenated tails of FDA-approved surfactants are poorly solvated by HFAs, due to its low polarizability. The poor solvation has resulted in low surfactant solubilities and poor steric stabilization of drug particles coated by these surfactants[10, 12, 22-24]. Consequently, pMDI formulations are often constrained by low mass loadings (<5% w/w) and fine particle fractions (FPF) between 5-30%[25]. The FPF is the percentage of delivered particles estimated to deposit in the deep lungs[1]. The low FPF is caused by irreversible particle aggregation after settling, which increases d_a and reduces deep lung deposition, and causes inconsistent dosing between actuations. Thus, pMDI administration has been primarily used to deliver high potency (low dose) drugs. Typical respirable doses delivered by pMDI are only 30-200 µg/actuation[1, 17, 25], relative to required doses for insulin and some anti-cancer agents of 1-10 mg/dose[26].

An alternative approach for enhancing the stability of primary particles in HFA-propellants is to modify particle morphology. Hollow particles with porous shells form stable suspensions in HFAs, with no visible settling up to four hours[17]. Their porous structure allows the HFA to fill the particle, minimizing the density difference between the suspended particles and the surrounding HFA, significantly reducing van der Waals attraction forces between particles[27]. Additionally, high FPFs are achieved with the hollow, porous particles when delivered as a pMDI, ranging from 40-70% for a wide variety of drugs [17, 27-29]. Particles with a similar morphology to hollow, porous particles include large porous particles (LPP) [4, 18] and large porous nanoparticle (LPNP) aggregates [30-34], which are produced by spray drying and have sizes ranging from 10-20 µm. These powders exhibit FPFs as high as 60% when administered as a dry powder due to their low density(< 0.4 g/cm^3) [4, 18, 30-32]. To extend this approach to pMDI delivery, large, porous, particles are stabilized as individual entities as a colloidal dispersion or suspension in HFA; however, over the course of several hours, they are expected to settle due to their large size. Furthermore, the ability to form large, porous particles often requires the inclusion of significant amounts of excipients, which reduces the active pharmaceutical ingredient (API) potency in the composition. API loadings in porous particles have been reported as high as 70%, but are typically less than 50% w/w, with respriable doses up to 300 µg/actuation[12, 17, 28].

To date, suspension-based pMDIs have utilized pre-formed particles that possess the proper aerodynamic diameter for deep lung deposition. Recently we introduced a new paradigm in which the particles are not pre-formed, but instead are templated by HFA droplets and formed in the airways. Anisotropic nanorods of bovine serum albumin (BSA) were purposely flocculated in an HFA to produce low density flocs that stack upon each other and fill the entire volume of the propellant to inhibit settling[35] (Fig. 4.1). Furthermore, the protein rods yielded stable suspensions in HFA without the need for surfactants or additional excipients, which is highly desirable to achieve increased doses, limit disruption of lung function, and avoid potential toxicity issues[36, 37]. The packing behavior in flocs may be contrasted for spheres and rods. The volume fraction occupied by spherical particles within a floc, φ_f, is approximated by

$$\varphi_{f,\mathrm{spheres}} \approx \left(\frac{d_{\mathrm{floc}}}{d_p} \right)^{D_f - 3} \qquad (4.1)$$

where d_{floc} and d_p are the diameter of the floc and primary particle, respectively, and D_f is the fractal dimension, a parameter that characterizes floc structure[38]. For cylindrical rods with a length, L, and diameter, D, [39]

$$\varphi_f \approx \frac{1}{r} \left(\frac{d_{\mathrm{floc}}}{V_p^{\frac{1}{3}}} \right)^{D_f - 3} \qquad (4.2)$$

where r, the aspect ratio, is L/D. Thus, for a given number of particles in a given volume, rods with $r \gg 1$ will form more open, lower density flocs than spheres[38-42]. The flocs were shown to be weakly held together by van der Waals (VDW) forces. Actuation of the pMDI produced a sufficient amount of force to shear off a portion of the weak, friable flocs within an HFA droplet. The droplet served as a template for the final aerosolized particle. Upon evaporation of the HFA droplet, capillary forces shrunk the flocs to produce porous particles that yielded the proper aerodynamic diameter to achieve high FPFs between 38-47% and an emitted dose of 700 μg/actuation. Thus, the final size of the aerosol particle delivered into the airways was templated by the evaporating HFA droplet.

Here, we extend our method of pMDI delivery of templated, open flocs of anisotropic particles to a poorly water soluble drug, Itz, to yield aerosol particles possessing optimal aerodynamic sizes for deep lung deposition. The effects of particle size, shape, and aspect ratio on floc formation and structure, as well as aerodynamic properties upon pMDI delivery are examined. The Itz morphologies include thin, rectangular plates (maximum dimension of 600 nm) and long, needle-shaped crystals (maximum dimension of 8 μm). Strong, attractive VDW forces between small contact points in the anisotropic primary particles are shown to "lock in" an open floc structure to inhibit floc collapse. In contrast, particles with an aspect ratio near unity sample a greater number of energetically favorable locations to reduce the interfacial surface area[38, 43, 44], which produces denser flocs. In the current study, the aspect ratios of the Itz particles are as low as 5 compared to 24 for the BSA nanorods in our previous study[35]. A key objective was to increase the emitted dose from pMDIs to more than 2 mg/actuation to advance pulmonary treatment of systemic diseases. Drug loadings were increased by a factor of 5, compared to our previous study[35], to characterize how loading affects floc density, suspension stability, and aerosol properties. The ability of the HFA droplets in the pMDI to shear off portions of the floc to form aerosol particles, and to compact the flocs upon droplet evaporation, is examined. The aerodynamic properties of the aerosolized particles are described and analyzed in terms of floc structures and aerosol particle formation mechanisms.

The final objective was to demonstrate that these aerosolized flocculated, high surface area nanoparticles exhibit improved dissolution rates relative to lower surface area milled aggregates. Thus, the ability to deliver nanoparticles to the lungs as micron-sized aggregates with the proper aerodynamic diameter has the potential to significantly improve drug absorption rates in the lungs. This approach satisfies simultaneously both the requirements of micron-sized particles for deep lung deposition and the delivery of nanoparticles to facilitate efficient drug dissolution rates to enhance absorption. Enhanced dissolution rates are extremely important for raising bioavailability of poorly water soluble drugs [45, 46].

4.2 EXPERIMENTAL

4.2.1 Materials

B.P. grade itraconazole (Itz) was acquired from Hawkins, Inc. (Minneapolis, MN). Bovine serum albumin (BSA) and polyoxyethylene sorbitan monolaurate (Tween 20) were purchased from Sigma (St. Louis, MO). The propellant 1,1,1,2,3,3,3-heptafluoroprane (HFA 227) was obtained from Hoechst (Frankfurt, Germany) and 2H,3H-Perfluoropentane (HPFP) from SynQuest Labs Inc. (Alachua, FL). A Micro BCA protein assay reagent kit was acquired from Pierce (Rockford, IL). Sodium dodecyl sulfate (SDS), HPLC grade acetonitrile (ACN), 1,4 dioxane, and diethanolamine (DEA) was used as received from Fisher Chemicals (Fairlawn, NJ). Stabilized pa grade 1,3 dioxolane was purchased from Acros Organics (Morris Plains, NJ). The deionized water (DI) was obtained by flowing distilled water through a series of 2x7 L mixed bed vessels (Water and Power Technologies, Salt Lake City, UT) containing 60:40 anionic:cationic resin blends.

4.2.2 Powder Preparation

4.2.2.1 Thin Film Freezing (TFF)

Anisotropic Itz and BSA nanoparticles were prepared by a thin film freezing (TFF) process described previously[47]. Briefly, Itz (0.4% w/v) was dissolved in 1,4 dioxane and dripped onto a stainless steel surface that was cooled by dry ice to maintain a surface temperature of 223K at a flow rate of 4 mL/min through a 17 gauge (1.1 mm ID, 1.5 mm OD) stainless steel syringe needle. Upon impact with the steel surface, the droplets spread into thin disks and froze. The frozen disks were collected and lyophilized to yield a dry powder. BSA particles were made using the same method, where the feed solution consisted of BSA (0.5% w/v) in 10 mM potassium phosphate buffer (pH 7.4).

4.2.2.2 Controlled precipitation (CP)

Itz particles were also prepared by a previously established controlled precipitation process[48, 49]. Briefly, 15 g of 1,3 dioxolane containing 33.3% w/w Itz was injected into an antisolvent DI water (50 g), cooled on ice to a temperature of 4^{o}C. Vacuum distillation was used to reduce the 1,3 dioxolane to very low residual levels in the aqueous dispersion. The aqueous dispersion was then frozen drop-wise into liquid nitrogen and lyophilized to yield a powder. An Itz/T20 powder was also produced by CP using the same method, where the antisolvent phase consisted of 0.75% w/w solution of Tween 20 in DI water. After precipitation, the aqueous dispersion was centrifuged at 10,000 rpm for 15 minutes at 4^{o}C to separate unadsorbed polymer from the drug particles. The final Itz composition in the Itz/Tween 20 powder was 95±2% w/w, determined by dissolving 20 mg of Itz/Tween 20 powder in 3 mL of ACN and then using HPLC to quantify the Itz concentration in that solution.

4.2.2.3 Wet Milling

Isotropic Itz particles were prepared by milling. Micronized Itz powder, as received, was suspended at 150 mg/mL in DI water and added to a ceramic container filled with 50 ceramic balls, approximately 1 cm in diameter. The suspension was milled on a mechanical roller for 2 weeks and then lyophilized to yield a dry powder.

4.2.3 Lyophilization

A Virtis Advantage Lyophilizer (The Virtis Company, Inc., Gardiner, NY) was used to dry the drug powders. For particles produced by TFF and CP, drying was conducted at -40ºC for 36 hrs at 300 mTorr, followed by a 12 hour linear ramp to 25ºC at 100 mTorr, and then 24 hours at 25ºC and 100 mTorr. The milled suspension was dried at 30^{o}C for 12 hours at 500 mTorr.

4.2.4 Particle Density

The tapped densities of the drug powders were measured using a Vankel tap density meter (Varian, Palo Alto, CA). Drug powder (100-300 mg) was placed into a 100 mL graduated cylinder and was tapped 200 times. The true particle densities of the powders were determined using a Micromemeritics AccuPyc 1330 helium pycnometer (Norcross, GA). Drug powder was added to a 10 cm^3 sample holder for measurements. Mean values and standard deviations were obtained from three measurements.

4.2.5 Scanning Electron Microscopy (SEM)

Powder samples were affixed to aluminum stages using double adhesive carbon conducting tape and then sputter coated with gold-palladium for 30 s using a K575 sputter coater (Emitech Products, Inc., Houston, TX). SEM micrographs were taken using a Hitachi S-4500 field emission scanning electron microscope (Hitachi Ltd., Tokyo, Japan) at an accelerating voltage of 10–15 kV.

Cross-sectional views of the aerosolized flocs were obtained by sectioning the region of interest using a dual beam system FEI Strata 235 including both a focused-ion beam (FIB) and SEM. Ga+ species that were accelerated at 30 kV were employed to mill the particles. A beam current of ~50 pA was employed to minimize risks of overheating the specimen. The sample was sectioned after finding the eucentric height and aligning the electron-beam (for SEM imaging) and the ion-beam (for material removal with heavy Ga ions).

4.2.6 Brunauer-Emmett-Teller (BET) surface area measurement

A BET apparatus (Quantichrome Instruments, Nova 2000 version 6.11 instrument, Boynton Beach, FL), using nitrogen as the adsorbate gas, was used to measure the specific surface areas of the drug powders. Weighed powder was added to a 9 mm Quantichrome bulb sample cell and degassed for 12 hours. Six points were taken over a range of relative pressures from 0.05 to 0.35. Analysis of the data was performed using the Brunauer-Emmett-Teller equation using Nova Enhanced Data Reduction Software (Version 2.13).

4.2.7 X-ray Diffraction (XRD)

The crystallinity of the dried powders was determined using x-ray diffraction patterns that were obtained using $CuK\alpha_1$ radiation with a wavelength of 1.5404 Ǻ at 40 kV and 20 mA from a Philips PW 1720 X-ray generator (Philips Analytical Inc., Natick, MA). Dried powder was pressed onto a glass slide to from a flat sample surface. A 2Θ step size of 0.05^{o} and a dwell time of 4 seconds were used from 5-40 2Θ degrees.

4.2.8 Preparation of HFA Suspensions

Unless otherwise noted, pMDI suspensions were produced by loading the drug powders (110 mg) into glass pMDI aerosol vials (SGD Pharmacy, Paris, France) that were fitted with 100 μL metering valves (DF10 RC 150, Valois of America, Inc., Congers, NY) using a Pamasol Model P2005 compressor pump (Pamasol Willi Mader AG, Pfaffikon, Switzerland). HFA 227 (11 mL) was loaded into the drug-containing pMDI vials using Pamasol filling equipment (Model P2008). For the 50 mg/mL pMDI suspensions, 550 mg of drug powder was loaded into the pMDI vial along with 11 mL of HFA 227.

4.2.9 Particle Size Analysis by Static Light Scattering (SLS)

The particle size distribution of the Itz particles was measured by static light scattering with a Malvern Mastersizer-S (Malvern Instruments, Ltd., Worcestershire, UK). The dried powder (60 mg) was pre-dispersed in a 2% Tween 20 aqueous solution (6 mL) and sonicated with a probe sonicator (Branson Sonifier 450, Brandon Ultrasonics Corporation, Danbury, CT) for ~ 2 minutes. The dispersion was then added drop-wise into the sample reservoir, containing 500 mL of pure DI water, to obtain an obscuration between 10-15%. Particle size distributions, weighted by volume, were calculated with a refractive index of 1.61 for Itz[50]. Particle size measurements of flocs in HPFP were measured similarly. The drug powder (20 mg) was pre-dispersed in HPFP (2 mL) and added drop-wise into the small volume sample cell, containing 15 mL of HPFP. However, due to the high porosity of the floc, an effective refractive index was determined in to obtain particle size distributions. The effective refractive index was calculated using the Bruggeman mixing rule, as described in the Supplementary Section.

The size distribution of the aerosolized particles, emitted from the pMDI, was also characterized by SLS. The pMDI was actuated directly into the laser beam of the Malvern Mastersizer S and 100 measurements were taken in 5 ms intervals. The recorded measurements were averaged, on a volume basis, to yield the size distribution of the aerosolized particles. An effective refractive index, calculated with the Bruggeman mixing rule, was used to determine the particle size distribution of the aerosol particles due to its high porosity.

4.2.10 Particle Size Analysis by Dynamic Light Scattering (DLS)

DLS was used to measure the particle size distribution of Itz particles when the drug concentration was too low to be measured by SLS. Particle size measurements were performed in triplicate using a custom-built dynamic light scattering (DLS) apparatus[51] at a scattering angle of 90° and temperature of 25 °C. Dispersion concentrations were adjusted to give a measured count rate between 300-400 kcps. Measurements were made over a period of 2 minutes. The data were analyzed with a digital autocorrelator (Brookhaven BI-9000AT) with 522 real time channels and a non-negative least-squares (NNLS) method (Brookhaven 9KDLSW32).

4.2.11 Optical Microscopy

Drug particles were dispersed in HPFP at a ~5 mg/mL drug loading and pipette onto a glass slide for observation using a Nikon OPTIPHOT 2-POL optical microscope with an attached MTI CCD-72X camera (Nikon, Tokyo, Japan).

4.2.12 Aerosol Characterization of Drug Particles after Actuation by pMDI

4.2.12.1 Dose Delivered Through the Valve (DDV) Determination

The pMDI suspensions were actuated once through the firing adaptor of a dosage unit sample tube (26.6 mm ID x 37.7 mm OD x 103.2 mm length; 50 mL volume, Jade Corporation, Huntingdon, PA). Then, 40 mL of an appropriate solvent, ACN or DI water for Itz or BSA, respectively, were added to the tubes, which were allowed to sit for at least 30 minutes to ensure sufficient dissolution of drug. The drug concentration in the rinse media were quantified using high performance liquid chromatography (HPLC) or a Micro BCA protein assay for Itz and BSA, respectively.

4.2.12.2 Andersen Cascade Impactor (ACI)

Aerodynamic characterization of pMDI aerosols was performed using an eight-stage Andersen cascade impactor (ACI) (Thermo-Andersen, Smyrna, GA). The ACI was operated with a 15 cm spacer (Aerochamber Plus®, Trudell Medical International, Ontario, Canada) and an air flow-rate of 28.3 L/min. Three actuations were sent to waste and the next five were made into the ACI. The interval between actuations was between 30-60 s and the pMDI was shaken between each actuation. After the last dose was discharged, the valve stem and actuator were rinsed with solvent. Each plate of the impactor was placed in a receptacle containing a known volume of solvent and soaked for at least 30 minutes to ensure complete drug/protein dissolution. Drug and protein concentrations were determined using HPLC or a Micro BCA protein assay for Itz and BSA, respectively. Quantification of the drug deposition on each stage was used to calculate mass median aerodynamic diameter (MMAD), geometric standard deviation (GSD), and fine particle fraction (FPF).

The geometric diameter of the aerosolized particles was also determined using the ACI. Double-sided carbon adhesive tape was applied to stage 3 of the ACI stage. The ACI was operated under the same conditions from above and a pMDI was actuated once into the impactor. The tape was applied to an aluminum SEM stage, sputter coated, and imaged using SEM. Particle sizes from the SEM micrographs were analyzed using imaging software (Scion, Frederick, MD). At least 50 particles were counted for each sample. The number averaged particle size obtained from image analysis was converted to a volume averaged diameter by[52]:

$$D_{Vol} = \frac{\sum d^4}{\sum d^3} \qquad (4.3)$$

where d is the particle diameter.

4.2.13 Dissolution

The dissolution rates of aerosolized particles, emitted from a pMDI, were measured in 0.02% w/v SDS phosphate buffer (pH = 7.4) at 37°C. The dissolution media (30 mL) were preheated in 100 mL dissolution vessels (Varian Inc., Cary, NC) and set in a VanKel VK6010 Dissolution Tester with a Vanderkamp VK650A heater/circulator (VanKel, Cary, NC). To introduce the drug particles to the dissolution media, the dissolution vessel was fitted with a home-made silicon adaptor, lifted out of the dissolution apparatus, and tilted at a ~45°angle. The silicon adaptor fit tightly around the dissolution vessel on one side and the actuator of the pMDI on the other side. The pMDI was actuated 10 times into the dissolution vessel and the vessel was placed back into the dissolution apparatus. A USP paddle method was used for the dissolution test. Sample aliquots (~1.2 mL) were withdrawn at various time points up to 120 minutes. The samples were filtered immediately using a 0.02 μm syringe filter. The filtrate (0.7 mL) was subsequently diluted with ACN (0.7 mL) to prevent precipitation of the drug. The Itz concentration in the samples was quantified by HPLC as described below.

4.2.14 High Performance Liquid Chromatography (HPLC)

Itz concentrations were quantified using a Shimadzu LC-600 HPLC system (Columbia, MD) equipped with a Hypersil C18 column (5 μm, 150 x 4.6mm) (Thermoelectron Corporation, Waltham, MA) protected by a C-18 guard column (5 mm, 7.5 x 4.6 mm) (Alltech Associates Inc., Deerfield, IL). The mobile phase consisted of ACN, DI water, and DEA (70:30:0.05 v/v/v) and was pumped at a rate of 1 mL/min. Using a detection wavelength of 263 nm, the Itz peak eluted at 5.4 min.

4.2.15 Quantitation of BSA

BSA content was measured using a Micro BCA Protein Assay (Pierce, Rockford, IL) according to manufacturer protocols. The absorbance of BSA solutions was measured at 562 nm using a 96 well plate spectrophotometer (µQuant Model MQX200; Biotek Instruments Inc., Winooski, VT). BSA solutions with concentrations between 2 and 30 µg/mL were prepared to produce a standard curve.

4.3 RESULTS

4.3.1 Powder Characterization

The morphologies of Itz particles prepared by TFF, CP, and milling were characterized by SEM (Fig. 4.2a-d). Itz primary particles produced by TFF (TFF Itz) without any stabilizers were spherical in shape and had an average diameter of 30 nm as determined from SEM micrographs, consistent with the powder surface area measured by BET (Table 4.1). Itz particles produced using CP without any stabilizers (CP Itz) were 1-3 µm in size as determined from SEM, again in agreement with the sizes measured by BET and SLS (Table 4.1, Fig. 4.3). The XRD patterns of both particles lacked the characteristic peaks of crystalline Itz, indicating an amorphous morphology (Fig. 4.4). However, upon addition of each of these amorphous powders to HFA 227, a change in particle morphology was observed by SEM (Fig. 4.2 e-f). The originally spherical particles of both powders transformed into thin, plates. The average dimensions of the crystallized TFF Itz particles were 600 nm x 300 nm x 60 nm, based on sizing of over 50 particles from SEM images. The maximum aspect ratio of 10 was used to characterize these plates. Similar sizes were observed for the crystallized CP Itz particles. Furthermore, the change in particle shape was accompanied by a shift in the x-ray diffractorgram to a crystalline pattern (Fig. 4.4). The time for crystallization to occur was less than 10 minutes, as determined by a control experiment where HFA, cooled to -80^{o}C, was mixed with the amorphous Itz powders and then allowed to immediately evaporate under ambient conditions, which took about 10 minutes for ~2 mL of HFA. After this short exposure, the change in the XRD pattern to a crystalline profile was observed. The same particle shape change (data not shown) and crystallization (Fig. 4.4) were also observed when the amorphous Itz particles were added to the HFA surrogate, HPFP, a non-volatile solvent with similar polarity and polarizability as HFA 227[53, 54]. Crystallization of the amorphous Itz powders may be attributed to the relatively low glass transition temperature (T_g) of Itz, approximately 60^{o}C based on DSC measurements[55]. Thus a small degree of the swelling of the amorphous Itz by the HFA would be sufficient to lower the T_g to room temperature. With the enhanced molecular mobility, the amorphous Itz relaxes to the lower energy crystalline state. Because CP Itz particles were essentially the same size and shape as TFF Itz particles after HFA exposure, the remainder of the paper will focus on the TFF Itz particles.

In contrast to the spherical particles produced by TFF and CP in the absence of any stabilizers, the morphology of Itz particles prepared by CP and stabilized using Tween 20 (T20) favored preferential growth in one direction to produce long, thin, needle-shaped particles. The needles had widths ranging between 1-2 μm and lengths between 6-10 μm, as determined by SEM. Although SLS particle sizing results are most accurate for spherical particles, they may still be applied for these needle-shaped particles by using the equivalent volume of a sphere to characterize the non-spherical particle's geometry[35]. For instance, the effective average particle diameter measured by SLS for the Itz needles was 3.08 μm (Fig. 4.3), which gives an equivalent spherical volume of

15.3 μm^3. Therefore, if the average width of the needles is 1.5 μm, and the shape of a needle is approximated as a long rectangular box with square ends, the corresponding length, L, would be 6.8 μm ($L=15.3/1.5^2$), consistent with the SEM micrographs. Therefore an aspect ratio of 5 ($L/w = 7/1.5$, where w is the width) was assigned to the needles. Itz particles processed by wet milling produced spheres 300 nm in diameter, as observed by SEM and from BET and SLS measurements. As determined from their XRD patterns, both CP Itz/T20 and milled Itz were crystalline (Fig. 4.4). SEM morphology and XRD patterns for CP Itz/T20 and milled Itz did not change after exposure to HFA 227.

4.3.2 Suspension Stability of Anisotropic Itz Particles in HFA

Measured amounts of Itz powders (110 mg) were loaded into the pMDI vials. Prior to the addition of HFA, for the TFF Itz (tapped density=0.012 g/cm^3), the powder filled the entire volume of the vial. In the case of CP Itz and CP Itz/T20 (tapped density=0.63 g/cm^3), about 75% of the vial was filled. However, the milled particles only formed a thin layer at the bottom of the vial (tapped density=1.53 g/cm^3). HFA 227 was then added to the powders to yield a 10 mg/mL suspension, corresponding to a volume fraction of particles in the vial, $\varphi_v = 0.0077$. The TFF Itz, CP Itz, and CP Itz/T20 particles filled the entire volume of the propellant as a homogenous, milky dispersion (Fig. 4.5a-c). No settling was observed in these samples for over two years. As a control, a pMDI composition was prepared using TFF Itz loaded at a φ_v of 0.0015, 20% of the original drug loading described above. Even at this lower φ_v, the particles still filled about 70% of the volume of the propellant (Fig. 4.5d), indicating extremely low density flocs, similar to what was observed previously by Engstrom et al.[35] To test the effect of drug loading on suspension stability, the TFF Itz loading was increased to 50 mg/mL ($\varphi_v = 0.039$). The resultant suspension was also homogenous in appearance, similar to that of the 10 mg/mL loading. No settling was observed over the lifetime of the pMDI (~2 weeks). In contrast to the particles prepared by TFF and CP, the milled particles settled rapidly, within 30 seconds. Within 5 minutes, the milled particles had settled completely (Fig. 4.5e).

To investigate the floc structure formed by the different anisotropic particles and milled Itz particles in HFA 227, analogous formulations prepared in a surrogate solvent HPFP were examined by optical microscopy (Fig. 4.6) at ambient pressure. Flocs formed by TFF Itz and CP Itz/T20 are clearly more open than those formed by the milled particles, with comparable floc sizes of about 150-200 μm. SLS measurements of TFF Itz particles in HPFP were performed to confirm the observed floc sizes. A measured D_{50} value of 318 μm was in agreement with the microscopy images (Fig. 4.7a). The flocs of milled Itz were of similar size to those formed by the anisotropic particles; however they were much more densely packed.

To demonstrate that the flocs of anisotropic particles are only weakly held together and can be easily broken apart by the shear during pMDI actuation, the valve of the pMDI was submerged in 10 mL of an aqueous Tween 20 solution (2% w/v) and actuated. The resultant dispersion (~0.1 mg/mL) was barely turbid and the emitted particles, which were measured immediately by DLS, had an average particle size of 700 nm, significantly smaller than the 150-318 μm floc diameter measured for TFF Itz flocs in HPFP (Fig. 4.7b).

4.3.3 Characterization of Aerosolized Anisotropic Itz Particles from a pMDI

DDV values provide insight into the stability of a pMDI composition. Unstable suspensions prone to settling and particle aggregation may not provide efficient or consistent doses. A pMDI with a drug concentration of 10 mg/mL should theoretically deliver 1 mg of drug/actuation with a 100 μL valve. The DDV values for the pMDI suspensions of TFF Itz and CP Itz/T20 at a 10 mg/mL drug loading were 97 and 82% of the theoretical dose, respectively, in comparison with 92% for the BSA nanorods reported in Engstrom et al.[35] (Table 4.2). Therefore, despite the smaller aspect ratios and larger sizes of the anisotropic Itz particles compared to the BSA nanorods, sufficiently stable pMDI suspensions were produced to facilitate efficient aerosol delivery. The milled Itz suspension pMDI only delivered 21% of the theoretical dose, which was expected based on previous reports in literature[12] given the poor suspension stability. When the drug loading for the TFF Itz and TFF BSA pMDI suspensions was increased by a factor of 5 to 50 mg/mL, the DDV values were between 2.3-2.9 mg/actuation. However, the dosing efficiency decreased to 46 and 68% for TFF Itz and TFF BSA, respectively.

The ability of a pMDI to efficiently deliver anisotropic Itz particles to the deep lungs was assessed using an Andersen Cascade Impactor (ACI) (Table 4.2). For TFF Itz and CP Itz/T20 pMDI suspensions, FPFs were 56% and 49%, respectively, compared to 47% for the BSA nanorods[35]. These high FPFs resulted in fine particle doses (FPD) and total emitted doses (TED) ranging from 377-525 μg/actuation and 754-942 μg/actuation, respectively. In contrast, milled pMDI suspensions produced a 15% FPF to yield a FPD and TED less than 30 and 200 μg/actuation, respectively. Increasing the drug concentration in the pMDI suspensions to 50 mg/mL did not adversely affect the FPF for either TFF Itz or TFF BSA particles. In each case, the FPFs actually increased to 64 and 50%, respectively. The high FPFs, and FPDs and TEDs as high as 1.2 mg and 2.4 mg, respectively, represent a considerable increase over most current commercial products[12].

The distribution of drug deposited on the ACI stages is shown in Fig. 4.8. At both drug concentrations, the highest amount of drug deposition occurred on stages 3 - 5, within the desirable range for deep lung deposition, for the anisotropic Itz particles. However, increased deposition in the spacer and throat was detected for a 50 mg/mL drug loading compared to 10 mg/mL. In contrast, the majority of the milled Itz particles were deposited in the spacer and throat region. MMADs were calculated based on the distribution of drug mass on the different stages in the impactor. Therefore, MMAD and GSD values between 3-4 μm and 1.8-3.3 μm, respectively, were achieved for the pMDI suspensions of anisotropic particles, within the optimal 1-5 μm range for deep lung delivery (Table 4.3). Aerosolized milled Itz particles had an MMAD of 6 μm and GSD of 2.9 μm.

The geometric diameters and morphologies of the anisotropic Itz particles emitted by the pMDI were determined by recovering the particles from stage 3 of the ACI (d_a = 3.5-4.7 μm), which had high deposition levels. The particles were imaged using SEM (Fig. 4.9). Similar to observations by Engstrom et al.[35], the actuation of the pMDI suspension of anisotropic particles produced large, porous aggregates of relatively monodisperse size that clearly are composed of the individual nanoparticles originally loaded into the pMDI vial. All pMDI suspensions of anisotropic particles, which possessed the same drug loading (10 mg/mL), emitted aerosol particles of comparable size, ~10 μm. In contrast, aerosolized milled particles were about a factor of two smaller than the aerosolized anisotropic Itz particles. The average geometric particle sizes observed by SEM (analysis of ~50 particles) were in excellent agreement to those measured using light scattering (Table 4.3). The densities of the aerosolized particles, ρ_g, were calculated using the following equation, which relates d_a (set at 4 μm, corresponding to stage 3 of ACI) to geometric diameter, d_g [4]:

$$d_a = d_g \sqrt{\rho_g} \qquad (4.4)$$

Values for ρ_g ranged between 0.1-0.2 g/cm^3 for the aerosolized anisotropic particles with a 10 mg/mL drug loading and between 0.04-0.09 g/cm^3 for the 50 mg/mL drug loading (Table 4.3).

4.3.4 Dissolution of Aerosolized Anisotropic Itz Particles from a pMDI

To demonstrate the ability of the aerosolized flocs of anisotropic particles to deaggregate into its constituent nanoparticles upon deposition in the lungs, the pMDI containing TFF Itz was actuated above dissolution media and the aerosolized particles were trapped and suspended in the media, which contained 0.02% w/v SDS. From SLS, the initial D_{50} of 9.0 µm was the same as the geometric diameters measured for the aerosolized particles in the previous section (Fig. 4.10). However, the size decreased to a D_{50} of 2.7 µm upon sonication over 2 minutes, indicating that the aerosolized flocs deaggregated and/or dissolved. The dissolution study shows that the aerosolized flocs of anisotropic TFF Itz nanoparticles dissolve more rapidly than a pMDI composition of milled nanoparticles of equal drug loading, achieving 55% dissolution after 2 hours, compared to only 25% for the aerosolized milled particles (Fig. 4.11a). The improved dissolution rate of the aerosolized TFF Itz flocs can be further explained by the SEM images of the two aerosol particles after actuation into dissolution media. The SEM images clearly show that the aerosolized TFF Itz flocs deaggregated into smaller entities relative to the original aerosol particle, while the milled Itz flocs appear to be the same size after 5 minutes of stirring in the dissolution media (Fig. 4.11b-c).

4.4 DISCUSSION

4.4.1 Role of van der Waals forces in suspension stability

Attractive VDW forces are used deliberately in this study to form the open space-filling flocs that produce stable suspensions in HFAs, as described in detail in this section and in a recent study[35]. This approach is the opposite of the traditional method in which the goal is to stabilize individual pre-formed particles against flocculation. VDW attractive forces are dominant for pure drug particles without a surfactant in HFA, compared to electrostatic and steric forces. Electrostatic stabilization is not well understood in HFAs because of ion paring resulting from the low dielectric constants. Atomic force microscopy (AFM) studies in HPFP have shown that electrostatic forces are negligible compared to VDW forces in HFA systems[54, 56]. As a consequence of the low polarizabilities of HFAs, traditional surfactants for chlorofluorocarbons are not solvated sufficiently well to provide steric stabilization[10, 12]. Novel surfactants with enhanced solvation in HFAs are being designed using simulation and AFM studies to address this problem[24, 57, 58].

To circumvent the lack of electrostatic and steric stabilization available in HFAs, spherical porous particles (LPPs, LPNPs) and hollow, porous particles (pulmospheres), have been designed to minimize VDW attractive forces. These porous particles are typically larger than 5 μm in diameter. The solvent penetrates the pores within the particles to lower the VDW attraction between particles, and thus the rate of particle aggregation. The porosity of the particle also improves its buoyancy, which minimizes settling. Both of these factors facilitate efficient aerosolization of these pre-formed particles, which is necessary to achieve desired aerodynamic properties for deep lung deposition. These suspensions may remain stable in HFAs for several hours, whereas solid particles of the same size rapidly flocculate and settle within minutes[17, 18]. The lower attractive forces are due to a lower effective Hamaker constant, A_{121}, for porous particles compared to solid particles[35]. For highly porous particles, the penetration of propellant within the particle lowers the particle's effective Hamaker constant, according to Bruggeman's mixing rule. As the effective Hamaker constant becomes more similar to that for the propellant, A_{121} decreases, thus reducing VDW forces (See Supplementary). The comparison of Φ_{VDW} for the different particle types was performed by calculating the separation distance, h, that corresponded to a Φ_{VDW} equal to the thermal energy $3/2\ k_BT$ at 298 K. A larger h required to overcome thermal energy indicates a stronger attraction between particles. Calculated separation distances clearly demonstrate that increasing the particle porosity will significantly reduce VDW attractive forces (Table 4.4), as described previously[12, 17, 28].

Relative to hollow and porous particles, the VDW forces are stronger for the primary particles prepared by TFF and CP due to their low porosities (Table 4.4). According to Eq. 4.2, the thin plates of TFF Itz and CP Itz and long needles of CP Itz/T20, with large aspect ratios >1, form open flocs that do not pack efficiently. The strong VDW attractive forces promote rapid flocculation. However, the contact area between primary particles is relatively small because of the high aspect ratios and poor packing. The VDW forces at the contact sites prevent the flocs from compacting to denser flocs to reduce the surface areas[59]. For spheres that pack efficiently, dense flocs form and settle rapidly within minutes. The formation of open space-filling flocs of the anisotropic particles is the basis for particle stability in the HFA, as seen in Fig. 4.5, relative to unstable spherical particles.

4.4.2 Effect of particle size, shape, and drug loading on suspension stability in HFA 227

The effect of particle size and shape on floc structure may be quantified by comparing the following characteristics: (1) volume fraction of particles within a floc (φ_f), (2) volume fraction of flocs in the HFA propellant (φ^{floc}), and (3) D_f. Values for φ_f were calculated based on observed floc settling rates, U_{floc}. A modified Stoke's settling rate expression [60, 61] was used to determine the density of the floc, ρ_f:

$$U_{floc} = \frac{d_{floc}^{\,2}(\rho_{floc} - \rho_L)g}{18\mu} \qquad (4.5)$$

where ρ_L and μ are the liquid density and viscosity, respectively, g is the gravitational constant, and d_{floc} was estimated from the optical microscope images in Fig. 4.6. The material balance $\rho_{floc} = \rho_L + \varphi_f(\rho_p - \rho_L)$, where ρ_p is the true density of the primary particle, was then used to determine φ_f [60, 61]. As seen in Table 4.5, the settling rate for CP Itz/T20 flocs was faster than that for TFF Itz flocs, likely due to their larger ρ_p. Milled particles settled the most rapidly, two orders of magnitude faster than the anisotropic particles, given the formation of dense aggregates with a high φ_f as seen in Fig. 4.6. Because the measured settling rate was over four orders of magnitude higher than that for a 300 nm particle from Eq. 4.5, the particles definitely aggregated. Therefore, both the TFF Itz plates and the CP Itz/T20 needles possessed a φ_f at least two orders of magnitude lower than milled particles. The low φ_f is in good agreement with the floc structures observed in Fig. 4.6, in contrast with the dense flocs from the milled particles. Furthermore, a slower settling rate yielded a lower φ_f for the plates than for the needles. The lower φ_f was consistent with the smaller size and higher aspect ratio for the plates, as seen in Eq 2. as well as Fig. 4.6.

The corresponding φ^{floc} values are obtained by φ_v/φ_f [35], where φ_v is the particle volume fraction in HFA (based on drug loading). The φ^{floc} describes the space-filling capabilities of the flocs within the HFA volume. Values of φ^{floc} for TFF Itz and CP Itz/T20 particles were one order of magnitude greater than for the milled particles, again indicating that the flocs composed of anisotropic particles fill more space. For a concentration of 2 mg/mL, the dispersion still occupied about 70% of the propellant volume (Fig. 4.5). This experimental observation is in excellent agreement with the φ^{floc} of 0.65, which was calculated based on the floc settling rate. The trends observed in φ_f and φ^{floc} were consistent with the calculated D_f values, obtained using Eq. 4.2. A D_f less than 2 corresponds to an extremely open, low density floc. Higher D_f values correspond to increasingly tight more dense floc, and a close-packed packed floc is assigned a D_f value of 3 [38]. For Eq. 4.2, the volume of a cylinder was used to obtain an effective spherical diameter to determine D_f [39]. The same approach was used for the plate-shaped particles. Flocs of TFF ITZ and CP Itz/T20 particles yielded D_f values of 2.3 and 2.2, respectively, whereas flocs of milled particles yielded a D_f value of 3.0.

Anisotropic particles, with aspect ratios as low as 5-10, were found to produce stable suspensions in HFA 227, as was the case for the BSA nanorods[35]. Despite the lower aspect ratio, the floc structure for the TFF Itz plates and CP Itz/T20 needles was similar to those of the TFF BSA nanorods with an aspect ratio of 24 [35]. All of the anisotropic particles formed flocs with very low φ_f values and D_f values between 2.3-2.5. Despite the factor of two lower aspect ratio of CP Itz/T20 needles compared to TFF Itz plates, the larger size of the needles gave a slightly lower D_f and packing density, as described by Eq. 4.2. No visible settling was observed in the suspensions of the three different types of anisotropic particles in HFA 227 over 2 years (10 mg/mL drug loading), indicating that the VDW attractive forces are sufficient to prevent collapse of the flocs. Furthermore, increased drug loadings up to 50 mg/mL did not adversely affect suspension stability, since φ_f was still an order of magnitude lower than for the milled particles at a 10 mg/mL loading. These results indicate that the space-filling, open flocs stack upon each other to prevent settling, even at a high drug loading.

4.4.3 Effect of particle size, shape, and drug loading on aerosol properties

Although the open, space-filling flocs of anisotropic particles form stable suspensions in HFA, the diameter of ~150 μm would be too large for efficient deep lung deposition. Recently, a mechanism was presented by Engstrom et al.[35] to explain how these large flocs are sheared apart to produce respirable particles that may be delivered to the deep lung. The shear forces generated during actuation template the flocs within ~25 μm HFA droplets. These forces easily overcome the attractive VDW interactions between the primary particles within the flocculated particles, as illustrated in Fig. 4.1 [35], given the small contact area between the primary particles. As the HFA droplets evaporate, capillary forces compact the flocs to produce porous aerosol particles. This compaction is illustrated in Appendix C Fig. C.1, where the volume of 100 mg of TFF Itz powder, with a tapped density of 0.012 g/cm^3 was compacted significantly upon HFA evaporation to yield a powder with a tapped density of 0.16 g/cm^3. The powder density after HFA evaporation was identical to the calculated density for the aerosolized TFF Itz particle, ρ_g, which was calculated using Eq. 4.4 based on experimentally measured d_a and d_g values. Thus, the final size of the aerosol particle was determined by the floc structure, the templating of the flocs within the HFA droplets, and compaction of the flocs during HFA evaporation.

For TFF Itz particles, actuation from the pMDI with the valve submerged in a 2% w/v Tween 20 solution yielded particles with sizes near those of the primary TFF Itz plates. They were considerably smaller than the flocs measured in HPFP, which did not deaggregate into primary colloidal particles. The shear generated upon actuation and HFA droplet formation contributes to the break up of the large flocs into smaller flocs. In addition, the Hamaker constant for water, $3.7*10^{-20}$ J [62, 63], is larger than for HFA 227 and closer to the Hamaker constant for Itz. Thus, the resulting VDW forces between primary particles in the aqueous solution are weaker and the flocs deaggregate into primary particles, as observed in previous studies[35]. Because of the small area of the contact points between the anisotropic particles, deaggregation took place more readily after actuation into water than would be the case for spherical particles with a larger area of these contact points.

The ability to break down the large ~150 μm friable flocs into respirable particles was evident in the favorable aerodynamic properties listed in Tables 4.2 and 4.3. pMDI suspensions of the TFF Itz plates and the CP Itz/T20 needles both produced higher DDVs and FPFs versus the milled Itz composition(Table 4.2). The DDV and FPF values of the CP Itz/T20 pMDI were slightly lower than those for the TFF Itz pMDI. The CP needles, with average needle lengths of 7 μm, may not fill the pMDI metering chamber as efficiently as the smaller TFF plates. The geometric sizes of the aerosol particles of both the TFF Itz and CP Itz/T20 were about 10-11 μm with a ρ_g of 0.10-0.16 g/cm^3, comparable to values for the aerosolized TFF BSA rods in Engstrom et al[35]. Therefore, for a given drug loading , the aerosol properties of the pMDI compositions produced by the templating/compaction mechanism were similar for different types of drugs and anisotropic shapes, as long as the level of anisotropy was sufficient for low φ_f values and high suspension stability.

Upon increasing the drug loading by a factor of 5 for 50 mg/mL, the dose efficiency (%DDV) decreased significantly, by at least 30% for the TFF Itz and TFF BSA, even though there was no observable change in suspension stability. However, the FPFs for the two concentrated pMDIs remained high. Perhaps the inflow of the flocs into the metering chamber is less efficient with a higher overall volume fraction of primary particles, than for the lower 10 mg/mL loading. Therefore, the drug concentration in the metering chamber may not be equal to the drug concentration in the rest of the vial. This behavior, along with potential of sticking to or clogging of the valve due to the high particle concentrations, may explain the reduced dosing efficiencies. However, the particles that are able to fill the metering chamber are still subjected to the same templating mechanism as described above, keeping FPFs high. As a consequence of the higher drug loading, the geometric sizes of the aerosolized particles increased by about 50%.

Aerosol particles produced by the templated open floc method yields extremely high emitted and respirable doses, up to 2.4 and 1.2 mg/actuation, respectively, compared to a maximum respirable dose of 300 μg for the hollow, porous particles[12]. For porous and hollow particles, drug mass/particle can be limited by high porosity as well as the need for high excipient levels. Furthermore, the total particle loading in the pMDI can be limited by the lack of efficient steric stabilizers. If the loading is to high, the particles may not form uniform suspensions. For our flocs, the drug mass/aerosolized particle is very high because the individual anisotropic particles contain no excipients and are uniformly distributed throughout the entire aerosolized particle. The homogenous distribution of drug throughout the entire aerosolized particle is shown in Appendix C Fig. C.3, where a slice of an aerosolized particle was shaved off using a focused ion beam (FIB) and imaged using SEM to view the interior particle morphology.

4.4.4 Dissolution of aerosolized particles in the lungs

In addition to improving suspension stability, the delivery of flocs of sub-micron particles enhances particle dissolution rates in the lungs compared to the more traditionally delivered solid, 5 µm particles (or a 5 µm dense aggregate of particles)[64, 65]. Particles that require long dissolution times are subject to more rapid clearance by macrophages in the lungs, especially for particles 1-5 um in size, or cause irritation to the lungs. Therefore, rapid dissolution rates are beneficial for efficient drug absorption, especially for poorly water soluble drugs. Enhanced dissolution rates may be achieved by particle size reduction, which increases the surface area, and decreases the boundary layer thickness, *h*, as predicted by the Noyes-Whitney equation:

$$\frac{\partial \mathrm{M}}{\partial \mathrm{t}} = \frac{\mathrm{DA}}{\mathrm{h}}(\Delta \mathrm{C}) \qquad (4.6)$$

where M is the mass of undissolved drug, D is the diffusion coefficient, and ΔC is the difference in equilibrium concentration of the drug adjacent to the particle surface and in the bulk.

To address the bioavailability of poorly water soluble drugs, LPNP aggregates have previously been shown to dissociate rapidly into constituent nanoparticles that dissolve rapidly when added to a liquid medium[30]. However, these LPNP particles had a maximum drug loading of 10% w/w with the remainder composed of polymer and/or phospholipid. In contrast, the flocs in the current study were pure drug.

For our highly porous aerosolized flocs produced by TFF, solvent permeates throughout the entire floc to enhance dissociation into the primary anisotropic particles, thereby increasing the available surface area for dissolution. The high BET surface area of the TFF powder will lead to high surface area flocs for high dissolution rates. Therefore, dissolution rates correspond more closely to that of the primary nanoparticles, as opposed to the larger open flocs. The ability of the TFF Itz aerosolized flocs to dissociate into entities with sizes on the order of the individual anisotropic nanoparticles was demonstrated in Fig. 4.11b, where particles roughly resembling the constituent 600 x 300 x 60 nm plates were observed by SEM after 5 minutes in dissolution media.

4.5 CONCLUSIONS

The novel concept of templating suspensions of open flocs of anisotropic particles in HFAs without surfactants, to produce particles for efficient deep lung delivery via pMDIs[35], has been extended to poorly water soluble drugs and higher drug loadings. Plate- and needle-shaped drug particles, with aspect ratios between 5-10, pack inefficiently and formed low density flocs that stacked upon each other to prevent settling for over two years at a 10 mg/mL drug loading. For highly concentrated and stable pMDI suspensions, with a drug loading of 50 mg/mL, total emitted doses (TED) reached 2.4 mg/actuation, a significant improvement over typical pMDIs with doses of 600-1000 μg/actuation[1, 12]. Aerosolization of the templated flocs produced high FPFs between 49-64%. The aerosolized particles were templated during HFA droplet formation and compacted during evaporation to yield optimal aerodynamic diameters for deep lung delivery, in contrast with the conventional approach of delivering pre-formed particles. Furthermore, the delivery of high surface area micron-sized porous flocs of nanoparticles to the lungs, as opposed to a solid, micron-sized particle was shown to enhance drug dissolution rates. Therefore, the delivery of micron-sized flocs of nanoparticles with a pMDI offers both efficient deep lung deposition as well as rapid dissolution, which is beneficial for the absorption of poorly water soluble drugs.

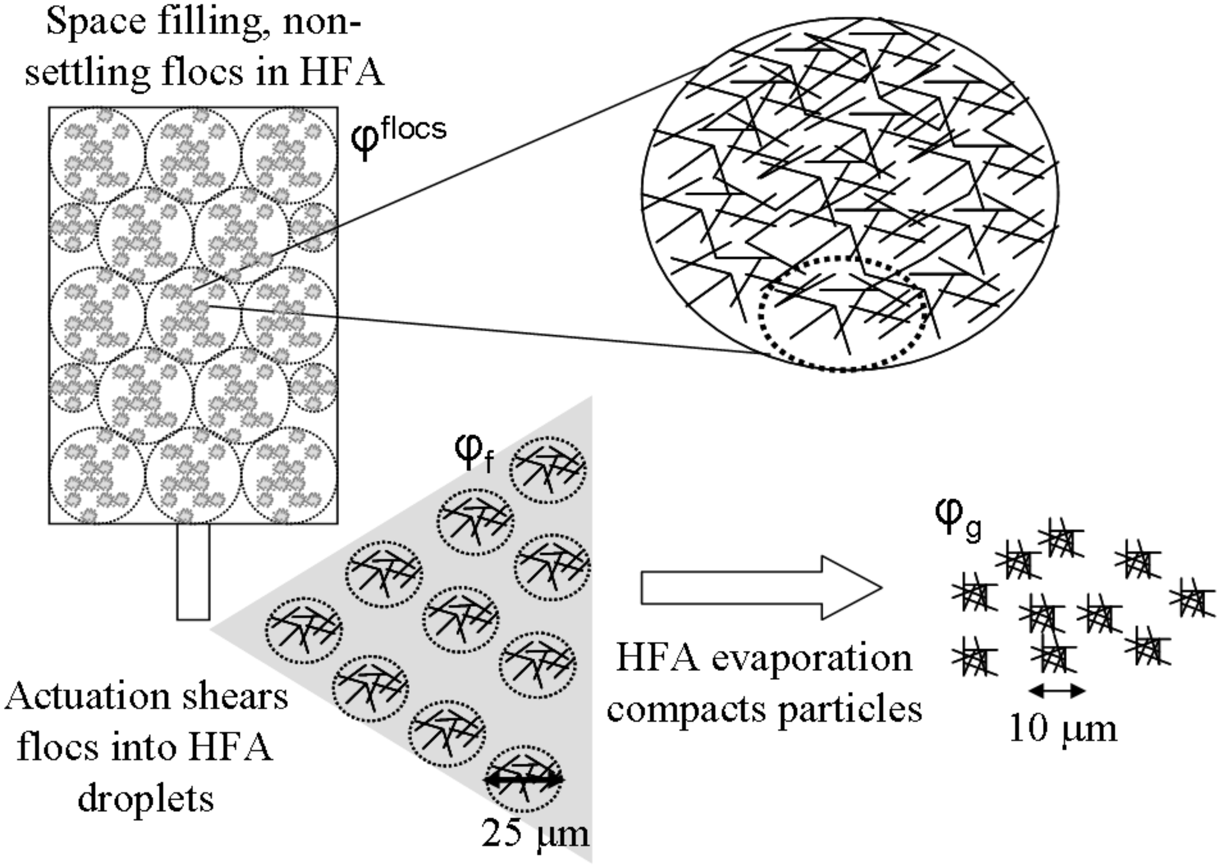

Figure 4.1 Schematic describing the mechanism by which anisotropic particles form stable suspensions in HFA for efficient pulmonary delivery via a pMDI. The anisotropic particles form loose, open flocs that stack upon each other and do not settle, to give an overall volume fraction of flocs in suspension of φflocs. Upon pMDI actuation, a portion of the floc is sheared within an HFA droplet to yield a volume fraction of particles within the floc of φf. HFA evaporation compacts the floc to produce the aerosol particle, in which the volume fraction of particles within the aerosol particle is φg

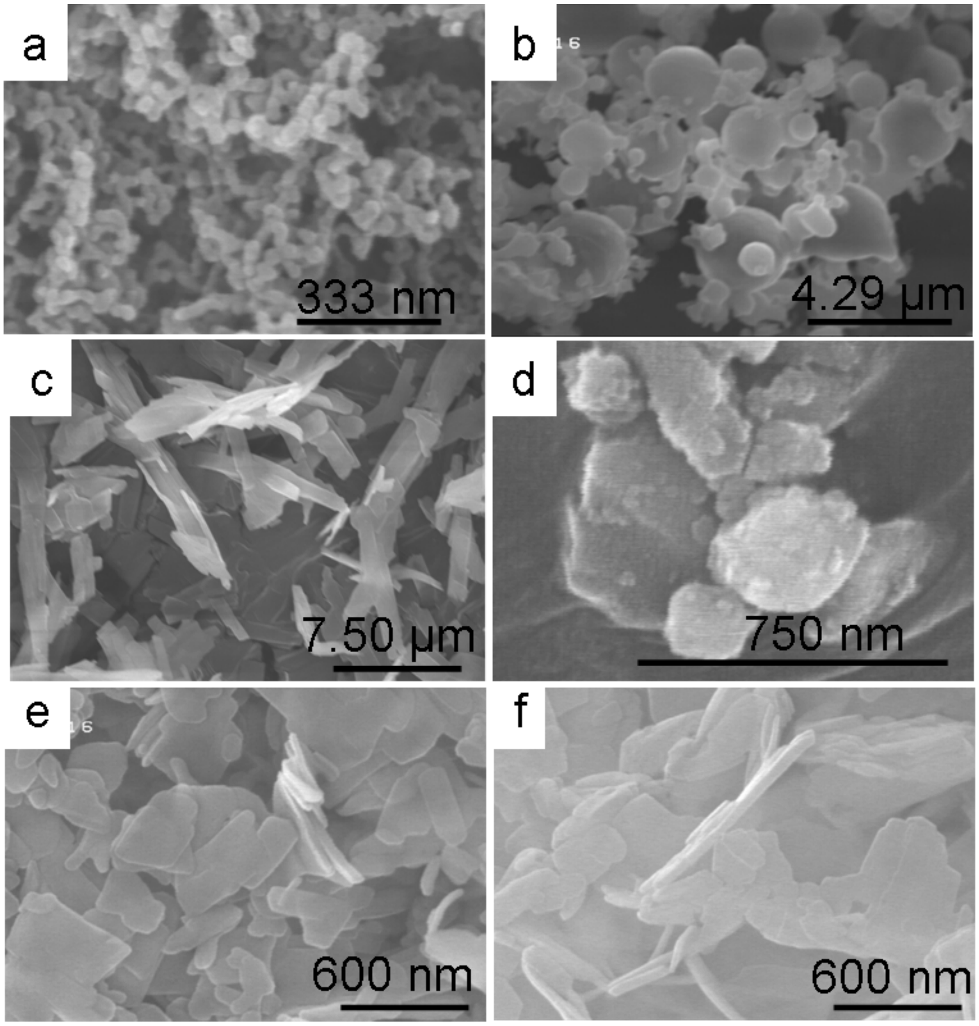

Figure 4.2 SEM micrographs of Itz particles made by (a) TFF (TFF Itz), (b) CP without stabilizers (CP Itz), (c) CP using Tween 20 as a stabilizer, 96% w/w Itz (CP Itz/T20), (d) and wet milling. Micrographs of TFF Itz and CP Itz after HFA exposure are shown in (e) and (f), respectively.

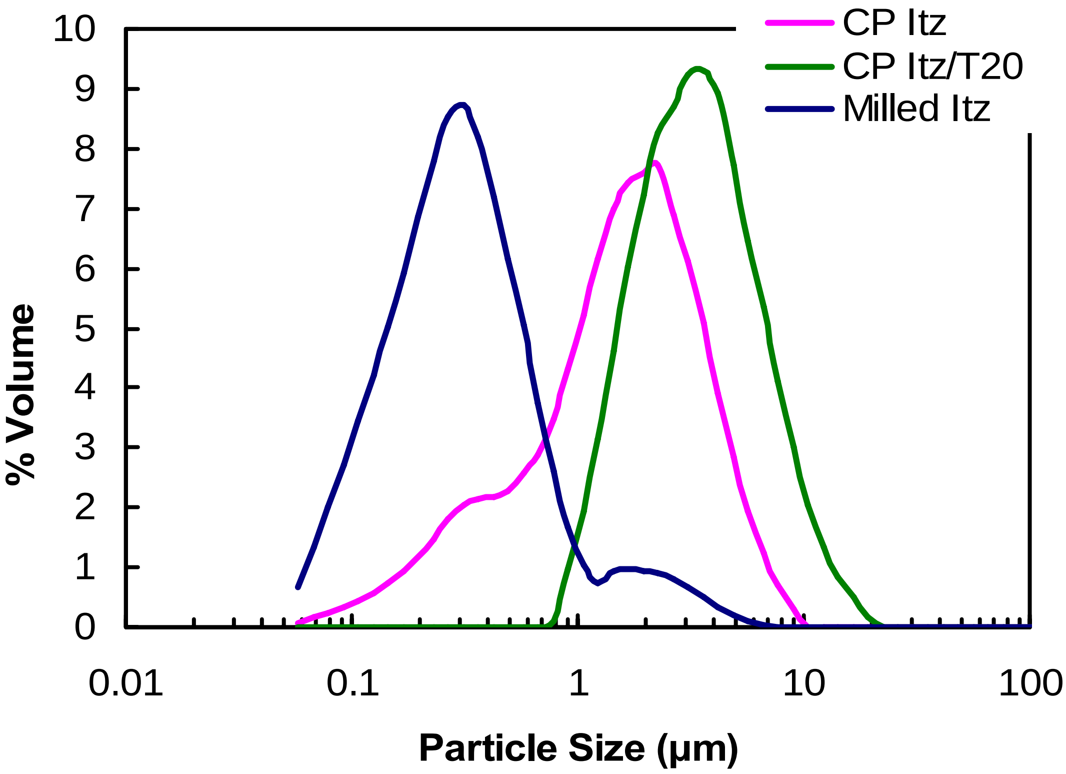

Figure 4.3 Particle size measurements of CP Itz, CP Itz/T20, and milled Itz particles using SLS.

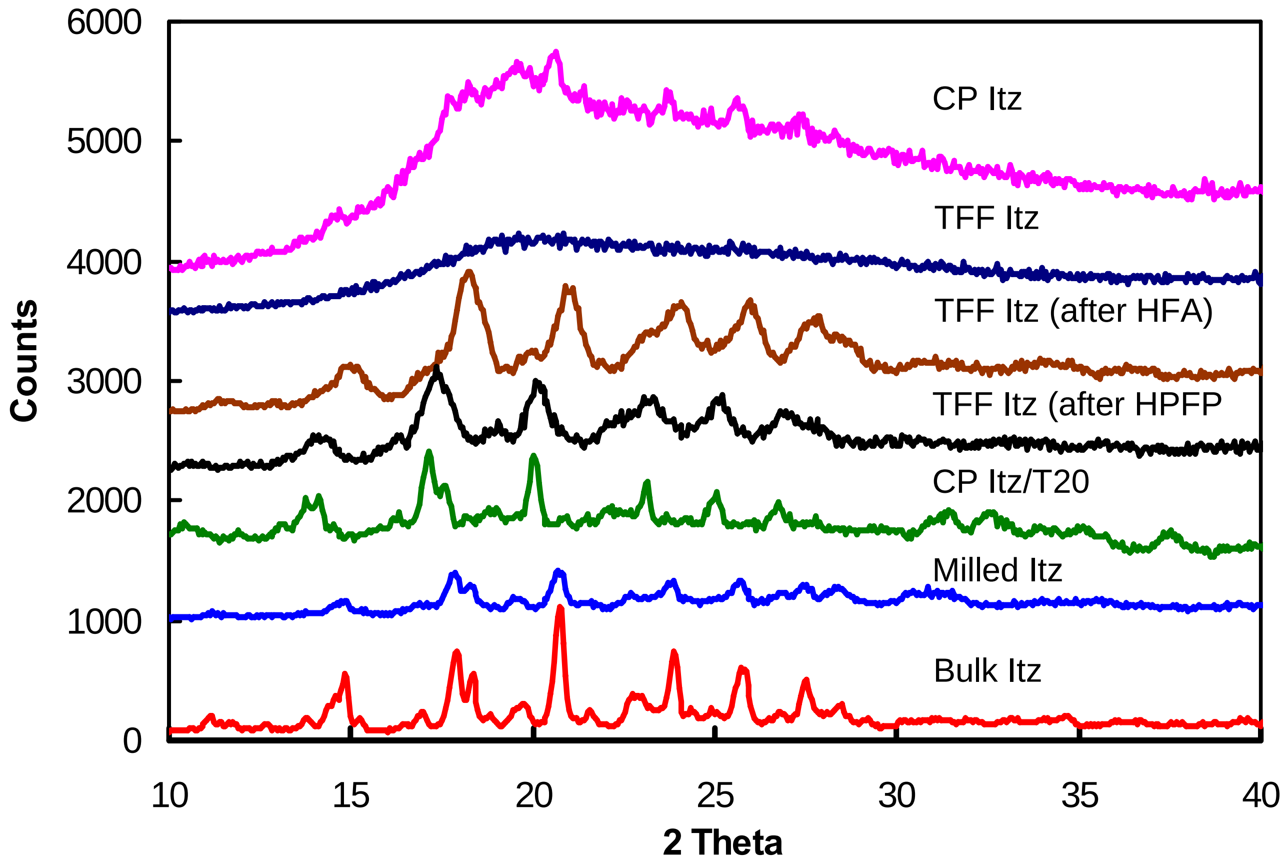

Figure 4.4 X-ray diffraction patterns for Itz particles prepared by TFF, CP, and milling before HFA 227 exposure. The diffractogram of TFF Itz particles after exposure to HFA 227 is also shown.

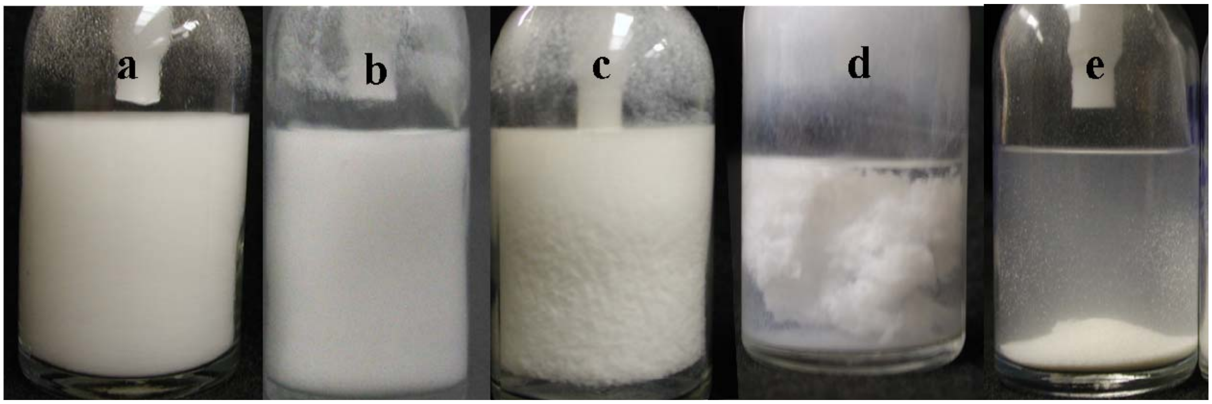

Figure 4.5 Photographs of pMDI suspensions 5 minute after shaking: (a) TFF ITZ, (b) CP ITZ, (c) CP ITZ/T20, (d) TFF ITZ-dilute, and (e) milled Itz. All Itz loadings were 10 mg/mL (1% w/w) except for the dilute suspension in (d), which was 2 mg/mL (0.2 % w/v).

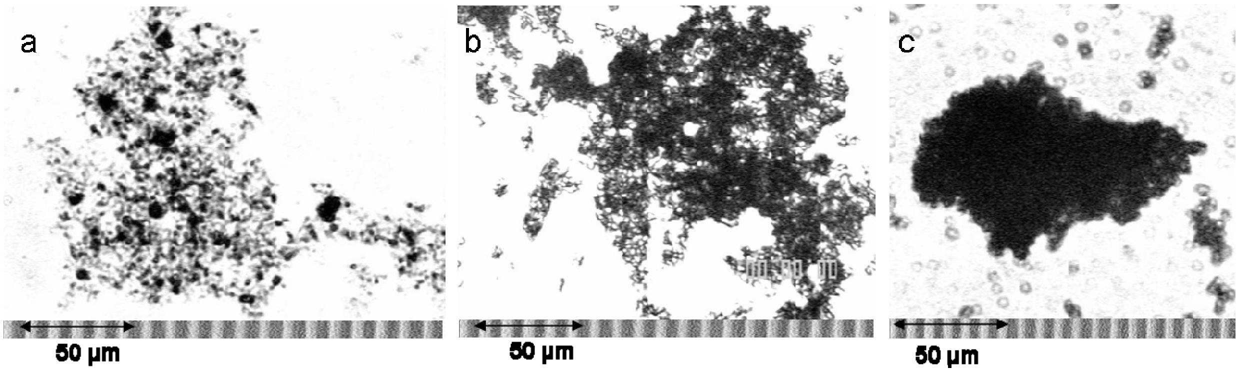

Figure 4.6 Optical microscopy images of Itz particles suspended in HPFP. Images of (a) TFF Itz, (b) CP Itz/T20, and (c) milled Itz particles were taken at 10x magnification.

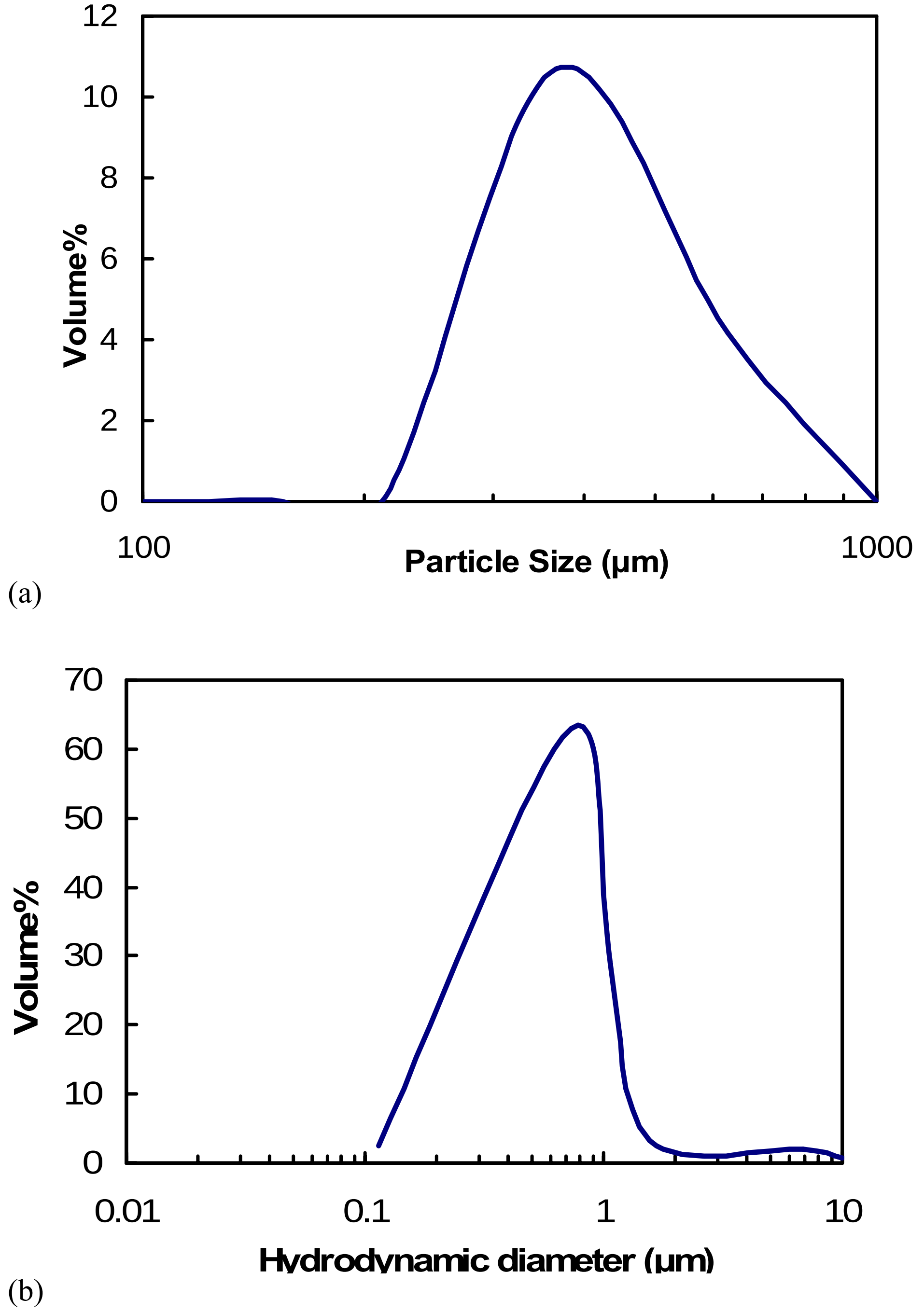

Figure 4.7 Particle size measurements of (a) TFF Itz in HPFP (D_{50} = 318 um) measured by SLS and of (b) TFF Itz particles after actuation by a pMDI, with the valve submerged in water (D_{50}=584 nm), as determined by DLS.

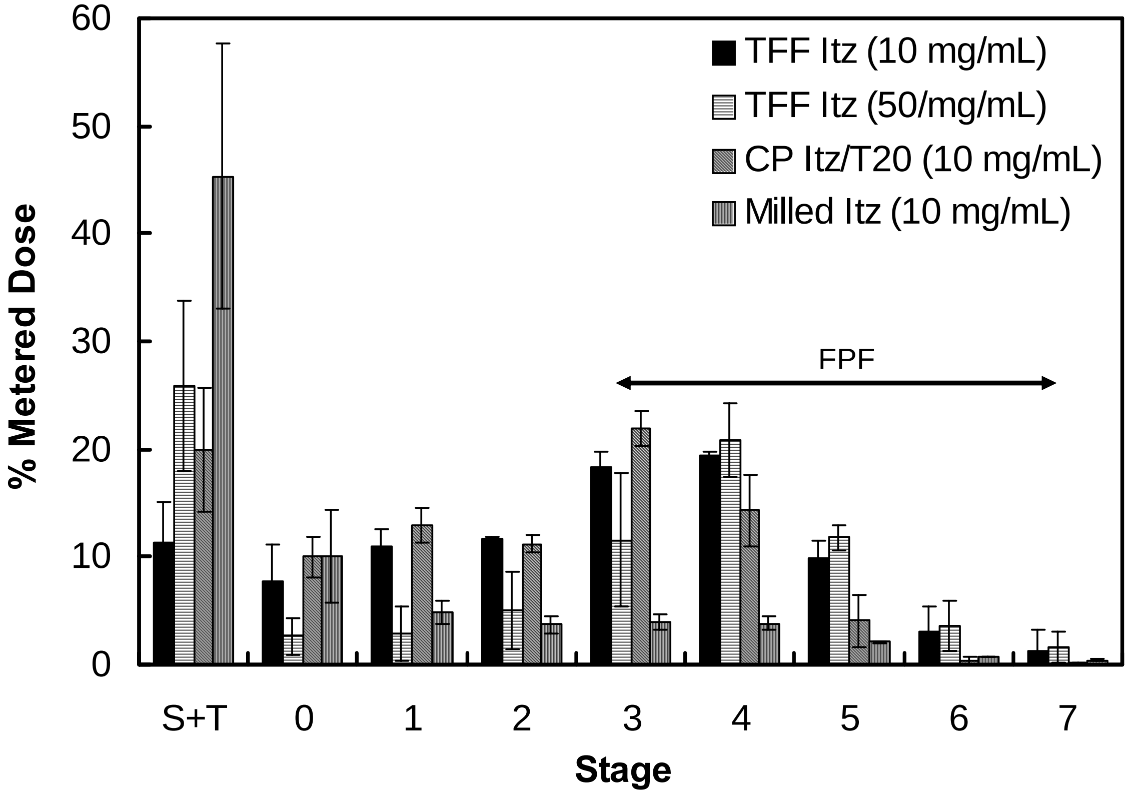

Figure 4.8 Anderson Cascade Impactor deposition profiles for pMDI suspensions of TFF Itz, CP Itz/T20, and milled Itz, accounting for drug deposited in the spacer and throat (S+T), and stages 0-F. A 10 mg/mL and 50 mg/mL drug loading was examined for pMDI suspensions of TFF Itz particles. The fine particle range was determined by the mass of drug deposited on stages 3-F.

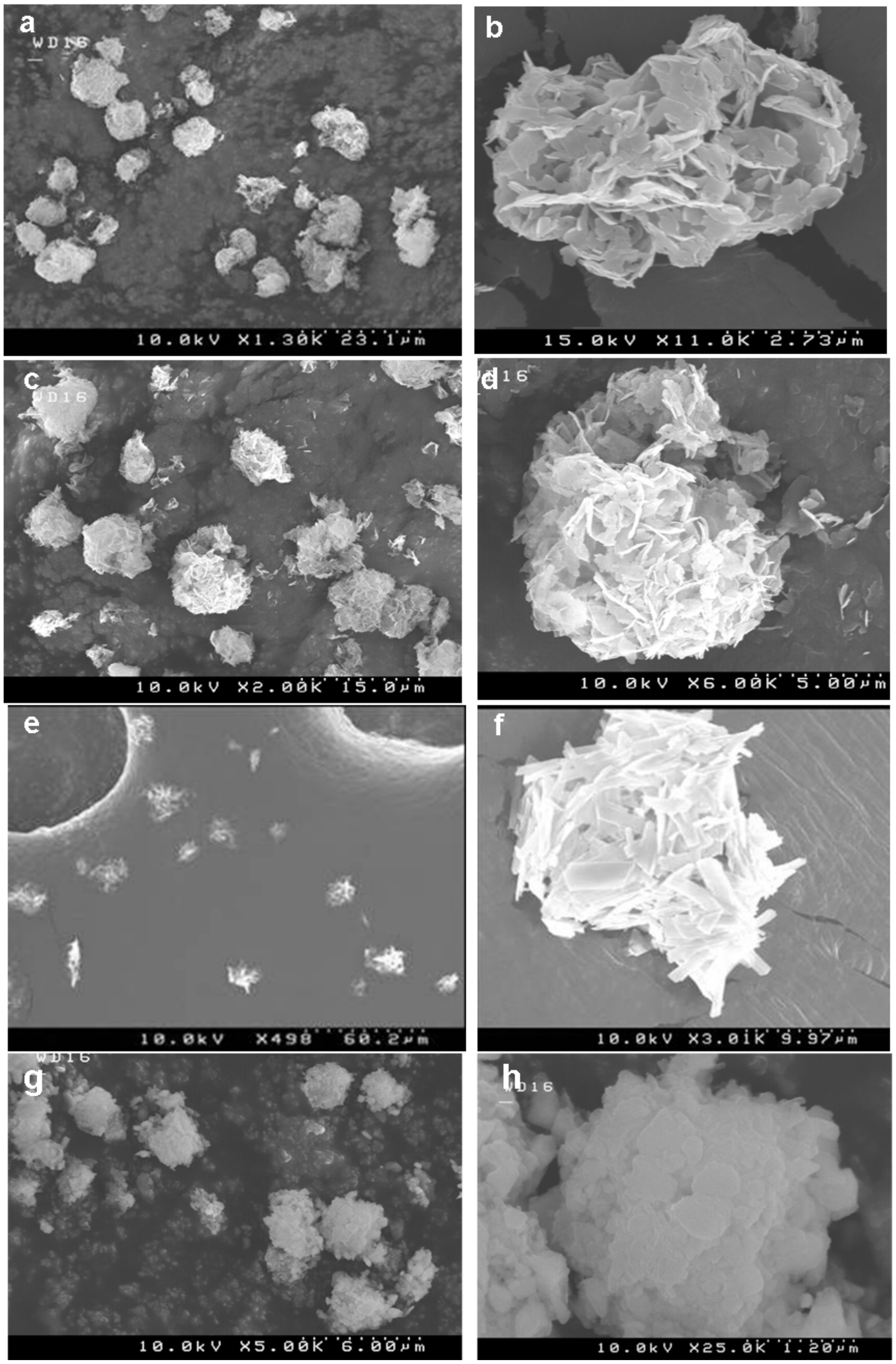

Figure 4.9 SEM images of aerosolized Itz particles collected from stage 3 of an ACI after actuation of a pMDI (10 mg/mL drug loading) through the ACI: (a-b) TFF Itz, (c-d) CP Itz, (e-f) CP Itz/T20, and (g-h) milled Itz.

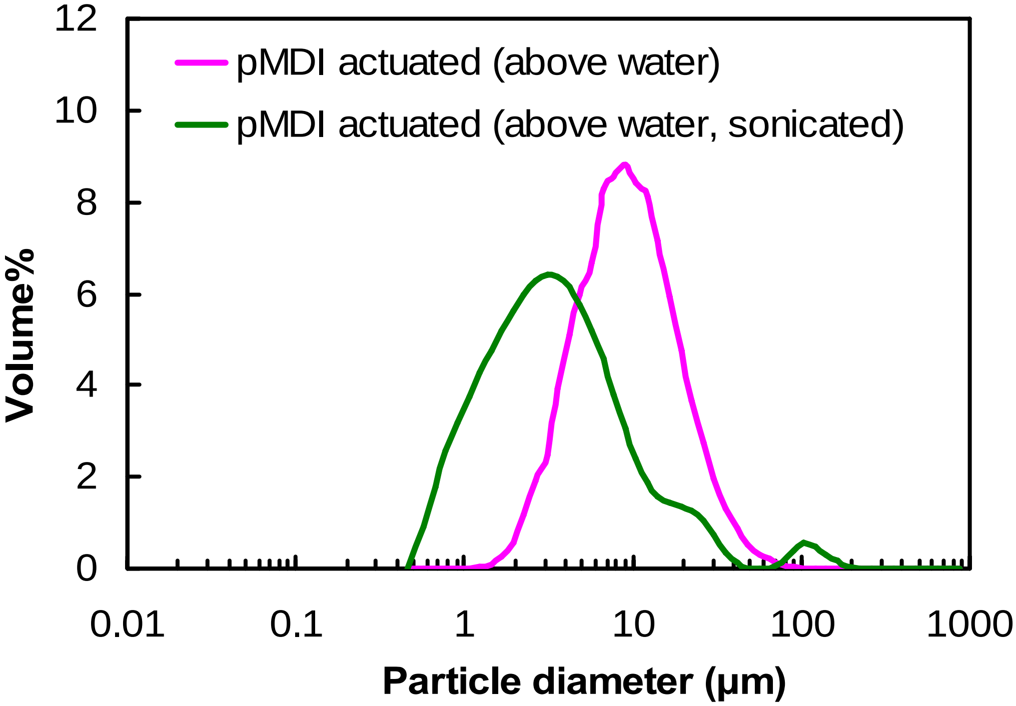

Figure 4.10 Particle size measurements of TFF Itz pMDI actuated above water with (D_{50} = 2.7 µm) and without sonication (D_{50} = 9.0 µm), measured by SLS.

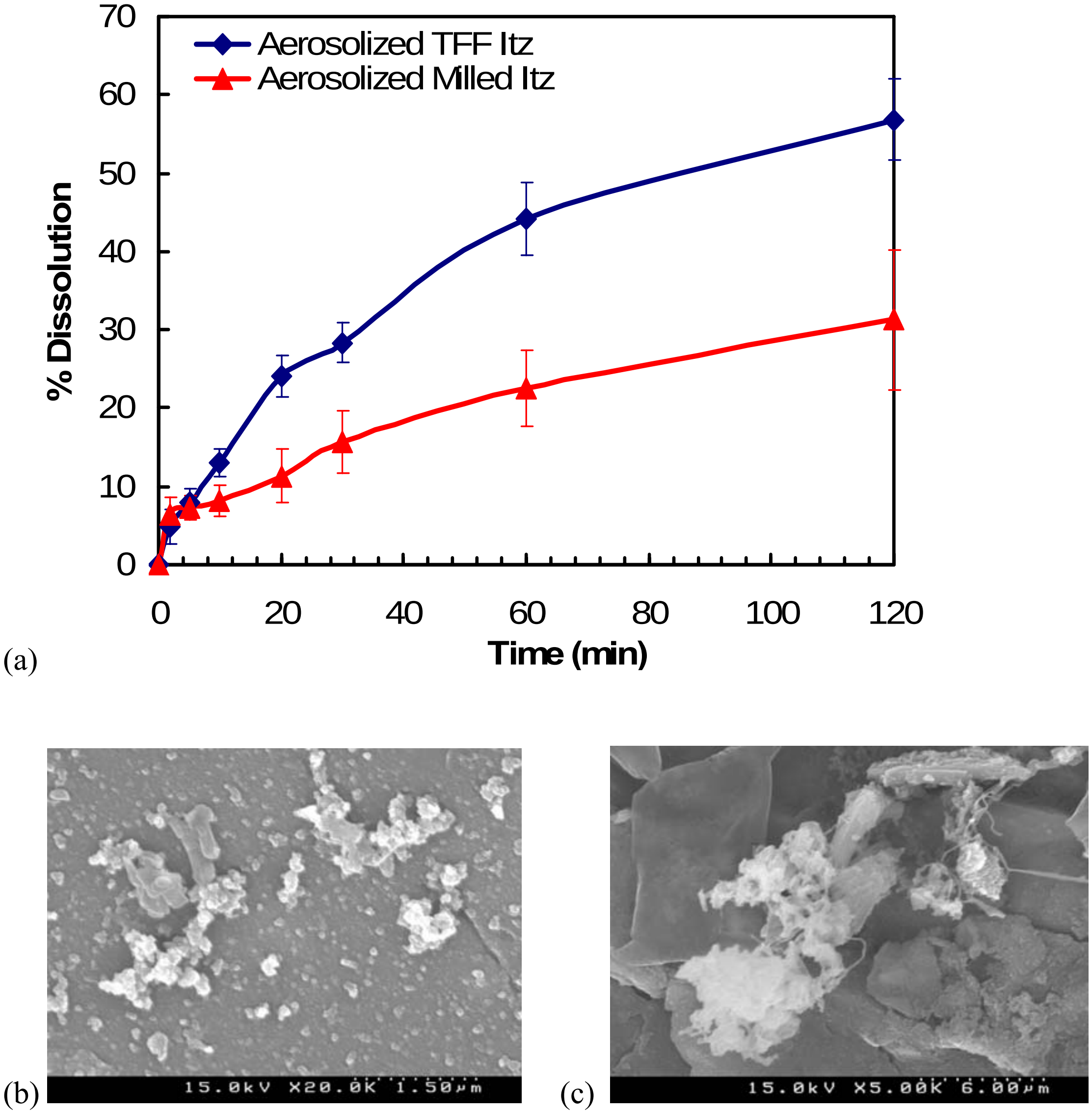

Figure 4.11 (a) Dissolution profile of Itz particles in pH 7.4 phosphate buffer with 0.02% w/v SDS after aerosolization from a pMDI for TFF Itz milled Itz. SEM images of Itz particles collected from dissolution media after 5 minutes of stirring for the suspension pMDI of (b) TFF Itz, and (c) milled Itz.

Table 4.1 BET surface area measurements and the effective spherical diameter, D_{eff}, corresponding to that specific surface area for Itz particles prepared by TFF, CP, and milling prior to addition of HFA 227.

Dry Powder Sample	**BET Surface Area (m^2/g)**	**D_{eff} (µm)**
TFF Itz	136 ± 5	0.034
CP Itz	9 ± 0.6	0.690
Milled Itz	24 ± 0.5	0.192

Table 4.2 Dosages and aerodynamic properties for pMDI suspensions of Itz and BSA particles for two drug loadings, 10 mg/mL and 50 mg/mL.

Sample	**DDV (µg)**	**% Theoretical DDV**	**FPF (%)**	**Fine Particle Dose/Actuation (µg)**	**TED/ Actuation (µg)**
TFF Itz (10 mg/mL)	965 ± 35	97	56 ± 3	525 ± 23	942 ± 13
CP Itz/T20 (10 mg/mL)	836 ± 44	82	49 ± 2	377 ± 7	754 ± 16
Milled Itz (10 mg/mL)	212 ± 152	21	15 ± 3	29 ± 8	194 ± 18
TFF Itz (50 mg/mL)	2315 ± 422	46	64 ± 6	1037 ± 26	1619 ± 193
TFF BSA (10 mg/mL)*	915 ± 21	92	47 ± 4	318 ± 31	695 ± 133
TFF BSA (50 mg/mL)	2910 ± 370	68	50 ± 3	1202 ± 38	2446± 155

* taken from Engstrom et al.[35]

Table 4.3 Aerodynamic (MMAD) and geometric (from SEM and SLS) particle sizes and densities of the aerosolized Itz and BSA particles from a pMDI. pMDI suspensions were prepared at a 10 mg/mL and 50 mg/mL drug loading.

Sample	**MMAD (µm)**	**GSD(µm)**	**$D_{v,Avg}$ (SEM) (µm)**	**$D_{v,50}$ (SLS) (µm)**	**ρ_g (g/cm^3)**
TFF Itz (10 mg/mL)	3.8 ± 0.3	1.9 ± 0.1	9.89	9.44 ± 1.53	0.16
CP Itz (10 mg/mL)	---	---	10.1	9.88 ± 1.07	0.16
CP Itz/T20 (10 mg/mL)	3.9 ± 0.5	1.8 ± 0.08	12.8	11.01 ± 1.25	0.098
Milled Itz (10 mg/mL)	6.0 ± 0.7	2.9 ± 0.6	3.95	3.33 ± 0.29 / 10.67 ± 0.29*	1.02
TFF BSA (10 mg/mL)**	3.1 ± 0.1	1.9 ± 0.1	9.40	9.10 ± 0.9	0.19
TFF Itz (50 mg/mL)	3.1 ± 0.1	1.9 ± 0.06	---	15.2 ± 2.41	0.040***
TFF BSA (50 mg/mL)	3.7 ± 0.3	3.3 ± 0.10	13.7	14.7 ± 1.87	0.085

* bimodal distribution – the size at which the maximum of each of the peaks was observed

** taken from Engstrom et al[35]

***calculated by using the $D_{v,50}$ (SLS) and MMAD in Eq. 4.3

Table 4.4 Calculation of VDW interaction potentials for drug particles of different morphologies in HFA 227, where *R* is the radius, *L* is the length, *w* is the width, and *y* is the height of the particle.

Particle	Particle dimensions (µm)	A_{121} x10^{21} (J)	Aspect ratio	Separation distance (nm) at $\Phi_{VDW} = 3/2k_BT$
Solid Itz sphere	R= 2.5	33	1	1129
Porous Itz sphere $\varphi_f = 0.50$	R = 2.5*	8.9	1	300
Hollow, porous Itz sphere $\varphi_{shell} = 0.50$	R = 2.5* shell thickness = 0.10*	8.9	1	96
TFF Itz plates**	L x w x y 0.6 x 0.3 x 0.06	33	10	150
CP Itz/T20 needles** (approx. as cylinder)	R= 0.75; L = 6.8	33	5	955
Milled Itz spheres***	R = 0.15	33	1	68

*taken from Engstrom et al. [35]
**particle dimensions estimated using SEM images
***particle dimensions determined by SLS

Table 4.5 Settling behavior of ITZ particles prepared by TFF, CP, and milling. A floc diameter, d_f, of 150 μm, was used based on optical microscopy images.

Sample	$U_{Experimental}$ (mm/s)	ρ_p (g/cm^3)	d_{floc} (μm)	φ_v	φ^{flocs}	φ_f	D_f
TFF Itz plates	0.0118	1.30	150	0.0015	0.65	0.0024	2.35
CP Itz/T20 needles	0.043	1.36	150	0.0010	0.15	0.0068	2.27
Milled Itz spheres	1.27	1.5	100	0.0077	0.011	0.70	3.00
TFF BSA* rods	0.023	1.30	250	0.00077	0.38	0.0020	2.50

*taken from Engstrom et al.[35]

4.6 REFERENCES

1. Courrier, H. M.; N. Butz; Vandamme, T. F., Pulmonary Drug Delivery Systems: Recent Developments and Prospects. *Critical Reviews in Therapeutic Drug Carrier Systems* **2002,** 19, (4 and 5), 425-498.

2. Bernstein, J. A.; Amin, H.; Smith, S., Therapeutic Uses of Lung Aerosol. In *Inhalation Aerosols: Physical and Biological Basis for Therapy*, Hickey, A. J., Ed. Informa healthcare USA, Inc.: New York, NY, 2007; Vol. 221, pp 219-252.

3. Benfait, C., Kos reports achievements of new research and development milestones. *Kos Press Release* **2004**.

4. Edwards, D.; Hanes, J.; Caponetti, G.; Mintzes, J.; Deaver, D.; Lotan, N.; Langer, R., Large Porous Particles for Pulmonary Delivery. *Science* **1997,** 276.

5. Patton, J. S., Unlocking the opportunity of tight glycaemic control: innovative delivery of insulin via the lung. *Diabetes, Obesity and Metabolism* **2005,** 7, (Suppl. 1), S5-S8.

6. Patton, J. S.; Bukar, J. G.; Eldon, M. A., Clinical pharmacokinetics and pharmacodynamics of inhaled insulin. *Clinical Pharmacokinetics* **2004,** 43, (12), 781-801.

7. White, S.; Bennett, D. B.; Cheu, S.; Conley, P. W.; Guzek, D. B.; Gray, S.; Howard, J.; Malcolmson, R.; Parker, J. M.; Roberts, P.; Sadrzadeh, N.; Schumacher, J. D.; Seshadri, S.; Sluggett, G. W.; Stevenson, C. L.; Harper, N. J., EXUBERA: Pharmaceutical Development of a Novel Product for Pulmonary Delivery of Insulin. *Diabetes Technology & Therapeutics* **2005,** 7, (6), 896-906.

8. Heyder, J.; Gebhart, J.; Rudolf, G.; Schiller, C. F.; Stahlhofen, W., Deposition of particles in the human respiratory tract in the size range 0.005-15 [mu]m. *Journal of Aerosol Science* **1986,** 17, (5), 811-825.

9. Heyder, J.; Rudolf, G., Mathematical models of particle deposition in the human respiratory tract. *Journal of Aerosol Science* **1984,** 15, (6), 697-707.

10. Smyth, H. D. C., The influence of formulation variables on the performance of alternative propellant-driven metered dose inhalers. *Advanced Drug Delivery Reviews* **2003,** 55, (7), 807-828.

11. Terzano, C., Pressurized Metered Dose Inhalers and Add-on Devices. *Pulmonary Pharmacology & Therapeutics* **2001,** 14, (5), 351-366.

12. Rogueda, P., Novel hydrofluoroalkane suspension formulations for respiratory drug delivery. *Expert Opinion on Drug Delivery* **2005,** 2, (4), 625-638.

13. Steckel, H.; Markefka, P.; te Wierik, H.; Kammelar, R., Effect of milling and sieving on functionality of dry powder inhalation products. *International Journal of Pharmaceutics* **2006,** 309, (1-2), 51-59.

14. Williams, R. O., III; Brown, J.; Liu, J., Influence of micronization method on the performance of a suspension triamcinolone acetonide pressurized metered-dose inhaler formulation. *Pharmaceutical Development and Technology* **1999,** 4, (2), 167-179.

15. Williams, R. O., III; Repka, M. A.; Barron, M. K., Application of co-grinding to formulate a model pMDI suspension. *European Journal of Pharmaceutics and Biopharmaceutics* **1999,** 48, (2), 131-140.

16. Ben-Jebria, A.; Chen, D.; Eskew, M. L.; Vanbever, R.; Langer, R.; Edwards, D. A., Large porous particles for sustained protection from carbachol-induced bronchoconstriction in guinea pigs. *Pharmaceutical Research* **1999,** 16, (4), 555-561.

17. Dellamary, L. A.; Tarara, T. E.; Smith, D. J.; Woelk, C. H.; Adractas, A.; Costello, M. L.; Gill, H.; Weers, J. G., Hollow porous particles in metered dose inhalers. *Pharmaceutical Research* **2000,** 17, (2), 168-174.

18. Vanbever, R.; Mintzes, J. D.; Wang, J.; Nice, J.; Chen, D.; Batycky, R.; Langer, R.; Edwards, D. A., Formulation and physical characterization of large porous particles for inhalation. *Pharmaceutical Research* **1999,** 16, (11), 1735-1742.

19. Michael, Y.; Snowden, M. J.; Chowdhry, B. Z.; Ashurst, I. C.; Davies-Cutting, C. J.; Riley, T., Characterisation of the aggregation behavior in a salmeterol and fluticasone propionate inhalation aerosol system. *International Journal of Pharmaceutics* **2001,** 221, (1-2), 165-174.

20. Williams, R. O., III, Hie Liu, Formulation of a Protein with Propellant HFA 134a for Aerosol Delivery. *European Journal of Pharmaceutical Sciences* **1998,** 7, 137-144.

21. Williams, R. O., III; Liu, J., Influence of formulation additives on the vapor pressure of hydrofluoroalkane propellants. *International Journal of Pharmaceutics* **1998,** 166, (1), 99-103.

22. McDonald, K. J.; Martin, G. P., Transition to CFC-free metered dose inhalers - into the new millennium. *International Journal of Pharmaceutics* **2000,** 201, (1), 89-107.

23. Johnson, K. A., Interfacial phenomena and phase behavior in metered-dose inhaler formulations. *Lung Biology in Health and Disease* **1996,** 94, (Inhalation Aerosols), 385-415.

24. Selvam, P.; Peguin, R. P. S.; Chokshi, U.; da Rocha, S. R. P., Surfactant Design for the 1,1,1,2-Tetrafluoroethane-Water Interface: ab initio Calculations and in situ High-Pressure Tensiometry. *Langmuir* **2006,** 22, (21), 8675-8683.

25. Keller, M., Innovations and perspectives of metered dose inhalers in pulmonary drug delivery. *International Journal of Pharmaceutics* **1999,** 186, (1), 81-90.

26. Patton, J. S., Pulmonary drug delivery comes of age: the outlook for 2005 & beyond. *Drug Delivery Technology* **2005,** 5, (4), 46-49.

27. Hirst, P. H.; Pitcairn, G. R.; Weers, J. G.; Tarara, T. E.; Clark, A. R.; Dellamary, L. A.; Hall, G.; Shorr, J.; Newman, S. P., In vivo lung deposition of hollow porous particles from a pressurized metered dose inhaler. *Pharmaceutical Research* **2002,** 19, (3), 258-264.

28. Tarara, T. E., MIchael S. Hartman, Howard Gill, Characterization of Suspension-Based Metered Dose Inhaler Formulations Composed of Spray-Dried Budesonide Microcrystals Dispersed in HFA-134a. *Pharmaceutical Research* **2004,** 21, (9), 1607-1614.

29. Weers, J. G.; Tarara, T. E.; Dellamary, L. A.; Kabalnov, A.; Schutt, E. G. Stabilized preparations for use in metered dose inhalers. 98-US20615
9916422, 19980929., 1999.

30. Tsapis, N.; Bennett, D.; Jackson, B.; Weitz, D. A.; Edwards, D. A., Trojan particles: large porous carriers of nanoparticles for drug delivery. *Proceedings of the National Academy of Sciences of the United States of America* **2002,** 99, (19), 12001-12005.

31. Hadinoto, K.; Phanapavudhikul, P.; Kewu, Z.; Tan, R. B. H., Dry powder aerosol delivery of large hollow nanoparticulate aggregates as prospective carriers of nanoparticulate drugs: Effects of phospholipids. *International Journal of Pharmaceutics* **2007,** 333, (1-2), 187-198.

32. Hadinoto, K.; Phanapavudhikul, P.; Zhu, K.; Tan, R. B. H., Novel Formulation of Large Hollow Nanoparticles Aggregates as Potential Carriers in Inhaled Delivery of Nanoparticulate Drugs. *Industrial & Engineering Chemistry Research* **2006,** 45, (10), 3697-3706.

33. Bailey, M. M.; Gorman, E. M.; Munson, E. J.; Berkland, C., Pure Insulin Nanoparticle Agglomerates for Pulmonary Delivery. *Langmuir* **2008,** 24, (23), 13614-13620.

34. Peek, L. J.; Roberts, L.; Berkland, C., Poly(d,l-lactide-co-glycolide) Nanoparticle Agglomerates as Carriers in Dry Powder Aerosol Formulation of Proteins. *Langmuir* **2008,** 24, (17), 9775-9783.

35. Engstrom, J. D.; Tam, J. M.; Miller, M. A.; Williams, R. O.; Johnston, K. P., Templated open flocs of nanorods for enhanced pulmonary delivery with pressurized metered dose inhalers *Pharmaceutical Research* **2009,** 26, (1), 101-117.

36. Patton, J. S., Mechanisms of macromolecule absorption by the lungs. *Advanced Drug Delivery Reviews* **1996,** 19, (1), 3-36.

37. Dailey, L. A.; Kleemann, E.; Wittmar, M.; Gessler, T.; Schmehl, T.; C. Roberts; Seeger, W.; Kissel, T., Surfactant-Free, Biodegradable Nanoparticles for Aerosol Therapy Based on the Branched Polyesters, DEAPA-PVAL-g-PLGA. *Pharmaceutical Research* **2003,** 20, (12), 2011-2020.

38. Hiemenz, P. C.; Rajagopalan, R.; Editors, *Principles of Colloid and Surface Chemistry, Third Edition, Revised and Expanded*. 1997; p 688 pp.

39. Philipse, A. P.; Wierenga, A. M., On the Density and Structure Formation in Gels and Clusters of Colloidal Rods and Fibers. *Langmuir* **1998,** 14, (1), 49-54.

40. Goodarz-Nia, I.; Sutherland, D. N., Floc simulation. Effects of particle size and shape. *Chemical Engineering Science* **1975,** 30, (4), 407-12.

41. Jiang, Z.; Guan, Y., Flocculation morphology: effect of particulate shape and coagulant species on flocculation. *Water Science and Technology* **2006,** 53, (7, Particle Separation 2005: Waste Water Treatment), 9-16.

42. Philipse, A. P., The Random Contact Equation and Its Implications for (Colloidal) Rods in Packings, Suspensions, and Anisotropic Powders. *Langmuir* **1996,** 12, (5), 1127-33.

43. Boal, A. K.; Ilhan, F.; DeRouchey, J. E.; Thurn-Albrecht, T.; Russell, T. P.; Rotello, V. M., Self-assembly of nanoparticles into structured spherical and network aggregates. *Nature* **2000,** 404, (6779), 746-748.

44. Pison, U.; Welte, T.; Giersig, M.; Groneberg, D. A., Nanomedicine for respiratory diseases. *European Journal of Pharmacology* **2006,** 533, (1-3), 341-350.

45. Amidon, G. L.; Lennernaes, H.; Shah, V. P.; Crison, J. R., A theoretical basis for a biopharmaceutic drug classification: the correlation of in vitro drug product dissolution and in vivo bioavailability. *Pharmaceutical Research* **1995,** 12, (3), 413-20.

46. Singhal, D.; Curatolo, W., Drug polymorphism and dosage form design: a practical perspective. *Advanced Drug Delivery Reviews* **2004,** 56, (3), 335-347.

47. Engstrom, J. D.; Lai, E. S.; Ludher, B.; Chen, B.; Milner, T. E.; Kitto, G. B.; Williams III, R. O.; Johnston, K. P., Formation of stable submicron protein particles by thin film freezing. *Pharmaceutical Research* **2008,** 25, (6), 1334-1336.

48. Rogers, T. L.; Gillespie, I. B.; Hitt, J. E.; Fransen, K. L.; Crowl, C. A.; Tucker, C. J.; Kupperblatt, G. B.; Becker, J. N.; Wilson, D. L.; Todd, C.; Broomall, C. F.; Evans, J. C.; Elder, E. J., Development and Characterization of a Scalable Controlled Precipitation Process to Enhance the Dissolution of Poorly Water-Soluble Drugs. *Pharmaceutical Research* **2004,** 21, (11), 2048-2057.

49. Matteucci, M. E.; Hotze, M. A.; Johnston, K. P.; Williams, R. O., III, Drug Nanoparticles by Antisolvent Precipitation: Mixing Energy versus Surfactant Stabilization. *Langmuir* **2006,** 22, (21), 8951-8959.

50. Wong, J.; Papadopoulos, P.; Werling, J.; Rebbeck, C.; Doty, M.; Kipp, J.; Neuberger, D. In *Itraconazole Nanosuspension for Intravenous Injection - Determination of the Real Component of Refractive Index Input for Laser Light Diffraction Particle Sizing*, American Association of Pharmaceutical Scientists Annual Meeting, Baltimore, MD, 2004; Baltimore, MD, 2004.

51. Ryoo, W.; Webber, S. E.; Johnston, K. P., Water-in-Carbon Dioxide Microemulsions with Methylated Branched Hydrocarbon Surfactants. *Ind. Eng. Chem. Res.* **2003,** 42, (25), 6348-6358.

52. Finlay, W. H., *The mechanics of inhaled pharmaceutical aerosols*. New York, NY, 2001.

53. Traini, D.; Young, P. M.; Rogueda, P.; Price, R., In Vitro Investigation of Drug Particulates Interactions and Aerosol Performance of Pressurized Metered Dose Inhalers. *Pharmaceutical Research* **2007,** 24, (1), 125-135.

54. Rogueda, P. G. A., HPFP, a model propellant for pMDIs. *Drug Development and Industrial Pharmacy* **2003,** 29, (1), 39-49.

55. Matteucci, M. E.; Miller, M. A.; Williams, R. O.; Johnston, K. P., Highly Supersaturated Solutions of Amorphous Drugs Approaching Predictions from Configurational Thermodynamic Properties. *Journal of Physical Chemistry B* **2008,** 112, (51), 16675-16681.

56. Traini, D.; Rogueda, P.; Young, P.; Price, R., Surface Energy and Interparticle Forces Correlations in Model pMDI Formulations. *Pharmaceutical Research* **2005,** 22, (5), 816-825.

57. Peguin, R. P. S.; da Rocha, S. R. P., Solvent-Solute Interactions in Hydrofluoroalkane Propellants. *J. Phys. Chem. B FIELD Full Journal Title:Journal of Physical Chemistry B* **2008,** 112, (27), 8084-8094.

58. Selvam, P.; Chokshi, U.; Gouch, A.; Wu, L.; Porcar, L.; da Rocha, S. R. P., Ethoxylated copolymer surfactants for the HFA134a-water interface: interfacial activity, aggregate microstructure and biomolecule uptake. *Soft Matter FIELD Full Journal Title:Soft Matter* **2008,** 4, (2), 357-366.

59. Matteucci, M. E.; Paguio, J. C.; Miller, M. A.; Williams, R. O., III; Johnston, K. P., Flocculated Amorphous Nanoparticles for Highly Supersaturated Solutions. *Pharmaceutical Research* **2008,** 25, (11), 2477-2487.

60. Fargues, C.; Turchiuli, C., Structural characterization of flocs in relation to their settling performances. *Chemical Engineering Research and Design* **2004,** 82, (A11), 1517.

61. Tang, P.; Greenwood, J.; Raper, J. A., A model to describe the settling behavior of fractal aggregates. *Journal of Colloid and Interface Science* **2002,** 247, (1), 210-219.

62. Hough, D. B.; White, L. R., The calculation of Hamaker constants from Lifshitz theory with applications to wetting phenomena. *Advances in Colloid and Interface Science* **1980,** 14, (1), 3-41.

63. Li, H.; Peng, X.; Wu, L.; Jia, M.; Zhu, H., Surface Potential Dependence of the Hamaker Constant. *The Journal of Physical Chemistry C* **2009,** 113, (11), 4419-4425.

64. Tam, J. M.; McConville, J. T.; Williams, R. O., 3rd; Johnston, K. P., Amorphous cyclosporin nanodispersions for enhanced pulmonary deposition and dissolution. *Journal of pharmaceutical sciences* **2008,** 97, (11), 4915-33.

65. Yang, W.; Tam, J.; Miller, D. A.; Zhou, J.; McConville, J. T.; Johnston, K. P.; Williams, R. O., High bioavailability from nebulized itraconazole nanoparticle dispersions with biocompatible stabilizers. *International Journal of Pharmaceutics* **2008,** 361, (1-2), 177-188.

Chapter 5: Controlled Assembly of Biodegradable Plasmonic Nanoclusters for Near-Infrared Imaging and Therapeutic Applications

Metal nanoparticles with surface plasmon resonance (SPR) in the near-infrared region (NIR), are of great interest for imaging and therapeutic application [1-6]. Presently, widely available gold nanoparticles that absorb in the NIR are typically larger than 50 nm[7-13], above the threshold size of approximately 5.5 nm required for efficient renal clearance from the body[14]. Because these nanoparticles are not biodegradable, concerns about their accumulation and long-term toxicity[14, 15] have restricted their translation into clinical practice. Herein, we describe the assembly of biodegradable clusters smaller than 100 nm from sub-5 nm constituent gold particles. The nanoclusters manifest intense NIR absorbance and strong optical contrast in live cells. Nanocluster size and spacing between constituent gold nanoparticles are controlled by regulating particle concentration during cluster formation, as well as controlling interactions between ligand-coated gold cores and a biodegradable polymer binder. Nanoclusters deaggregate completely into sub-5 nm primary gold particles upon degradation of the polymer binder under physiologically relevant conditions in solution and in live cells. This general concept for the assembly of hybrid polymer/inorganic nanoclusters combines advantages of the biodegradability of a polymer binder/stabilizer with the strong imaging contrast and therapeutic capabilities afforded by the NIR-active closely-spaced metal nanoparticle assembly.

5.1 INTRODUCTION

Various plasmonic particles including nanoshells[7-9], nanorods[10, 11], nanocages[12, 13], and nanoroses[16], which scatter and absorb in the NIR region (650-900 nm), where soft tissues and blood are most transparent, may be used for molecular-specific imaging, therapy and multi-modal application[8, 13, 17-21]. Intravenous administration of nanoparticles provides an effective method for rapid delivery throughout the body. In general, particles with diameters between 6-100 nm exhibit sufficiently long blood residence times for accumulation at disease sites, such as cancer and cardiovascular plaques[22-24]. However, the potential accumulation and long-term toxicity of these inorganic nanoparticles are a major roadblock in their translation to clinical practice for systemic targeting of diseases. Particles smaller than ~6 nm are removed too rapidly by the kidneys to achieve sufficient accumulation, although this clearance is highly desirable from a toxicity stand point[14]. Furthermore, the synthesis of ultra-small functionalized nanoparticles <6 nm is challenging[14], as the strength of plasmon resonances rapidly decreases with size[25]. The discrepancy in the particle size needed for imaging and therapy versus efficient excretion from the body creates a serious conflict in biomedical applications.

Herein, we present a flexible platform for the kinetically-controlled assembly of sub-5 nm gold particles to produce ~100 nm metal/polymer biodegradable nanoclusters with strong NIR absorbance for multimodal application. The nanoclusters are bound together with a biodegradable triblock copolymer of polylactic acid and polyethylene glycol, PLA(2K)-*b*-PEG(10K)-*b*-PLA(2K), that degrades under physiological conditions to release the constituent clearable gold nanoparticles. Thus, these clusters have the potential to satisfy the requirements of sufficient blood residence time for clinical application, followed by effective clearance from the body after biodegradation (Figure 5.1A). The close-spacing between gold nanoparticles within the nanoclusters facilitates strong NIR scattering and absorption. Both nanocluster size and physical properties, especially interparticle spacing, are controlled by varying particle volume fractions during solvent evaporation. The changes in electrostatic, van der Waals (VDW), depletion, and steric interactions upon concentrating the gold nanoparticles and polymer micelles govern the kinetic assembly of the nanoclusters, as well as their disassembly after polymer degradation. Without the presence of a polymeric stabilizer, clusters of lysine-[26-28], cysteine-[29], or glutathione-[30] capped gold nanoparticles, produced by varying pH, demonstrate no control over cluster size, forming irregular micron-sized aggregates. Polymer-templated self-assembly has been used to produce small clusters of metal nanoparticles[31-34]. However, metal loadings and interparticle spacings have rarely been sufficient to provide strong NIR absorbance, and further, the templating agents are often highly specialized. In contrast, our wide-ranging kinetically-controlled assembly platform requires only common copolymers as binders and simple capping ligands on gold, such as citrate and/or lysine, which are acceptable for *in vivo* application.

5.2 METHODS SUMMARY

5.2.1 Nanocluster synthesis:

Gold nanoparticles (~4 nm) stabilized with citrate ligands were synthesized based on a well known method[35] (See Appendix C). To add lysine ligands to the citrate-capped gold nanoparticles, a 1% lysine in pH 8.4 phosphate buffer (10 mM) solution was added to 1.2 mL of a 3.0 mg/mL colloidal gold solution to yield a final lysine concentration of 0.4 mg/mL. The dispersion was stirred for 12 hours[26, 28]. PLA(2K)-PEG(10K)-PLA(2K) (Sigma Aldrich Co., St. Louis, MO) (60 mg) was added to the aqueous dispersion of ligand capped gold nanoparticles, yielding a final polymer concentration of 50 mg/mL. The dispersion was sonicated in a bath sonicator for 5 minutes. Unless otherwise indicated, the polymer/gold dispersion was placed under an air stream and dried to completion over 2 hours. The dried film was redispersed with 10 mL of DI water to yield a blue dispersion at ~0.30 mg Au/mL.

5.2.2 Nanocluster deaggregation:

To characterize deaggregation in solution, an aliquot of the nanocluster dispersion (1.0 mL) was acidified with 0.1N HCl to pH=5, and monitored using UV-vis spectrophotometry and TEM. Nanocluster deaggregation was assessed in a murine macrophage cell line, (J477A.1, American Type Culture Collection, Manassas, VA), in which the cells were cultured in a 12-well plate in phenol-free DMEM media (Gibco, Grand Island, NY) supplemented with 5% fetal bovine serum (Hyclone, Logan, UT) and antibiotics (Gibco, Grand Island, NY) and incubated at 37°C in a 5% CO_2 environment for 1 week. The nanoclusters were filtered through a 0.45 μm filter (Corning, Corning, NY), spun down, and resuspended in DMEM medium prior to their addition to each well (0.4 mg cells/well). Incubation of the cells with the nanoclusters occurred over 24 hours, after which the excess, un-engulfed nanoparticles were removed by aspiration and the cells were allowed to proliferate to 72 or 168 hours time points. Optical measurements were taken at 24, 72, and 168 hours. The cells were washed three times in 1x phosphate buffered saline (PBS), harvested, and centrifuged at 110x g for 3 minutes. The supernatant was discarded. The cells were resuspended in 10 μL of PBS, placed on a microscope slide, and imaged using a combination of darkfield reflectance and hyperspectral imaging. Darkfield reflectance microscopy images of the cells and nanoclusters were taken with a Leica DM6000 upright microscope and the hyperspectral images were acquired with a PARISS spectral imager (Lightform Inc.). The same 20x, 0.5 NA objective and a 75 W Xe light source were used for both imaging modalities. The hyperspectral system was calibrated using a standard wavelength calibration lamp (low pressure Hg, Lightform, Inc.). All hyperspectral spectra from cells were normalized by the spectrum of the Xe excitation light source on a pixel by pixel basis. RGB images were taken with a Q-imaging Retiga EXi CCD camera with color LCD attachment. Images were white balanced with a Spectralon (Labsphere, North Sutton, NH), and the acquisition settings were chosen such that all samples were acquired under identical conditions.

5.2.3 TEM of cells:

To acquire TEM images of cells, $3x10^4$ macrophage cells were seeded overnight on Aclar Embedding Film (Electron Microscopy Sciences, Hatfield, PA). All samples for TEM imaging were treated identically and were run in parallel to the samples used for optical imaging. At each time point (24 hrs, 96 hrs, 168 hrs), the cells were fixed in a 1% glutaraldehyde, 1% paraformaldehyde solution for 1 hour at room temperature and then washed 3 times in PBS. Subsequently, cells were stained with 2% osmium tetroxide in water for 10 minutes then washed for 10 minutes in water. The sample was then dehydrated using increasing ratios of ethanol to acetone solutions, and finally embedded in an epoxy-acetone mixture and allowed to bake at 60°C for 24 hours. Ultrathin sections were sliced using a Leica Ultracut microtome (Leica, Deerfield, IL) and imaged with a Tecnai G2 TEM at a voltage of 80 kV.

5.3 RESULTS AND DISCUSSION

To control cluster growth, we have mediated interactions between gold particles, capped with a mixture of citrate and lysine ligands, with the biodegradable polymer, PLA(2K)-*b*- PEG(10K)-*b*-PLA(2K), as shown in Fig. 5.1B. The initial dispersed gold particles were ruby red, with an average diameter of 4.1±0.8 nm (Fig. 5.2A, Table 5.1). However, the dispersion turned blue after addition of the biodegradable polymer, in conjunction with evaporation of ~80% of the solvent. Complete solvent evaporation produced a smooth blue film, indicating absorption in the red. Reconstitution of the film with deionized (DI) water to a concentration of ~0.3 mg/mL yielded a dark blue dispersion of sub-100 nm clusters composed of primary gold nanoparticles as shown by scanning electron (SEM) and transmission election microscopy (TEM) (Fig. 5.2). TEM images titled at various angles reveal closely-spaced primary gold nanoparticles throughout the cluster. The hydrodynamic diameter measured by dynamic light scattering (DLS) was 83.0±4.6 nm, by volume (Fig. 5.3A, Table 5.1), in agreement with the TEM results. In the SEM image, a polymer-rich shell a few nanometers thick is apparent on the exterior of the clusters, which likely provides steric stabilization of the nanoclusters.

Thermogravimetric analysis indicated that the nanoclusters contained only 20 ± 5% organic material (polymer and ligands), 10-15% of which was polymer. These low polymer loadings favor close-spacing of the gold primary particles. Measured interparticle distances between constituent gold particles within the cluster were estimated to be 1.80±0.6 nm based on the more discernible particles in the periphery of TEM images (Appendix C Figure C.1) and are consistent with the calculated length scale of a lysine-lysine dipeptide in solution of 1.49 nm[27]. The ability to simultaneously control cluster size and spacing of gold nanoparticles within the nanocluster was achieved by manipulating particle volume fractions upon solvent evaporation, as well as the electrostatic, VDW, depletion, and steric interactions between the gold primary particles and the polymer (see Appendix C). Furthermore, the depletion interactions facilitate, along with the propensity of hydrophilic PEG blocks to migrate to the exterior of the clusters towards the interface with water, low polymer loadings in the clusters.

The extinction spectra changed markedly upon cluster formation (Fig. 5.3B). The initial red dispersion of gold nanoparticles had a maximum absorbance at 520 nm, characteristic of isolated gold spheres. For the blue nanocluster dispersion, a broad, relatively constant, absorbance was observed in the NIR region from 700 to 900 nm, which is important for *in vivo* applications. The extinction coefficient at the maximum absorbance, $\varepsilon_{703,}$ was 0.020 $cm^2/\mu g$ for a 56 μg/mL gold dispersion. Assuming that the gold nanoparticles are in a closest-packed state (based on SEM and TEM images in Fig. 5.2B-E), the estimated particle extinction cross section was $\sim 10^{-14}$ m^2 (see Appendix C), comparable to the value for nanoshells[19], nanocages[13], nanorods[19], and nanoroses[16]. The high NIR absorbance observed for nanoclusters is attributed to a combination of the following factors: close interparticle spacing between constituent gold nanoparticles, non-uniform spatial distribution of the constituent particles within the nanocluster, roughness of the nanocluster boundary surface, and finally, any deviation in the overall aspect ratio of the entire nanocluster from that of a sphere. The close spacing between gold particles is well within the fraction of the particle diameter known to produce significant red-shift in the SPR[19, 36-39]. TEM images (Fig. 5.2) also show that short oligomers of primary particles and sub-clusters may be discerned, indicative of a non-uniform volume-packing distribution of the constituent particles. When combined with strong plasmonic coupling, this non-uniform distribution significantly enhances the red-shift of the SPR[19, 37]. The NIR absorbance per total particle mass is much higher compared to previous composite particles with smaller amounts of gold nanoparticles templated with liposomes, block copolymer micelles, or DNA[34, 40, 41].

Nanoclusters with strong NIR absorbance were also produced by clustering more negatively charged citrate-capped gold nanoparticles, which possess a zeta potential of -44.0±4.9 mV, compared to -30.1±2.4 mV for the lysine/citrate-capped nanoparticles (Table 5.1). The remainder of the paper will focus on the lysine/citrate-capped nanoclusters due to their slightly smaller sizes.

The initial stability and degradation of the nanoclusters were examined at pH 7.4 and 5, simulating normal cellular environments and the interior of cellular lysosomes, respectively [42]. After storage for 168 hours (1 week) in pH 7.4 buffer, the DLS peak shifted modestly towards smaller sizes (Fig. 5.3A). This limited degradation is consistent with the long half-life of PLA (MW=2K) of about 4 weeks at neutral pH. Upon incubation in pH 5 buffer for one week, nearly complete nanocluster deaggregation was observed by TEM. The mean particle size of the deaggregated particles was 4.3±0.1 nm (Fig. 5.3C, Table 5.1), comparable to the initial size of the ligand-capped gold particles of 4.1±0.8 nm (Appendix C Figure C.2). Upon degradation of the polymer, the electrostatic repulsion between the gold particles is sufficient to overcome the attractive VDW forces to enable deaggregation. The extinction spectra of the nanocluster dispersions undergo a substantial shift towards the original spectra of the colloidal gold spheres, along with a change in the color of the dispersion back towards red (Fig. 5.3B). The discrepancy between the absorption spectra of the deaggregated particles compared to that of the initial colloidal gold dispersion is attributed to the presence of a small number of clusters still present in the dispersion. Deaggregation to constituent nanoparticles was also observed for the clusters produced using citrate-only capped nanoparticles (Table 5.1).

After demonstrating the ability of the nanoclusters to deaggregate in solution, interactions of the nanoclusters inside living cells were examined. Scattering spectra from image pixels (Fig. 5.4A,B), dark-field reflectance (DR) (Fig. 5.4C and D, a-c), and hyperspectral images (Fig. 5.4C and D, d-f) were acquired at 24, 96, and 168 hours after cells were treated with nanoclusters. High nanocluster uptake was evident in the DR images, where nanoclusters strongly scattered illumination light (Fig. 5.4C, a). The scattering intensity decreased over time as macrophages divided and nanoclusters were distributed between daughter cells (Fig. 5.4C, a-c). A significant increase in the red-NIR scattering signal of the labeled cells was seen compared to unlabeled cells (Fig. 5.4A, B), consistent with the high scattering efficiency of the nanoclusters in solution (Fig. 5.4A, red curve). The relative intensity of the red-NIR scattering signal decreased after 96 hours and the scattering from labeled cells showed a marked blue shift to ~550 nm that is consistent with scattering from the constituent lysine/citrate-capped gold nanoparticles

(Appendix C Fig. C.3). Hyperspectral images showed a gradual progression from very strong scattering in the 650-700 nm region at t=24 hours to a less intense scattering signal predominantly in the 500-550 nm region at t= 168 hours (Fig. 5.4C, d-f). As expected, the scattering for the control macrophages did not significantly change with time. The biodegradation of nanoclusters inside live cells was further confirmed by TEM. After 24 hours, large ~100 nm nanoclusters were observed throughout the cell interior (Fig. 5.4E, a-b). However, after 168 hours, cells contained only particles less than 5 nm in diameter (5.4E,c-d). These TEM results are in excellent agreement with optical measurements and deaggregation results in solution, providing unambiguous proof of essentially complete biodegradation of the initial ~100 nm nanoclusters into sub-5 nm primary particles (Appendix C Fig. C.2).

In this study we developed a general assembly platform for the design of hybrid polymer/gold nanoclusters smaller than 100 nm with strong absorbance in the NIR. In contrast to other plasmonic nanoparticles under development for biomedical applications, these nanoclusters degrade under physiological conditions to components that can be easily excreted from the body. Thus, these nanoclusters can provide strong optical cross-sections required for imaging and therapy, prolonged blood residence times for systemic delivery, as well as effective clearance from the body to facilitate the translation of plasmonic nanoparticle applications into clinical practice. This nanocluster assembly method is applicable to gold particles with varying surface charge, which plays an important role in clearance. Furthermore, it can be extended to the multiplexing of different types of primary particles into multimodal and multifunctional nanoclusters.

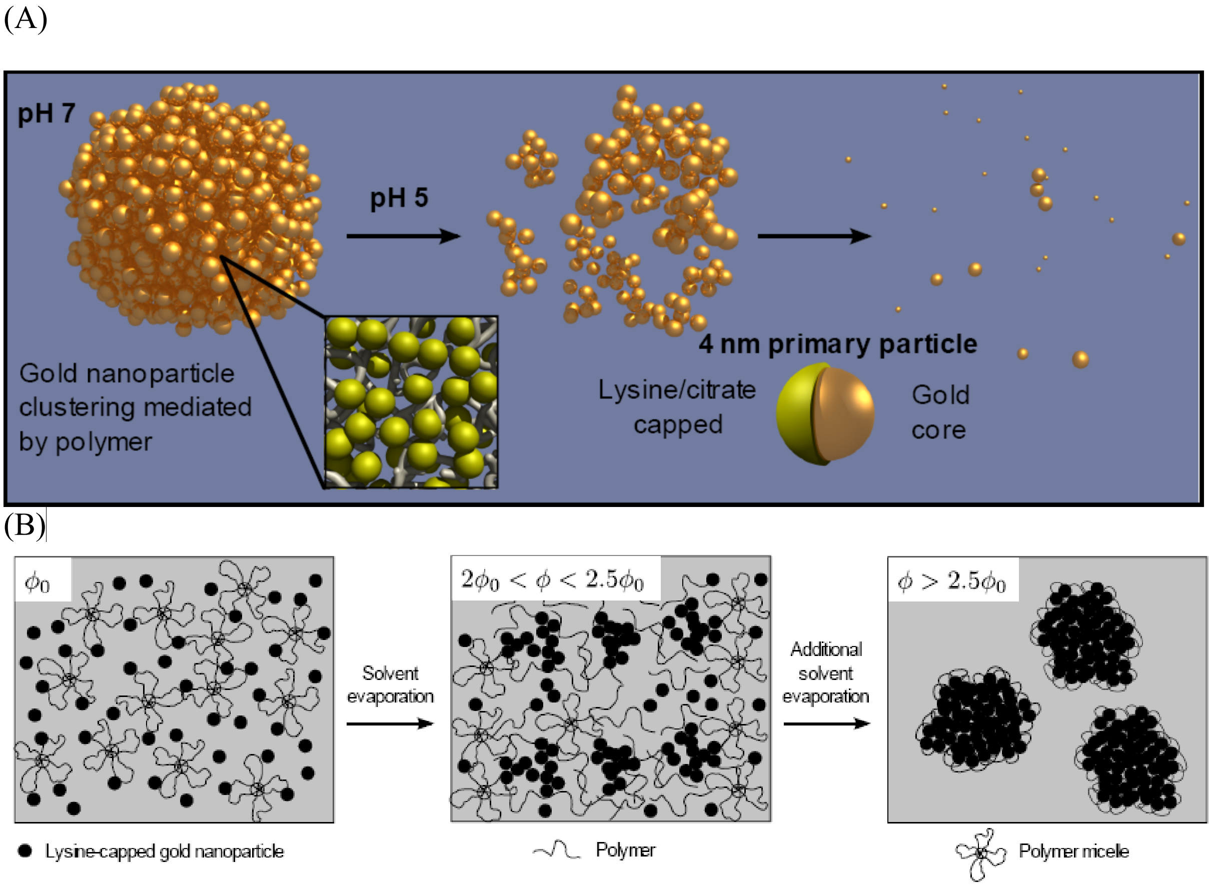

Figure 5.1 Schematic of synthesis and degradation of gold nanoclusters. (A) Illustration of a biodegradable nanocluster, which is composed of 4 nm primary gold particles held together with a biodegradable polymer. Upon polymer degradation, catalyzed by low pH in endosomal compartments of cells, the nanocluster deaggregates into primary gold nanoparticles. (B) Schematic of nanocluster formation process, in which primary gold nanoparticles aggregate in the presence of a micelle-forming polymer in a controlled manner to yield sub-100 nm clusters. Polymer adsorption to the nanoparticle surface and an increase in the volume fraction of particles, φ, via solvent evaporation promotes cluster formation. Long PEG loops on the polymer extend into the aqueous environment and provide steric stabilization for clusters.

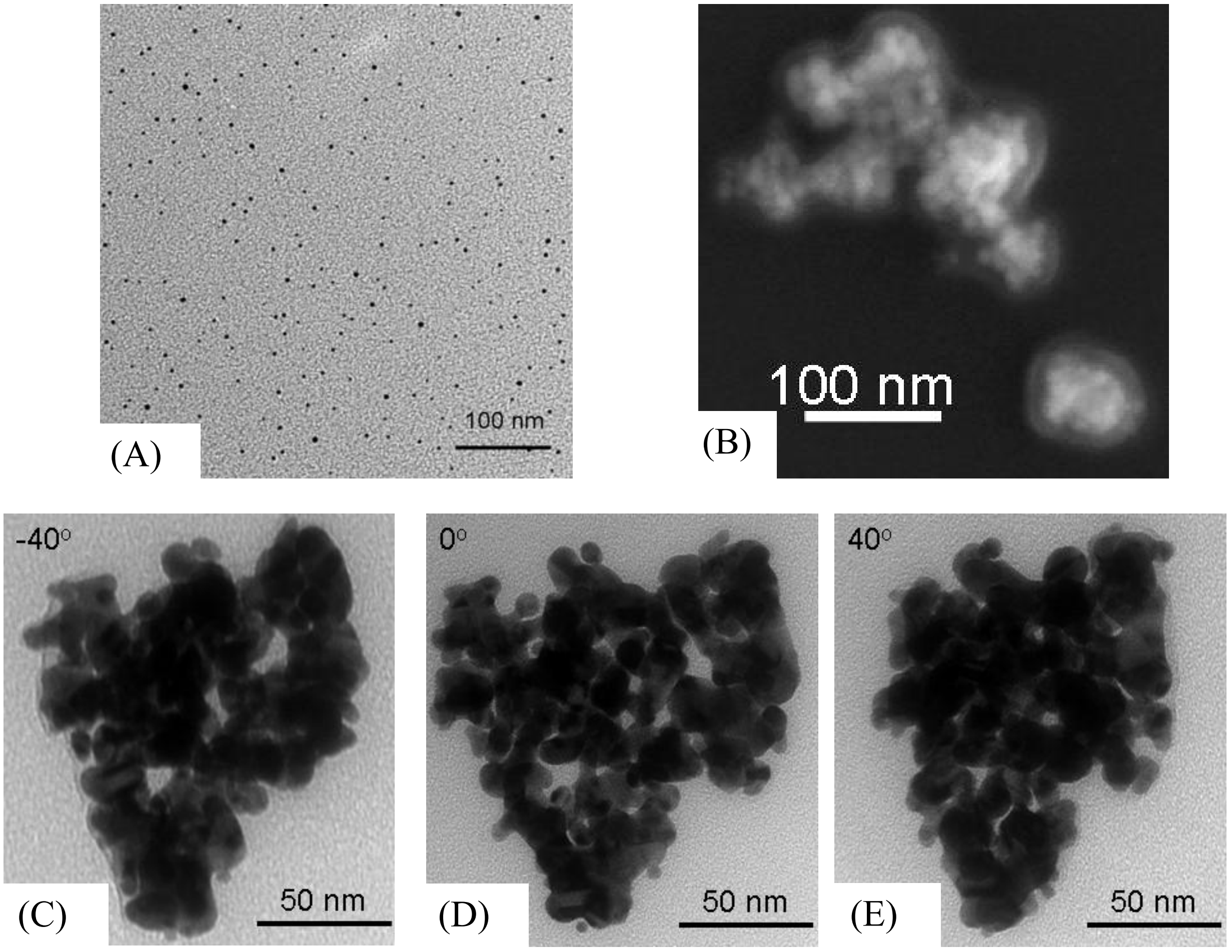

Figure 5.2 Electron microscopy characterization of gold nanoclusters. (A) TEM of initial 4 nm lysine/citrate-capped gold nanoparticles before clustering. (B) SEM and (C-E) TEM micrographs of nanoclusters templated using PLA(2K)-PEG(10K)-PLA(2K) at a 16/1 polymer/Au ratio (w/w). For TEM micrographs, the TEM stage was tilted at an angle of -40o, 0o(no tilt), and 40o in C, D, and E, respectively.

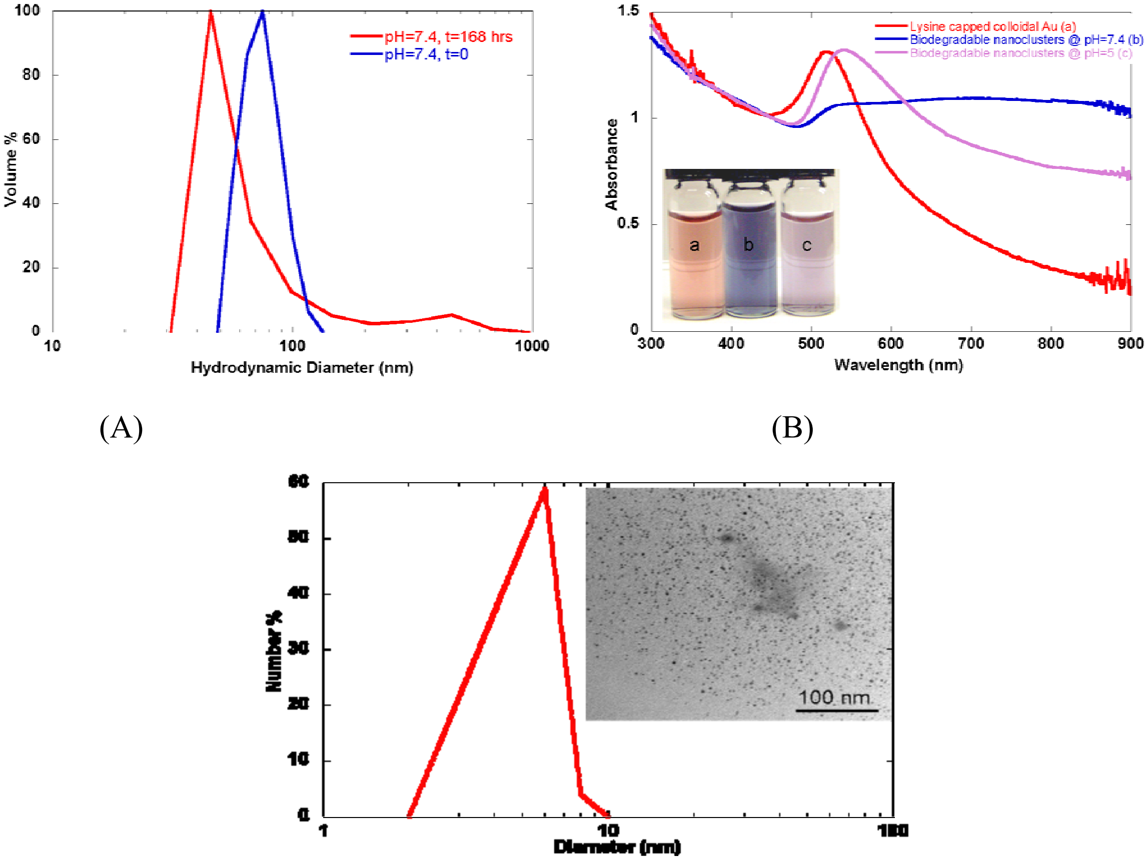

(A)

(B)

(C)

Figure 5.3 Degradation of gold nanoclusters in solution. (A) Particle size distribution, measured by DLS, of the nanoclusters in pH 7.4 media immediately after preparation and after 168 hours (1 week) of incubation. (B) UV-vis absorbance spectra and photographs of the (a) colloidal dispersion of lysine/citrate-capped gold nanoparticles, (b) biodegradable nanoclusters (pH=7.4), and (c) deaggregated nanoclusters (pH=5). (C) Number distribution of nanocluster sizes after deaggregation in pH=5 media, as determined by image analysis of TEM micrographs (over 200 particles measured). Inset : TEM micrograph of nanoclusters after incubation at pH=5 for 1 week.

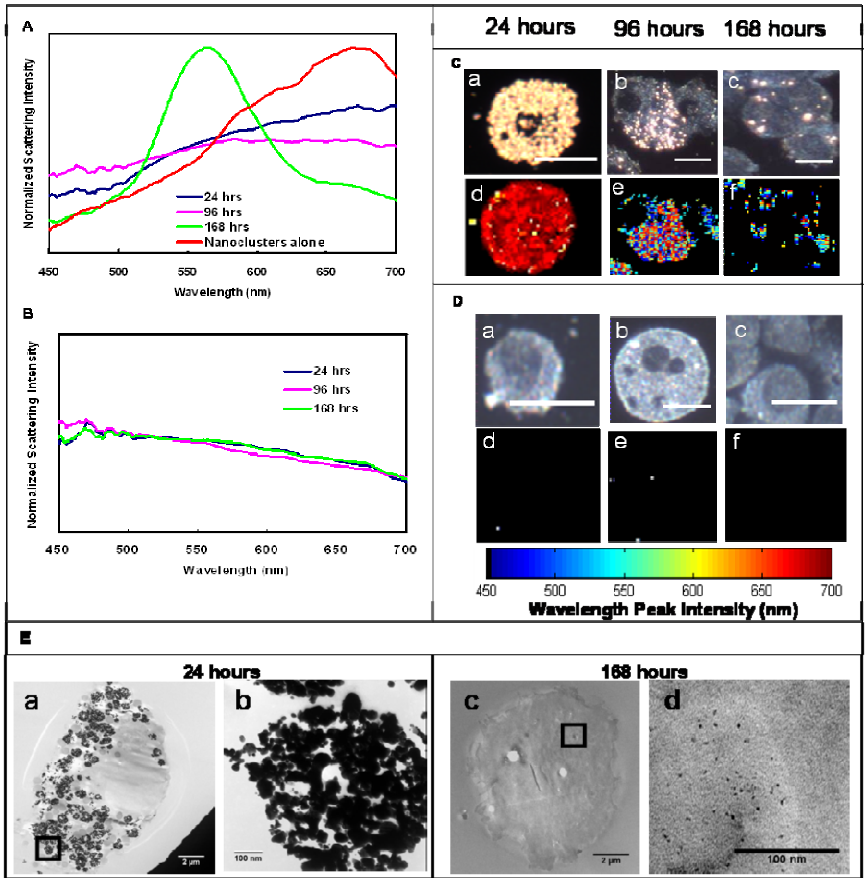

Figure 5.4 Biodegradation of gold nanoclusters inside live cells. Scattering spectra (normalized by area under the curve) of (A) nanoclusters in live cells and (B) control cells without nanoclusters. The spectra were taken after 24, 96, and 168 hours of incubation time. (C,D) Dark-field reflectance (DR) images of cells treated with nanoclusters and control cells over time (a-c) and corresponding color coded images indicating the scattering peak position at each pixel in the field of view (d-f). The scale bar in the dark-field images is 20 µm. The color bar was used to obtain images in (C and D, d-f). Pixels that did not have an identifiable peak in a corresponding spectrum were not assigned a color. (E) TEM images of cells treated with nanoclusters at low magnification (a,c) and high magnification (b,d) at 24 hours (a,b) and 168 hours (c,d). Boxes in (a) and (c) are magnified in (b) and (d), respectively. Scale bars in (a) and (c) are 2 um and scale bars in (b) and (d) are 100 nm. DR images were taken with a Leica DM6000 upright microscope and hyperspectral measurements were acquired with a PARISS spectral imager (Lightform Inc.) using a 20x, 0.5 NA objective and a 75 W Xe light source. TEM images were taken with a Tecnai G2 TEM at an accelerating voltage of 80 kV.

Table 5.1 Characterization of gold primary particles and nanoclusters with lysine and citrate ligands. Absorbance measurements were recorded at gold concentrations of ~56 μg/mL. All nanoclusters were formed at 100% evaporation using the polymer PLA(2K)-*b*-PEG(10K)-*b*-PLA(2K). Average diameters, D_{avg}, for nanoclusters were determined by DLS. D_{avg} for primary particles and deaggregated particles ($D_{avg\ deag}$) were measured by image analysis of TEM micrographs.

Ligand	Absorbance (750 nm)	$D_{avg,\ primary\ particle}$ (nm)	$D_{avg,\ cluster\ pH=7.4}$ (nm)	$D_{avg,\ deag,\ pH=5}$ (nm)
Lysine/citrate	1.10	4.1 ± 0.8	83.0 ± 4.6	4.4 ± 0.8
Citrate	1.09	4.0 ± 0.8	119.4 ± 22.5	4.0 ± 0.9

5.4 REFERENCES

1. Weissleder, R., A clearer vision for in vivo imaging. *Nature Biotechnology* **2001,** 19, (4), 316-317.

2. Peer, D.; Karp, J. M.; Hong, S.; Farokhzad, O. C.; Margalit, R.; Langer, R., Nanocarriers as an emerging platform for cancer therapy. *Nature Nanotechnology* **2007,** 2, (12), 751-760.

3. Jain, P. K.; El-Sayed, I. H.; El-Sayed, M. A., Gold Nanoparticles Target Cancer. *NanoToday* **2007,** 2, (1), 18-29.

4. Alivisatos, P., The use of nanocrystals in biological detection. *Nature Biotechnology* **2004,** 22, 47-52.

5. Anker, J. N.; Hall, W. P.; Lyandres, O.; Shah, N. C.; Zhao, J.; Van Duyne, R. P., Biosensing with plasmonic nanosensors *Nature Materials* **2008** 7 442-453.

6. Aslan, K.; Luhrs, C. C.; Perez-Luna, V. H., Controlled and Reversible Aggregation of Biotinylated Gold Nanoparticles with Streptavidin. *Journal of Physical Chemistry B* **2004,** 108, (40), 15631-15639.

7. Adler, D. C.; Huang, S.-W.; Huber, R.; Fujimoto, J. G., Photothermal detection of gold nanoparticles using phase-sensitive optical coherence tomography. *Optics Express* **2008,** 16, (7), 4376-4393.

8. Loo, C.; Lowery, A.; Halas, N.; West, J.; Drezek, R., Immunotargeted Nanoshells for Integrated Cancer Imaging and Therapy. *Nano Letters* **2005,** 5, (4), 709-711.

9. Hirsch, L. R.; Stafford, R. J.; Bankson, J. A.; Sershen, S. R.; Rivera, B.; Price, R. E.; Hazle, J. D.; Halas, N. J.; West, J. L., Nanoshell-mediated near-infrared thermal therapy of tumors under magnetic resonance guidance. *Proceedings of the National Academy of Sciences of the United States of America* **2003,** 100, (23), 13549-13554.

10. Pissuwan, D.; Valenzuela, S. M.; Killingsworth, M. C.; Xu, X.; Cortie, M. B., Targeted destruction of murine macrophage cells with bioconjugated gold nanorods. *Journal of Nanoparticle Research* **2007,** 9, (6), 1109-1124.

11. Huang, X.; El-Sayed, I. H.; Qian, W.; El-Sayed, M. A., Cancer Cell Imaging and Photothermal Therapy in the Near-Infrared Region by Using Gold Nanorods. *Journal of the American Chemical Society* **2006,** 128, (6), 2115-2120.

12. Chen, J.; Saeki, F.; Wiley, B. J.; Cang, H.; Cobb, M. J.; Li, Z.-Y.; Au, L.; Zhang, H.; Kimmey, M. B.; Li, X.; Xia, Y., Gold Nanocages: Bioconjugation and Their Potential Use as Optical Imaging Contrast Agents. *Nano Letters* **2005,** 5, (3), 473-477.

13. Skrabalak, S. E.; Chen, J.; Au, L.; Lu, X.; Li, X.; Xia, Y., Gold nanocages for biomedical applications. *Advanced Materials* **2007,** 19, (20), 3177-3184.

14. Choi, H. S.; Liu, W.; Misra, P.; Tanaka, E.; Zimmer, J. P.; Ipe, B. I.; Bawendi, M. G.; Frangioni, J. V., Renal clearance of quantum dots. *Nature Biotechnology* **2007,** 25, (10), 1165-1170.

15. Lewinski, N.; Colvin, V.; Drezek, R., Cytotoxicity of nanoparticles. *Small* **2008,** 4, (1), 26-49.

16. Ma, L. L.; Feldman, M. D.; Tam, J. M.; Paranjape, A. S.; Cheruku, K. K.; Larson, T. A.; Tam, J. O.; Ingram, D. R.; Paramita, V.; Villard, J. W.; Clarke, G. D.; Jenkins, J. T.; Asmis, R.; Sokolov, K.; Chandrasekar, B.; Milner, T. E.; Johnston, K. P., Small multifunctional nanoclusters (Nanoroses) for targeted cellular imaging and therapy. *ACS Nano* **Submitted**.

17. Larson, T. A.; Bankson, J.; Aaron, J.; Sokolov, K., Hybrid plasmonic magnetic nanoparticles as molecular specific agents for MRI/optical imaging and photothermal therapy of cancer cells. *Nanotechnology* **2007,** 18, (32), 325101/1-325101/8.

18. Ji, X. J.; Shao, R. P.; Elliott, A. M.; Stafford, R. J.; Esparza-Coss, E.; Bankson, J. A.; Liang, G.; Luo, Z. P.; Park, K.; Markert, J. T.; Li, C., Bifunctional gold nanoshells with a superparamagnetic iron oxide-silica core suitable for both MR imaging and photothermal therapy. *Journal of Physical Chemistry C* **2007,** 111, (17), 6245-6251.

19. Jain, P. K.; Lee, K. S.; El-Sayed, I. H.; El-Sayed, M. A., Calculated Absorption and Scattering Properties of Gold Nanoparticles of Different Size, Shape, and Composition: Applications in Biological Imaging and Biomedicine. *Journal of Physical Chemistry B* **2006,** 110, (14), 7238-7248.

20. Lee, S. E.; Liu, G. L.; Kim, F.; Lee, L. P., Remote Optical Switch for Localized and Selective Control of Gene Interference. *Nano Letters* **2009,** 9, (2), 562-570.

21. Kumar, S.; Aaron, J.; Sokolov, K., Directional conjugation of antibodies to nanoparticles for synthesis of multiplexed optical contrast agents with both delivery and targeting moieties. *Nature Protocols* **2008,** 3, (2), 314-320.

22. Kooi, M. E.; et al, Accumulation of Ultrasmall Superparamagnetic Particles of Iron Oxide in Human Atherosclerotic Plaques Can Be Detected by In Vivo Magnetic Resonance Imaging. . *Circulation* **2003,** 107, (19), 2453-2458.

23. Schipper, M. L.; Iyer, G.; Koh , A. L.; Cheng, Z.; Ebenstein, Y.; Aharoni, A.; Keren, S.; Bentolila, L. A.; Li, J. Q.; Rao, J. H.; Chen, X. Y.; Banin, U.; Wu, A. M.; Sinclair, R.; Weiss, S.; Gambhir, S. S., Particle Size, Surface Coating, and PEGylation Influence the Biodistribution of Quantum Dots in Living Mice *Small* **2009** 5 126-134.

24. Betancourt, T.; Brown, B.; Brannon-Peppas, L., Doxorubicin-loaded PLGA nanoparticles by nanoprecipitation: preparation, characterization and *in vitro* evaluation. *Nanomedicine* **2007,** 2, (2), 220-232.

25. Kreibig, U.; Vollmer, M., *Optical Properties of Metal Clusters* Springer: Berlin, Germany, 1995 Vol. 25.

26. Horovitz, O.; Mocanu, A.; Tomoaia, G.; Bobos, L.; Dubert, D.; Daian, I.; Yusanis, T.; Tomoaia-Cotisel, M., Lysine mediated assembly of gold nanoparticles. *Studia Universitatis Babes-Bolyai, Chemia* **2007,** 52, (1), 97-108.

27. Xu, L.; Guo, Y.; Xie, R.; Zhuang, J.; Yang, W.; Li, T., Three-dimensional assembly of Au nanoparticles using dipeptides. *Nanotechnology* **2002,** 13, (6), 725-728.

28. Selvakannan, P. R.; Mandal, S.; Phadtare, S.; Pasricha, R.; Sastry, M., Capping of Gold Nanoparticles by the Amino Acid Lysine Renders Them Water-Dispersible. *Langmuir* **2003,** 19, (8), 3545-3549.

29. Lim, I. I. S.; Ip, W.; Crew, E.; Njoki, P. N.; Mott, D.; Zhong, C.-J.; Pan, Y.; Zhou, S., Homocysteine-mediated reactivity and assembly of gold nanoparticles. *Langmuir* **2007,** 23, (2), 826-833.

30. Basu, S.; Pal, T., Glutathione-induced aggregation of gold nanoparticles: electromagnetic interactions in a closely packed assembly. *Journal of Nanoscience and Nanotechnology* **2007,** 7, (6), 1904-1910.

31. Ofir, Y.; Samanta, B.; Rotello, V. M., Polymer and biopolymer mediated self-assembly of gold nanoparticles. *Chemical Soceity Reviews* **2008,** 37, (9), 1814-1825.

32. Boal, A. K.; Ilhan, F.; DeRouchey, J. E.; Thurn-Albrecht, T.; Russell, T. P.; Rotello, V. M., Self-assembly of nanoparticles into structured spherical and network aggregates. *Nature* **2000,** 404, (6779), 746-748.

33. Gopidas, K. R.; Whitesell, J. K.; Fox, M. A., Nanoparticle-Cored Dendrimers: Synthesis and Characterization. *Journal of the American Chemical Society* **2003,** 125, 6491-6502.

34. Gindy, M. E.; Panagiotopoulos, A. Z.; Prud'homme, R. K., Composite Block Copolymer Stabilized Nanoparticles: Simultaneous Encapsulation of Organic Actives and Inorganic Nanostructures. *Langmuir* **2008,** 24, (1), 83-90.

35. Katherine C. Grabar; Keith J. Allison; Bonnie E. Baker; Robin M. Bright; Kenneth R. Brown; R. Griffith Freeman; Audrey P. Fox; Christine D. Keating; Michael D. Musick; Natan, M. J., Two-dimensional arrays of colloidal gold particles: a flexible approach to macroscopic metal surfaces. *Langmuir* **1996,** 12, 23535-2361.

36. DeVries, G. A.; Brunnbauer, M.; Hu, Y.; Jackson, A. M.; Long, B.; Neltner, B. T.; Uzun, O.; Wunsch, B. H.; Stellacci, F., Divalent Metal Nanoparticles. *Science* **2007,** 315, (5810), 358-361.

37. Khlebtsov, B.; Zharov, V.; Melnikov, A.; Tuchin, V.; Khlebtsov, N., Optical amplification of photothermal therapy with gold nanoparticles and nanoclusters. *Nanotechnology* **2006,** 17, (20), 5167-5179.

38. Aaron, J.; Nitin, N.; Travis, K.; Kumar, S.; Collier, T.; Park, S. Y.; Jose-Yacaman, M.; Coghlan, L.; Follen, M.; Richards-Kortum, R.; Sokolov, K., Plasmon resonance coupling of metal nanoparticles for molecular imaging of carcinogenesis in vivo. *Journal of Biomedical Optics* **2007,** 12, (3), 034007/1-034007/11.

39. Sokolov, K. V.; Follen, M.; Aaron, J.; Pavlova, I.; Malpica, A.; Lotan, R.; Richards-Kortum, R., Real-time vital optical imaging of precancer using anti-epidermal growth factor receptor antibodies conjugated to gold nanoparticles. *Cancer Research* **2003,** 63, 1999-2004.

40. Herrera, A. P.; Resto, O.; Briano, J. G.; Rinaldi, C., Synthesis and agglomeration of gold nanoparticles in reverse micelles. *Nanotechnology* **2005,** 16, S618-S625.

41. Troutman, T. S.; Barton, J. K.; Romanowski, M., Biodegradable plasmon resonant nanoshells. *Advanced Materials* **2008,** 20, (13), 2604-2608.

42. Vasir, J. K.; Labhasetwar, V., Biodegradable nanoparticles for cytosolic delivery of therapeutics. *Advanced Drug Delivery Reviews* **2007,** 59, (8), 718-728.

Chapter 6: Kinetic Assembly of Near-IR Active Gold Nanoclusters Using Weakly Adsorbing Polymers to Control Size

Clusters of metal nanoparticles, with an overall size less than 100 nm and high metal loadings for strong optical functionality, are of interest in various fields including microelectronics, sensors, optoelectronics and biomedical imaging and therapeutics. Herein we assemble ~5 nm gold particles into clusters with controlled size, as small as 30 nm and up to 100 nm, which contain only small amounts of polymeric stabilizers. The assembly is kinetically controlled with weakly adsorbing polymers, PLA(2K)-*b*-PEG(10K)-*b*-PLA(2K) or PEG (MW = 3350), by manipulating electrostatic, van der Waals (VDW), steric, and depletion forces. The cluster size and optical properties are tuned as a function of particle volume fractions and polymer/gold ratios to modulate the interparticle interactions. The close spacing between the constituent gold nanoparticles and high gold loadings (80-85% w/w gold) produce a strong absorbance cross section of $\sim 9\times10^{-15}$ m^2 in the NIR at 700 nm. This morphology results from VDW and depletion attractive interactions that exclude the weakly adsorbed polymeric stabilizer from the cluster interior. The generality of this kinetic assembly platform is demonstrated for gold nanoparticles with a range of surface charges from highly negative to neutral, with the two different polymers.

6.1 INTRODUCTION

Optical and electronic properties of 1D[1], 2D, and 3D clusters of metal nanocrystals, 20 to 500 nm in diameter, have been studied extensively, especially for applications involving sensors, memory devices, microelectronics[2-4], and more recently, for cellular imaging and therapy[5-9]. For a variety of applications, robust and broadly applicable synthetic strategies are needed to pack high levels of functionality (i.e. high metal loadings) into clusters with an overall size smaller than ~30 to 100 nm. Most often, clusters are formed by thermodynamic self assembly. Rotello and co-workers developed a "bricks and mortar" technique for the templated assembly of metal nanoparticles into clusters using polymers, proteins, and DNA[2, 10] and Glotzer et al. have demonstrated assembly with polymer-tethered nanoparticles[11]. Gold nanoparticles have been assembled in the cores of block copolymer micelles[12-15] and on the surface of micelles[16, 17]. Amphiphilic gold Janus spheres, containing hydrophobic and hydrophilic domains self-assemble into clusters[18-21] upon manipulation of pH or solvent quality. For clusters formed thermodynamically, high concentrations of templating agents and strong interactions between these agents and the particles are typically required to drive the self-assembly. Consequently, these agents are usually highly retained in the final cluster and limit the metal loading, typically well below 50% w/w.

An alternative approach is to form clusters of metal nanoparticles by kinetic assembly to achieve extremely high metal loadings by manipulating van der Waals (VDW), electrostatic, and steric interactions. For example, variation of pH or ionic strength of dilute dispersions of citrate-capped gold nanoparticles screens electrostatic repulsion and induces cluster growth[22, 23]. Similarly, lysine-[24-27] and cysteine-[28] capped gold nanoparticles at high loadings aggregate reversibly in response to changes in charge with pH. Gold nanoparticles coated with associating proteins, such as biotin and streptavidin[29], or with complementary DNA strands[30, 31] also form clusters. However, in each of these cases, uncontrolled growth often yields irregularly shaped aggregates greater than several hundred nanometers in diameter. Therefore, a conflict arises in both thermodynamically- and kinetically-controlled assembly between the need for sufficient levels of stabilizers to arrest growth to produce small sub-100 nm clusters, while simultaneously achieving high metal loadings for high functionality.

Metal nanoparticles with high NIR absorbance are of great interest in biomedical imaging and therapy because soft tissues and water are relatively transparent from 650 to 900 nm. The surface plasmon resonance (SPR) of a spherical gold particle exhibits a maximum at 530 nm, but undergoes a red shift to the NIR for particles with a hollow or non-spherical geometry, such as nanoshells[32-34], nanorods[35, 36], and nanocages[37, 38]. These particles are typically 50-100 nm in diameter. NIR absorbance has rarely been achieved for particles smaller than 50 nm, where it becomes challenging to synthesize the types of asymmetric morphologies needed for strong red-shifts[39]. Significant NIR absorbance also has been demonstrated *in vitro* and *in vivo* for the assembly of 40 nm gold spheres, conjugated with antibodies, by receptors in cancer cells into clusters[5, 6, 40]. Small gold clusters that have been formed by equilibrium self assembly methods often contain high concentrations of templating agents, which result in particle separations greater than one particle diameter and thus small red shifts[41, 42].

Nanoparticle components may be assembled into clusters with properties that are challenging to achieve including, sizes below 50 nm[3, 7, 12, 43], strong optical absorbance[7, 43], multifunctionality[7], and/or biodegradability[9, 43]. Recently, there has been great interest in the development of sub-30 nm particles, which penetrate cell membranes and leaky vasculature in cancerous tumors more efficiently than particles >50 nm[44-48]. Furthermore, these small nanoparticles elicit profound changes in biological pathways in targeted cells. Sub-30 nm particles have been reported for gold nanocages[49] and multifunctional nanocluster hybrids containing gold and iron oxide, referred to as nanoroses[7]. Despite their small sizes, both types of nanoparticles absorb strongly in the NIR. The nanorose clusters, composed of nanocomposite primary particles, are formed by kinetic assembly during the reduction of gold precursors onto iron oxide nanoparticles. They exhibit intense magnetic relaxivity as well as NIR absorbance[7]. To further advance the functional properties in nanoclusters, especially biodegradability, we recently introduced a physical, rather than chemical, method for the kinetically controlled colloidal assembly of ~5 nm gold spheres into ~100 nm NIR plasmonic clusters stabilized by PLA(2K)-*b*-PEG(10K)-*b*-PLA(2K). These clusters were shown to biodegrade nearly completely in solution and in macrophage cells back to the original 5 nm primary spheres, which are small enough for renal clearance [9]. This physical, kinetic, colloidal assembly method is general and likely to enable synthesis of many types of clusters over a wide size range.

Herein we assemble kinetically sub-5 nm gold particles into clusters of controlled sizes, as small as 30 nm and up to 100 nm, stabilized by small amounts of a weakly adsorbing polymer, either PLA-*b*-PEG-*b*-PLA or PEG 3350. The physical cluster assembly process, introduced recently in Tam et al.[9], is illustrated in Fig. 6.1. The gold nanoparticles are nucleated rapidly at high volume fractions in the presence of a weakly adsorbing polymer to form small clusters[9]. The nucleation and growth of the gold clusters is controlled by increasing gold and polymer concentrations simultaneously, either by solvent evaporation or by mixing of a concentrated gold dispersion with a concentrated polymer solution. A mechanism is presented to describe the cluster growth and gold particle spacing in terms of the electrostatic, VDW, steric and depletion forces. The combination of high gold particle volume fractions and exclusion of the weakly adsorbed polymeric stabilizer from the cluster interior towards the exterior surface are utilized to produce low polymer loadings and closely spaced gold particles for strong NIR absorbance. In contrast, high polymer loadings and larger gold particle spacings are typically obtained in equilibrium assembly processes that rely on strong interactions with templating agents, such as micelles[12-17, 50, 51]. Finally, the small amount of polymer on the exterior surface provides sufficient steric stabilization to prevent unregulated cluster growth, in contrast with previous studies without polymer stabilizers[23-28]. Relative to our previous study[9], the size of the clusters is over three fold smaller, and furthermore, a wider range of ligands (to modify particle charge), polymers, and polymer/gold ratios are examined. An advantage of this kinetic assembly approach is its use of readily available polymer stabilizers and simple ligands on the gold surface, such as citrate and lysine, in contrast to templating agents that often require complicated synthetic approaches.

6.2 EXPERIMENTAL

6.2.1 Materials

$HAuCl_4•3H_2O$ was purchased from MP Biomedicals LLC (Solon, OH) and $Na_3C_3H_5O(COO)_3$ •2 H_2O and $NaBH_4$ were acquired from Fisher Scientific (Fair Lawn, NJ). L(+)-lysine was obtained from Acros Chemicals (Morris Plains, NJ). PEG (MW=3350) was ordered from Union Carbide (Danbury, CT) and PLA(2K)-*b*-PEG(10K)-*b*-PLA(2K) was purchased from Sigma Aldrich (St. Louis, MO).

6.2.2 Nanocluster formation

Gold nanoparticles (3.8-nm) stabilized with citrate ligands were synthesized based on a well known method[52]. Briefly, DI water (100 mL) was heated to 97°C. While stirring, 1 mL of 1% $HAuCL_4•3H_2O$, 1 mL of 1% $Na_3C_3H_5O(COO)_3$ •2 H_2O, and 1 mL of 0.075% $NaBH_4$ in a 1% $Na_3C_3H_5O(COO)_3•2\ H_2O$ solution were added in 1 minute intervals. The solution was stirred for 5 minutes and then removed to an ice bath to cool to room temperature. The gold particles were then centrifuged at 10,000 rpm for 10 minutes at 4°C to remove any large aggregates. Centrifugal filter devices (Ultracel YM-30, Millipore Co.) were used to removed unadsorbed citrate ligands as well as concentrate the gold dispersion to ~3.0 mg Au/mL. Gold concentrations were determined using flame atomic absorption spectroscopy (FAAS).

In most cases, lysine ligands were added to the citrate stabilized gold nanoparticles by adding a 1% lysine in pH 8.4 phosphate buffer (10 mM) solution to 1.2 mL of the colloidal citrate-capped gold solution to yield a final lysine and gold concentration of 0.4 mg/mL and 3.0 mg/mL, respectively. In the cases where a 1.0 mg/mL gold solution was used to produce nanoclusters, the 3.0 mg/mL stock gold solution was diluted using deionized (DI) water. The dispersion was stirred for at least 12 hours[25, 53]. PLA-*b*-PEG-*b*-PLA was added to the aqueous dispersion of ligand capped gold nanoparticles to yield polymer/gold ratios ranging from 1/10 – 40/1. The dispersions were then sonicated in a bath sonicator for 5 minutes. Unless otherwise noted, the concentration of the gold solutions used in this study to produce nanoclusters was 3.0 mg/mL with a polymer/gold ratio of 16/1.

In some cases, the polymer/gold dispersion was placed under an air stream and a certain percentage of the solvent, between 50-100%, was evaporated. When the dispersion was not dried to completion, it was quenched with DI water after the chosen amount of solvent evaporation. Upon quenching, the concentration of the dispersion was approximately an order of magnitude lower than that of the original gold stock prior to solvent evaporation. In the case of 100% solvent evaporation, which took place over ~20-30 minutes, the dried film was redispersed with 10 mL of DI water to yield a blue dispersion of ~0.30 mg Au/mL. Nanoclusters were also formed using a mixing procedure, in which highly concentrated solutions of gold colloid and polymer were mixed together using a probe sonicator (Branson Sonifier 450, Branson Ultrasonics Corporation, Danbury, CT) with a 102 converter and tip operated in pulse mode at 35 W.

6.2.3 Nanocluster characterization

Nanocluster morphology was observed by transmission electron (TEM) and scanning electron microscopy (SEM). TEM was performed on a FEI TECNAI G2 F20 X-TWIN TEM using a high-angle annular dark field detector. TEM samples were prepared using a "flash-freezing" technique, in which a 200 mesh carbon-coated copper TEM grid was cooled using liquid nitrogen and then dipped into a dilute aqueous nanocluster dispersion. The TEM grid was dried using a Virtis Advantage Tray Lyophilizer (Virtis Company, Gardiner, NY) with 2 hours of primary drying at -40°C followed by a 12 hour ramp to +25°C and then 2 hours of secondary drying at 25°C. Separation distances between primary particles within the nanoclusters were measured by analyzing TEM images using Scion Image software (Frederick, Maryland). A Zeiss Supra 40VP field emission SEM was operated at an accelerating voltage of 5−10 kV. SEM samples were prepared by depositing a dilute aqueous dispersion of the nanoclusters onto a silicon wafer. The sample was dried in a hood, washed with DI water to remove excess polymer, and dried again. UV−visible spectra were measured using a Varian Cary 5000 spectrophotometer for a 1 cm path length. Dynamic light scattering (DLS) measurements of hydrodynamic diameter and zeta potential measurements were performed in triplicate on a Brookhaven Instruments ZetaPlus dynamic light scattering apparatus at a scattering angle of 90° and temperature of 25 °C[54]. Dispersion concentrations were adjusted with either DI water for DLS measurements or pH=7.4 buffer (10 mM) for zeta potential measurements to give a measured count rate between 300-400 kcps. For DLS measurements, all dispersions were filtered through a 0.2 µm filter and probe sonicated for 2 min prior to measurement. The data were analyzed using a digital autocorrelator (Brookhaven BI-9000AT) with a non-negative least-squares (NNLS) method (Brookhaven 9KDLSW32). A distribution of hydrodynamic diameters was obtained based on the Stokes-Einstein equation for the diffusion coefficient of a sphere. All distributions were weighted by volume. Reported average diameters correspond to the D_{50}, or diameter at which the cumulative sample volume was under 50%. For zeta potential measurements, the average value of at least three data points was reported. Thermogravimetric analysis (TGA) was used to determine the amount of adsorbed ligand mass on the primary gold nanoparticles and the final polymer/gold ratio of the nanoclusters. TGA was performed using a Perkin–Elmer TGA 7 under nitrogen atmosphere at a gas flow rate of 20 mL/min. Excess, unadsorbed organic material, either ligands and/or polymer, was removed from particles, either colloidal gold or nanoclusters, by centrifuging the dispersions at 10,000 rpm for 5 minutes at 4^{o}C. For the colloidal gold particles, which were too small to settle efficiently during centrifugation, centrifugal filter devices were used to separate and filter the particles from the smaller unadsorbed ligands. The supernatants were discarded and the pellets were dried to a powder. The powder samples were held at 50°C for 120 minutes to remove any moisture in the sample and then heated at a constant rate of 20 °C/min from 50°C to 800 °C and held at 800°C for 30 minutes. The loss in mass after heating accounted for the organic component of the particles. Flame atomic absorption spectroscopy (FAAS) was used to determine the gold concentration in the dispersion and the yield for the gold particles that were incorporated into the clusters. A GBC 908AA flame atomic absorption spectrometer (GBC Scientific Equipment Pty Ltd) was used to determine the amount of gold present in a sample. All measurements were conducted at 242.8 nm using an air-acetylene flame. To determine clustering efficiency, a dispersion of nanoclusters of known concentration was centrifuged at 10,000 rpm for 10 minutes at 4^{o}C. FAAS measurements were conducted on the supernatant.

6.2.4 Determination of stability ratio and half-life for aggregation

The stability of the nanoparticles may be quantified using a stability ratio, *W*, defined as the ratio of the rate of fast, diffusion controlled aggregation to slow, kinetically-controlled aggregation[23, 55]. Alternately, *W* may also be determined using the respective half-lives for fast and slow aggregation.

$$W = \frac{k_f}{k_s} = \frac{t_{1/2,s}}{t_{1/2,f}} \tag{6.1}$$

where k_f and k_s are the rate constants for fast and slow flocculation, respectively, and $t_{1/2,f}$ and $t_{1/2,s}$ are the half-lives for fast and slow flocculation, respectively. The half life for fast, diffusion-controlled aggregation according to Smoluchowski[23, 55] is given as:

$$t_{1/2,f} = \frac{3\eta}{4k_b T N_0} \tag{6.2}$$

where η is the solution viscosity, k_B is the Boltzmann constant, T is temperature, and N_0 is the initial number density of nanoparticles. Slow flocculation half-lives were estimated experimentally based on the observed time required for a visual color change in the nanocluster dispersion to occur, t_{col}. The observed t_{col} may be used to estimate half-lives using the assumption that a color change corresponds to the collision of 11 particles[56] and solving the equation for second order reaction kinetics, $1/N(t) = kt + 1/N_0$, to yield:

$$t_{1/2,s} = t_{col}/10 \tag{6.3}$$

where N is the number of particles in the system at time, t, and k is the reaction rate constant.

6.3 RESULTS

6.3.1 Effect of particle volume fraction on nanocluster size and optical properties

The amount of ligands on the surface of the gold particles was determined prior to the formation of nanoclusters. For the red citrate-capped gold nanoparticles, the average diameter was 3.8 ± 1.0 nm (data not shown) and the zeta potential was -44.0 ± 4.7 mV (Table 6.1) at a pH of ~7.2. The citrate coverage on the gold nanoparticles was estimated to be about 6.3% w/w, based on calculations assuming saturated ligand coverage on the 4 nm gold particle surface, in good agreement with the 7% w/w citrate measured by TGA(See supplementary). The adsorption of lysine to gold did not significantly change the particle size, which was 4.1 ± 0.8 nm (Fig. 6.2a), nor the pH of the gold dispersion. Lysine contains two NH_3^+ charges and one COO^- charge over a pH range from 3 to 10 [25] (Appendix D Fig. D.1). The ligand exchange with the positively charged lysine increased the zeta potential to -30.1 ± 2.4 mV (Table 6.1), indicating about 30% of the adsorbed citrate was exchanged(See supplementary). The citrate/lysine-capped particles were coated with 11% total ligand, according to TGA results, compared with 7% for the citrate-only stabilized nanoparticles. The color did not vary for the citrate-only and citrate/lysine-capped gold nanoparticle dispersions for ~1 month, corresponding to a very high W of $\sim 7\times10^9$ (Table 6.2) for an N_0 of $\sim 10^{21}$ particles/m^3 and $t_{1/2,f}$ of 3.93×10^{-5} s, which is based on a gold loading of 3 mg/mL. The high stability is due to strong repulsive charges on the ligands of the particles, in good agreement with previous reports in literature[25, 57].

To form gold clusters, interactions between citrate/lysine gold particles were mediated with a weakly adsorbing polymer, either PLA-*b*-PEG-*b*-PLA, as shown in Fig. 6.1, or PEG (MW=3350) homopolymer. Without any solvent evaporation, the addition of either polymer to the ligand-capped gold particles at a 16/1 polymer/gold ratio (gold concentration = 3 mg/mL) did not produce a color change over a period of one hour, indicating that clusters of closely-spaced gold were not formed[9]. After an hour, the color slowly changed. A one hour stability (t_{col} =1 hr) corresponds to a maximum W of ~4×10^5, as determined from Eqs. 1-3 (Table 6.2). To more fully probe the kinetics of nanocluster formation, the nanocluster size was monitored as a function of solvent evaporation by quenching cluster growth with the addition of DI water after a specified level of solvent evaporation. The harvested nanoclusters were observed by TEM (Fig. 6.2) and their sizes determined by DLS (Fig. 6.3a). For PLA-*b*-PEG-*b*-PLA, the formation of dimers and trimers was detected, indicating nucleation, after 50% solvent evaporation (Figs. 6.2, 6.3a), which occurred over ~5 minutes for a 1.4 mL sample. This time corresponds to a maximum W of ~2.5×10^5, as $t_{1/2,s}$ could have been even smaller than 5 minutes. These small oligomers produced a shoulder in the DLS size distribution. When the suspension, from which 50% of the solvent had been evaporated, was allowed to sit over the course of one week, still no color change was observed, indicating that the oligomers did not grow to produce larger clusters. However, additional solvent reduction to 60% evaporation, approximately one minute later, led to clusters 35-60 nm in size, as seen both by TEM and DLS. Further solvent evaporation, to 80% and 100%, produced additional growth, with D_{50} values of 60 nm and 80 nm, respectively, with low polydispersities between 1.1-1.8 (See supplementary for calculation). From 50 to 95% evaporation, the cluster size was monotonic with the extent of evaporation. Yields of gold in the clusters, or the percent of the loaded primary particles that are incorporated into clusters after quenching the growth, was determined using FAAS (Table 6.3). After 60% and 100% solvent evaporation, 95.1% and 99.7%, respectively, of the initially loaded gold nanoparticles by mass were incorporated into clusters. Therefore, cluster yields, as well as size, continued to increase with the extent of solvent evaporation. The ability to tune the cluster size over a wide range and to achieve low polydispersities is of great scientific and practical interest.

Extents of solvent evaporation greater than 60% resulted in a color change of the dispersion to blue, but it was difficult to observe the kinetics given the dark, opaque dispersions at the high volume fractions. Thus, the spectra were measured after the clusters were quenched by dilution. The red shifts in the absorbance to the NIR were consistent with the morphologies observed by TEM and the sizes measured by DLS. Before polymer was added, the characteristic spectrum for individual gold particles exhibited a maximum at 530 nm (Fig. 6.3b). For the dimers and trimers (Fig. 6.2b), the red-shift was modest as expected[41, 42, 58]. Much larger shifts were observed for 60% evaporation (Fig. 6.3b), where sizable clusters of 35-60 nm were observed by TEM and DLS, as expected from theoretical calculations[41, 42, 58]. The NIR absorbance continued to increase as the extent of evaporation and nanocluster size increased.

Complete solvent evaporation produced a smooth blue film on the glass surfaces of the vials, indicating a shift in the absorbance spectra of gold to the NIR. Reconstitution of the film with DI water yielded a dark blue dispersion of sub-100 nm clusters composed of primary gold nanoparticles (Fig. 6.2). SEM images of nanoclusters formed after 100% solvent evaporation reveal a polymer-rich shell a few nanometers thick surrounding the exterior of each cluster. The spectra of the nanoclusters formed after 100% solvent evaporation exhibited a broad, relatively constant, absorbance in the important NIR region from 700 to 900 nm, corresponding to an extinction coefficient at the maximum absorbance, $\varepsilon_{703,}$ of 0.017 $cm^2/\mu g$ for a 56 μg/mL gold dispersion. Assuming that the gold nanoparticles occupy ~72% of the cluster volume (based on SEM and TEM images in Fig. 6.2), characteristic of a closest-packed volume fraction, the estimated particle extinction cross section was 9.0×10^{-15} m^2 (See supplementary), comparable to the value for nanoshells[41], nanocages[38], nanorods[41], and nanoroses[7]. The mean spacing between primary gold particles within the clusters was estimated to be 1.80 ± 0.6 nm based on the more discernible particles in the periphery of TEM images, well within the range of interparticle spacing known to produce a significant red-shift in the

SPR (Appendix D Fig. D.2)[1, 41, 42]. The ability of the gold nanoparticles to pack tightly together is supported by TGA results, which indicated that after 100% solvent evaporation, nanoclusters contained only 20 ± 5% organic material. From the known amount of ligand reported above, 10-15% of this material was polymer. The ability to reproducibly produce nanoclusters using 100% evaporation, with respect to both size and optical properties, is shown in Appendix D Fig. D.3. The zeta potentials of the resultant nanoclusters of citrate-only and citrate/lysine-capped nanoparticles were -13.0 ± 3.3 mV and -16.3 ± 4.0 mV, respectively, approximately half that of the initial colloidal gold nanoparticles (Table 6.1). Interestingly, the zeta potential of clusters formed using citrate-only and citrate/lysine-capped gold, stabilized with PLA-*b*-PEG-*b*-PLA, had similar zeta potential values, somewhat larger than that of the pure polymer. The value of -8.0 ± 0.2 mV for the PLA-*b*-PEG-*b*-PLA polymer is attributed to the ionized PLA end groups.

Nanoclusters were also formed using PEG (MW=3350), instead of PLA-*b*-PEG-*b*-PLA, as the stabilizing polymer. The PEG-stabilized clusters were, on average, ~1.5 times larger than those stabilized using PLA-*b*-PEG-*b*-PLA, as reported by DLS and TEM (Fig. 6.4a-c). Similar to observations for PLA-*b*-PEG-*b*-PLA-stabilized clusters, a reduction in solvent evaporation from 100% to 60% yielded a ~30% reduction in cluster size and slightly lower NIR absorbances. The strong NIR absorbance of the PEG-stabilized clusters indicated that tight packing of gold nanoparticles within the cluster was achieved (Fig. 6.4d). In fact, the clusters formed at 60% solvent evaporation show a slightly stronger NIR peak than the clusters formed after 60% solvent evaporation using PLA-*b*-PEG-*b*-PLA, likely due to the larger cluster size. Similar trends were obtained for nanoclusters produced using citrate-only capped gold nanoparticles and PEG 3350 (data not shown).

6.3.2 Clusters of lysine/citrate particles with PLA-b-PEG-b-PLA formed by mixing

Assembly of nanoclusters was also demonstrated without solvent evaporation by mixing together highly concentrated gold and polymer solutions. The resulting concentrations of gold particles and polymer corresponded to those achieved by certain solvent evaporation extents. For example, a 6 mg/mL dispersion of gold nanoparticles was mixed with a 100 mg/mL polymer solution to produce clusters that were equivalent to the concentrations achieved after 50% evaporation. However, the cluster sizes were at least 2.5 times larger than those where the particle volume fractions were increased gradually by solvent evaporation (Fig. 6.5a). Because of their larger sizes, nanoclusters produced by this method displayed even more shifted NIR absorbance (Fig. 6.5b). Similar trends in optical properties were observed when clusters of citrate-only-capped gold nanoparticles were produced using this mixing method (Appendix D Fig. D.4). The high viscosities of the extremely concentrated polymer solutions, ranging from 9×10^{-4} Pa s (~10 times that of water) to 0.8 Pa s (~900 times that of water) for solutions corresponding to 60% and 90% solvent evaporation (Appendix D Fig. D.5), respectively, resulted in inadequate mixing rates, poorer polymer diffusion, and thus the larger clusters.

6.3.3 Clusters formed with citrate-only capped particles and PEG-SH coated particles

Nanoclusters were produced using gold nanoparticles capped with two other types of ligands: negatively charged citrate, and neutral PEG-SH to compliment the above studies which used lysine (positively charged) and citrate ligands, simultaneously. Clusters of gold primary particles capped with either citrate or a citrate/lysine mixture exhibited strong NIR absorbance (Fig. 6.6). However, nanoparticles capped with PEG-SH did not produce a significant red-shift, although the shift was larger for PEG-SH with a MW of 0.13K versus 5K. PEG-SH 5K has a reported radius of gyration of 3.1 nm[59]. Therefore, the corresponding particle separations between two PEG-SH coated particles of at least 6.2 nm is larger than the diameter of a gold primary particle and the strongly bound PEG-SH 5K ligands prevented the gold nanoparticles from packing together tightly enough for a strong red shift.

Relative to citrate/lysine-capped particles, very similar behavior was observed for clusters assembled with citrate-only capped gold nanoparticles and PLA-*b*-PEG-*b*-PLA upon solvent evaporation, according toDLS, TEM, and UV-vis/NIR measurements (Appendix D Fig. D.6). Again, there was a very strong correlation between cluster size and NIR absorbance. However, the clusters did not form until ~ 85% solvent evaporation, as compared to 60% for citrate/lysine capped gold (Fig. 6.7). The greater repulsion for the citrate-only-capped particles, as is evident in the more negative zeta potentials, appeared to delay cluster formation. The slightly smaller sizes and larger SPR red-shifts of the nanocluster composed of citrate/lysine nanoparticles may be influenced by the attractive electrostatic attraction between the positive and negative charges on the lysine (Appendix D Fig. D.1)[25]. These interactions may further promote polymer exclusion from the cluster interior.

6.3.4 Tuning cluster size with polymer/gold ratio

To demonstrate the ability to tune the cluster size, the gold loading was lowered to 1.0 mg/mL, compared to 3.0 mg/mL in our previous study[9], and the polymer/gold ratio was varied over a wide range for 100% solvent evaporation. Cluster sizes decreased considerably as polymer/gold ratios were reduced from 16/1 to 1/1 (Fig. 6.8a), with an average diameter of 28.4 nm for the 1/1 ratio. Despite the reduction in cluster size, clusters produced at a polymer/gold ratio between 1/1 to 16/1 still exhibited a broad and intense NIR absorbance, similar to that shown in Fig. 6.3b. However, for polymer/gold ratios below 1/1, the absorbance did not shift significantly from that of colloidal gold

(Fig. 6.8b). For a given polymer/gold ratio, similar results were obtained for the cluster size and spectra for the higher gold loading of 3.0 mg/mL, as shown in Appendix D Fig. D.7, although the sizes were slightly smaller for the 1.0 versus the 3.0 mg/mL loading. As an example of the extent by which the cluster sizes could be tuned, the much smaller clusters formed with a 1/1 polymer/gold ratio at a gold loading of 1.0 mg/mL versus a 16/1 polymer/gold ratio at a 3.0 mg/mL loading is shown in TEM micrographs (Fig. 6.8c-d). Additionally, a small decrease in the absorbance spectra was observed for clusters formed at a 40/1 polymer/gold ratio and a 3.0 mg/mL gold loading (Appendix D Fig. D.7b). Here, an extremely high polymer concentration of 1200 mg/mL was generated when the level of solvent evaporation reached 90%, resulting in excessive polymer that likely interfered with close-spacing between the gold nanoparticles, and thus, lowered the red shift[42]. This interference was not present for lower polymer/gold ratios. Further decreasing gold loadings as low as 0.19 mg/mL and increasing the polymer/gold ratio up to 260/1 led to the formation of increasingly larger clusters with reduced NIR absorbance (Appendix D Table D.1, Fig. D.8). Nanoclusters produced at a 1/1 gold/polymer ratio and a 1.0 mg/mL gold concentration were approximately 85% gold w/w, comparable to 80% w/w gold in nanoclusters formed with a 16/1 gold/polymer ratio and a starting gold concentration of 3.0 mg/mL, as determined by TGA.

6.4 DISCUSSION

6.4.1 Interaction potential and stability ratio

The kinetic assembly of nanoparticles into clusters may be controlled by adjusting the stability ratio for a pair of particles, which is dependent upon the total interaction potential between particles:

$$V_{\text{total}} = V_{\text{electrostatic}} + V_{\text{VDW}} + V_{\text{steric}} + V_{\text{depletion}} \tag{6.4}$$

The first two terms are described by DLVO theory, as discussed in the supplementary section. The addition of a weakly or non-adsorbing polymer introduces attractive depletion interactions, which arise from the exclusion of polymer from the gap region between two particle surfaces. The depletion potential for hard sphere colloids and polymers treated as "penetrable hard spheres" is given by[60-62]:

$$\frac{V_{\text{depletion}}(H)}{k_bT} = -\rho_\infty \pi\left[\frac{4}{3}r^3 + 2r^2a - r^2H - 2raH + \frac{aH^2}{2} + \frac{H^3}{12}\right], 0 \le H < 2r \tag{6.5}$$

where H is the distance between particle surfaces, r is the polymer radius, a is the nanoparticle radius, and ρ_∞ is the number density of polymer particles in solution. If the polymer forms micelles, the micellar properties are used (See supplementary). The ability of depletion forces to cause particle flocculation, and even phase separation, in colloid-polymer mixtures is well known both experimentally and theoretically[63-65]. The kinetic stability ratio, in terms of V_{total}, is described by [55]

$$W = 2a\int_{2a}^{\infty} \frac{\frac{D_\infty}{D(u)}\left[\exp\left(\frac{V_{\text{total}}}{k_bT}\right)\right]}{H^2} dH \tag{6.6}$$

where u is a dimensionless variable defined as $(H-2a)/a$, and the ratio $D_\infty/D(u)$ is the hydrodynamic correction factor:

$$\frac{D_\infty}{D(u)} = \frac{6u^2 + 13u + 2}{6u^2 + 4u} \tag{6.7}$$

The first parts of the discussion section compare the kinetically controlled nanocluster assembly with previous studies based on the terms for V_{total} and the manipulation of the particle concentrations. A quantitative expression is not presented herein for V_{steric}, given the complexity of hydration of PEG at high concentrations where gels are formed.

6.4.2 Cluster assembly in the absence of polymer (VDW and electrostatic forces)

In the absence of a polymer, the VDW and electrostatic terms play a primary role in cluster formation, whereas steric and depletion interactions are small. Electrostatic repulsion of the nanoparticles may be weakened by a change in pH or salinity to reduce the charge. For dilute dispersions of gold coated with citrate (0.1 mg gold/mL), the growth from attractive VDW forces may be controlled over a period of hours to form clusters >100 nm in size[22, 23]. For these dilute conditions, the clusters are typically relatively low density with a low fractal dimension. In contrast, clusters formed at high particle concentrations are more likely to be composed of gold particles with close spacing that favors strong NIR absorbance. However, for concentrated gold dispersions (20-50 mg/mL), it becomes difficult to balance the electrostatic repulsion and VDW attraction to control the growth, and substantial aggregation has been observed over a period of several minutes[25]. For instance, when gold nanoparticles are capped with lysine ligands, a change in pH simultaneously produces both positive and negative charges (Appendix D Fig. D.1) that result in electrostatic attraction and irregularly shaped aggregates up to several microns in diameter[22, 24-27]. Additional concepts in kinetic assembly are needed to better control V_{total} and thus the particle size and gold spacing

6.4.3 Cluster assembly in the presence of polymer

The key challenge in this study was to control nanocluster size and gold particle spacing within the clusters by manipulation of the particle concentration pathways and V_{total}. High gold particle concentrations (>>0.1 mg/mL) were utilized in order to achieve sufficiently close gold particle spacing for strong NIR absorbance. However, they can also cause unmitigated cluster growth. This dilemma was addressed by the addition of a weakly adsorbing polymer to manipulate the electrostatic, steric, and depletion forces. The polymer initiates nucleation and growth, while simultaneously providing steric stabilization, but with low final polymer loadings[2, 17, 50].

The initial citrate-only and citrate/lysine-capped gold nanoparticles in this study were extremely stable, evidenced by large negative zeta potentials of -44 and -30 mV, respectively, and a V_{total} of at least 23 k_BT (Fig. 6.9) (See supplementary). Nanocluster formation was initiated by raising the polymer and gold particle concentrations either by solvent evaporation or mixing to raise the adsorption of the polymer on gold. The weakly adsorbed polymer decreases the local dielectric constant near the charged ligands and thus weakens the ion hydration, causing ion pairing. This decrease in particle charge is directly evident in the decrease in the zeta potential with the addition of polymer (Table 6.1). The decrease in electrostatic repulsion causes a marked decrease in the experimentally determined W (Table 6.2) from $\sim 10^{10}$ for the citrate/lysine-capped primary particles to $\sim 10^5$ after the addition of polymer and 50% solvent evaporation. At this condition, the polymer adsorption did not reduce the particle charge enough to produce clusters larger than dimers or trimers within several hours.

At an extent of 50% solvent evaporation, the charge on an individual gold particle was regressed from the theoretical W in Eq. 6.6, given the known experimental W described above (Table 6.2). In this regression, V_{total} included electrostatic, VDW, and depletions terms, as described in the supplementary section. All of the properties were known except the surface potential (and thus surface charge) on a gold nanoparticle. The reduction in the regressed surface charge of 1.6 after 50% solvent evaporation, relative to that of the initial colloidal gold particles, was found to be comparable to the reduction in zeta potential given in Table 6.1. The loss in charge is further characterized by the large decrease in V_{total} to about 11 k_BT (Fig. 6.9), which may be attributed to the significant drop in $V_{electrostatic}$ upon charge reduction caused by the polymer, as V_{VDW} did not change. Thus, this large decrease in $V_{electrostatic}$, and consequently V_{total}, produced a decrease in W at 50% solvent evaporation of 5 orders of magnitude, relative to the initial colloidal gold particles (Fig. 6.10). It was not possible to regress any changes in the particle charge with higher extents of solvent evaporation because the dispersions were too turbid to determine W experimentally. The regressed charge at 50% was used to calculate the $\mathrm{V_{total}}$ and thus W for greater solvent evaporation levels. $\mathrm{V_{total}}$ decreased as solvent evaporation increased, primarily due to a reduction in $\mathrm{V_{electrostatic}}$. Using Eq. 6.6, the steady decrease in $V_{electrostatic}$, and thus V_{total}, with solvent evaporation (i.e. increasing particle volume fraction) was found to cause a further decrease in W (Fig. 6.10). The $V_{electrostatic}$ decreases with an increase in the number density of charged gold nanoparticles as the extent of evaporation increases. For electro-neutrality, the resulting increase in counter-ion concentration reduces the Debye length according to Appendix D Eq. D.10. However this change in $V_{electrostatic}$ changes W by less than an order of magnitude, significantly smaller than the changes observed with polymer induced ion pairing. Therefore, the initial cluster growth is driven primarily by the attractive VDW forces upon reduction of particle charge and electrostatic repulsion upon weak polymer adsorption[63, 66]. As the number of closely-spaced gold particles in the cluster increases, the number of water molecules in the coordination shells about each particle decreases, given that the gold surface is hydrophobic. This decrease in hydration may further contribute to ion pairing and weakened electrostatic repulsion.

The smaller clusters produced using PLA-*b*-PEG-*b*-PLA as a stabilizer versus PEG homopolymer may be attributed to the stronger adsorption of the more hydrophobic PLA-*b*-PEG-*b*-PLA[15, 67], which produces greater charge reduction and thus more rapid nucleation. The larger number of nuclei and greater steric stabilization for reduced growth would lead to small clusters. Furthermore, the presence of micelles for PLA-*b*-PEG-*b*-PLA may provide greater steric stabilization than the homopolymer in the early stages of growth. Similarly, smaller clusters formed for the less charged citrate/lysine-capped gold versus citrate-only capped gold (Fig. 6.7) may also be attributed to more rapid nucleation. In addition, the attractive electrostatic interactions between the lysine ligands may enhance polymer exclusion from the cluster interior.

The decrease in $V_{electrostatic}$ to drive cluster growth may also be achieved simply by adding salts. However, without the steric and depletion contributions to the potential, control over the final cluster size for high initial gold particle concentrations has not been successful[22, 23]. Thus, manipulation of these additional terms with polymer concentration and structure is important to achieve greater control over kinetic self-assembly. The nucleation of clusters via an adsorbed polymer to reduce the surface charge and simultaneously provide steric stabilization enables significantly improved control over cluster growth even with the high gold particle concentrations.

6.4.4 Spacing between gold particles in the nanoclusters

The final polymer weight fraction in the clusters was only on the order of 10 to 15% w/w according to TGA, even with starting polymer/gold ratios well above unity, for example our most common case of 16/1. The small spacing between the gold particles of only 1.80 nm (Appendix D Fig. D.2) for PLA-*b*-PEG-*b*-PLA stabilized nanoclusters is considerably smaller than the size of a PLA-*b*-PEG-*b*-PLA polymer micelle, measured to be 10-14 nm (Appendix D Fig. D.9) or the R_g of the PEG homopolymer of 6.1 nm[68]. Thus, the polymers were excluded from the cluster interior. Various properties of gold contribute to the low polymer loadings, which favor small interparticle distances. The Hamaker constant is 60 k_BT for Au versus only 0.6 k_BT for the PEG, calculated using Lifshitz theory[11]. The gold surface is not highly hydrophilic given that polypropylene oxide adsorbs more strongly to gold than PEG[67]. Thus, the gold particles are strongly attracted to each other by VDW and hydrophobic forces. Additionally, the polymer chains are depleted from the overlap regions in the interior of the clusters towards the cluster exterior in order to raise their conformation entropy, as described by Eq. 6.5. These depletion forces, along with the propensity for hydrophilic PEG segments to orient towards the aqueous exterior, drive the weakly adsorbed and hence highly mobile polymer away from the cluster interior and towards the exterior cluster interface with water and into bulk water. This mechanism is supported by the polymer shell observed in the SEM image (Fig. 6.2f), as well as the low polymer loadings. Thus, the hydrophilic PEG segments of the polymer, which are oriented preferentially towards the exterior cluster interface, extend into the aqueous environment and provide steric stabilization. In essence, the close spacing of the gold particles is driven by the strong VDW attraction between the gold particles and the depletion forces which exclude the polymer.

In the case where a strongly adsorbing polymer is used to regulate cluster formation and growth, the polymer is often retained at significantly higher levels within the final cluster than in the present study. Prud'homme et al. have developed a "flash nanoprecipitation" method to achieve relatively high 35% w/w particle loadings in clusters by inducing high supersaturation with rapid "micro-mixing" to kinetically control nucleation and growth[50, 51]. The polymer adsorption was sufficiently strong to passivate the surface of nucleating particles under high supersaturation conditions to produce clusters as small as 80 nm[50]. However, the resultant clusters did not exhibit a red-shift into the NIR due to the strong interactions between the polymer and the gold, which likely prevented close-packing between the gold particles.

6.4.5 Condensation versus coagulation

Size distribution moments calculated from DLS results (Fig. 6.3a) suggest that the nanoclusters were formed more by condensation than by coagulation, yet some coagulation was present (See supplementary, Table 6.3). A high yield of 95% of gold in the cluster was observed after only 60% solvent evaporation. Here, exhaustion of primary particles slows down nanocluster growth by condensation. The substantial growth in cluster size from 60% to 100% solvent evaporation cannot be caused by the remaining 5% gold, since the mass of the clusters is proportional to the diameter cubed. Thus, coagulation was the primary cause of growth at this stage. Close inspection of the TEM images in Fig. 6.2 shows that the larger nanoclusters, formed after larger extents of evaporation (i.e. greater than 60%), are more irregular in shape relative to a spherical geometry. In fact, one may even discern that the larger clusters are partially composed of smaller, 35-60 nm, clusters, indicating a small degree of coagulation. By quenching the nanocluster dispersion with DI water soon after cluster formation, after only 60% solvent evaporation, the potential for additional coagulation was reduced, thus preserving smaller nanocluster sizes and low polydispersities.

6.4.6 Tuning cluster size with polymer/gold ratio

A reduction in the polymer/gold ratio from 16/1 to 1/1 resulted in a marked decrease in cluster size from ~80 nm to ~30 nm (Fig. 6.8), as well as a reduction in polymer loading from 20 to 15%, as shown by TGA. This decrease is the opposite of what is expected for steric stabilization alone, indicating other factors were operative. For lower initial polymer/gold ratios and thus polymer concentrations, the lower adsorption onto gold produces a smaller degree of ion pairing and thus a larger $V_{electrostatic}$. The greater repulsion will favor slower growth as observed. Furthermore, the lower polymer concentration reduces the collision frequency between polymer chains and gold clusters, leading to less trapping of polymer in the clusters. Rheological factors are also present. The viscosity of PLA-*b*-PEG-*b*-PLA solutions increases markedly with concentration in the dilute to semi-dilute transition (Appendix D Fig. D.5). During gold cluster formation via solvent evaporation, the viscosity of the dispersion will increase sooner for higher polymer/gold ratios, increasing the amount of entangled polymer that may get trapped within the gold clusters. This behavior was observed as the polymer/gold ratio was raised from 1/1 to 16/1, and was even more prevalent for the 40/1 polymer/gold ratio (Appendix D Fig. D.7). Coagulation was particularly evident at this highest ratio, according to size distribution moment calculations (μ_1=1.55, μ_3=0.81). To examine the effect of polymer gelation, a 50 mg/mL solution of PLA-*b*-PEG-*b*-PLA without gold particles was dried by solvent evaporation. The precipitate was redispersed to give large aggregates (> 500 nm) that did not break up into block copolymer micelles, indicating that gelation was not fully reversible (Appendix D Fig. D.9). For the formation of gold clusters, the gelation of the polymer may make the polymer less available for steric stabilization. Finally, the depletion attraction forces mediate cluster growth both during condensation and coagulation. For smaller polymer/gold ratios, the depletion attraction will decrease, which would favor smaller clusters, as observed (Fig. 6.8a). As the volume of the gap region increases between particles, the depletion attraction also increases. Thus, the depletion attraction will be larger for two 20 nm, growing clusters than for two primary colloidal 5 nm gold particles. Thus depletion attraction may play a larger role in the later coagulation stage than for the initial growth of the smallest embryos.

6.4.7 Comparison to thermodynamic self assembly methods

The mechanism by which our nanoclusters are formed is fundamentally different from equilibrium-based processes, in which particles are assembled into the cores of micelles or at the interface between the core and the corona. In the case of thermodynamic self-assembly, the polymer-gold interactions are inherently stronger and play a much more dominant role, leading to higher polymer loadings and larger gold spacings.

The loadings into micelles are governed by entropic and enthalpic interactions between the solute and the micelle core, as well as the interfacial free energy between the core and corona of a micelle, $\Delta\overline{F_{int}}$ [69]. The change in free energy for mixing solute molecules and micelles is given by [69]

$$\Delta\overline{F_1} = -T\Delta S_m + \Delta H_m + \Delta\overline{F_{int}} \quad (6.8)$$

where ΔS_m and ΔH_m are the change in entropy and enthalpy upon mixing, respectively. The amount of work required for expansion of the interface between the core and corona upon imbibing a solute molecule increases as the micelle size decreases, due to larger Laplace pressures. This interfacial term becomes especially significant for micelles smaller than 200 nm[69]. The loadings of small molecules such as pharmaceuticals in the cores of micelles are often less than 25% by weight[69] and typically less than 10%. The loading of a gold particle in a micelle will be even lower because ΔS_m will be less favorable, given the high molecular weight of the particle. For example, loadings of only < 2% w/w of ~2.4 nm gold particles in ~20 nm polymer micelles has been observed using small angle x-ray scattering (SAXS)[70]. Thus, thermodynamic assembly methods are not likely to incorporate sufficient gold loadings to yield a strong red-shift in the SPR for clusters, especially for sizes smaller than 50 nm.

The kinetic nanocluster assembly method in the present study is not restricted by the thermodynamic constraints of micelle encapsulation. Clusters were formed by purposely aggregating gold nanoparticles with a weakly adsorbing polymer to control nucleation and growth by manipulation of the electrostatic, steric, and depletion interactions. The strong van der Waals interactions between the gold particles were the primary driving force for cluster growth. Furthermore, depletion effects promote exclusion of the polymer to the cluster surface. These interactions lead to much higher loadings than for thermodynamic assembly of gold particles with micelles.

6.4.8 Application to biomedical imaging and therapeutics

Gold nanoparticles with intense NIR absorbance, including nanoshells[32-34], nanorods[35, 36], and nanocages[37, 38], have received extensive attention as biomedical imaging and therapeutic agents. However, while these particles are within the optimal size range of 6-100 nm to exhibit sufficiently long blood residence times for accumulation at disease sites, they are above the threshold size of 5.5 nm required for efficient clearance by the kidneys [71 72]. Furthermore, the metallic bonds between the gold atoms in these particles do not biodegrade. In contrast, our gold nanoclusters, using PLA-b-PEG-b-PLA as the stabilizer , were shown to biodegrade nearly completely in solution and in macrophage cells back to the original 5 nm gold spheres[9]. The ability to further tune the size to 30 nm and to vary composition, as demonstrated in the current study, broadens the scope of biodegradable nanoclusters significantly.

6.5 CONCLUSIONS

A general kinetic self-assembly method has been introduced to tune the size of hybrid polymer/gold nanoclusters, as small as 30 nm, with closely-spaced gold particles along with unusually low polymer loadings. These properties are achieved by the combination of high initial gold particle volume fractions and the depletion of the weakly adsorbed polymeric stabilizer from the cluster interior. Either solvent evaporation or mixing may be utilized to produce high initial gold particle and polymer concentrations simultaneously to manipulate growth. Here, the polymer adsorbs weakly on the gold and thereby reduces the electrostatic repulsion to nucleate cluster growth. The growth is arrested by small amounts of polymer on the exterior cluster surface, as characterized by SEM and TGA, which provide steric stabilization and minimize coagulation. The closely-spaced particles provide intense NIR absorbance even in clusters as small as 30 nm, a size which is of great interest for manipulation of biological pathways and signaling at the cellular level[56]. This kinetic assembly platform may be used to tune the size, morphology, and optical properties of a widespread variety of clusters with high metal loadings, simply by varying the particle concentration pathways to adjust the colloidal forces. Additionally, the method has been generalized for initial gold particles with varying surface charge. In contrast, higher polymer loadings along with more widely spaced metal particles are often obtained in nanoclusters formed by thermodynamic self-assembly, which requires stronger metal particle-polymer interactions. Kinetically-controlled nanocluster assembly using physical methods offers broad opportunities for the design of nanoclusters for sensors, optoelectronics and biomedical applications, including multi-modal imaging/therapeutic systems, cell-specific targeting, and biodegradable clusters for rapid clearance from the body.

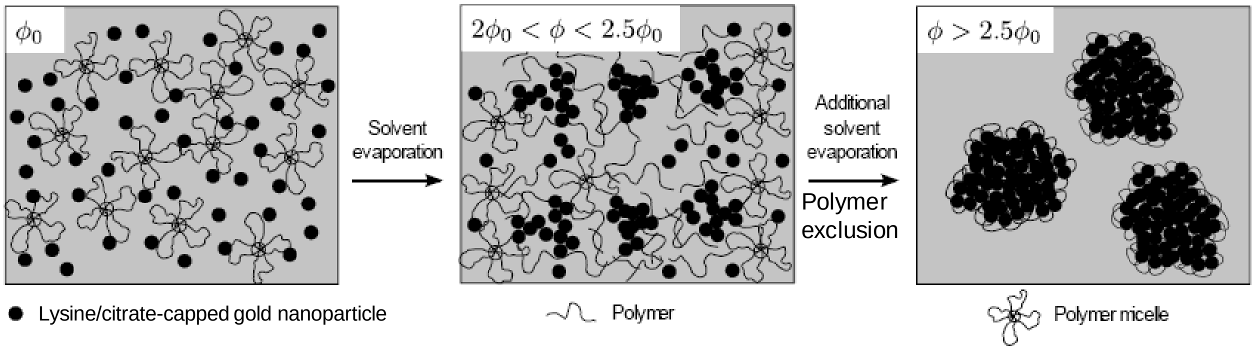

Figure 6.1 Schematic of kinetically controlled assembly process of nanocluster formation, in which primary gold nanoparticles aggregate in the presence of a weakly adsorbing polymer, PLA-*b*-PEG-*b*-PLA micelles, in a controlled manner to yield sub-100 nm clusters. Weak polymer adsorption increases counter ion binding and reduces the surface charge on the gold nanoparticles to facilitate cluster nucleation. Cluster growth is facilitated by increasing the volume fraction of particles,φ, via solvent evaporation. PEG blocks on the polymer extend into the aqueous environment and provide steric stabilization to clusters.

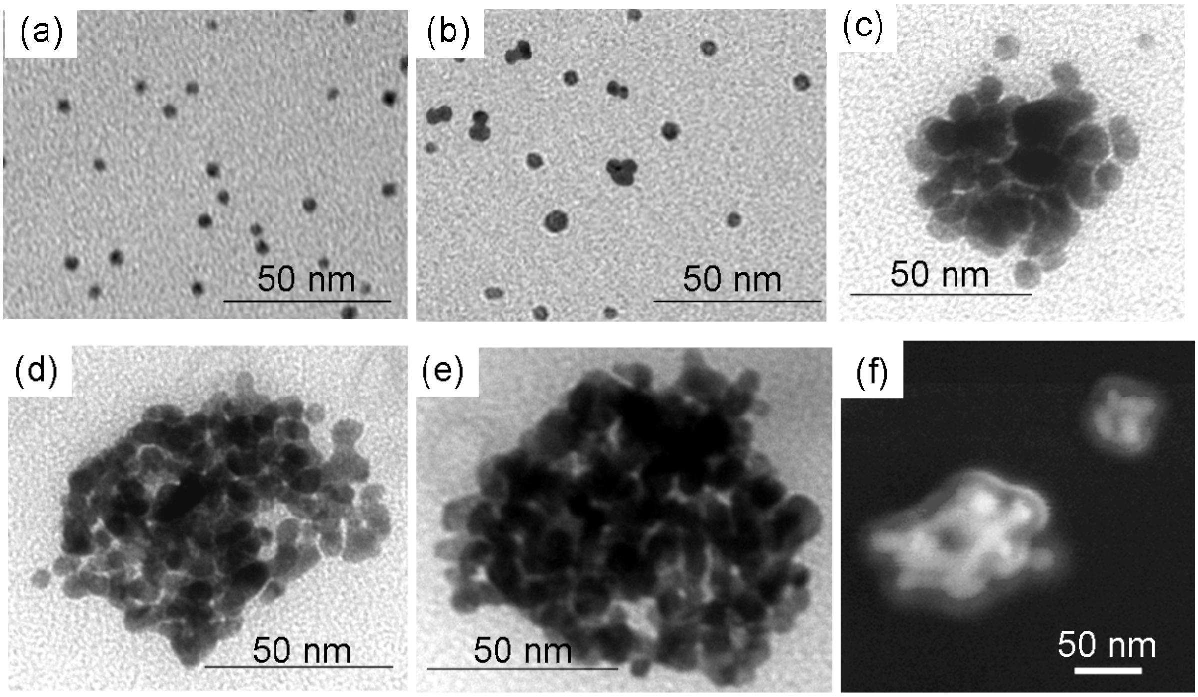

Figure 6.2 TEM images of nanoclusters produced after (a) 0%, (b) 50%, (c) 60%, (d) 80%, (e) 100% solvent evaporation. (f) SEM image of nanoclusters produced after 100% solvent evaporation. The nanoclusters were formed at an initial gold concentration of 3 mg/mL and a PLA-*b*-PEG-*b*-PLA concentration of 50 mg/mL.

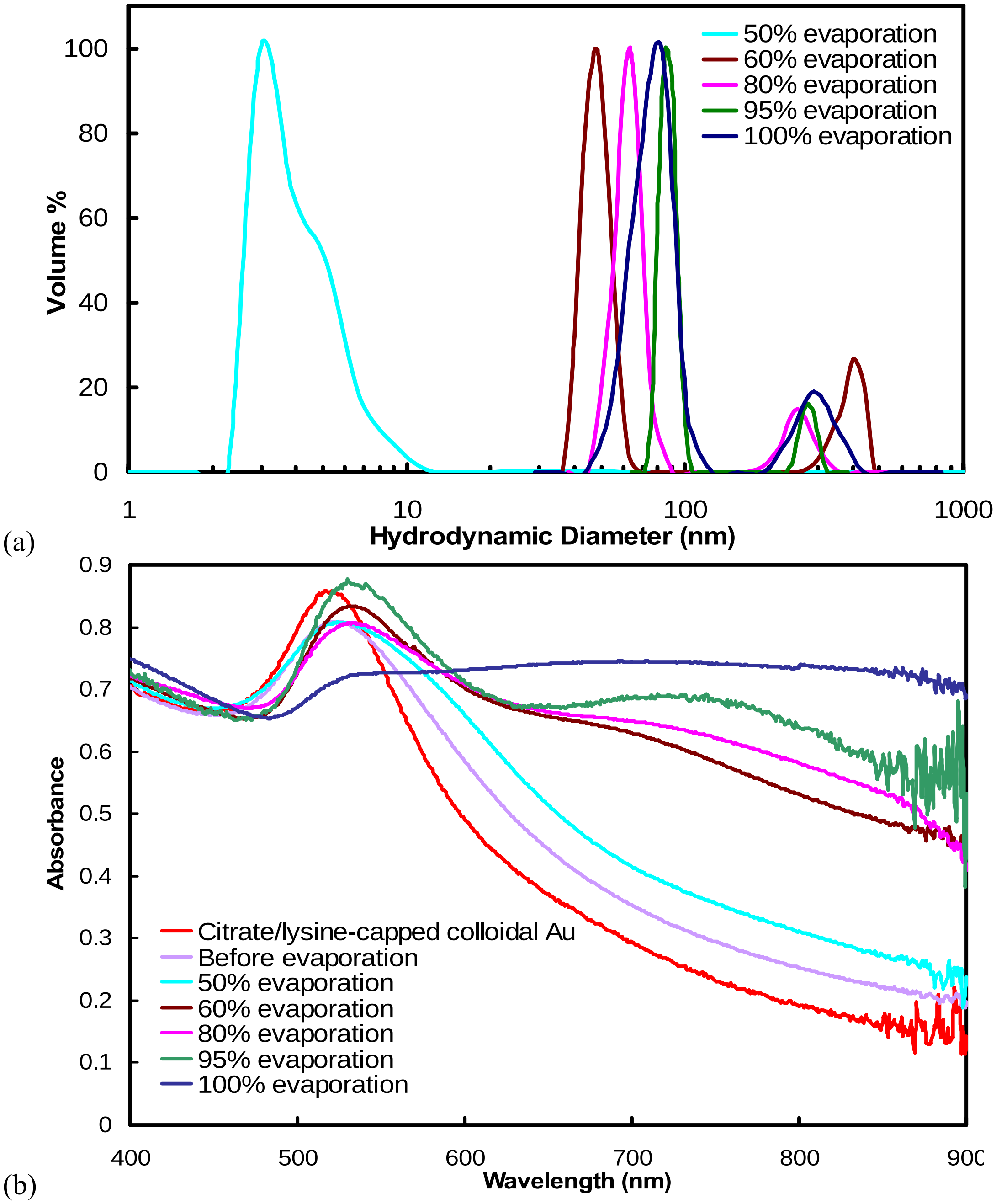

Figure 6.3 (a) Particle size measurements, by DLS, and (b) UV-vis absorbance spectra for nanoclusters composed of citrate/lysine-capped gold nanoparticles produced after different extents of evaporation. Nanoclusters were produced at a starting gold concentration of 3 mg/mL and bound together with PLA-*b*-PEG-*b*-PLA at a polymer/gold ratio of 16/1.

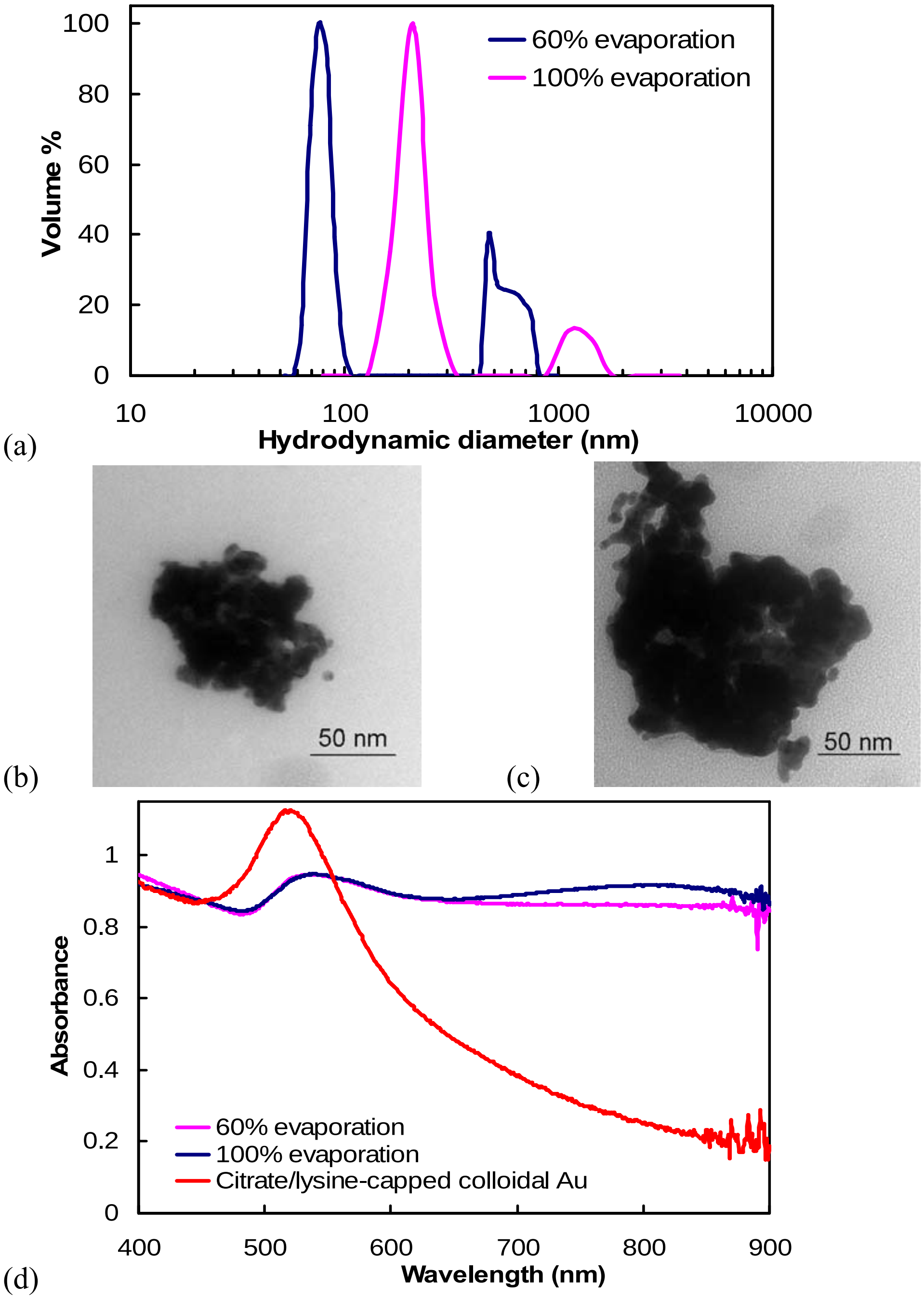

Figure 6.4 (a) Particle size measurements, by DLS, TEM images of nanoclusters after (b) 60% and (c) 100% solvent evaporation, and (d) UV-vis absorbance spectra of nanoclusters composed of citrate/lysine-capped nanoparticles assembled using PEG homopolymer (MW=3350). The starting gold and polymer concentrations were 3 mg/mL and 50 mg/mL, respectively.

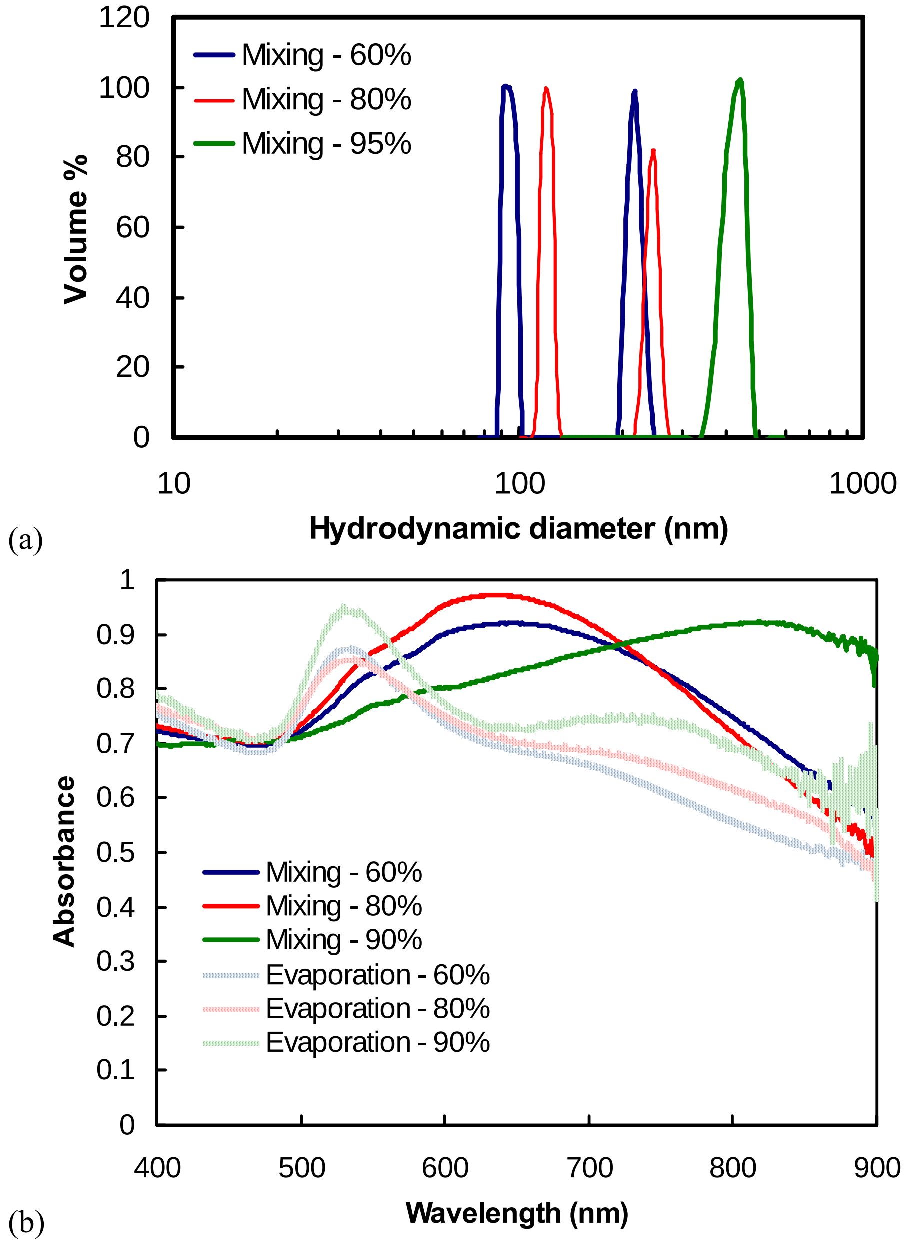

Figure 6.5 (a) Particle size distribution, as measured by DLS, and (b) UV-vis spectra of clusters of citrate/lysine-capped nanoparticles made with the mixing protocol. The conditions of cluster formation are equivalent to that for clusters formed by solvent evaporation at a starting gold concentration of 3 mg/mL and a PLA-*b*-PEG-*b*-PLA/Au ratio of 16/1. In (b), the UV-vis spectra are compared to that for nanoclusters produced using solvent evaporation.

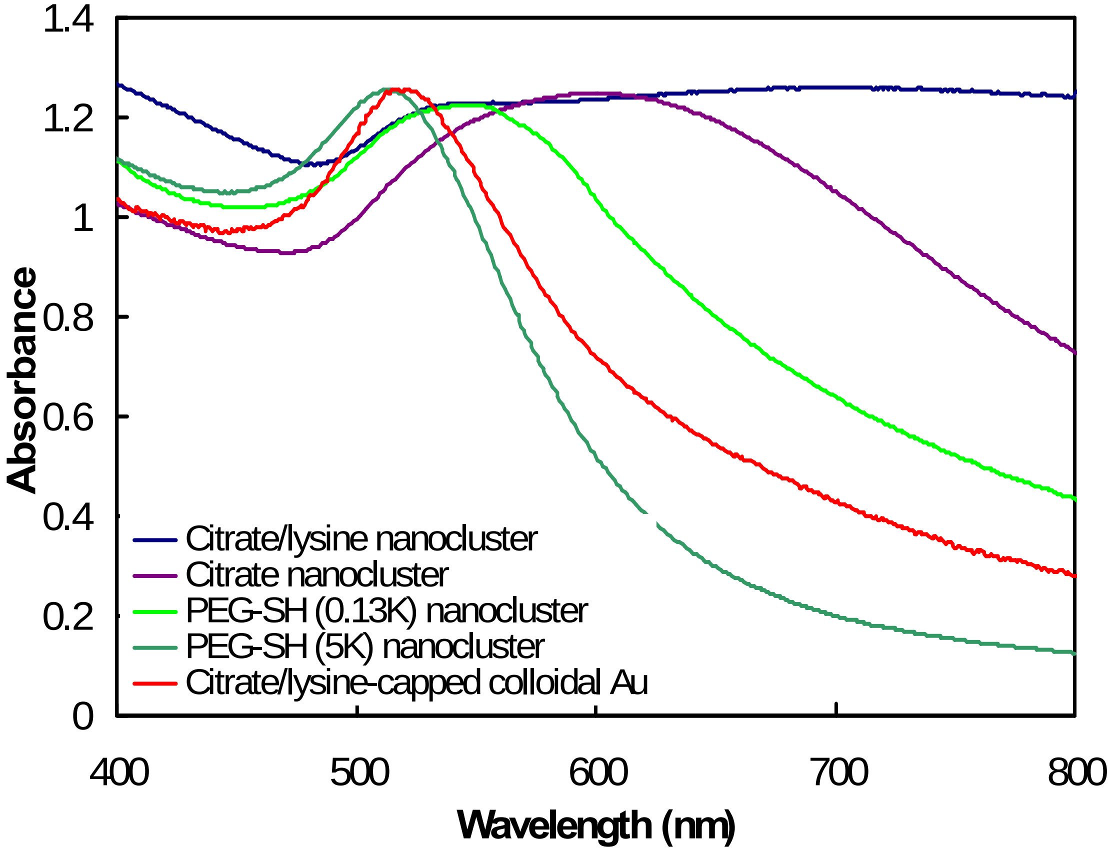

Figure 6.6 UV-vis absorbance spectra for clusters made with gold primary particles capped with different ligands. The clusters were produced using a starting gold concentration of 3 mg/mL and bound together using PLA-*b*-PEG-*b*-PLA at a 16/1 polymer/Au ratio. The clusters were formed under 100% solvent evaporation.

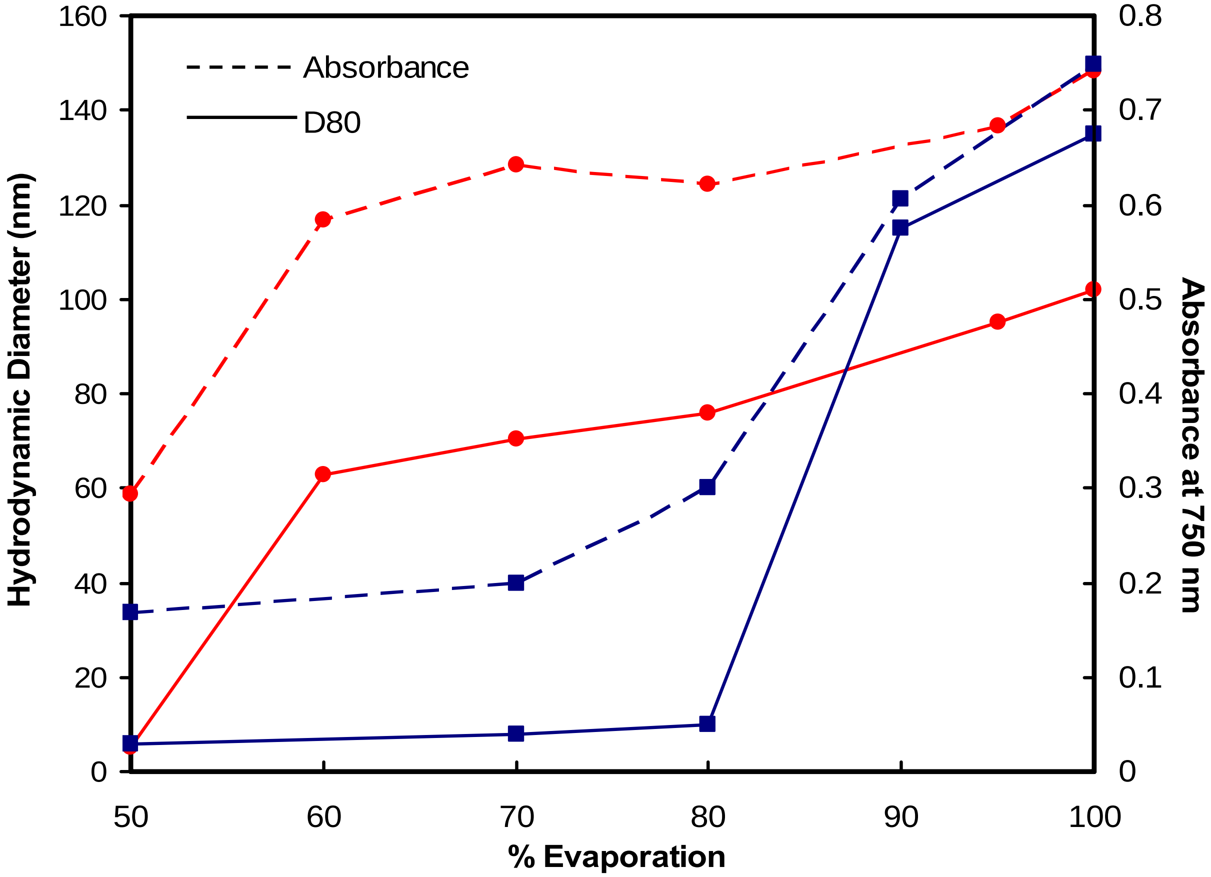

Figure 6.7 Hydrodynamic diameter (D80) and absorbance values for nanoclusters composed of primary particles capped with citrate (■) or a combination of citrate and lysine (●) ligands. The clusters were produced using a starting gold concentration of 3 mg/mL and bound together using PLA-*b*-PEG-*b*-PLA at a 16/1 polymer/Au ratio.

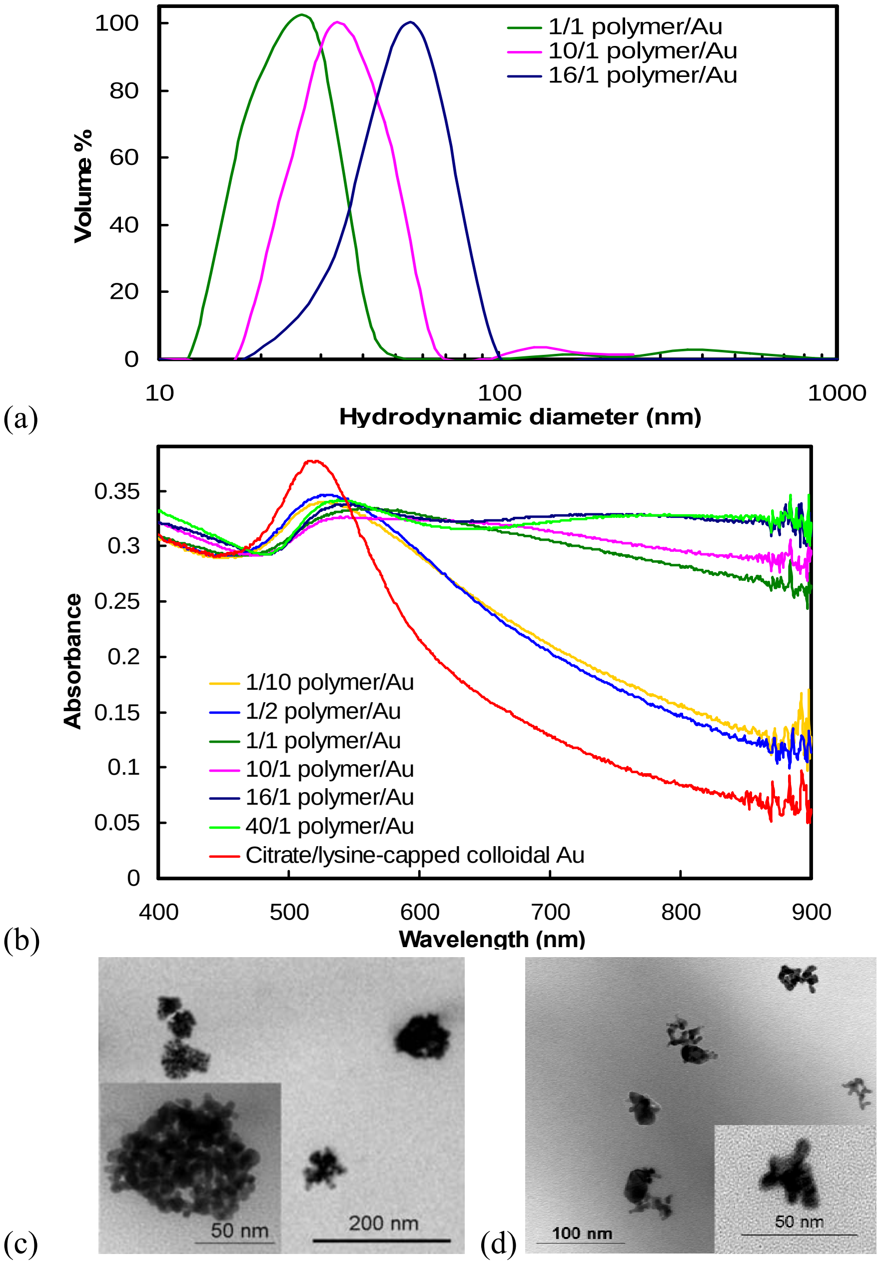

Figure 6.8 (a) Particle size distribution, as measured by DLS, and (b) UV-vis absorbance spectra of nanoclusters of citrate/lysine-capped nanoparticles produced with varying PLA-*b*-PEG-*b*-PLA/gold ratios at an initial gold concentration of 1 mg/mL and 100% solvent evaporation. TEM images of nanoclusters: (c) 16/1 polymer/gold ratio and an initial gold concentration of 3 mg/mL and (d) a 1/1 polymer/gold ratio with an initial gold concentration of 1 mg/mL after 100% solvent evaporation.

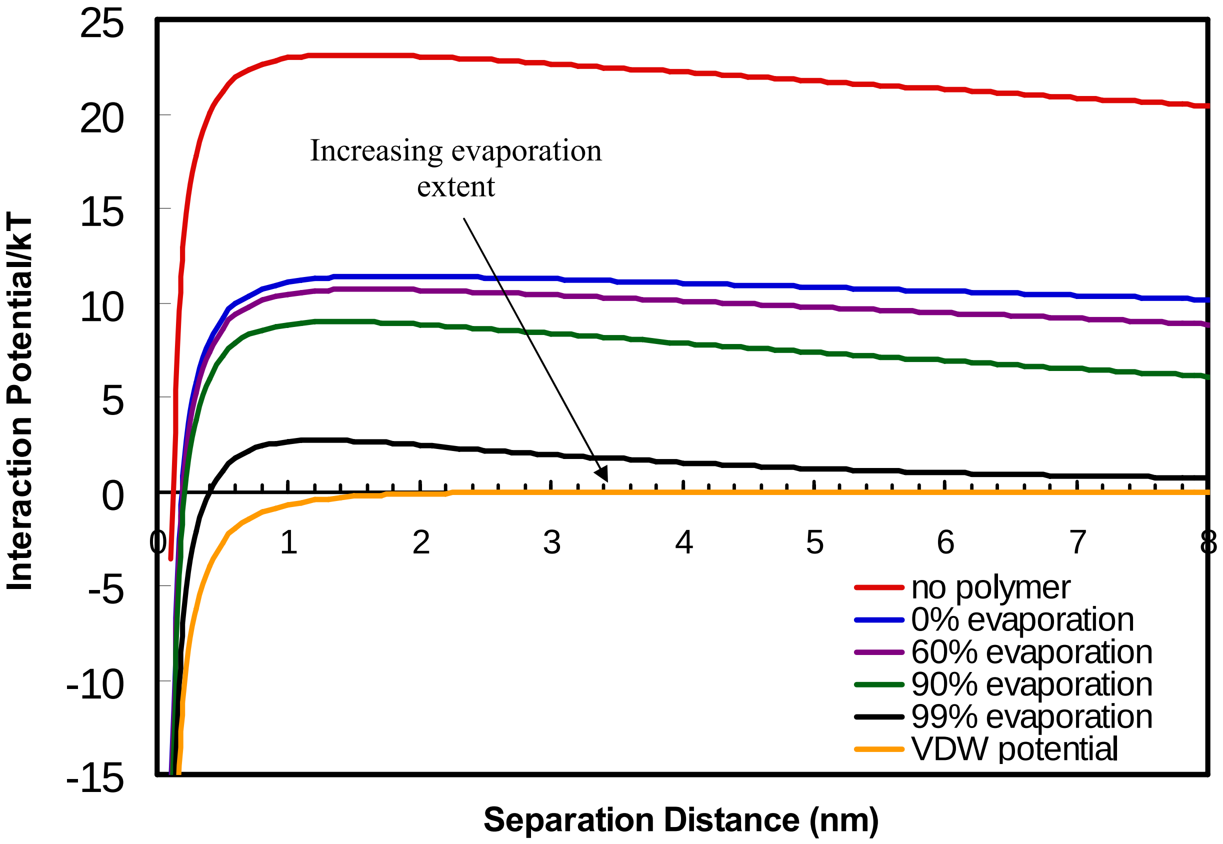

Figure 6.9 Van der Waals and total interaction potentials describing the stability of citrate/lysine- capped gold nanoparticles in the absence of PLA-*b*-PEG-*b*-PLA and after the addition of PLA-*b*-PEG-*b*-PLA. Effects of solvent evaporation on the total interaction potentials are shown.

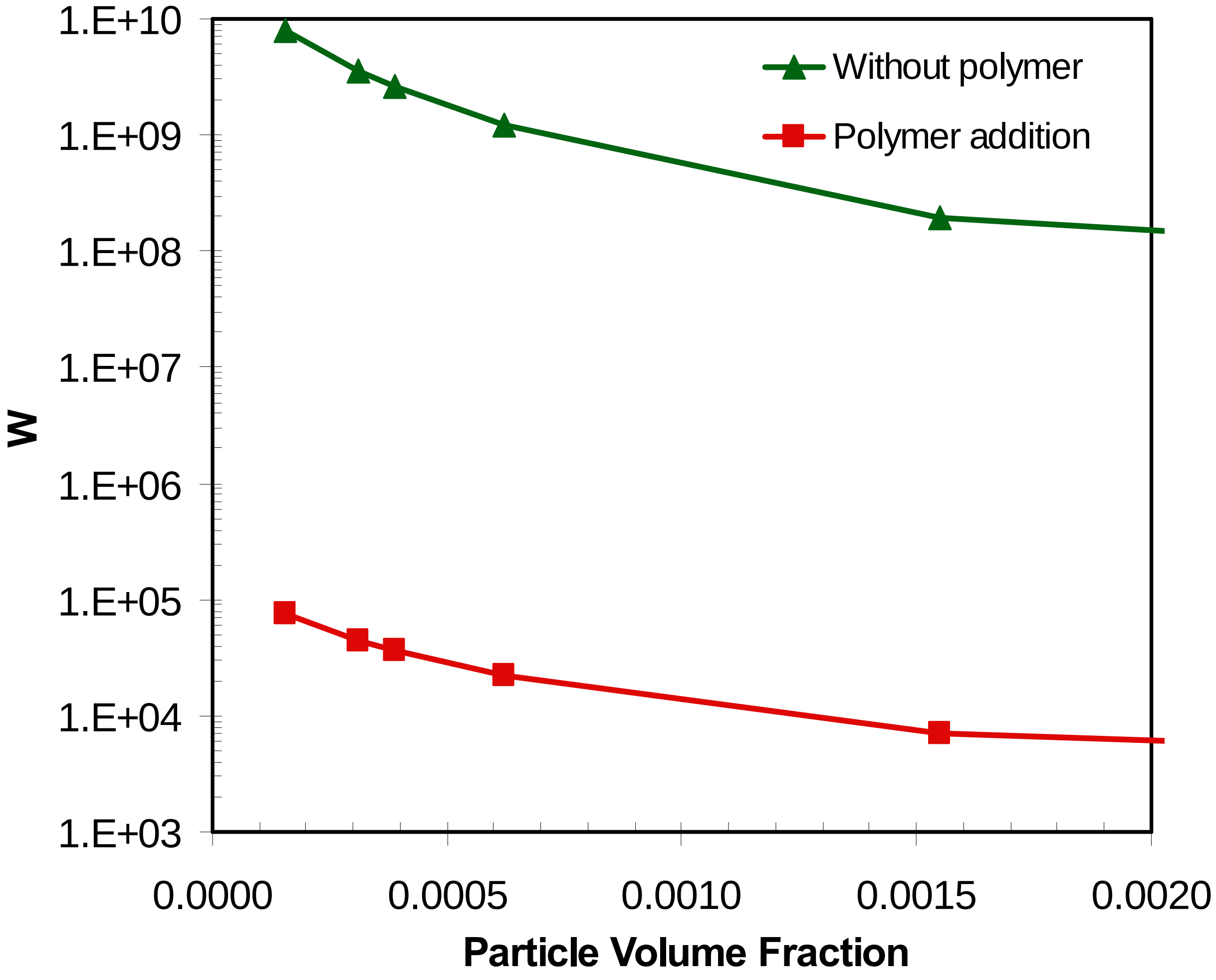

Figure 6.10 Stability ratio of a system of citrate/lysine-capped gold nanoparticles in the absence and presence of PLA-*b*-PEG-*b*-PLA determined using DLVO theory, as a function of particle volume fraction.

Table 6.1 Zeta potentials of gold primary particles and nanoclusters capped with citrate or a combination of citrate and lysine ligands.

Ligand	Zeta potential (mV)
Citrate (primary particle)	-44.0 ± 4.9
Citrate/lysine (primary particle)	-30.1 ± 2.4
PLA(2K)-*b*-PEG(10K)-*b*-PLA(2K)	-8.0 ± 0.2
Citrate/lysine 16/1 PLA-*b*-PEG-*b*-PLA /Au (nanocluster – 100% evaporation)	-16.3 ± 4.0
Citrate 16/1 PLA-*b*-PEG-*b*-PLA /Au (nanocluster – 100% evaporation)	-13.0 ± 3.3

Table 6.2 Calculated stability ratios for nanoclusters produced using citrate/lysine-capped nanoparticles at a 16/1 PLA-*b*-PEG-*b*-PLA /Au ratio and a starting gold concentration of 3 mg/mL.

Evaporation Extent (%)	N_0 (particles/m^3)	$t_{1/2,f}$ (s)	t_{col} (s)	$t_{1/2,s}$ (s)	W
0, no polymer	5×10^{21}	3.93×10^{-5}	2.59×10^{6}	256634	6.60×10^{9}
0, polymer	5×10^{21}	1.51×10^{-4}	3.60×10^{3}	356	3.97×10^{5}
50	1×10^{22}	1.30×10^{-4}	300	30	2.50×10^{5}

Table 6.3 Size distribution moments and cluster yields, as determined by FAAS, for nanoclusters produced using different extents of evaporation. The initial gold concentration was 3 mg/mL and the PLA-*b*-PEG-*b*-PLA /gold ratio was 16/1.

Sample	Cluster yield (%)	μ_1	μ_3
Citrate/lysine-capped nanoclusters 100% evaporation	99.7	1.11	0.93
Citrate/lysine-capped nanoclusters 80% evaporation	96.8	1.04	0.97
Citrate/lysine-capped nanoclusters 60% evaporation	95.1	1.09	0.93
Citrate-capped nanoclusters 100% evaporation	98.5	1.01	0.99

6.6 REFERENCES

1. DeVries, G. A.; Brunnbauer, M.; Hu, Y.; Jackson, A. M.; Long, B.; Neltner, B. T.; Uzun, O.; Wunsch, B. H.; Stellacci, F., Divalent Metal Nanoparticles. *Science* **2007,** 315, (5810), 358-361.

2. Ofir, Y.; Samanta, B.; Rotello, V. M., Polymer and biopolymer mediated self-assembly of gold nanoparticles. *Chemical Soceity Reviews* **2008,** 37, (9), 1814-1825.

3. Boal, A. K.; Ilhan, F.; DeRouchey, J. E.; Thurn-Albrecht, T.; Russell, T. P.; Rotello, V. M., Self-assembly of nanoparticles into structured spherical and network aggregates. *Nature* **2000,** 404, (6779), 746-748.

4. Ditsch, A.; Laibinis, P. E.; Wang, D. I. C.; Hatton, T. A., Controlled Clustering and Enhanced Stability of Polymer-Coated Magnetic Nanoparticles. *Langmuir* **2005,** 21, (13), 6006-6018.

5. Aaron, J.; Nitin, N.; Travis, K.; Kumar, S.; Collier, T.; Park, S. Y.; Jose-Yacaman, M.; Coghlan, L.; Follen, M.; Richards-Kortum, R.; Sokolov, K., Plasmon resonance coupling of metal nanoparticles for molecular imaging of carcinogenesis in vivo. *Journal of Biomedical Optics* **2007,** 12, (3), 034007/1-034007/11.

6. Larson, T. A.; Bankson, J.; Aaron, J.; Sokolov, K., Hybrid plasmonic magnetic nanoparticles as molecular specific agents for MRI/optical imaging and photothermal therapy of cancer cells. *Nanotechnology* **2007,** 18, (32), 325101/1-325101/8.

7. Ma, L. L.; Feldman, M. D.; Tam, J. M.; Paranjape, A. S.; Cheruku, K. K.; Larson, T. A.; Tam, J. O.; Ingram, D. R.; Paramita, V.; Villard, J. W.; Clarke, G. D.; Jenkins, J. T.; Asmis, R.; Sokolov, K.; Chandrasekar, B.; Milner, T. E.; Johnston, K. P., Small multifunctional nanoclusters (Nanoroses) for targeted cellular imaging and therapy. *ACS Nano* **Submitted**.

8. Sokolov, K. V.; Follen, M.; Aaron, J.; Pavlova, I.; Malpica, A.; Lotan, R.; Richards-Kortum, R., Real-time vital optical imaging of precancer using anti-epidermal growth factor receptor antibodies conjugated to gold nanoparticles. *Cancer Research* **2003,** 63, 1999-2004.

9. Tam, J. M.; Tam, J. O.; Murthy, A. K.; Ingram, D. R.; Ma, L. L.; Travis, K. A.; Sokolov, K. V.; Johnston, K. P., Controlled Assembly of Polymer/Inorganic Nanoclusters: A Flexible Platform for the Synthesis of Biodegradable Near-Infrared Absorbing Agents for Imaging and Therapeutic Applications. **In preparation**.

10. Srivastava, S.; Samanta, B.; Arumugam, P.; Han, G.; Rotello, V. M., DNA-mediated assembly of iron platinum (FePt) nanoparticles. *Journal of Materials Chemistry* **2007,** 17, (1), 52-55.

11. Iacovella, C. R.; Horsch, M. A.; Glotzer, S. C., Local ordering of polymer-tethered nanospheres and nanorods and the stabilization of the double gyroid phase. *The Journal of Chemical Physics* **2008,** 129, 044902-1 - 0440902-10.

12. Frankamp, B. L.; Uzun, O.; Ilhan, F.; Boal, A. K.; Rotello, V. M., Recognition-Mediated Assembly of Nanoparticles into Micellar Structures with Diblock Copolymers. *Journal of the American Chemical Society* **2002,** 124, (6), 892-893.

13. Gopidas, K. R.; Whitesell, J. K.; Fox, M. A., Nanoparticle-Cored Dendrimers: Synthesis and Characterization. *Journal of the American Chemical Society* **2003,** 125, 6491-6502.

14. Uzun, O.; Frankamp, B. L.; Sanyal, A.; Rotello, V. M., Recognition-Mediated Assembly of Nanoparticle-Diblock Copolymer Micelles with Controlled Size. *Chemistry of Materials* **2006,** 18, (23), 5404-5409.

15. Sakai, T.; Alexandridis, P., Metal nanoparticle synthesis and organization in 1D, 2D and 3D structures formed by amphiphilic block copolymers. *PMSE Preprints* **2005,** 93, 798-799.

16. Li, J.; He, W.-D.; Sun, X.-L., Preparation of poly(styrene-b-N-isopropylacrylamide) micelles surface-linked with gold nanoparticles and thermo-responsive ultraviolet-visible absorbance. *Journal of Polymer Science, Part A: Polymer Chemistry* **2007,** 45, (22), 5156-5163.

17. Bae, K. H.; Choi, S. H.; Park, S. Y.; Lee, Y.; Park, T. G., Thermosensitive Pluronic Micelles Stabilized by Shell Cross-Linking with Gold Nanoparticles. *Langmuir* **2006,** 22, (14), 6380-6384.

18. Isojima, T.; Suh, S. K.; Vander Sande, J. B.; Hatton, T. A., Controlled Assembly of Nanoparticle Structures: Spherical and Toroidal Superlattices and Nanoparticle-Coated Polymeric Beads. *Langmuir* **2009,** 25, (14), 8292-8298.

19. Harada, T.; Hatton, T. A., Formation of Highly Ordered Rectangular Nanoparticle Superlattices by the Cooperative Self-Assembly of Nanoparticles and Fatty Molecules. *Langmuir* **2009,** 25, (11), 6407-6412.

20. Isojima, T.; Lattuada, M.; Vander Sande, J. B.; Hatton, T. A., Reversible Clustering of pH- and Temperature-Responsive Janus Magnetic Nanoparticles. *ACS Nano* **2008,** 2, (9), 1799-1806.

21. Lattuada, M.; Hatton, T. A., Preparation and Controlled Self-Assembly of Janus Magnetic Nanoparticles. *Journal of the American Chemical Society* **2007,** 129, (42), 12878-12889.

22. Wilcoxon, J. P.; Martin, J. E.; Schaefer, D. W., Aggregation in colloidal gold. *Physical Review A: Atomic, Molecular, and Optical Physics* **1989,** 39, (5), 2675-88.

23. Chow, M. K.; Zukoski, C. F., Gold sol formation mechanisms: role of colloidal stability. *Journal of Colloid and Interface Science* **1994,** 165, (1), 97-109.

24. Guo, Y.; Ma, Y.; Xu, L.; Li, J.; Yang, W., Conformational Change Induced Reversible Assembly/Disassembly of Poly-L-lysine-Functionalized Gold Nanoparticles. *Journal of Physical Chemistry C* **2007,** 111, (26), 9172-9176.

25. Horovitz, O.; Mocanu, A.; Tomoaia, G.; Bobos, L.; Dubert, D.; Daian, I.; Yusanis, T.; Tomoaia-Cotisel, M., Lysine mediated assembly of gold nanoparticles. *Studia Universitatis Babes-Bolyai, Chemia* **2007,** 52, (1), 97-108.

26. Murthy, V. S.; Cha, J. N.; Stucky, G. D.; Wong, M. S., Charge-Driven Flocculation of Poly(L-lysine)-Gold Nanoparticle Assemblies Leading to Hollow Microspheres. *Journal of the American Chemical Society* **2004,** 126, (16), 5292-5299.

27. Xu, L.; Guo, Y.; Xie, R.; Zhuang, J.; Yang, W.; Li, T., Three-dimensional assembly of Au nanoparticles using dipeptides. *Nanotechnology* **2002,** 13, (6), 725-728.

28. Lim, I. I. S.; Ip, W.; Crew, E.; Njoki, P. N.; Mott, D.; Zhong, C.-J.; Pan, Y.; Zhou, S., Homocysteine-mediated reactivity and assembly of gold nanoparticles. *Langmuir* **2007,** 23, (2), 826-833.

29. Aslan, K.; Luhrs, C. C.; Perez-Luna, V. H., Controlled and Reversible Aggregation of Biotinylated Gold Nanoparticles with Streptavidin. *Journal of Physical Chemistry B* **2004,** 108, (40), 15631-15639.

30. Lazarides, A. A.; Schatz, G. C., DNA-Linked Metal Nanosphere Materials: Structural Basis for the Optical Properties. *Journal of Physical Chemistry B* **2000,** 104, (3), 460-467.

31. Mirkin, C. A.; Letsinger, R. L.; Mucic, R. C.; Storhoff, J. J., A DNA-based method for rationally assembling nanoparticles into macroscopic materials. *Nature (London)* **1996,** 382, (6592), 607-609.

32. Adler, D. C.; Huang, S.-W.; Huber, R.; Fujimoto, J. G., Photothermal detection of gold nanoparticles using phase-sensitive optical coherence tomography. *Optics Express* **2008,** 16, (7), 4376-4393.

33. Hirsch, L. R.; Stafford, R. J.; Bankson, J. A.; Sershen, S. R.; Rivera, B.; Price, R. E.; Hazle, J. D.; Halas, N. J.; West, J. L., Nanoshell-mediated near-infrared thermal therapy of tumors under magnetic resonance guidance. *Proceedings of the National Academy of Sciences of the United States of America* **2003,** 100, (23), 13549-13554.

34. Loo, C.; Lowery, A.; Halas, N.; West, J.; Drezek, R., Immunotargeted Nanoshells for Integrated Cancer Imaging and Therapy. *Nano Letters* **2005,** 5, (4), 709-711.

35. Huang, X.; El-Sayed, I. H.; Qian, W.; El-Sayed, M. A., Cancer Cell Imaging and Photothermal Therapy in the Near-Infrared Region by Using Gold Nanorods. *Journal of the American Chemical Society* **2006,** 128, (6), 2115-2120.

36. Pissuwan, D.; Valenzuela, S. M.; Killingsworth, M. C.; Xu, X.; Cortie, M. B., Targeted destruction of murine macrophage cells with bioconjugated gold nanorods. *Journal of Nanoparticle Research* **2007,** 9, (6), 1109-1124.

37. Chen, J.; Saeki, F.; Wiley, B. J.; Cang, H.; Cobb, M. J.; Li, Z.-Y.; Au, L.; Zhang, H.; Kimmey, M. B.; Li, X.; Xia, Y., Gold Nanocages: Bioconjugation and Their Potential Use as Optical Imaging Contrast Agents. *Nano Letters* **2005,** 5, (3), 473-477.

38. Skrabalak, S. E.; Chen, J.; Au, L.; Lu, X.; Li, X.; Xia, Y., Gold nanocages for biomedical applications. *Advanced Materials* **2007,** 19, (20), 3177-3184.

39. Kreibig, U.; Vollmer, M., *Optical Properties of Metal Clusters* Springer: Berlin, Germany, 1995 Vol. 25.

40. Kumar, S.; Harrison, N.; Richards-Kortum, R.; Sokolov, K., Plasmonic Nanosensors for Imaging Intracellular Biomarkers in Live Cells. *Nano Letters* **2007,** 7, (5), 1338-1343.

41. Jain, P. K.; Lee, K. S.; El-Sayed, I. H.; El-Sayed, M. A., Calculated Absorption and Scattering Properties of Gold Nanoparticles of Different Size, Shape, and Composition: Applications in Biological Imaging and Biomedicine. *Journal of Physical Chemistry B* **2006,** 110, (14), 7238-7248.

42. Khlebtsov, B.; Zharov, V.; Melnikov, A.; Tuchin, V.; Khlebtsov, N., Optical amplification of photothermal therapy with gold nanoparticles and nanoclusters. *Nanotechnology* **2006,** 17, (20), 5167-5179.

43. Troutman, T. S.; Barton, J. K.; Romanowski, M., Biodegradable plasmon resonant nanoshells. *Advanced Materials* **2008,** 20, (13), 2604-2608.

44. Ferrari, M., Cancer nanotechnology: opportunities and challenges. *Nature Reviews Cancer* **2005,** 5, (3), 161-171.

45. Zhou, Y.; Jiang, K.; Chen, Y.; Liu, S., Gold nanoparticle-incorporated core and shell crosslinked micelles fabricated from thermoresponsive block copolymer of N-isopropylacrylamide and a novel primary-amine containing monomer. *Journal of Polymer Science, Part A: Polymer Chemistry* **2008,** 46, (19), 6518-6531.

46. Reddy, S. T.; Swartz, M. A.; Hubbell, J. A., Targeting dendritic cells with biomaterials: developing the next generation of vaccines. *Trends in Immunology* **2006,** 27, (12), 573-579.

47. Wang, A. Z.; Bagalkot, V.; Vasilliou, C. C.; Gu, F.; Alexis, F.; Zhang, L.; Shaikh, M.; Yuet, K.; Cima, M. J.; Langer, R.; Kantoff, P. W.; Bander, N. H.; Jon, S.; Farokhzad, O. C., Superparamagnetic iron oxide nanoparticle-aptamer bioconjugates for combined prostate cancer imaging and therapy. *ChemMedChem* **2008,** 3, (9), 1311-1315.

48. Weissleder, R., Molecular Imaging in Cancer. *Science* **2006,** 312, (5777), 1168-1171.

49. Xia, Y. In *Gold nanocages: A new class of plasmonic nanostructures for biomedical applications*, ACS National Meeting, Boston, MA, United States, August 19-23, 2007 2007; Boston, MA, United States, 2007; pp COLL-528.

50. Gindy, M. E.; Panagiotopoulos, A. Z.; Prud'homme, R. K., Composite Block Copolymer Stabilized Nanoparticles: Simultaneous Encapsulation of Organic Actives and Inorganic Nanostructures. *Langmuir* **2008,** 24, (1), 83-90.

51. Gindy, M. E.; Prud'homme, R. K.; Ji, S.; Hoye, T. R.; Macosko, C. W., Functional block copolymer nanoparticles for targeted drug delivery and imaging. *PMSE Preprints* **2006,** 95, 989-990.

52. Grabar, K. C.; Allison, K. J.; Baker, B. E.; Bright, R. M.; Brown, K. R.; Freeman, R. G.; Fox, A. P.; Keating, C. D.; Musick, M. D.; Natan, M. J., Two-dimensional arrays of colloidal gold particles: a flexible approach to macroscopic metal surfaces. *Langmuir* **1996,** 12, 23535-2361.

53. Selvakannan, P. R.; Mandal, S.; Phadtare, S.; Pasricha, R.; Sastry, M., Capping of Gold Nanoparticles by the Amino Acid Lysine Renders Them Water-Dispersible. *Langmuir* **2003,** 19, (8), 3545-3549.

54. Ryoo, W.; Webber, S. E.; Johnston, K. P., Water-in-Carbon Dioxide Microemulsions with Methylated Branched Hydrocarbon Surfactants. *Ind. Eng. Chem. Res.* **2003,** 42, (25), 6348-6358.

55. Hiemenz, P. C.; Rajagopalan, R.; Editors, *Principles of Colloid and Surface Chemistry, Third Edition, Revised and Expanded*. 1997; p 688 pp.

56. Jiang, W.; Kim, B. Y. S.; Rutka, J. T.; Chan, W. C. W., Nanoparticle-mediated cellular response is size-dependent. *Nature Nanotechnology* **2008,** 3, (3), 145-150.

57. Brewer, S. H.; Glomm, W. R.; Johnson, M. C.; Knag, M. K.; Franzen, S., Probing BSA Binding to Citrate-Coated Gold Nanoparticles and Surfaces. *Langmuir* **2005,** 21, 9303-9307.

58. Blatchford, C. G.; Campbell, J. R.; Creighton, J. A., Plasma Resonance-Enhanced Raman Scattering by Adsorbates on Gold Colloids: The Effects of Aggregation. *Surface Science* **1982,** 120, 445-455.

59. Riley, T.; Stolnik, S.; Heald, C. R.; Xiong, C. D.; Garnett, M. C.; Illum, L.; Davis, S. S., Physicochemical Evaluation of Nanoparticles Assembled from Poly(lactic acid)-Poly(ethylene glycol) (PLA-PEG) Block Copolymers as Drug Delivery Vehicles. *Langmuir* **2001,** 17, 3168-3174.

60. Kleshchanok, D.; Tuinier, R.; Lang, P. R., Direct measurements of polymer-induced forces. *Journal of Physics: Condensed Matter* **2008,** 20, (7), 073101/1-073101/25.

61. Mondain-Monval, O.; Leal-Calderon, F.; Phillip, J.; Bibette, J., Depletion Forces in the Presence of Electrostatic Double Layer Repulsion. *Physical Review Letters* **1995,** 75, 3364-3367.

62. Vrij, A., Polymers at Interfaces and the Interactions in Colloidal Dispersions *Pure and Applied Chemistry* **1976,** 48, 471-483

63. Gögelein, C.; Nägele, G.; Buitenhuis, J.; Tuinier, R.; Dhont1, J. K. G., Polymer depletion-driven cluster aggregation and initial phase separation in charged nanosized colloids. *The Journal of Chemical Physics* **2009,** 130, (20), 204905-1 - 204905-15.

64. Mutch, K. J.; Duijneveldt, J. S. v.; Eastoe, J., Colloid–polymer mixtures in the protein limit. *Soft Matter* **2007,** 3, 155-167.

65. Mutch, K. J.; Duijneveldt, J. S. v.; Eastoe, J.; Grillo, I.; Heenan, R. K., Small-Angle Neutron Scattering Study of Microemulsion Polymer Mixtures in the Protein Limit. *Langmuir* **2008,** 24, 3053-3060.

66. Kline, S. R.; Kaler, E. W., Aggregation of Colloidal Silica by n-Alkyl Sulfates. *Langmuir* **1996,** 12, 2402-2407.

67. Sakai, T.; Alexandridis, P., Mechanism of Gold Metal Ion Reduction, Nanoparticle Growth and Size Control in Aqueous Amphiphilic Block Copolymer Solutions at Ambient Conditions. *Journal of Physical Chemistry B* **2005,** 109, (16), 7766-7777.

68. Agrawal, S. K.; Sanabria-DeLong, N.; Tew, G. N.; Bhatia, S. R., Structural Characterization of PLA-PEO-PLA Solutions and Hydrogels: Crystalline vss Amorphous PLA Domains. *Macromolecules* **2008,** 41, 1774-1784.

69. Varun, K.; Robert, K. P. h., Thermodynamic limits on drug loading in nanoparticle cores. *Journal of Pharmaceutical Sciences* **2008,** 97, (11), 4904-4914.

70. Sun, Y.-L.; Chen, Y.-Z.; Wu, R.-J.; Chavali, M.; Huang, Y.-C.; Su, P.-G.; Lin, C.-C., Poly(l-lactide) stabilized gold nanoparticles based QCM sensor for low humidity detection. *Sensors and Actuators B* **2007,** 126, 441-446.

71. Betancourt, T.; Brown, B.; Brannon-Peppas, L., Doxorubicin-loaded PLGA nanoparticles by nanoprecipitation: preparation, characterization and *in vitro* evaluation. *Nanomedicine* **2007,** 2, (2), 220-232.

72. Kooi, M. E.; et al, Accumulation of Ultrasmall Superparamagnetic Particles of Iron Oxide in Human Atherosclerotic Plaques Can Be Detected by In Vivo Magnetic Resonance Imaging. . *Circulation* **2003,** 107, (19), 2453-2458.

Chapter 7: Conclusions and Recommendations

7.1 CONCLUSIONS

7.1.1 Amorphous Cyclosporin Nanodispersions for Enhanced Pulmonary Deposition and Dissolution

Stable dispersions of amorphous, 300 nm cyclopsorin (CsA) nanoparticles, containing only 10 wt% excipient, were produced using controlled antisolvent precipitation. The stable dispersions, when nebulized to mice, produced efficacious drug concentrations in both the lung tissue and blood stream and remained within the therapeutic window. This accomplishment is particularly useful for lung transplant recipients or for those patients requiring non-steroid asthma treatment, where the effectiveness of CsA has been limited due to a narrow therapeutic window. Nebulization of CsA nanoparticle dispersions circumvents problems in solution-based pulmonary formulations that often cause irritation to lung tissues due to the use of organic solvents or large amounts of excipients. Furthermore, nebulization of the drug generated much higher lung tissue concentrations (10.5 μg drug/g lung tissue) than oral and parenteral administration routes reported in literature, while maintaining lower systemic concentrations (370 ng/mL), below the toxicity level. Thus, the development of an aerosolized nanoparticle formulation to target the deep lungs will not only make CsA a more viable option for treatment of lung diseases, but this methodology can also be applied to other drugs that have narrow therapeutic windows.

Successful nebulization of nanoparticles to the lungs requires that the length scale of the drug particles be significantly less than that of the carrier droplets, in order to facilitate uniform distribution of drug particles throughout the aerosolized droplets. The aerosolized water droplets possessed optimal aerodynamic properties for deep lung deposition, achieving high fine particle fractions up to 77%, whereas the small size of the drug particles favored enhanced dissolution. Thus, nebulization of nanoparticle dispersions simultaneously enables efficient deep lung deposition and dissolution in the lung tissue. The amorphous CsA nanoparticles generated *in-vitro* supersaturation levels up to 18 times the equilibrium solubility. Finally, to better understand the absorption of poorly water soluble drugs in the lungs, a model was developed to characterize the effects of particle size, morphology, solubility, and drug dose on the two mechanisms that regulate drug absorption: drug dissolution and permeation through tissues. For example, the absorption half-life for a 3 μm drug particle with a solubility of 1 μg/mL is predicted to decrease from 500 to 5 minutes with an increase in supersaturation to 100 μg/mL, indicating that the absorption of this poorly water soluble drug is dissolution-rate limited. Increased absorption rates may be achieved by the formation of an amorphous drug form[1] or a particle size reduction to 300 nm. Thus, the model indicates that modification of drug properties to enhance drug dissolution can significantly affect drug absorption times. The flexibility of the model allows it to be applied in the development of other pulmonary poorly water soluble drug formulations to predict how particle size and morphology impact absorption rates, as well as if absorption rates will be sufficient to avoid clearance by macrophages.

7.1.2 Templated Open Flocs for the Delivery of Nanoparticles to the Lungs Using a Pressurized Metered Dose Inhaler (pMDI)

Anisotropic nanoparticles, in the shape of rods, thin plates, and needles (aspect ratios ranging between 5-24), suspended in a HFA propellant without the inclusion of surfactants or cosolvents were stable against settling for two years at a 10 mg/mL drug loading. The anisotropic particles formed highly open, low density, space-filling flocs in HFA which stacked upon each other to prevent settling. Rapid and sticky attractive collisions, driven by van der Waals attractive forces, between the anisotropic particles, as well as the inefficient packing of these particles, are believed to facilitate the formation of the low density flocs. In contrast, isotropic particles (spheres or cubes) produced by milling or spray drying formed dense aggregates that settled within one minute. Aerosolization of the floc suspension with a pMDI produced high fine particle fractions (47-64%) with an emitted dose up to 2.4 mg/actuation. These desirable aerodynamic properties and high doses were facilitated by the ability to produce highly stable suspensions, even at increased drug loadings up to 50 mg/mL.

The aerosolized particles were templated during HFA droplet formation and compacted during evaporation to yield optimal aerodynamic diameters for deep lung delivery, in contrast with the conventional approach of delivering pre-formed particles. The attractive van der Waals interactions between primary particles within the floc were demonstrated to be sufficiently weak such that the atomized HFA droplets could shear off portions of the floc within the droplet upon pMDI actuation. Upon evaporation of HFA, capillary forces compact the templated flocs to produce porous particles with optimal aerodynamic properties for pulmonary delivery. Thus, the final size of the aerosol particle was templated by the evaporating HFA droplet. Furthermore, the delivery of a high surface area micron-sized porous floc of nanoparticles to the lungs, as opposed to a solid, micron-sized particle was shown to enhance drug dissolution rates. Therefore, the delivery of a micron-sized floc of nanoparticles using a pMDI offers both efficient deep lung deposition as well as rapid dissolution, which is beneficial to enhance the absorption of poorly water soluble drugs in the lungs. This novel concept for forming extremely stable suspensions of open flocs of anisotropic particles, and templating and compacting the flocs to produce particles for efficient pMDI deep lung delivery was demonstrated for the poorly water soluble drug, itraconazole, and the water soluble protein, bovine serum albumin, and thus is applicable to a wide variety of drugs.

7.1.3 Controlled Kinetic Assembly of Biodegradable Plasmonic Nanoclusters for Near-Infrared Imaging and Therapeutic Applications

A general kinetic self-assembly method has been introduced to tune the size of hybrid polymer/gold nanoclusters, as small as 30 nm and up to 100 nm in diameter, in which the 5 nm constituent gold nanoparticles are closely-spaced together and contain unusually low polymer loadings. These properties are achieved by the combination of high initial gold particle volume fractions during the clustering process and the exclusion of a weakly adsorbed polymeric stabilizer from the cluster interior due to depletion attraction forces. Either solvent evaporation or a mixing process may be utilized to produce the high initial gold particle and polymer concentrations that are required to simultaneously manipulate cluster growth and optical properties. Here, the polymer adsorbs weakly on the gold and thereby reduces the electrostatic repulsion to nucleate cluster growth. Thus, cluster growth is simultaneously arrested by the small amounts of polymer on the exterior cluster surface, as characterized by scanning electron microscopy and thermogravimetric analysis, which provide steric stabilization and minimize coagulation. The closely-spaced particles provide intense NIR absorbance in even clusters as small as 30 nm, a size which is of great interest for the manipulation of biological pathways and signaling at the cellular level[2]. Furthermore, the formation of nanoclusters using a biodegradable polymer stabilizer enabled deaggregation of the clusters into its constituent, clearable particles upon polymer degradation, as demonstrated in physiologically relevant media as well as in live cells. Thus, these nanoclusters can provide strong optical contrast required for imaging and therapy, as well as effective clearance from the body to minimize toxicity concerns and facilitate the translation of plasmonic nanoparticle applications into clinical practice.

Additionally, this kinetically controlled nanocluster assembly method has been generalized for initial gold particles with varying surface charge. In contrast, higher polymer loadings, along with more widely spaced metal particles, are often obtained in nanoclusters formed by thermodynamic self-assembly methods, which require stronger metal particle-polymer interactions. This kinetic assembly platform may be used to tune the size, morphology, and optical properties of a widespread variety of clusters in which high metal loadings are desirable, simply by varying the particle concentration pathways to adjust the colloidal forces. Therefore, kinetically-controlled nanocluster assembly using physical methods offers broad opportunities for the design of nanoclusters for sensors, optoelectronics and biomedical applications, including multi-modal imaging/ therapeutic systems, cell-specific targeting, and biodegradable clusters for rapid clearance from the body.

7.2 RECOMMENDATIONS AND FUTURE RESEARCH

7.2.1 Pulmonary delivery of nanoparticles

The absorption of BCS class II drugs, such as itraconazole (aqueous solubility < 1 ng/mL at neutral pH [3]) by the body is generally considered to be dissolution rate limited, due to extremely low aqueous solubilities. Therefore, extensive efforts have been invested in the production and stabilization of amorphous nanoparticles of poorly water soluble drugs, with sizes as low as ~200 nm, to enhance dissolution rates in the lungs, and thus systemic absorption[4-6]. However, a recent examination of drug absorption rates of poorly water soluble drugs in the lungs using the dissolution/permeation model described in chapter 2 of this dissertation suggests that continued particle size reduction or increasing supersaturation levels may not necessarily enhance systemic absorption rates beyond a certain point[6]. According to the model, the absorption half-life for a crystalline 3 μm particle (solubility of 10 ng/mL) may be reduced by 3 orders of magnitude by raising the solubility by a factor of 10 (a reasonable increase upon the formation of an amorphous drug morphology[1]) and a reduction in particle size to 230 nm. However, a further decrease in particle size to 50 nm would not result in a significant improvement in the absorption rate. Therefore, additional efforts in producing smaller nanoparticles would no longer be beneficial because at this point, absorption becomes permeation limited. Therefore, improvements in systemic absorption rates would be more efficiently accomplished by incorporating permeation enhancers into the pulmonary composition. Phospholipids such as dipalmitoylphosphatidylcholine (DPPC) and lecithin are known to enhance permeability through lung tissue[7, 8]. Yang et al. demonstrated higher systemic rates of a nebulized itraconazole formulation containing lecithin compared to a similar nebulized itraconazole formulation that did not contain a permeation enhancer[5, 6]. Therefore, it would be of interest to further examine this concept that the absorption of BCS class II drugs may become permeation limited once saturation of the fluid in the lung lining is reached, which is easily achieved due to the small volume of liquid in the deep lungs (~10 μL)[9]. In order to thoroughly understand the effects of permeation enhancers in pulmonary compositions on systemic absorption rates, pulmonary delivery of comparable drug formulations with and without permeation enhancers to animals and subsequent analysis of blood levels are needed.

Additionally, dissolution rates of aerosolized particles may be more accurately studied by utilizing a novel dissolution method currently being developed by Son et al.[10], in which the dissolution rates of the particles that deposit on each plate of an aerosol impactor device may be studied separately. This knowledge will provide additional insight into the viability of a pulmonary composition to be efficiently absorbed in the lungs. Furthermore, the ability of an aerosolized composition to perform a specific cellular function may be tested by coating the stages of an aerosol impactor with a desired marker. After aerosolization into the impactor, the specific markers may be analyzed to determine if a sufficient amount of drug was able to reach the desired location in the lungs and elicit a therapeutic effect. This technique was demonstrated by Haynes et al.[11], where the ability of an aerosolized cyclooxygenase-2 (COX-2) inhibitor, nimesulide, to facilitate cytotoxicity and an apoptotic response against a human lung adenocarcinoma cell line was examined.

For pMDI delivery specifically, additional studies on the long term storage stability of the pMDI suspensions on aerosol performance is recommended. The ability of the flocs to form respirable particles over an extended period of time is of practical interest, as this knowledge influences the shelf-life of a product. Furthermore, pMDI dosing to an animal model would be beneficial to demonstrate the efficacy of these novel aerosol pMDI compositions. Several pMDI commercial products contain more than one active ingredient[12, 13]. Therefore, it would also be interesting to study how floc formation and structure, and thus suspension stability and aerosol performance, are affected upon the addition of two particles with different morphologies.

7.2.2 Controlled Assembly of Nanoparticle Clusters for Biomedical Imaging and Therapy

Multifunctional nanoparticles that possess specific targeting capabilities have the potential to revolutionize health care for numerous diseases, especially cancer[14, 15]. Thus, it is recommended that the nanocluster assembly method presented in chapter 5 of this dissertation be extended to the incorporation of magnetic nanoparticles and/or therapeutic agents. The ability to simultaneously deliver a combination of imaging/therapeutic modalities is a tremendous advancement over current commercialized options because it would provide more efficient treatment of diseases, as well as facilitate early detection of diseases. However, a key challenge in the development of such a product is to devise a robust strategy to load an extremely high degree of targeting, imaging, and therapeutic functionality into small, yet stable particles. The generality of our nanocluster assembly method is highly advantageous because it is not dependent on specific chemical interactions for cluster formation. Therefore, it is likely that additional materials such as iron oxide nanoparticles, which impart magnetic capabilities, and therapeutic agents may be easily incorporated into the nanoclusters. The effect of incorporating these additional materials on the size and optical properties of the cluster will need to be examined. For instance, if all the constituent particles, gold, iron oxide, and a drug, are homogenously mixed throughout the cluster, the cluster is not as likely to maintain strong NIR absorbance, as the separation distance between each gold particle will likely increase. Therefore, the morphology of these new multifunctional nanoclusters must be carefully considered. One potential method of producing a multifunctional nanoparticle would be to first produce nanoclusters containing only drug and iron oxide nanoparticles. Then, those initial drug/iron oxide nanoclusters may be incorporated into a larger cluster with gold nanoparticles, bound together with a polymeric binder, to maintain strong NIR absorbance. Furthermore, active targeting of these nanoclusters may be achieved by functionalizing the gold nanoparticles with antibodies, using methods described by Sokolov et al.[14, 16-20].

7.3 REFERENCES

1. Matteucci, M. E.; Brettmann, B. K.; Rogers, T. L.; Elder, E. J.; Williams, R. O.; Johnston, K. P., Design of Potent Amorphous Drug Nanoparticles for Rapid Generation of Highly Supersaturated Media. *Molecular Pharmaceutics* **2007,** 4, (5), 782-793.

2. Jiang, W.; Kim, B. Y. S.; Rutka, J. T.; Chan, W. C. W., Nanoparticle-mediated cellular response is size-dependent. *Nature Nanotechnology* **2008,** 3, (3), 145-150.

3. Peeters, J.; Neeskens, P.; Tollenaere, J. P.; Van Remoortere, P.; Brewster, M. E., Characterization of the interaction of 2-hydroxypropyl-beta-cyclodextrin with itraconazole at pH 2, 4 and 7 *Journal of Pharmaceutical Sciences* **2002,** 91, 1414–1422.

4. McConville, J. T.; Overhoff, K. A.; Sinswat, P.; Vaughn, J. M.; Frei, B. L.; Burgess, D. S.; Talbert, R. L.; Peters, J. I.; Johnston, K. P.; Williams, R. O., III, Targeted High Lung Concentrations of Itraconazole Using Nebulized Dispersions in a Murine Model. *Pharmaceutical Research* **2006,** 23, (5), 901-911.

5. Vaughn, J. M.; McConville, J. T.; Burgess, D.; Peters, J. I.; Johnston, K. P.; Talbert, R. L.; Williams, R. O., III, Single dose and multiple dose studies of itraconazole nanoparticles. *European Journal of Pharmaceutics and Biopharmaceutics* **2006,** 63, (2), 95-102.

6. Yang, W.; Tam, J.; Miller, D. A.; Zhou, J.; McConville, J. T.; Johnston, K. P.; Williams, R. O., High bioavailability from nebulized itraconazole nanoparticle dispersions with biocompatible stabilizers. *International Journal of Pharmaceutics* **2008,** 361, (1-2), 177-188.

7. Liu, F.; Shao, Z.; Kildsig, D. O.; Mitra, A. K., Pulmonary delivery of free and liposomal insulin. *Pharmaceutical Research* **1993,** 10, (2), 228-32.

8. Mitra, R.; Pezron, I.; Li, Y.; Mitra, A. K., Enhanced pulmonary delivery of insulin by lung lavage fluid and phospholipids. *International Journal of Pharmaceutics* **2001,** 217, (25-31).

9. Patton, J. S., Mechanisms of macromolecule absorption by the lungs. *Advanced Drug Delivery Reviews* **1996,** 19, (1), 3-36.

10. Son, Y. J.; McConville, J. T. In *Improvements of an In Vitro Dissolution Test Method For Dry Inhalation Formulations*, American Association of Pharmaceutical Scientists Annual Meeting, Atlanta, GA, 2008; Atlanta, GA, 2008.

11. Haynes, A.; Shaik, M. S.; Chatterjee, A.; Singh, M., Evaluation of an aerosolized selective COX-2 inhibitor as a potentiator of doxorubicin in a non-small-cell lung cancer cell line. *Pharmaceutical Research* **2003,** 20, (9), 1485-1495.

12. Courrier, H. M.; N. Butz; Vandamme, T. F., Pulmonary Drug Delivery Systems: Recent Developments and Prospects. *Critical Reviews in Therapeutic Drug Carrier Systems* **2002,** 19, (4 and 5), 425-498.

13. Smyth, H. D. C., The influence of formulation variables on the performance of alternative propellant-driven metered dose inhalers. *Advanced Drug Delivery Reviews* **2003,** 55, (7), 807-828.

14. Larson, T. A.; Bankson, J.; Aaron, J.; Sokolov, K., Hybrid plasmonic magnetic nanoparticles as molecular specific agents for MRI/optical imaging and photothermal therapy of cancer cells. *Nanotechnology* **2007,** 18, (32), 325101/1-325101/8.

15. Wang, A. Z.; Bagalkot, V.; Vasilliou, C. C.; Gu, F.; Alexis, F.; Zhang, L.; Shaikh, M.; Yuet, K.; Cima, M. J.; Langer, R.; Kantoff, P. W.; Bander, N. H.; Jon, S.; Farokhzad, O. C., Superparamagnetic iron oxide nanoparticle-aptamer bioconjugates for combined prostate cancer imaging and therapy. *ChemMedChem* **2008,** 3, (9), 1311-1315.

16. Aaron, J.; Nitin, N.; Travis, K.; Kumar, S.; Collier, T.; Park, S. Y.; Jose-Yacaman, M.; Coghlan, L.; Follen, M.; Richards-Kortum, R.; Sokolov, K., Plasmon resonance coupling of metal nanoparticles for molecular imaging of carcinogenesis in vivo. *Journal of Biomedical Optics* **2007,** 12, (3), 034007/1-034007/11.

17. Aaron, J. S.; Oh, J.; Larson, T. A.; Kumar, S.; Milner, T. E.; Sokolov, K. V., Increased optical contrast in imaging of epidermal growth factor receptor using magnetically actuated hybrid gold/iron oxide nanoparticles. *Optics Express* **2006,** 14, (26), 12930-12943.

18. Kumar, S.; Harrison, N.; Richards-Kortum, R.; Sokolov, K., Plasmonic Nanosensors for Imaging Intracellular Biomarkers in Live Cells. *Nano Letters* **2007,** 7, (5), 1338-1343.

19. Sokolov, K. V.; Follen, M.; Aaron, J.; Pavlova, I.; Malpica, A.; Lotan, R.; Richards-Kortum, R., Real-time vital optical imaging of precancer using anti-epidermal growth factor receptor antibodies conjugated to gold nanoparticles. *Cancer Research* **2003,** 63, 1999-2004.

20. Kumar, S.; Aaron, J.; Sokolov, K., Directional conjugation of antibodies to nanoparticles for synthesis of multiplexed optical contrast agents with both delivery and targeting moieties. *Nature Protocols* **2008,** 3, (2), 314-320.

Appendix A: Templated Open Flocs of Nanorods for Enhanced Pulmonary Delivery with Pressurized Metered Dose Inhalers

Bruggeman mixing rule

For porous particles or suspensions with a BSA particle volume fraction ϕ, the effective refractive index n_e and dielectric constant ε_e can be calculated from the following Bruggeman mixing relationships

$$(1-\phi)\frac{{n_A}^2-{n_e}^2}{{n_A}^2+2{n_e}^2}+\phi\frac{{n_B}^2-{n_e}^2}{{n_B}^2+2{n_e}^2}=0 \qquad \text{(A.1)}$$

$$(1-\phi)\frac{\varepsilon_A-\varepsilon_e}{\varepsilon_A+2\varepsilon_e}+\phi\frac{\varepsilon_B-\varepsilon_e}{\varepsilon_B+2\varepsilon_e}=0 \qquad \text{(A.2)}$$

where ϕ can be either ϕ_g or ϕ_f, the subscript A denotes air or HFA 227, and B denotes BSA.

Attractive van der Waals equations

The Φ_{vdw} is directly proportional to the Hamaker constant A_{121} for one particle interacting with another (subscript 1) across solvent, such as HFA 227 or acetonitrile, (subscript 2) as a function of the particle geometry [1]. The Hamaker constant A_{121} may be approximated by

$$A_{121}=\left(\sqrt{A_{11}}-\sqrt{A_{22}}\right)^2 \qquad \text{(A.3)}$$

where A_{11} and A_{22} are the pure Hamaker constants for BSA and the suspending media interacting across a vacuum, respectively. These values were calculated from Lifshitz theory [1, 2]. To determine A_{11} for porous BSA particles in HFA 227, ε_e and n_e were calculated with the Bruggeman mixing rule (Eq. A.1 and A.2) at ϕ = 0.5 in HFA 227 [3, 4]. The van der Waals attractive potential between identical spherical particles [1]

$$\Phi_{vdw} = -\frac{A_{121}R}{12h} \qquad \text{(A.4)}$$

which has an attractive force F_{vdw} given as

$$F_{vdw} = \frac{A_{121}R}{12h^2} \qquad \text{(A.5)}$$

where R is the spherical particle radius and h is the separation distance between the particle surfaces and for identical hollow spheres with solid shells [5]

$$\Phi_{vdw} = -\frac{A_{121}R}{12}\left(\frac{1}{h+2t} - \frac{2}{h+t} + \frac{1}{h}\right) - \frac{A_{121}}{6}\ln\left(\frac{h(h+2t)}{(h+t)^2}\right) \qquad \text{(A.6)}$$

where t is the shell thickness. For identical rods, E_{vdw} can be calculated for parallel

$$\Phi_{vdw} = -\frac{A_{121}LR^{1/2}}{24h^{3/2}} \qquad \text{(A.7)}$$

or crossed cylinders

$$\Phi_{vdw} = -\frac{A_{121}R}{6h} \qquad \text{(A.8)}$$

where L is the cylinder length. The values from Eq. A.7 and A.8 were averaged to give equal weight to the two orientations (Table 3.3).

Space filling floc derivation

A vial filled with protein particles of total mass m and primary particle density ρ_p into a given volume V of HFA 227 has a volume fraction ϕ_v defined as

$$\phi_v = \frac{m / \rho_p}{V} \quad \text{(A.9)}$$

The volume fraction of particles in a floc ϕ_f is

$$\phi_f = \frac{V_p \cdot k}{V_f} \quad \text{(A.10)}$$

where V_p and V_f are the volume of a spherical primary particle and a spherical floc, respectively, and k is the number of primary particles in a floc.

The volume fraction of flocs in HFA ϕ^{flocs} is defined as

$$\phi^{flocs} = \frac{V_f \cdot N_f}{V} \quad \text{(A.11)}$$

where N_f is the total number of flocs in suspension. $N_f = N_p / k$ where $N_p = m / m_p$ is the total number of primary particles in suspension and $m_p = V_p \cdot \rho_p$ is the mass of a primary particle. Substitution into Eq A.11 gives

$$\phi^{flocs} = \frac{V_f \cdot m}{V_p \cdot k \cdot V \cdot \rho_p} = \frac{\phi_v}{\phi_f} \quad \text{(A.12)}$$

References

1. Israelachvili J. Intermolecular and surface forces. San Diego: Academic Press, 1992.
2. Takashima S. Journal of Physical Chemistry 1965;69(7):2281-2286.
3. Sihvola A. Electromagnetic mixing formulas and applications, 1999.
4. Vanbever R, Mintzes JD, Wang J, Nice J, Chen D, Batycky R, Langer R, and Edwards DA. Pharmaceutical Research 1999;16(11):1735-1742.
5. Tadmor R. Journal of Physics: Condensed Matter 2001;13(9):L195-L202.

Appendix B: Templated Open Flocs of Anisotropic Particles for Pulmonary Delivery with Pressurized Metered Dose Inhalers

Bruggeman mixing rule

The effective refractive index, n_e, and effective dielectric constant, ε_e, for porous particles or open flocs, with a particle volume fraction, φ, may be determined using the following Bruggeman mixing relationships:

$$(1-\varphi)\frac{n_A^2 - n_e^2}{n_A^2 + 2n_e^2} + \phi\frac{n_B^2 - n_e^2}{n_B^2 + 2n_e^2} = 0 \qquad \text{(B.1)}$$

$$(1-\varphi)\frac{\varepsilon_A - \varepsilon_e}{\varepsilon_A + 2\varepsilon_e} + \phi\frac{\varepsilon_B - \varepsilon_e}{\varepsilon_B + 2\varepsilon_e} = 0 \qquad \text{(B.2)}$$

where φ is either φ_g or φ_f, depending on the suspension media, the subscript A denotes the appropriate medium, air or HFA 227, and B denotes the drug.

Attractive van der Waals equations

The VDW attractive potential, Φ_{vdw}, is directly proportional to the effective Hamaker constant, A_{121}, for a pair of particles (subscript 1) interacting across a medium (subscript 2)[1]. The Hamaker constant A_{121} may be determined by

$$A_{121} = \left(\sqrt{A_{11}} - \sqrt{A_{22}}\right)^2 \qquad \text{(B.3)}$$

where A_{11} and A_{22} are the Hamaker constants for the drug and the media interacting across a vacuum, respectively. A_{11} and A_{22} values were calculated using Lifshitz theory [1, 2].

For porous Itz particles, A_{11} was determined using n_e and ε_e values calculated using the Bruggeman mixing rule (Eq. B.1-B.2) at φ = 0.5[3, 4]. The van der Waals attractive potential between two particles is dependent on the particle geometry. For two identical spheres, Φ_{vdw} is determined by [1]

$$\Phi_{\mathrm{vdw}} = -\frac{A_{121}R}{12h} \qquad (B.4)$$

where R is the radius and h is the separation distance between the particle surfaces. For identical hollow spheres[5]

$$\Phi_{\mathrm{vdw}} = -\frac{A_{121}R}{12}\left(\frac{1}{h+2t} - \frac{2}{h+t} + \frac{1}{h}\right) - \frac{A_{121}}{6}\ln\left(\frac{h(h+2t)}{(h+t)^2}\right) \quad (B.5)$$

where t is the shell thickness. For identical rods, Φ_{vdw} can be calculated for two configurations, parallel

$$\Phi_{\mathrm{vdw}} = -\frac{A_{121}LR^{1/2}}{24h^{3/2}} \quad (B.6)$$

or crossed cylinders

$$\Phi_{\mathrm{vdw}} = -\frac{A_{121}R}{6h} \qquad (B.7)$$

where L is the cylinder length. The two possible orientations for cylinders were given equal weight to yield an average value for Φ_{vdw}. For two thin plates, Φ_{vdw} is determined to be

$$\Phi_{\mathrm{vdw}} = -\frac{A_{121}}{12\pi}\left(\frac{1}{h^2} + \frac{1}{(h+2\delta)^2} - \frac{2}{(h+\delta)^2}\right) \qquad \text{(B.8)}$$

where δ is the thickness of the plate.

Figure B.1 pMDI (a) vial prior to addition of HFA 227 and (b) after exposure to HFA 227.

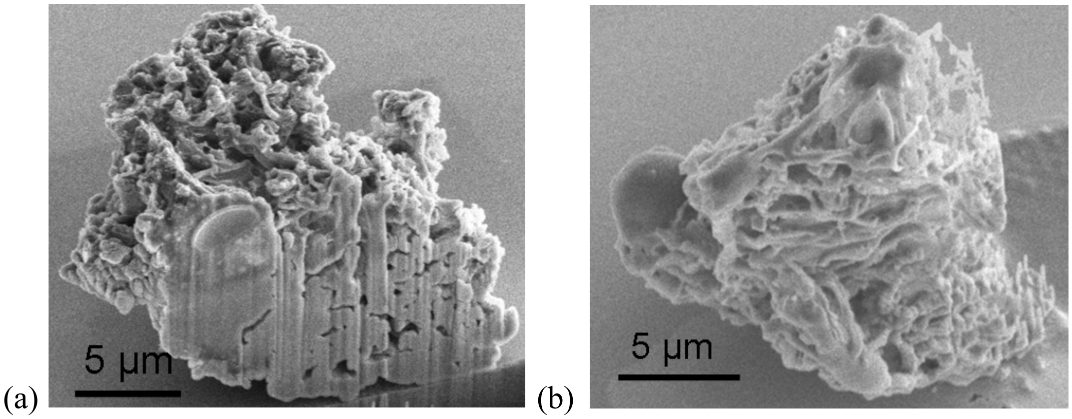

Figure B.2 SEM image of an aerosolized (a) TFF Itz and (b) TFF BSA from a pMDI (drug loading of 10 mg/mL). A focused ion beam laser was used to slice of a portion of the particle in order to view the morphology of the interior of the aerosolized particle.

References

1. Israelachvili, J., *Intermolecular and Surface Forces*. 2 ed.; Academic Press, Inc.: San Diego, 1992.

2. Takashima, S., Proton fluctuation in protein. Experimental study of the Kirkwood-Shumaker theory. *Journal of Physical Chemistry* **1965,** 69, (7), 2281-6.

3. Sihvola, A., *Electromagnetic mixing formulas and applications*. 1999; Vol. 47.

4. Vanbever, R.; Mintzes, J. D.; Wang, J.; Nice, J.; Chen, D.; Batycky, R.; Langer, R.; Edwards, D. A., Formulation and physical characterization of large porous particles for inhalation. *Pharmaceutical Research* **1999,** 16, (11), 1735-1742.

5. Tadmor, R., The London-van der Waals interaction energy between objects of various geometries. *Journal of Physics: Condensed Matter* **2001,** 13, (9), L195-L202.

Appendix C: Controlled Assembly of Biodegradable Plasmonic Nanoclusters for Near-Infrared Imaging and Therapeutic Applications

Methods:

Gold particle synthesis:

To synthesize the citrate-capped gold nanoparticles, 100 mL of DI water was heated to 97°C. While stirring, 1 mL of 1% $HAuCL_4•3H_2O$, 1 mL of 1% $Na_3C_3H_5O(COO)_3$ •2 H_2O, and 1 mL of 0.075% $NaBH_4$ in a 1% $Na_3C_3H_5O(COO)_3$•2 H_2O solution was added in one minute intervals. The solution was stirred for five minutes and then removed to an ice bath to cool to room temperature. The gold particles were then concentrated using centrifugal filter devices (Ultracel YM-30, Millipore Co.) to 3.0 mg Au/mL. Gold concentrations were determined using flame atomic absorption spectroscopy (FAAS), as described below.

Nanocluster characterization:

The nanocluster morphology was observed by scanning electron (SEM) and transmission electron microscopy (TEM). A Zeiss Supra 40VP field emission SEM was operated at an accelerating voltage of 5−10 kV. SEM samples were prepared by depositing a dilute aqueous dispersion of the nanoclusters onto a silicon wafer. The sample was dried and washed with DI water to remove excess polymer. TEM was performed on a FEI TECNAI G2 F20 X-TWIN TEM using a high-angle annular dark field detector. A dilute aqueous dispersion of the nanoclusters was deposited onto a 200 mesh carbon-coated copper TEM grid for observation. Separation distances between primary particles within the nanoclusters were measured by analyzing TEM images using Scion Image software (Frederick, Maryland). UV−vis spectra were obtained with a

Varian Cary 5000 spectrophotometer and a 1 cm path length. Dynamic light scattering (DLS) measurements of hydrodynamic diameter and zeta potential measurements were performed in triplicate on a Brookhaven Instruments ZetaPlus dynamic light scattering apparatus (scattering angle of 90°) at a temperature of 25°C[1]. Dispersion concentrations were adjusted with either DI water for DLS measurements or pH=7.4 buffer (10 mM) for zeta potential measurements to yield a measured count rate between 300-400 kcps. Prior to all DLS measurements, the nanocluster dispersions were filtered through a 0.2 μm filter and probe sonicated for 2 minutes. Data analysis was performed using a digital autocorrelator (Brookhaven BI-9000AT) with a non-negative least-squares (NNLS) method (Brookhaven 9KDLSW32). Reported average diameters correspond to the D_{50}, or diameter at which the cumulative sample volume was under 50%. For zeta potential measurements, the average value of at least three data points was reported. Thermogravimetric analysis (TGA) was conducted using a Perkin–Elmer TGA 7 under nitrogen atmosphere at a gas flow rate of 20 mL/min. The samples were cleaned to remove excess polymer by centrifuging nanocluster dispersions at 8000 rpm for 5 minutes at 4^{o}C. TGA samples were heated at a constant rate of 20 °C/min from 30°C to 800 °C and then held at 800°C for 30 minutes. Flame atomic absorption spectroscopy (FAAS) was used to determine the gold concentration in the nanocluster dispersions using a GBC 908AA flame atomic absorption spectrometer (GBC Scientific Equipment Pty Ltd). Measurements were conducted at 242.8 nm using an air-acetylene flame. To determine clustering efficiency, a dispersion of nanoclusters of known concentration was centrifuged at 10,000 rpm for 10 minutes at 4^{o}C. FAAS measurements were conducted on the supernatant.

Hyperspectral characterization of nanoclusters in solution:

Microscope slides were submerged in a warm, aqueous gelatin solution (3% w/v) for 10 minutes. The slides were removed from the gelatin and 10 μL of a dilute nanocluster dispersion (~0.01 mg/mL) were placed on the gelatin coated slide and covered with a cover slip. The gelatin was allowed to cool for 2 hours, to allow the nanoparticles to solidify into the gelatin. Hyperspectral images were acquired under the same conditions described previously.

Additional Results and Discussion

Proposed mechanism for nanocluster formation:

The ability to simultaneously control cluster size and spacing of gold nanoparticles within the nanocluster was achieved by manipulating particle volume fractions upon solvent evaporation, as well as the interactions between the gold primary particles and the polymer binder. In the absence of polymer, primary gold nanoparticles formed undesirably large aggregates (> 1 μm) upon complete solvent evaporation to form a film. Thus, the polymer was needed to provide steric stabilization to the clusters. In another control experiment, the addition of polymer to the colloidally stable gold nanoparticle dispersion without solvent evaporation resulted in a mild color change to a red-purple after approximately one hour. However, clusters capable of significant NIR absorbance were not produced, as seen in Figure C.4, where the size of the gold particles did not change significantly according to DLS, and consequently, the extinction spectrum was essentially identical to that of the initial colloidal gold dispersion even four hours after the addition of the polymer. At these dilute conditions, the polymer formed stable micelles with a hydrodynamic diameter of 10-14 nm (data not shown), and the electrostatic repulsion between ligand-capped gold particles prevented significant particle aggregation. However, it is likely that the polymer addition resulted in the formation of dimmers and trimers, which were able to cause a mild color change[2, 3] but too small to elicit a strong red-shift into the NIR. Therefore, cluster formation was likely initiated by the adsorption of the PLA block of the polymer to gold, as PLA homopolymer is known to sterically stabilize gold nanoparticles in organic solvents[4]. Upon polymer adsorption, the local dielectric constant decreases and causes significant ion pairing of the charges on the ligands on the gold nanoparticles. The decrease in electrostatic repulsion upon polymer adsorption was evidenced by a shift in zeta potential from -30.1 ± 2.4 mV for the lysine/citrate-capped gold nanoparticles to -14.99 ± 2.3 mV after the addition of polymer.

When particle volume fractions in the polymer/gold dispersion were increased by only a factor of 2 (50% evaporation), only a modest red-shift in the SPR was produced, indicating that particle aggregation was still very limited. However, a further increase to 80% evaporation, which raised the gold concentration from an initial concentration of 3 to 15 mg/mL and the polymer concentration from 50 to 250 mg/mL, produced nanoclusters with strong NIR absorbances. Thus, high particle volume fractions were required to drive nanocluster growth. Interestingly, the average sizes of nanoclusters produced after 80% and 100% solvent evaporation were similar (Figure C.4A). Upon 100% evaporation, approximately 99% by weight of the gold in the initial dispersion was incorporated within the clusters, as determined by FAAS. The calculated moments in the particle size distribution measured by dynamic light scattering (μ_1 and μ_3 were 1.1 ±0.02 and 0.93±0.01, respectively) indicate that the clusters were predominantly formed by condensation, with only a moderate amount of coagulation[5]. Thus, the lack of free gold nanocrystals likely causes termination in the cluster growth by condensation.

Experimental observations during the cluster formation process may be explained by changes in the stability ratio, *W*, which is defined as the rate of slow, kinetically-controlled particle assembly to fast, diffusion controlled assembly[6, 7]

$$W = \frac{t_{1/2,s}}{t_{1/2,f}} \qquad \text{(C.1)}$$

where $t_{1/2,f}$ and $t_{1/2,s}$ are the half-lives for fast and slow flocculation, respectively, and $t_{1/2,f}$ is calculated by[6, 7]

$$t_{1/2,f} = \frac{3\eta}{4k_b TN_0} \tag{C.2}$$

where η is the viscosity, and N_0 is the initial number density of nanoparticles. Values for $t_{1/2,s}$ may be estimated using experimentally observed times required for the occurrence of a color change in solution[8]. The initial colloidal gold nanoparticle dispersion, without the addition of polymer, was extremely stable, with no observable change in the color of the dispersion for ~1 month, corresponding to a very high W of $\sim 10^{10}$, given the low particle densities and strong electrostatic stabilization from the charged ligands. The experimentally determined W decreased to $\sim 10^5$ for 50% evaporation (based on an estimated time of ~5 minutes to observe a color change) due to the surface charge reduction on the particles upon polymer adsorption and the factor of 2 increase in particle concentration. Experimental values of W may also be related to the interaction potentials between two particles[7]. The expression for V_{total} includes the electrostatic and van der Waals DLVO forces, as well depletion attraction and steric repulsion

$$V_{total} = V_{electrostatic} + V_{VDW} + V_{depletion} + V_{steric} \tag{C.3}$$

The “depletion” attraction is an osmotic force arising from the exclusion of polymer micelles from the space between two gold particles or embryonic clusters[9]. The depletion force, along with the propensity for the hydrophilic PEG loops to drive the mobile, weakly adsorbed polymer away from the gold cluster interior and to the exterior interface with water, explains the low polymer loadings in the clusters. Thus, the control of both the polymer micelle and gold particle volume fractions during evaporation facilitated the attraction that led to cluster formation. Furthermore, the cluster size is maintained by steric repulsion from the PEG loops on the nanocluster exterior for the short period until the nanoclusters are harvested.

The nearly complete deaggregation of the clusters to the original gold primary particles may also be explained by the total potential, as well as positive entropy of mixing of the individual gold nanoparticles. For the redispersed nanoclusters in a pure solvent, without excess polymer, the electrostatic repulsion becomes much stronger and the particles deaggregate.

To determine the size distribution moments in the nanocluster population:

Size distribution moments, μ_1 and μ_3, were used to determine whether cluster formation was dominated by condensation or coagulation[5].

$$\mu_1 = \frac{r_3}{r_h} = \frac{\sqrt[3]{\Sigma r_i^3 / N_{Tot}}}{N_{Tot} / \Sigma \frac{1}{r_i}} \qquad (C.4)$$

$$\mu_3 = \frac{r_1}{r_3} = \frac{\Sigma r_i / N_{Tot}}{\sqrt[3]{\Sigma r_i^3 / N_{Tot}}} \qquad (C.5)$$

where r_1 is the arithmetic mean radius, r_3 is the cube mean radius, r_h is the harmonic mean radius, and N_{Tot} is the total number of particles in the system. When $\mu_1 = \mu_3 = 1$, the size distribution moments reflect a monodisperse system where aggregates have been formed by condensation. Size distribution moments where $\mu_1 > 1.25$ and $\mu_3 < 0.905$ suggest that aggregates were formed by coagulation.

To determine the nanocluster extinction cross section:

For a dilute solution, absorbance (A) follows Beer–Lambert's Law:

$$A = \varepsilon(\lambda)\, C \ell \qquad \text{(C.6)}$$

where ε is the extinction coefficient , which is dependent on wavelength, C is the dispersion concentration, and ℓ is the path length through which light travels. For a path length of 1 cm, determined by cuvette dimensions, and a gold concentration of 56 μg/mL, the maximum absorbance, found at a wavelength of 703 nm, was 1.10. Using Eq. C.6, we determined that $\varepsilon_{703\text{nm}}$ was 0.020 $\text{cm}^2/\mu\text{g}$. Assuming that the nanoclusters are spherical, with an average diameter of 100 nm, and the nanoparticles are in a closest-packed state, the particle extinction cross section was calculated by:

$$\varepsilon_{703\text{ nm}} \text{ x } M_{\text{Au in 1 nanocluster}} \qquad \text{(C.7)}$$

where $M_{\text{Au in 1 nanocluster}}$ is the mass of gold per nanocluster. The particle extinction cross section was calculated to be ~1.0 x 10^{-14} m^2.

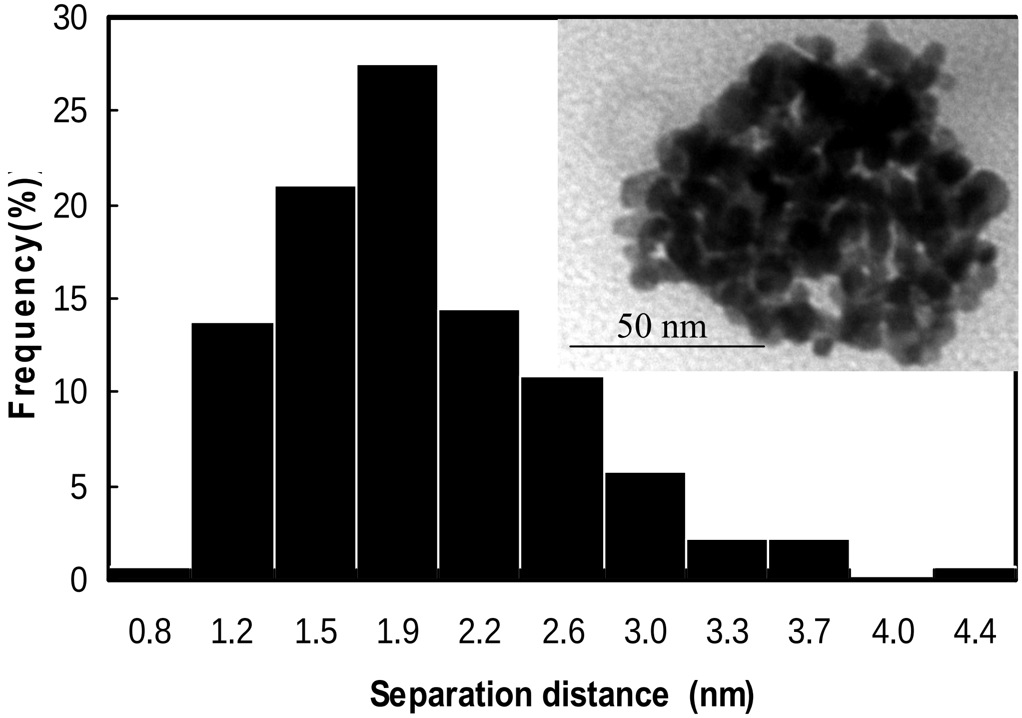

Figure C.1 Histogram of separation distances between primary gold nanoparticles within a nanocluster. Measurements (>130 data points) were taken using particles on the periphery of the nanoclusters. Inset is a TEM image of one of the clusters that was used in this measurement.

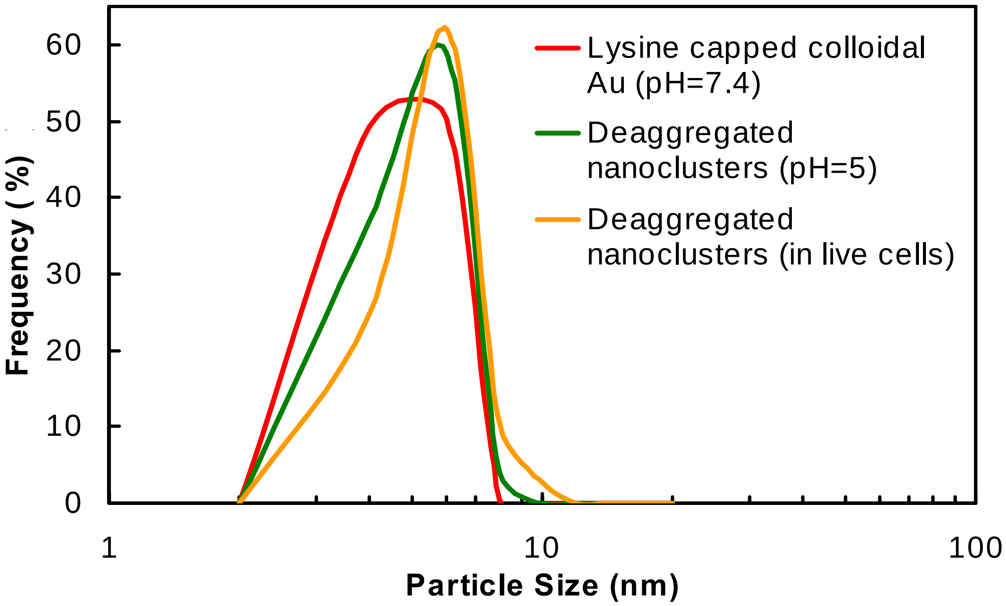

Figure C.2 Particle size distribution of primary lysine/citrate-capped Au particles (green curve), nanoclusters deaggregated at pH=5 (red curve), and nanoclusters after biodegradation in live cells (blue curve) determined by image analysis of over 100 particles per sample in TEM micrographs.

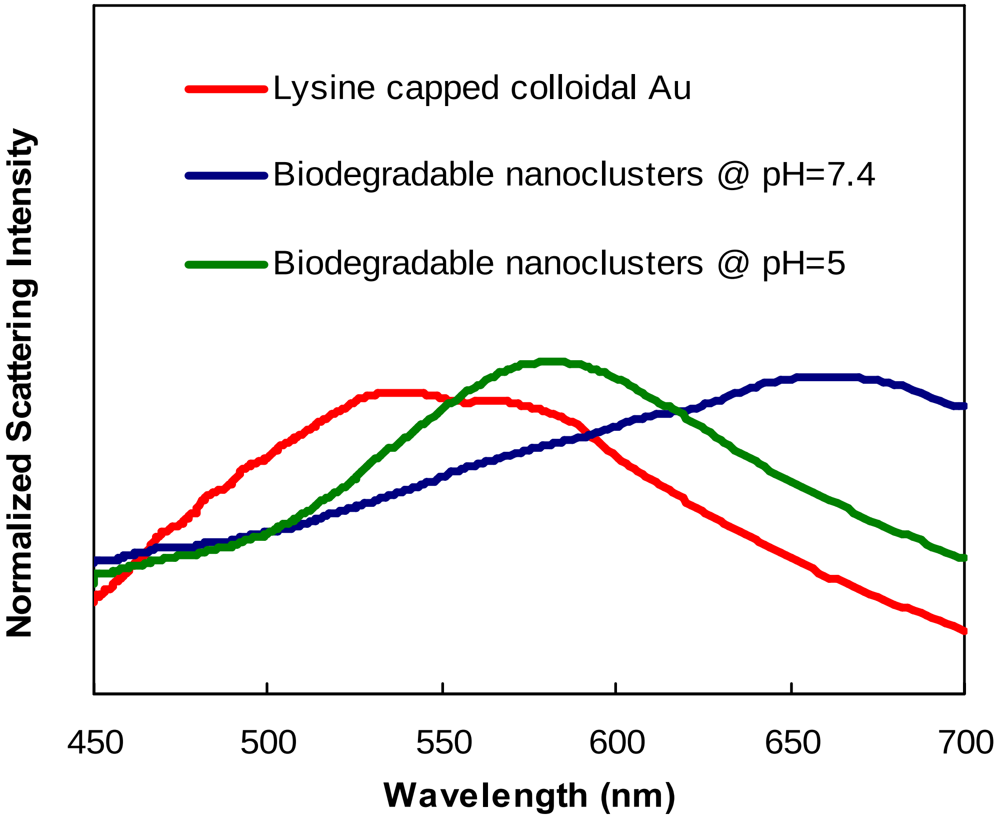

Figure C.3 Hyperspectral scattering spectra (normalized to the area under the curve) of biodegradable nanoclusters at pH=7.4 (dark-blue curve), deaggregated nanoclusters at pH=5 (green curve), and the primary lysine/citrate-capped colloidal Au (red curve).

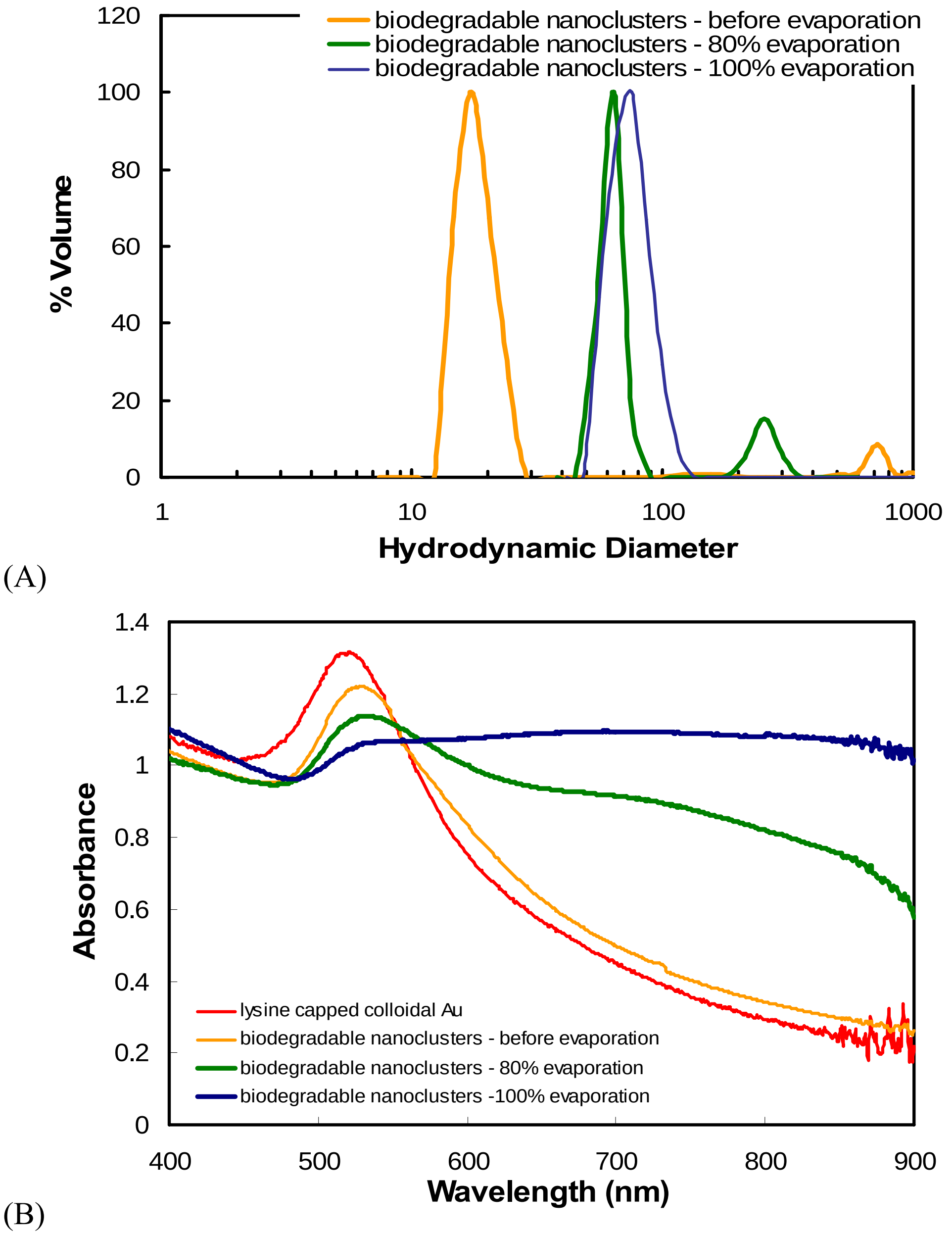

Figure C.4 (A) UV-vis absorbance and (B) particle size distribution of a solution of PLA-*b*-PEG-*b*-PLA with lysine/citrate-capped gold nanoparticles four hours after polymer addition (without evaporation) and after 80% solvent evaporation to form the nanoclusters

References

1. Ryoo W, Webber SE, and Johnston KP. Ind. Eng. Chem. Res. 2003;42(25):6348-6358.

2. Blatchford CG, Campbell JR, and Creighton JA. Surface Science 1982;120:445-455.

3. Khlebtsov B, Zharov V, Melnikov A, Tuchin V, and Khlebtsov N. Nanotechnology 2006;17(20):5167-5179.

4. Sun Y-L, Chen Y-Z, Wu R-J, Chavali M, Huang Y-C, Su P-G, and Lin C-C. Sensors and Actuators B 2007;126:441-446.

5. Shah PS, Husain S, Johnston KP, and Korgel BA. Journal of Physical Chemistry B 2002;106(47):12178-12185.

6. Chow MK and Zukoski CF. Journal of Colloid and Interface Science 1994;165(1):97-109.

7. Hiemenz PC, Rajagopalan R, and Editors. Principles of Colloid and Surface Chemistry, Third Edition, Revised and Expanded, 1997.

8. Kim T, Lee C-H, Joo S-W, and Lee K. Journal of Colloid and Interface Science 2008;318:238-243.

9. Mondain-Monval O, Leal-Calderon F, Phillip J, and Bibette J. Physical Review Letters 1995;75:3364-3367.

Appendix D: Kinetic Assembly of Near-IR Active Gold Nanoclusters Using Weakly Adsorbing Polymers to Control Size

Calculation of ligand coverage:

The saturation coverage of citrate ligands on ~4 nm gold particles was compared with the experimentally determined citrate/gold ratio obtained by TGA. The saturation coverage of a gold particle by citrate was reported to be 4.6×10^{-10} mol/cm^2 [1], which corresponds to a footprint of 0.36 nm^2/ citrate ligand. The surface area of the particle was divided by the footprint of the ligand to determine the maximum number of citrate ligands that could cover the gold particle was ~140. This amount of citrate coverage on the gold nanoparticle corresponds to 6.3% citrate by weight, which agrees well with the experimentally determined value of 7% obtained by TGA. Therefore, the gold surface was saturated by citrate ligands.

Calculation of polydispersity index (PDI):

The PDI was calculated as M_w/M_n, where M_w and M_n are the weight averaged and number averaged masses, respectively and may be calculated using[2]

$$M_w = \frac{\sum M_i^2 N_i}{\sum M_i N_i} \qquad \text{(D.1)}$$

$$M_n = \frac{\sum M_i N_i}{\sum N_i} \qquad \text{(D.2)}$$

where M is mass and N is the number of particles. PDI determinations were obtained using number weighted particle size distributions obtained using DLS.

Calculation of displacement of citrate ligands by lysine:

The displacement of citrate ligands by lysine on gold nanoparticles was estimated using the difference in zeta potentials measured for the citrate-only-capped nanoparticles,

-44 mV, versus the citrate/lysine-capped nanoparticles, -30 mV. The charge on the particles, Q, was related to the surface potential, ψ_0, using

$$Q = \varepsilon_r \varepsilon_0 \Psi_0 a(1 + \kappa a) \qquad \text{(D.3)}$$

where ε_r, the dielectric constant of the aqueous medium, is 80, ε_0 is the permittivity of free space, *a* is the particle radius, and κ is the inverse Debye length, which is defined as

$$\kappa = e\sqrt{\frac{2N_A I}{\varepsilon_r \varepsilon_0 k_b T}} \qquad \text{(D.4)}$$

where *e* is the elementary charge of an electron, N_A is Avagadro's number, and *I* is the ionic strength. *I* was calculated to be 0.0053M, shown in detail below, using ligand/gold ratios determined from TGA using the following equation:

$$I = 0.5\sum_{i=1}^{n} c_i z_i^2 \qquad \text{(D.5)}$$

where c_i is the molar concentration of ion *i* and z_i is the charge of an ion. In this system, sodium ions are assumed to be the only free ions in solution. Surface potential was estimated using the experimentally measured zeta potential for this calculation. The ratio of charge for the citrate-only capped nanoparticles to that for the citrate/lysine capped nanoparticles was used to estimate the displacement of citrate by lysine.

Calculation of size distribution moments:

Size distribution moments, μ_1 and μ_3, were used to determine whether cluster formation was dominated by condensation or coagulation.

$$\mu_1 = \frac{r_3}{r_h} = \frac{\sqrt[3]{\Sigma r_i^3 / N_{Tot}}}{N_{Tot} / \Sigma \frac{1}{r_i}} \qquad \text{(D.6)}$$

$$\mu_3 = \frac{r_1}{r_3} = \frac{\Sigma r_i / N_{Tot}}{\sqrt[3]{\Sigma r_i^3 / N_{Tot}}} \qquad \text{(D.7)}$$

where r_1 is the arithmetic mean radius, r_3 is the cube mean radius, r_h is the harmonic mean radius, and N_{Tot} is the total number of particles in the system. When $\mu_1 = \mu_3 = 1$, the size distribution moments reflect a monodisperse system where aggregates have been formed by condensation. Size distribution moments where $\mu_1 > 1.25$ and $\mu_3 < 0.905$ suggest that aggregates were formed by coagulation[3].

Calculation of nanocluster extinction cross section:

For a dilute solution, absorbance, *A*, follows Beer–Lambert's Law:

$$A = \varepsilon(\lambda)\, C\ell \qquad \text{(D.8)}$$

where ε is the extinction coefficient, *C* is the dispersion concentration, and ℓ is the path length through which light travels. For a path length of 1 cm, and a gold concentration of 56 μg/mL, the maximum absorbance, found at a wavelength of 700 nm, was 1.10. Using Eq. D.8, we determined that the average $\varepsilon_{700\ nm}$ was 0.017±0.003 $cm^2/\mu g$ for three dispersions. Assuming that the nanoclusters are spherical, 100 nm in diameter, and in a closest-packed state, the particle extinction cross section was calculated by, $\varepsilon_{700\ nm} \times M_{Au}$, where M_{Au} is the mass of gold per nanocluster, and was estimated to be 1.0×10^{-5} ng/cluster ($M_{Au} = V_p \times \rho_p \times 0.72$, where V_p and ρ_p are the particle volume and density, respectively). The average particle extinction cross section was calculated to be ~$9.0 \times 10^{-15}\ m^2$.

Calculation of total interaction potentials and theoretical stability ratios:

Total interaction potentials were calculated by summing van der Waals (VDW), electrostatic, and depletion contributions. The VDW attractive component is described by [2]:

$$V_{VDW} = \frac{-A}{6}\left[\frac{2a^2}{H(4a+H)} + \frac{2a^2}{(2a+H)^2} + \ln\left(\frac{H(4a+H)}{(2a+H)^2}\right)\right] \qquad (D.9)$$

where A is the Hamaker constant of particles interacting in an aqueous medium and H is the surface to surface separation distance between particles. The electrostatic interaction contribution is described by[2]:

$$V_{electrostatic} = \frac{64\pi a k_b T \Gamma_0^2 n_\infty}{\kappa^2}\exp[-\kappa H] \qquad (D.10)$$

where n_∞ is the bulk ion concentration, and Γ_0 is a ratio of constants related to the surface potential, defined as[2]:

$$\Gamma_0 = \frac{\exp\left[\frac{ze\psi_0}{2k_bT}\right]-1}{\exp\left[\frac{ze\psi_0}{2k_bT}\right]+1} \qquad (D.11)$$

where z is the valence of the electrolyte, taken to be 1 in this model, e is the elementary charge unit of an electron, and ψ_0 is the surface potential of the gold nanoparticle.

To construct the interaction potential curves, the necessary input parameters were calculated as described below. In order to determine the bulk ion concentration, n_∞, the number of citrate ligands per gold particle was estimated based on an experimentally observed W of ~7×10^9 for a colloidal gold suspension with no added polymer (Table 6.2). Using Eq. 6.6, the stability ratio W may be related to the interaction potential, V_{total}, and thus surface potential, ψ_0. Therefore, values for ψ_0.were obtained by matching experimentally determined W values to an interaction potential. The corresponding ψ_0 was calculated to be -95 mV. This value was then used to calculate the charge on the particle using Eq. D.3[4]. The calculated particle charge was used to determine the number of charged citrate ligands per particle, which resulted in an estimated value of 11 charged citrate ligands per gold nanoparticle. By using an initial gold concentration of approximately 3 mg/ml, the number density of gold particles can be determined. From this value and the estimated charged citrate ligand coverage, the initial n_∞ was approximately 5.1×10^{22} charged citrate molecules per cubic meter. In order to determine κ, electro-neutrality was assumed, such that the ionic strength of the solution balances the charge on the gold particles. Therefore, κ is defined as[5]

$$\kappa = e\sqrt{\frac{z_{particle}n_{particle}}{\varepsilon_r\varepsilon_0 k_b T}} \qquad \text{(D.12)}$$

where $z_{particle}$ is the valence of the gold nanoparticle, equivalent to the number of citrate ligands per particle, $n_{particle}$ is the number density of gold particles, and ε_r is 80 in this case.

The depletion contribution to the total potential is described in the text (Eq. 6.5). The number density of micelles, required for the depletion calculation, was dependent on the polymer concentration in the system[6].

$$\rho_\infty = \frac{(C_p - CMC)N_A}{N_{agg}} \qquad \text{(D.13)}$$

where C_p is the polymer concentration, CMC is the critical micelle concentration for the PLA(2k)-PEG(10k)-PLA(2k) triblock copolymer, which was reported as 7 μg/ml[7], and N_{agg} is the aggregation number for the polymer, reported as 165 [8]. The summation of the potentials determines the total interaction potential (V_{total}), which was normalized by k_bT and then plotted as a function of surface to surface separation distance for various evaporation extents in Fig. 6.9. In order to calculate the potential for a dispersion of nanoclusters, the reduction in surface potential due to ion pairing caused by polymer adsorption was regressed from experimentally determined W values using Eq. D.6, taking into account the electrostatic, VDW and depletion terms for V_{total}. Since it was not possible to perform a regression for evaporation extents greater than 50% because of the excessive turbidity of the solutions, the experimental W value corresponding to 50% solvent evaporation, obtained from the observed time required to elicit a change in the dispersion color after 50% evaporation, was chosen. The surface potential reduction from ion pairing was thus determined to be approximately 1.6. This value was then used to calculate the interaction potential and W values at other evaporation extents.

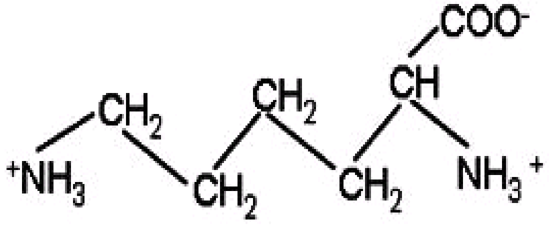

Figure D.1 Schematic of lysine ligand

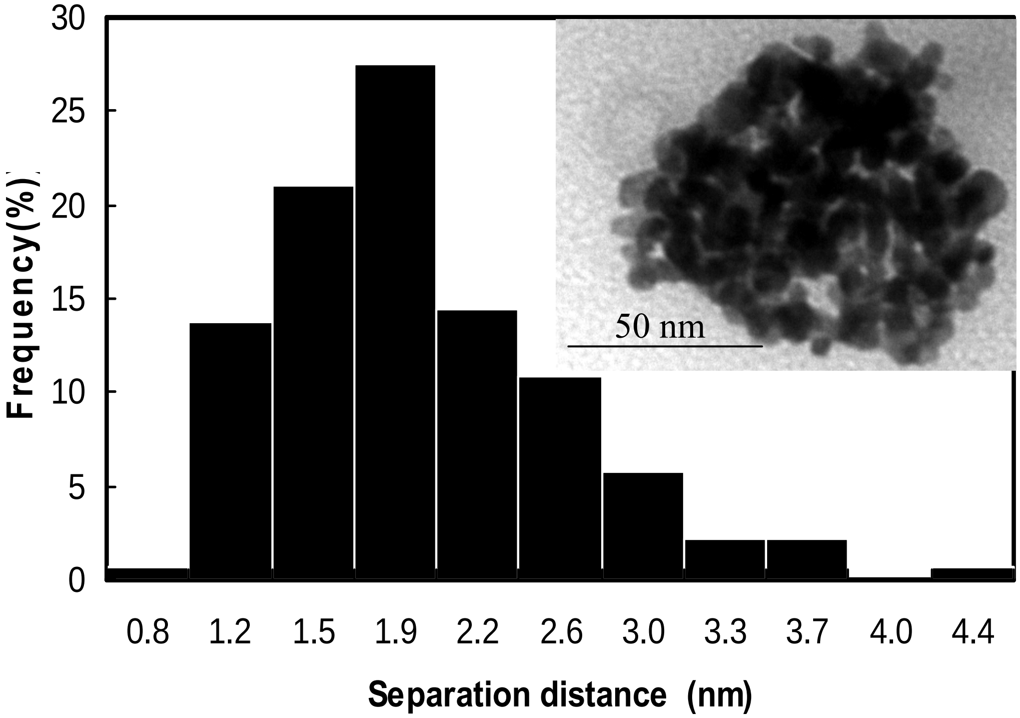

Figure D.2 Histogram of separation distances between primary gold nanoparticles within a nanocluster produced after 100% solvent evaporation (starting gold concentration of 3 mg/mL and a PLA-*b*-PEG-*b*-PLA/Au ratio of 16/1). Measurements taken using particles on the periphery of the nanoclusters. Over 130 measurements were taken. Inset is a TEM image of one of the clusters that was used in this measurement.

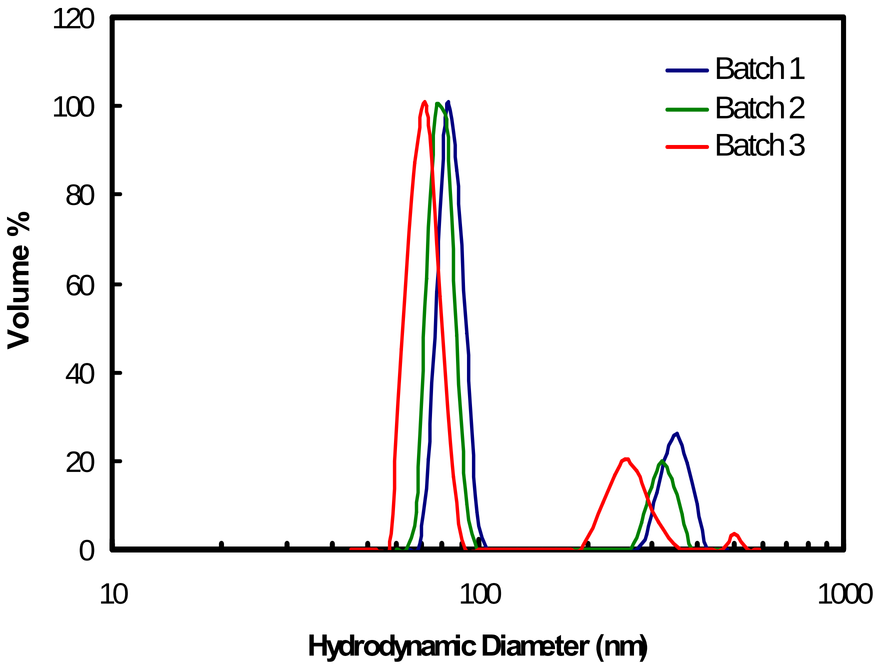

(a)

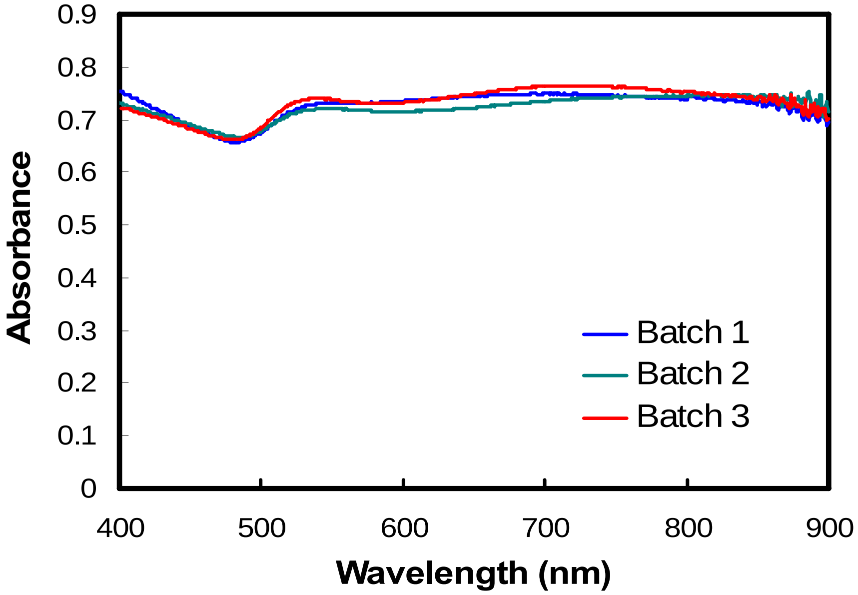

(b)

Figure D.3 Reproducibility of nanoclusters of citrate/lysine-capped gold nanoparticles in terms of (a) size and (b) optical properties. Starting gold and PLA-*b*-PEG-*b*-PLA concentrations were 3 and 50 mg/mL, respectively. Nanoclusters were produced after 100% solvent evaporation.

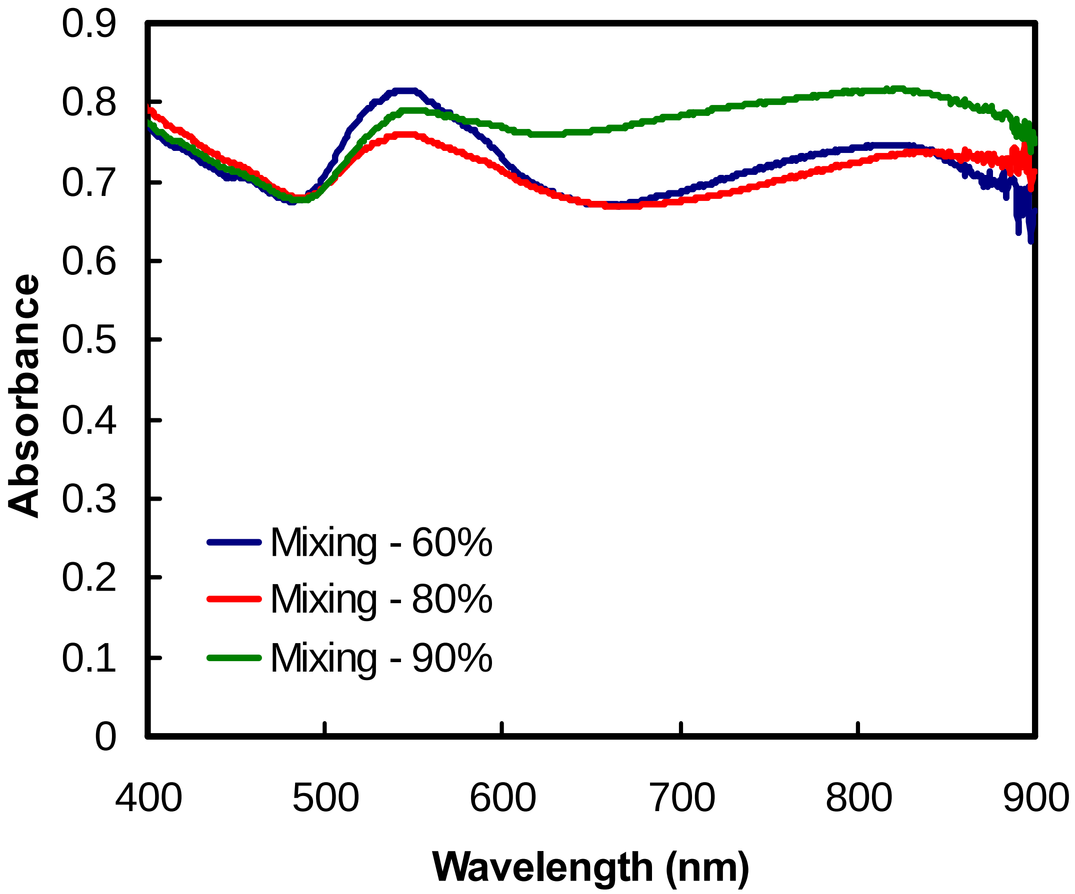

Figure D.4 UV-vis spectra of clusters of citrate-capped nanoparticles made with the mixing protocol. The starting gold concentration was 3 mg/mL and the PLA-*b*-PEG-*b*-PLA /Au ratio was 16/1.

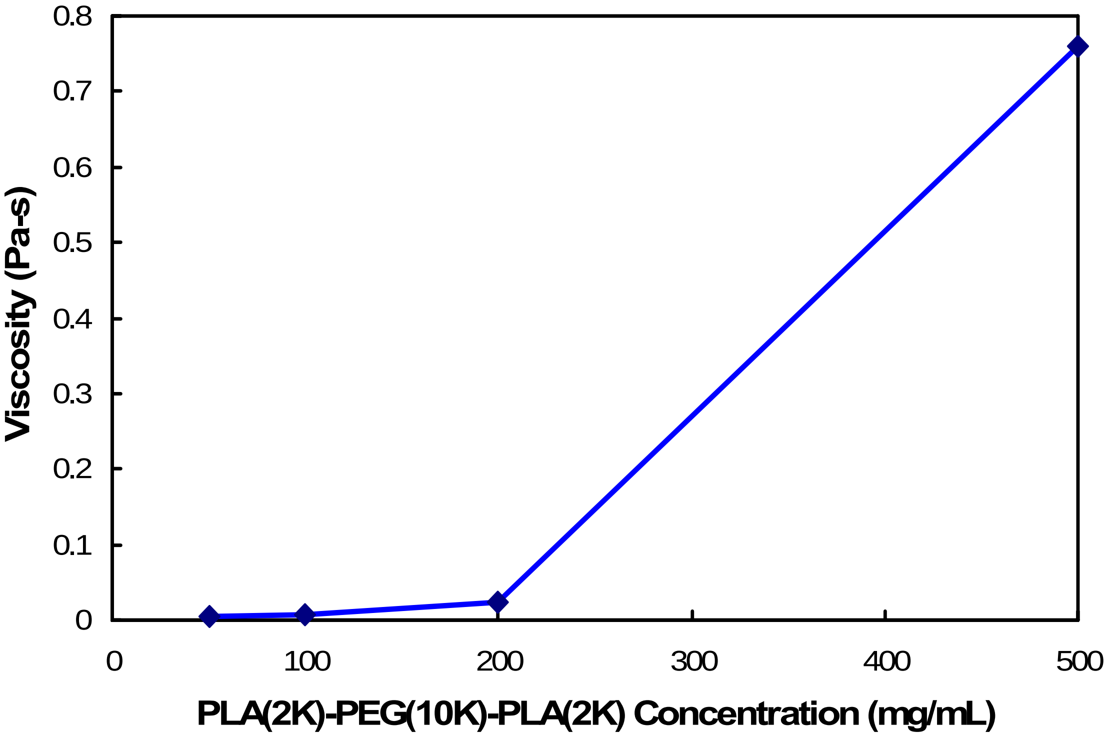

Figure D.5 Viscosity of PLA-*b*-PEG-*b*-PLA as a function of concentration. Viscosity measurements were performed using a cone and plate viscometer (TA Instruments AR 2000ex with a Peltier plate base and aluminum cone, with a diameter of 40 mm, angle of 1^{o} 59 minutes and 56 seconds and a truncation distance of 55 μm).

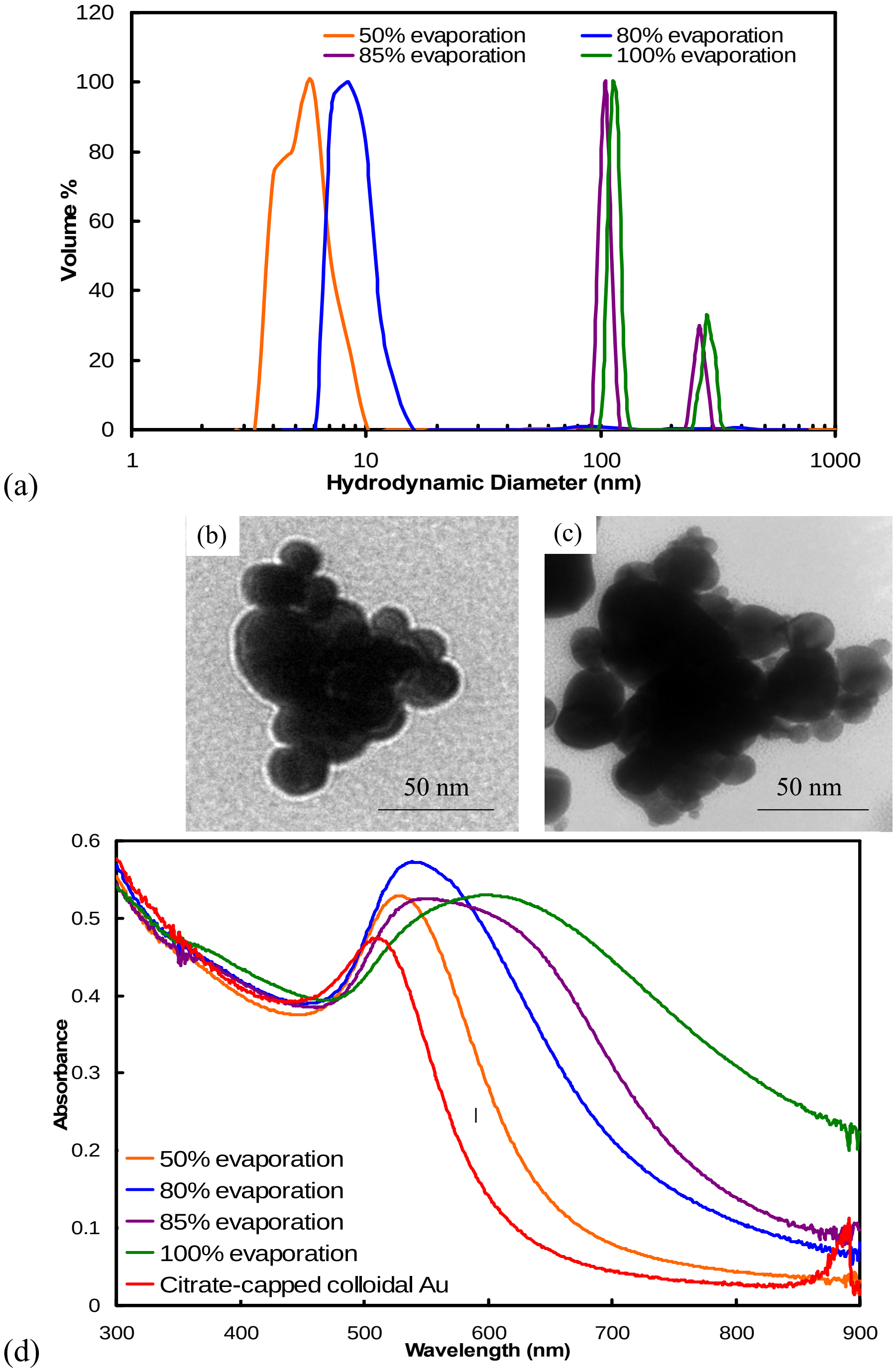

Figure D.6 (a) DLS measurements, TEM images after (b) 85% and (c) 100% solvent evaporation, respectively, and (d) UV-vis, absorbance spectra for nanoclusters composed of citrate-capped gold nanoparticles produced after different extents of evaporation with a starting gold concentration of 3 mg/mL and a PLA-*b*-PEG-*b*-PLA/gold ratio of 16/1.

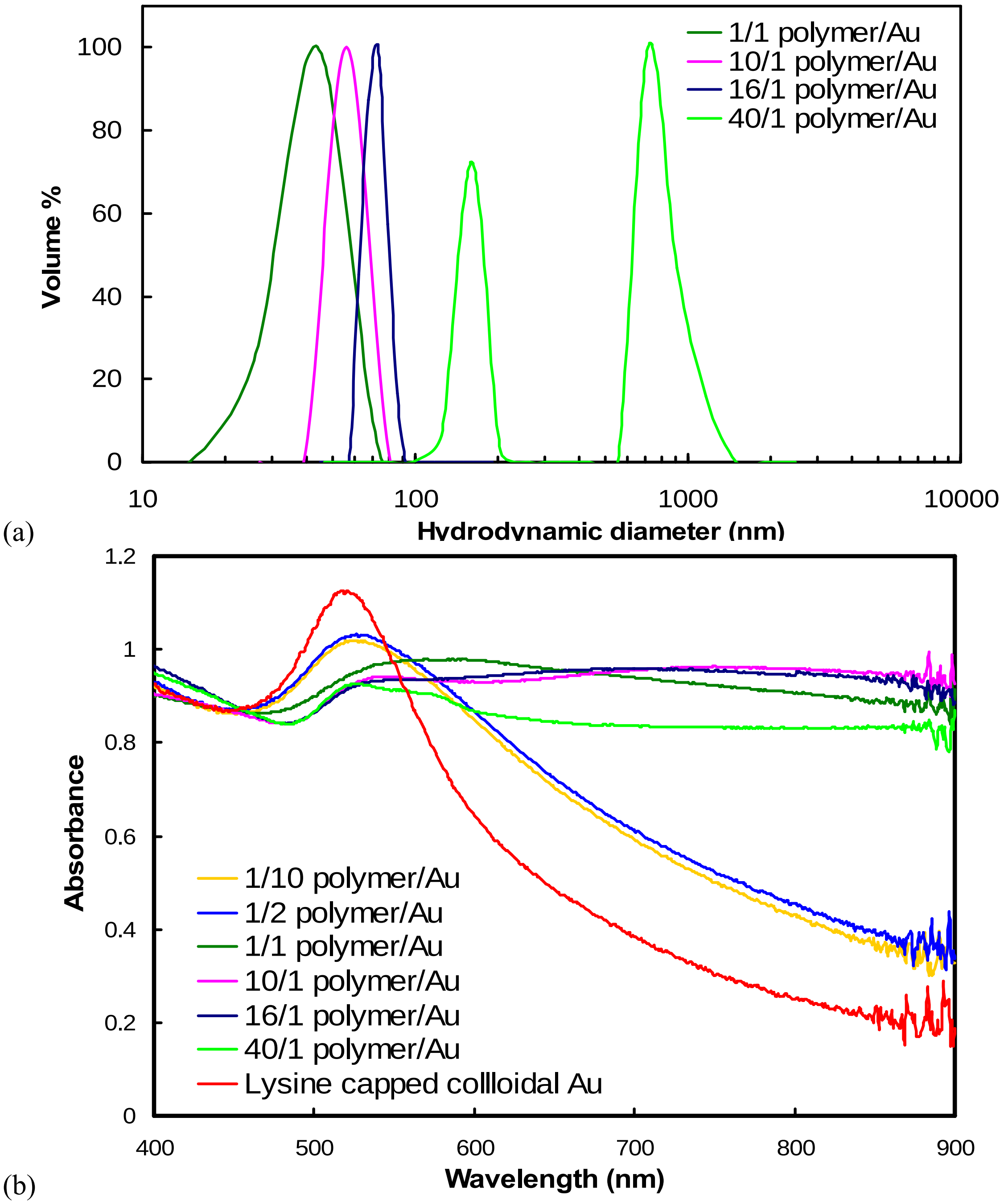

Figure D.7 (a) Particle size measurements by DLS and (b) UV-vis absorbance spectra of clusters of citrate/lysine-capped nanoparticles formed when varying the PLA-*b*-PEG-*b*-PLA /Au ratio. The starting gold concentration was 3 mg/mL and the clusters were formed under 100% solvent evaporation.

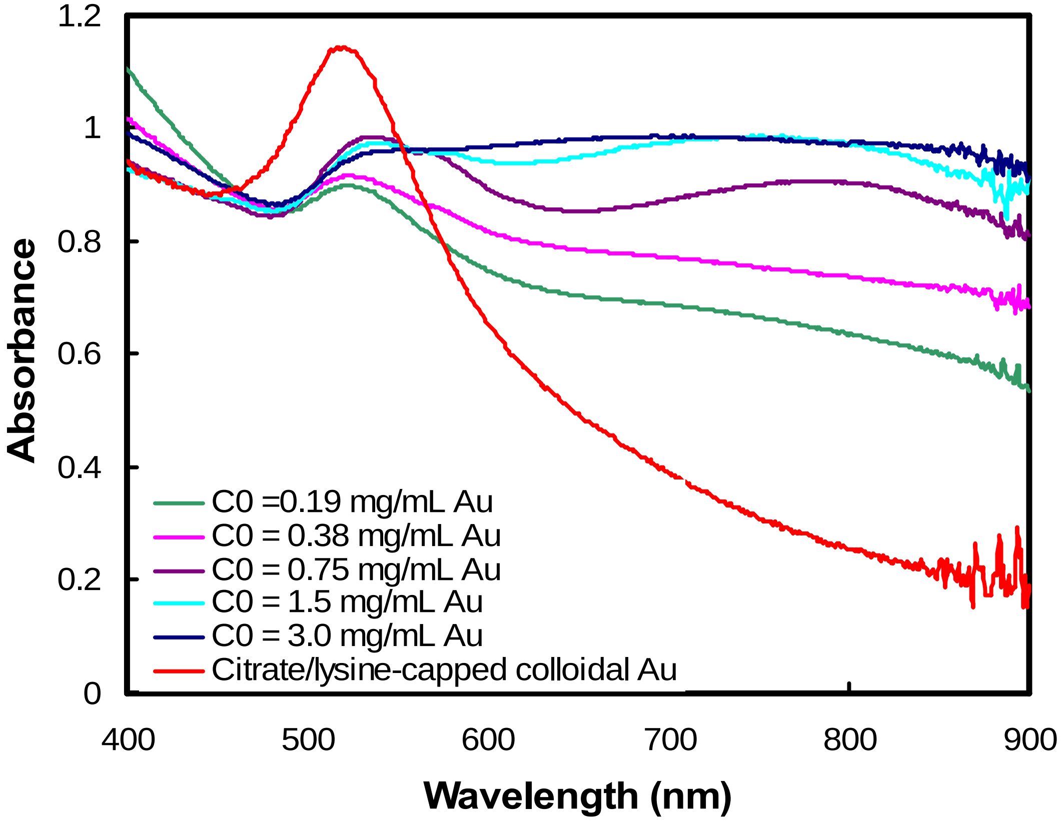

Figure D.8 UV-vis absorbance spectra of citrate/lysine-capped nanoclusters formed when varying the starting concentration of the colloidal gold solution. The starting PLA-*b*-PEG-*b*-PLA concentration was 50 mg/mL.

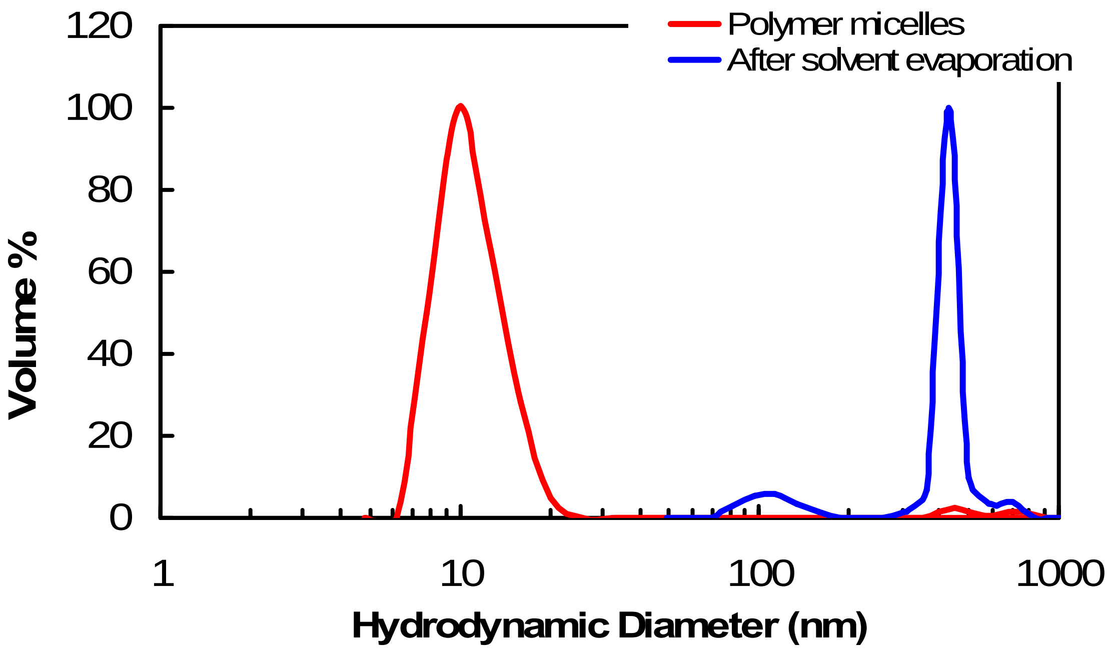

Figure D.9 DLS measurement of PLA-*b*-PEG-*b*-PLA micelles prior to solvent evaporation and after solvent evaporation. A 50 mg/mL polymer solution was prepared. To measure the micelle size, the solution was diluted to 1 mg/mL for analysis by DLS. To determine the effect of solvent evaporation on the polymer, the solution was evaporated to dryness and then redispersed in DI water to a concentration of 5 mg/mL.

Table D.1 Particle sizes, as determined by DLS, of citrate/lysine-capped nanoclusters formed when varying the starting concentration of the colloidal gold solution. The starting PLA-*b*-PEG-*b*-PLA concentration was 50 mg/mL.

Sample	Particle Size Range (nm)
C_0 = 0.19 mg/mL Au	74-118 (12%), 380-608 (80%)
C_0 = 0.38 mg/mL Au	82-122 (62%), 502-613 (38%)
C_0 = 0.75 mg/mL Au	44-57 (68%), 250-377 (32%)
C_0 = 1.5 mg/mL Au	56-100 (89%), 316-562 (11%)
C_0 = 3.0 mg/mL Au	54-101 (82%), 236-359 (18%)

References

1. Kunze, J.; Burgess, I.; Nichols, R.; Buess-Herman, C.; Lipkowski, J., Electrochemical evaluation of citrate adsorption on Au(111) and the stability of citrate-reduced gold colloids. *Journal of Electroanalytical Chemistry* **2007,** 599, 147-159.

2. Hiemenz, P. C.; Rajagopalan, R.; Editors, *Principles of Colloid and Surface Chemistry, Third Edition, Revised and Expanded*. 1997; p 688 pp.

3. Friedlander, S. K., *Smoke, dust, and haze : fundamentals of aerosol dynamics* Oxford University Press: New York, NY, 2000.

4. Hunter, R. J., *Zeta Potential in Colloid Science*. Academic Press: 1981.

5. Smith, P. G.; Patel, M. N.; Kim, J.; Milner, T. E.; Johnston, K. P., Effect of Surface Hydrophilicity on Charging Mechanism of Colloids in Low-Permittivity Solvents. *Journal of Physical Chemistry C* **2007,** 111, 840-848.

6. Mondain-Monval, O.; Leal-Calderon, F.; Phillip, J.; Bibette, J., Depletion Forces in the Presence of Electrostatic Double Layer Repulsion. *Physical Review Letters* **1995,** 75, 3364-3367.

7. Venkatraman, S. S., Jie, P. Min, F., Freddy, B.Y.C., Leong-Huat, G., Micelle-like nanoparticles of PLA-PEG-PLA triblock copolymer as chemotherapeutic carrier. *International Journal of Pharmaceutics* **2005,** 298, 219-232.

8. Agrawal, S. K.; Sanabria-DeLong, N.; Tew, G. N.; Bhatia, S. R., Structural Characterization of PLA-PEO-PLA Solutions and Hydrogels: Crystalline vss Amorphous PLA Domains. *Macromolecules* **2008,** 41, 1774-1784.

Bibliography

Aaron, J.; Nitin, N.; Travis, K.; Kumar, S.; Collier, T.; Park, S. Y.; Jose-Yacaman, M.; Coghlan, L.; Follen, M.; Richards-Kortum, R.; Sokolov, K., Plasmon resonance coupling of metal nanoparticles for molecular imaging of carcinogenesis in vivo. *Journal of Biomedical Optics* **2007,** 12, (3), 034007/1-034007/11.

Aaron, J. S.; Oh, J.; Larson, T. A.; Kumar, S.; Milner, T. E.; Sokolov, K. V., Increased optical contrast in imaging of epidermal growth factor receptor using magnetically actuated hybrid gold/iron oxide nanoparticles. *Optics Express* **2006,** 14, (26), 12930-12943.

Abramowitz, H.; Shah, P. S.; Green, P. F.; Johnston, K. P., Welding Colloidal Crystals with Carbon Dioxide. *Macromolecules* **2004,** 37, (19), 7316-7324.

Adjei, A.; Gupta, P., Pulmonary delivery of therapeutic peptides and proteins. *Journal of Controlled Release* **1994,** 29, (3), 361-73.

Adjei, A. L.; Gupta, P. K., *Inhalation Delivery of Therapeutic Peptides and Proteins*. New York, 1997; Vol. 107, p 913 pp.

Adjei, A. L.; Gupta, P. K., *Inhalation Delivery of Therapeutic Peptides and Proteins*. 1997; p 913.

Adler, D. C.; Huang, S.-W.; Huber, R.; Fujimoto, J. G., Photothermal detection of gold nanoparticles using phase-sensitive optical coherence tomography. *Optics Express* **2008,** 16, (7), 4376-4393.

Agrawal, S. K.; Sanabria-DeLong, N.; Tew, G. N.; Bhatia, S. R., Structural Characterization of PLA-PEO-PLA Solutions and Hydrogels: Crystalline vss Amorphous PLA Domains. *Macromolecules* **2008,** 41, 1774-1784.

Agu, R. U.; Ugwoke, M. I.; Armand, M.; Kinget, R.; Verbeke, N., The lung as a route for systemic delivery of therapeutic proteins and peptides. *Respiratory Research* **2001,** 2, (4), 198-209.

Alivisatos, P., The use of nanocrystals in biological detection. *Nature Biotechnology* **2004,** 22, 47-52.

Amidon, G. L.; Lennernaes, H.; Shah, V. P.; Crison, J. R., A theoretical basis for a biopharmaceutic drug classification: the correlation of in vitro drug product dissolution and in vivo bioavailability. *Pharmaceutical Research* **1995,** 12, (3), 413-20.

Anker, J. N.; Hall, W. P.; Lyandres, O.; Shah, N. C.; Zhao, J.; Van Duyne, R. P., Biosensing with plasmonic nanosensors *Nature Materials* **2008** 7 442-453.

Ashayer, R.; Luckham, P. F.; Manimaaran, S.; Rogueda, P., Investigation of the molecular interactions in a pMDI formulation by atomic force microscopy. *European Journal of Pharmaceutical Sciences* **2004,** 21, (4), 533-543.

Aslan, K.; Luhrs, C. C.; Perez-Luna, V. H., Controlled and Reversible Aggregation of Biotinylated Gold Nanoparticles with Streptavidin. *Journal of Physical Chemistry B* **2004,** 108, (40), 15631-15639.

Atkins, P. J.; Barker, N. P.; Mathisen, D., The design and development of inhalation drug delivery systems. In *Pharmaceutical Inhalation Aerosol Technology*, Hickey, A. J., Ed. Marcel Dekker Inc.: New York, New York, 1992; Vol. 54, pp 155-185.

Bae, K. H.; Choi, S. H.; Park, S. Y.; Lee, Y.; Park, T. G., Thermosensitive Pluronic Micelles Stabilized by Shell Cross-Linking with Gold Nanoparticles. *Langmuir* **2006,** 22, (14), 6380-6384.

Bailey, M. M.; Gorman, E. M.; Munson, E. J.; Berkland, C., Pure Insulin Nanoparticle Agglomerates for Pulmonary Delivery. *Langmuir* **2008,** 24, (23), 13614-13620.

Balwani, G.; Boyd, B.; Whatley, J. Compositions methods and systems for pulmonary delivery of recombinant human interferon alpha-2b. 2002-159083
2003223936, 20020531., 2003.

Basu, S.; Pal, T., Glutathione-induced aggregation of gold nanoparticles: electromagnetic interactions in a closely packed assembly. *Journal of Nanoscience and Nanotechnology* **2007,** 7, (6), 1904-1910.

Ben-Jebria, A.; Chen, D.; Eskew, M. L.; Vanbever, R.; Langer, R.; Edwards, D. A., Large porous particles for sustained protection from carbachol-induced bronchoconstriction in guinea pigs. *Pharmaceutical Research* **1999,** 16, (4), 555-561.

Benfait, C., Kos reports achievement of new research and development milestones. *Kos Press Release* **2004**.

Benfait, C., Kos reports achievements of new research and development milestones. *Kos Press Release* **2004**.

Berlin, E.; Pallansch, M. J., Densities of several proteins and L-amino acids in the dry state. *Journal of Physical Chemistry* **1968,** 72, (6), 1887-9.

Bernstein, J. A.; Amin, H.; Smith, S., Therapeutic Uses of Lung Aerosol. In *Inhalation Aerosols: Physical and Biological Basis for Therapy*, Hickey, A. J., Ed. Informa healthcare USA, Inc.: New York, NY, 2007; Vol. 221, pp 219-252.

Betancourt, T.; Brown, B.; Brannon-Peppas, L., Doxorubicin-loaded PLGA nanoparticles by nanoprecipitation: preparation, characterization and *in vitro* evaluation. *Nanomedicine* **2007,** 2, (2), 220-232.

Bevan, M. A. Effect of Adsorbed Polymer on the Interparticle Potential. PhD Dissertation, Carnegie Mellon University, Pittsburgh, 1999.

Bhavane, R.; Karathanasis, E.; Annapragada Ananth, V., Agglomerated vesicle technology: a new class of particles for controlled and modulated pulmonary drug delivery. *Journal of controlled release : official journal of the Controlled Release Society* **2003,** 93, (1), 15-28.

Blatchford, C. G.; Campbell, J. R.; Creighton, J. A., Plasma Resonance- Enhanced Raman Scattering by Adsorbates on Gold Colloids: The Effects of Aggregation. *Surface Science* **1982,** 120, 445-455.

Blondino, F. E.; Byron, P. R., Surfactant dissolution and water solubilization in chlorine-free liquified gas propellants. *Drug Development and Industrial Pharmacy* **1998,** 24, (10), 935-945.

Blot, F.; Faurisson, F.; Bernard, N.; Sellam, S.; Friard, S.; Tavakoli, R.; Carbon, C.; Stern, M.; Bisson, A.; Pocidalo, J. J.; Caubarrere, I., Nebulized cyclosporine in the rat: assessment of regional lung and extrapulmonary deposition. *Transplantation* **1999,** 68, (2), 191-5.

Boal, A. K.; Ilhan, F.; DeRouchey, J. E.; Thurn-Albrecht, T.; Russell, T. P.; Rotello, V. M., Self-assembly of nanoparticles into structured spherical and network aggregates. *Nature* **2000,** 404, (6779), 746-748.

Brewer, S. H.; Glomm, W. R.; Johnson, M. C.; Knag, M. K.; Franzen, S., Probing BSA Binding to Citrate-Coated Gold Nanoparticles and Surfaces. *Langmuir* **2005,** 21, 9303-9307.

Bridges, P. A.; Taylor, K. M. G., An investigation of some of the factors influencing the jet nebulization of liposomes. *International Journal of Pharmaceutics* **2000,** 204, (1-2), 69-79.

Brown, R. A., Jr.; Schanker, L. S., Absorption of aerosolized drugs from the rat lung. *Drug metabolism and disposition: the biological fate of chemicals* **1983,** 11, (4), 355-60.

Brust, M.; Walker, M.; Bethell, D.; Schiffrin, D. J.; Whyman, R., Synthesis of thiol-derivatized gold nanoparticles in a two-phase liquid-liquid system. *Journal of the Chemical Society, Chemical Communications* **1994**, (7), 801-2.

Bunjes, H.; Rades, T., Thermotropic liquid crystalline drugs. *Journal of Pharmacy and Pharmacology* **2005,** 57, (7), 807-816.

Burckart, G.; G. Smaldone; M. Eldon; R. Venkataramanan; J. Dauber; A. Zeevi; K. McCurry; T. McKaveney; T. Corcoran; B. Griffith; Ionoco, A., Lung Deposition and Pharacokinetics of Cyclosproine after Aeroslization in Lung Transplant Patients. *Pharmaceutical Research* **2003,** 20, (2), 252-256.

Burckart, G. J.; Keenan, R. J.; Iacono, A. T.; Griffith, B. P., Cyclosporine aerosol in lung transplantation. *Local Immunosuppression of Organ Transplants* **1996**, 131-139.

Burckart, G. J.; Smaldone, G. C.; Eldon, M. A.; Venkataramanan, R.; Dauber, J.; Zeevi, A.; McCurry, K.; McKaveney, T. P.; Corcoran, T. E.; Griffith, B. P.; Iacono, A. T., Lung Deposition and Pharmacokinetics of Cyclosporine After Aerosolization in Lung Transplant Patients. *Pharmaceutical Research* **2003,** 20, (2), 252-256.

Cabral Marques, H. M.; Hadgraft, J.; Kellaway, I. W.; Taylor, G., Studies of cyclodextrin inclusion complexes. IV. The pulmonary absorption of salbutamol from a complex with 2-hydroxypropyl-b-cyclodextrin in rabbits. *International Journal of Pharmaceutics* **1991,** 77, (2-3), 303-7.

Carpenter, J. F.; Chang, B. S.; Garzon-Rodriguez, W.; Randolph, T. W., Rational design of stable lyophilized protein formulations: theory and practice. In *Pharmaceutical Biotechnology. 13. Rational Design of Stable Protein Formulations*, Carpenter, J. F.; Manning, M. C., Eds. Kluwer Academic/Plenum Press: New York, 2002; Vol. 13, pp 109-133.

Casarett, L. J.; Milley, P. S., Alveolar Reactivity Following Inhalation of Particles. *Health Physics* **1964,** 10, 1003-11.

Chan, H.-K.; Chew, N. Y. K., Novel alternative methods for the delivery of drugs for the treatment of asthma. *Advanced Drug Delivery Reviews* **2003,** 55, (7), 793-805.

Chan, H. K.; Gonda, I., Development of a systematic theory of suspension inhalation aerosols. II. Aggregates of monodisperse particles nebulized in polydisperse droplets. *International Journal of Pharmaceutics* **1988,** 41, (1-2), 147-57.

Charnick, S. B.; Yu, Z.; Athill, L. V.; Karara, A. H.; Tse, F. L. S.; Lau, D. T. W., Pharmacokinetics of SDZ 64-412, a novel antiasthmatic agent, following intravenous, oral, and inhalation dosing in the rat. *Biopharmaceutics & Drug Disposition* **1994,** 15, (4), 317-27.

Chen, J.; Saeki, F.; Wiley, B. J.; Cang, H.; Cobb, M. J.; Li, Z.-Y.; Au, L.; Zhang, H.; Kimmey, M. B.; Li, X.; Xia, Y., Gold Nanocages: Bioconjugation and Their Potential Use as Optical Imaging Contrast Agents. *Nano Letters* **2005,** 5, (3), 473-477.

Chen, X.; Young, T. J.; Sarkari, M.; Williams, R. O.; Johnston, K. P., Preparation of cyclosporine A nanoparticles by evaporative precipitation into aqueous solution. *International Journal of Pharmaceutics* **2002,** 242, (1-2), 3-14.

Cheng, W. P.; Gray, A. I.; Tetley, L.; Hang, T. L. B.; Schaetzlein, A. G.; Uchegbu, I. F., Polyelectrolyte Nanoparticles with High Drug Loading Enhance the Oral Uptake of Hydrophobic Compounds. *Biomacromolecules* **2006,** 7, (5), 1509-1520.

Chetty, D. J.; Chien, Y. W., Novel methods of insulin delivery: an update. *Critical Reviews in Therapeutic Drug Carrier Systems* **1998,** 15, (6), 629-670.

Choi, H. S.; Liu, W.; Misra, P.; Tanaka, E.; Zimmer, J. P.; Ipe, B. I.; Bawendi, M. G.; Frangioni, J. V., Renal clearance of quantum dots. *Nature Biotechnology* **2007,** 25, (10), 1165-1170.

Chow, M. K.; Zukoski, C. F., Gold sol formation mechanisms: role of colloidal stability. *Journal of Colloid and Interface Science* **1994,** 165, (1), 97-109.

Codrons, V.; Vanderbist, F.; Verbeeck, R. K.; Arras, M.; Lison, D.; Preat, V.; Vanbever, R., Systemic delivery of parathyroid hormone (1-34) using inhalation dry powders in rats. *Journal of Pharmaceutical Sciences* **2003,** 92, (5), 938-950.

Courrier, H. M.; Butz, N.; Vandamme, T. F., Pulmonary drug delivery systems: recent developments and prospects. *Critical Reviews in Therapeutic Drug Carrier Systems* **2002,** 19, (4 & 5), 425-498.

Courrier, H. M.; N. Butz; Vandamme, T. F., Pulmonary Drug Delivery Systems: Recent Developments and Prospects. *Critical Reviews in Therapeutic Drug Carrier Systems* **2002,** 19, (4 and 5), 425-498.

Dailey, L. A.; Kleemann, E.; Wittmar, M.; Gessler, T.; Schmehl, T.; C. Roberts; Seeger, W.; Kissel, T., Surfactant-Free, Biodegradable Nanoparticles for Aerosol Therapy Based on the Branched Polyesters, DEAPA-PVAL-g-PLGA. *Pharmaceutical Research* **2003,** 20, (12), 2011-2020.

Davies, N. M.; Feddah, M. R., A novel method for assessing dissolution of aerosol inhaler products. *International Journal of Pharmaceutics* **2003,** 255, (1-2), 175-187.

Dellamary, L. A.; Tarara, T. E.; Smith, D. J.; Woelk, C. H.; Adractas, A.; Costello, M. L.; Gill, H.; Weers, J. G., Hollow porous particles in metered dose inhalers. *Pharmaceutical Research* **2000,** 17, (2), 168-174.

DeVries, G. A.; Brunnbauer, M.; Hu, Y.; Jackson, A. M.; Long, B.; Neltner, B. T.; Uzun, O.; Wunsch, B. H.; Stellacci, F., Divalent Metal Nanoparticles. *Science* **2007,** 315, (5810), 358-361.

Ditsch, A.; Laibinis, P. E.; Wang, D. I. C.; Hatton, T. A., Controlled Clustering and Enhanced Stability of Polymer-Coated Magnetic Nanoparticles. *Langmuir* **2005,** 21, (13), 6006-6018.

Eckstein Jens, W.; Fung, J., A new class of cyclosporin analogues for the treatment of asthma. *Expert opinion on investigational drugs* **2003,** 12, (4), 647-53.

Edwards, D.; Hanes, J.; Caponetti, G.; Mintzes, J.; Deaver, D.; Lotan, N.; Langer, R., Large Porous Particles for Pulmonary Delivery. *Science* **1997,** 276.

Edwards, D. A.; Hanes, J.; Caponetti, G.; Hrkach, J.; Ben-Jebria, A.; Eskew, M. L.; Mintzes, J.; Deaver, D.; Lotan, N.; Langer, R., Large porous particles for pulmonary drug delivery. *Science* **1997,** 276, (5320), 1868-1871.

Engstrom, J. D.; Lai, E. S.; Ludher, B.; Chen, B.; Milner, T. E.; Kitto, G. B.; Williams III, R. O.; Johnston, K. P., Formation of stable submicron protein particles by thin film freezing. *Pharmaceutical Research* **2008,** 25, (6), 1334-1346.

Engstrom, J. D.; Lai, E. S.; Ludher, B.; Chen, B.; Milner, T. E.; Kitto, G. B.; Williams III, R. O.; Johnston, K. P., Formation of stable submicron protein particles by thin film freezing. *Pharmaceutical Research* **2008,** 25, (6), 1334-1336.

Engstrom, J. D.; Simpson, D. T.; Cloonan, C.; Lai, E.; Williams III, R. O.; Kitto, G. B.; Johnston, K. P., Stable high surface area lactate dehydrogenase particles produced by spray freezing into liquid nitrogen. *European Journal of Pharmaceutics and Biopharmaceutics* **2007,** 65, (2), 163-174.

Engstrom, J. D.; Simpson, D. T.; Cloonan, C.; Lai, E. S.; Williams, R. O., III; Kitto, G. B.; Johnston, K. P., Stable high surface area lactate dehydrogenase particles produced by spray freezing into liquid nitrogen. *European Journal of Pharmaceutics and Biopharmaceutics* **2007,** 65, (2), 163-174.

Engstrom, J. D.; Simpson, D. T.; Lai, E.; Williams III, R. O.; Johnston, K. P., Morphology of protein particles produced by spray freezing of concentrated solutions. *European Journal of Pharmaceutics and Biopharmaceutics* **2007,** 65, (2), 149-162.

Engstrom, J. D.; Tam, J. M.; Miller, M. A.; Williams, R. O.; Johnston, K. P., Templated open flocs of nanorods for enhanced pulmonary delivery with pressurized metered dose inhalers *Pharmaceutical Research* **2009,** 26, (1), 101-117.

Enna, S. J.; Schanker, L. S., Absorption of drugs from the rat lung. *American Journal of Physiology* **1972,** 223, (5), 1227-31.

Esmailpour, N.; Hoegger, P.; Rabe, K. F.; Heitmann, U.; Nakashima, M.; Rohdewald, P., Distribution of inhaled fluticasone propionate between human lung tissue and serum in vivo. *European Respiratory Journal* **1997,** 10, (7), 1496-1499.

Evora, C.; Soriano, I.; Rogers, R. A.; Shakesheff, K. M.; Hanes, J.; Langer, R., Relating the phagocytosis of microparticles by alveolar macrophages to surface chemistry: the effect of 1,2-dipalmitoylphosphatidylcholine. *Journal of Controlled Release* **1998,** 51, (2,3), 143-152.

Evrard, B.; Bertholet, P.; Gueders, M.; Flament, M. P.; Piel, G.; Delattre, L.; Gayot, A.; Leterme, P.; Foidart, J. M.; Cataldo, D., Cyclodextrins as a potential carrier in drug nebulization. *Journal of Controlled Release* **2004,** 96, (3), 403-410.

Fahr, A., Cyclosporin clinical pharmacokinetics. *Clinical pharmacokinetics* **1993,** 24, (6), 472-95.

Farahnaky, A.; Badii, F.; Farhat, I. A.; Mitchell, J. R.; Hill, S. E., Enthalpy relaxation of bovine serum albumin and implications for its storage in the glassy state. *Biopolymers* **2005,** 78, (2), 69-77.

Fargues, C.; Turchiuli, C., Structural characterization of flocs in relation to their settling performances. *Chemical Engineering Research and Design* **2004,** 82, (A11), 1517.

Feng, S.-S.; Li, M.; Chen, B.-H.; Pack, D., Polymeric nanospheres fabricated with natural emulsifiers for clinical administration of an anticancer drug paclitaxel (Taxol). *Materials Science & Engineering, C: Biomimetic and Supramolecular Systems* **2002,** C20, (1-2), 85-92.

Ferrari, M., Cancer nanotechnology: opportunities and challenges. *Nature Reviews Cancer* **2005,** 5, (3), 161-171.

Fiegel, J.; Fu, J.; Hanes, J., Poly(ether-anhydride) dry powder aerosols for sustained drug delivery in the lungs. *Journal of Controlled Release* **2004,** 96, (3), 411-423.

Finlay, W. H., *The mechanics of inhaled pharmaceutical aerosols*. New York, 2001.

Forbes, B.; Ehrhardt, C., Human respiratory epithelial cell culture for drug delivery applications. *European Journal of Pharmaceutics and Biopharmaceutics* **2005,** 60, (2), 193-205.

Forsgren, P.; Modig, J.; Gerdin, B.; Axelsson, B.; Dahlback, M., Intrapulmonary deposition of aerosolized Evans blue dye and liposomes in an experimental porcine model of early ARDS. *Upsala Journal of Medical Sciences* **1990,** 95, (2), 117-36.

Frankamp, B. L.; Uzun, O.; Ilhan, F.; Boal, A. K.; Rotello, V. M., Recognition-Mediated Assembly of Nanoparticles into Micellar Structures with Diblock Copolymers. *Journal of the American Chemical Society* **2002,** 124, (6), 892-893.

French, D. L.; Edwards, D. A.; Niven, R. W., The influence of formulation on emission, deaggregation and deposition of dry powders for inhalation. *Journal of Aerosol Science* **1996,** 27, (5), 769-783.

Friedlander, S. K., *Smoke, dust, and haze : fundamentals of aerosol dynamics* Oxford University Press: New York, NY, 2000.

Fukaya, H.; Limura, A.; Hoshiko, K.; Fuyumuro, T.; Noji, S.; Nabeshima, T., A cyclosporin A/maltosyl-a-cyclodextrin complex for inhalation therapy of asthma. *European Respiratory Journal* **2003,** 22, (2), 213-219.

Garcia-Contreras, L.; Hickey, A. J., Aerosol treatment of cystic fibrosis. *Critical Reviews in Therapeutic Drug Carrier Systems* **2003,** 20, (5), 317-356.

Garcia-Contreras, L.; Smyth, H. D. C., Liquid-spray or dry-powder systems for inhaled delivery of peptide and proteins? *American Journal of Drug Delivery* **2005,** 3, (1), 29-45.

Gazeley, M. J. S.; Lees, I. W.; Payne, A. N.; Webbon, P. M.; Woolley, G. E., Anatomical deposition and early distribution of an inhaled radioaerosol in conscious and anaesthetized rats. *British Journal of Pharmacology* **1986,** 87, 122.

Geelhaar, A.; Weibel, E. R., Morphometric estimation of pulmonary diffusion capacity. 3. The effect of increased oxygen consumption in Japanese Waltzing mice. *Respiration Physiology* **1971,** 11, (3), 354-66.

Gilbert, B. E.; Wilson, S. Z.; Garcon, N. M.; Wyde, P. R.; Knight, V., Characterization and administration of cyclosporine liposomes as a small-particle aerosol. *Transplantation* **1993,** 56, (4), 974-7.

Gindy, M. E.; Panagiotopoulos, A. Z.; Prud'homme, R. K., Composite Block Copolymer Stabilized Nanoparticles: Simultaneous Encapsulation of Organic Actives and Inorganic Nanostructures. *Langmuir* **2008,** 24, (1), 83-90.

Gindy, M. E.; Prud'homme, R. K.; Ji, S.; Hoye, T. R.; Macosko, C. W., Functional block copolymer nanoparticles for targeted drug delivery and imaging. *PMSE Preprints* **2006,** 95, 989-990.

Gögelein, C.; Nägele, G.; Buitenhuis, J.; Tuinier, R.; Dhont1, J. K. G., Polymer depletion-driven cluster aggregation and initial phase separation in charged nanosized colloids. *The Journal of Chemical Physics* **2009,** 130, (20), 204905-1 - 204905-15.

Gonda, I., Development of a systematic theory of suspension inhalation aerosols. I. A framework to study the effects of aggregation on the aerodynamic behavior of drug particles. *International Journal of Pharmaceutics* **1985,** 27, (1), 99-116.

Goodarz-Nia, I.; Sutherland, D. N., Floc simulation. Effects of particle size and shape. *Chemical Engineering Science* **1975,** 30, (4), 407-12.

Gopidas, K. R.; Whitesell, J. K.; Fox, M. A., Nanoparticle-Cored Dendrimers: Synthesis and Characterization. *Journal of the American Chemical Society* **2003,** 125, 6491-6502.

Grabar, K. C.; Allison, K. J.; Baker, B. E.; Bright, R. M.; Brown, K. R.; Freeman, R. G.; Fox, A. P.; Keating, C. D.; Musick, M. D.; Natan, M. J., Two-dimensional arrays of colloidal gold particles: a flexible approach to macroscopic metal surfaces. *Langmuir* **1996,** 12, 23535-2361.

Guo, Y.; Ma, Y.; Xu, L.; Li, J.; Yang, W., Conformational Change Induced Reversible Assembly/Disassembly of Poly-L-lysine-Functionalized Gold Nanoparticles. *Journal of Physical Chemistry C* **2007,** 111, (26), 9172-9176.

Hadinoto, K.; Phanapavudhikul, P.; Kewu, Z.; Tan, R. B. H., Dry powder aerosol delivery of large hollow nanoparticulate aggregates as prospective carriers of nanoparticulate drugs: Effects of phospholipids. *International Journal of Pharmaceutics* **2007,** 333, (1-2), 187-198.

Hadinoto, K.; Phanapavudhikul, P.; Zhu, K.; Tan, R. B. H., Novel Formulation of Large Hollow Nanoparticles Aggregates as Potential Carriers in Inhaled Delivery of Nanoparticulate Drugs. *Industrial & Engineering Chemistry Research* **2006,** 45, (10), 3697-3706.

Handschumacher, R. E.; Harding, M. W.; Rice, J.; Drugge, R. J.; Speicher, D. W., Cyclophilin: a specific cytosolic binding protein for cyclosporin A. *Science (Washington, DC, United States)* **1984,** 226, (4674), 544-7.

Hanes, J.; Dawson, M.; Har-el, Y.-e.; Suh, J.; Fiegel, J., Gene delivery to the lung. *Drugs and the Pharmaceutical Sciences* **2004,** 134, (Pharmaceutical Inhalation Aerosol Technology (2nd Edition)), 489-539.

Harada, T.; Hatton, T. A., Formation of Highly Ordered Rectangular Nanoparticle Superlattices by the Cooperative Self-Assembly of Nanoparticles and Fatty Molecules. *Langmuir* **2009,** 25, (11), 6407-6412.

Haynes, A.; Shaik, M. S.; Chatterjee, A.; Singh, M., Evaluation of an aerosolized selective COX-2 inhibitor as a potentiator of doxorubicin in a non-small-cell lung cancer cell line. *Pharmaceutical Research* **2003,** 20, (9), 1485-1495.

Herrera, A. P.; Resto, O.; Briano, J. G.; Rinaldi, C., Synthesis and agglomeration of gold nanoparticles in reverse micelles. *Nanotechnology* **2005,** 16, S618-S625.

Heyder, J.; Gebhart, J.; Rudolf, G.; Schiller, C. F.; Stahlhofen, W., Deposition of particles in the human respiratory tract in the size range 0.005-15 [mu]m. *Journal of Aerosol Science* **1986,** 17, (5), 811-825.

Heyder, J.; Gebhart, J.; Rudolf, G.; Schiller, C. F.; Stahlhofen, W., Deposition of particles in the human respiratory tract in the size range 0.005-15 μm. *Journal of Aerosol Science* **1986,** 17, 811-825.

Heyder, J.; Rudolf, G., Mathematical models of particle deposition in the human respiratory tract. *Journal of Aerosol Science* **1984,** 15, (6), 697-707.

Hickey, A. J., Aerosol delivery and asthma therapy. *Advanced Drug Delivery Reviews* **2003,** 55, (7), 777.

Hiemenz, P. C.; Rajagopalan, R., *Principles of colloid and surface chemistry*. 1997.

Hiemenz, P. C.; Rajagopalan, R.; Editors, *Principles of Colloid and Surface Chemistry, Third Edition, Revised and Expanded*. 1997; p 688 pp.

Hirsch, L. R.; Stafford, R. J.; Bankson, J. A.; Sershen, S. R.; Rivera, B.; Price, R. E.; Hazle, J. D.; Halas, N. J.; West, J. L., Nanoshell-mediated near-infrared thermal therapy of tumors under magnetic resonance guidance. *Proceedings of the National Academy of Sciences of the United States of America* **2003,** 100, (23), 13549-13554.

Hirst, P. H.; Pitcairn, G. R.; Weers, J. G.; Tarara, T. E.; Clark, A. R.; Dellamary, L. A.; Hall, G.; Shorr, J.; Newman, S. P., In vivo lung deposition of hollow porous particles from a pressurized metered dose inhaler. *Pharmaceutical Research* **2002,** 19, (3), 258-264.

Ho, S.; Clipstone, N.; Timmermann, L.; Northrop, J.; Graef, I.; Fiorentino, D.; Nourse, J.; Crabtree, G. R., The mechanism of action of cyclosporin A and FK506. *Clinical Immunology and Immunopathology* **1996,** 80, (3, Pt. 2), S40-S45.

Horovitz, O.; Mocanu, A.; Tomoaia, G.; Bobos, L.; Dubert, D.; Daian, I.; Yusanis, T.; Tomoaia-Cotisel, M., Lysine mediated assembly of gold nanoparticles. *Studia Universitatis Babes-Bolyai, Chemia* **2007,** 52, (1), 97-108.

Hough, D. B.; White, L. R., The calculation of Hamaker constants from Lifshitz theory with applications to wetting phenomena. *Advances in Colloid and Interface Science* **1980,** 14, (1), 3-41.

Huang, X.; El-Sayed, I. H.; Qian, W.; El-Sayed, M. A., Cancer Cell Imaging and Photothermal Therapy in the Near-Infrared Region by Using Gold Nanorods. *Journal of the American Chemical Society* **2006,** 128, (6), 2115-2120.

Hunter, R. J., *Zeta Potential in Colloid Science*. Academic Press: 1981.

Iacono Aldo, T.; Johnson Bruce, A.; Grgurich Wayne, F.; Youssef, J. G.; Corcoran Timothy, E.; Seiler Deidre, A.; Dauber James, H.; Smaldone Gerald, C.; Zeevi, A.; Yousem Samuel, A.; Fung John, J.; Burckart Gilbert, J.; McCurry Kenneth, R.; Griffith Bartley, P., A randomized trial of inhaled cyclosporine in lung-transplant recipients. *The New England journal of medicine* **2006,** 354, (2), 141-50.

Iacono, A. T.; Burckart, G. J.; Zeevi, A.; Kunter, E.; Griffith, B. P., Local immunosuppression: The lung. *Immunology and Medicine Series* **2001,** 29, (Therapeutic Immunosuppression), 333-356.

Iacono, A. T.; Corcoran, T. E.; Griffith, B. P.; Grgurich, W. F.; Smith, D. A.; Zeevi, A.; Smaldone, G. C.; McCurry, K. R.; Johnson, B. A.; Dauber, J. H., Aerosol cyclosporin therapy in lung transplant recipients with bronchiolitis obliterans. *European Respiratory Journal* **2004,** 23, (3), 384-390.

Iacovella, C. R.; Horsch, M. A.; Glotzer, S. C., Local ordering of polymer-tethered nanospheres and nanorods and the stabilization of the double gyroid phase. *The Journal of Chemical Physics* **2008,** 129, 044902-1 - 0440902-10.

Ismailos, G.; Reppas, C.; Dressman, J. B.; Macheras, P., Unusual solubility behaviour of cyclosporin A in aqueous media. *The Journal of Pharmacy and Pharmacology* **1991,** 43, (4), 287-9.

Isojima, T.; Lattuada, M.; Vander Sande, J. B.; Hatton, T. A., Reversible Clustering of pH- and Temperature-Responsive Janus Magnetic Nanoparticles. *ACS Nano* **2008,** 2, (9), 1799-1806.

Isojima, T.; Suh, S. K.; Vander Sande, J. B.; Hatton, T. A., Controlled Assembly of Nanoparticle Structures: Spherical and Toroidal Superlattices and Nanoparticle-Coated Polymeric Beads. *Langmuir* **2009,** 25, (14), 8292-8298.

Israelachvili, J., *Intermolecular and surface forces*. Academic Press: San Diego, 1992.

Jacobs, C.; Kayser, O.; Muller, R. H., Nanosuspensions as a new approach for the formulation for the poorly soluble drug tarazepide. *Int J Pharm* **2000,** 196, 161-164.

Jacobs, C.; Muller, R. H., Production and characterization of a budesonide nanosuspension for pulmonary administration. *Pharmaceutical Research* **2002,** 19, (2), 189-194.

Jain, P. K.; El-Sayed, I. H.; El-Sayed, M. A., Gold Nanoparticles Target Cancer. *NanoToday* **2007,** 2, (1), 18-29.

Jain, P. K.; Lee, K. S.; El-Sayed, I. H.; El-Sayed, M. A., Calculated Absorption and Scattering Properties of Gold Nanoparticles of Different Size, Shape, and Composition: Applications in Biological Imaging and Biomedicine. *Journal of Physical Chemistry B* **2006,** 110, (14), 7238-7248.

Ji, X. J.; Shao, R. P.; Elliott, A. M.; Stafford, R. J.; Esparza-Coss, E.; Bankson, J. A.; Liang, G.; Luo, Z. P.; Park, K.; Markert, J. T.; Li, C., Bifunctional gold nanoshells with a superparamagnetic iron oxide-silica core suitable for both MR imaging and photothermal therapy. *Journal of Physical Chemistry C* **2007,** 111, (17), 6245-6251.

Jiang, W.; Kim, B. Y. S.; Rutka, J. T.; Chan, W. C. W., Nanoparticle-mediated cellular response is size-dependent. *Nature Nanotechnology* **2008,** 3, (3), 145-150.

Jiang, Z.; Guan, Y., Flocculation morphology: effect of particulate shape and coagulant species on flocculation. *Water Science and Technology* **2006,** 53, (7, Particle Separation 2005: Waste Water Treatment), 9-16.

Johnson, B. K. Flash nanoprecipitation of organic actives via confined micromixing and block copolymer stabilization. Princeton University, 2003.

Johnson, K. A., Interfacial phenomena and phase behavior in metered-dose inhaler formulations. *Lung Biology in Health and Disease* **1996,** 94, (Inhalation Aerosols), 385-415.

Johnson, K. A., Interfacial phenomena and phase behavior in metered dose inhaler formulations. In *Inhalation Aerosols: Physical and biological basis for therapy*, 2 ed.; Hickey, A. J., Ed. 2007; Vol. 221.

Kahan, B. D., Cyclosporine. *New England Journal of Medicine* **1989,** 321, (25), 1725-38.

Katherine C. Grabar; Keith J. Allison; Bonnie E. Baker; Robin M. Bright; Kenneth R. Brown; R. Griffith Freeman; Audrey P. Fox; Christine D. Keating; Michael D. Musick; Natan, M. J., Two-dimensional arrays of colloidal gold particles: a flexible approach to macroscopic metal surfaces. *Langmuir* **1996,** 12, 23535-2361.

Kawashima, Y.; Yamamoto, H.; Takeuchi, H.; Fujioka, S.; Hino, T., Pulmonary delivery of insulin with nebulized dl-lactide/glycolide copolymer (PLGA) nanospheres to prolong hypoglycemic effect. *Journal of Controlled Release* **1999,** 62, (1-2), 279-287.

Keenan, R. J.; Duncan, A. J.; Yousem, S. A.; Zenati, M.; Schaper, M.; Dowling, R. D.; Alarie, Y.; Burckart, G. J.; Griffith, B. P., Improved immunosuppression with aerosolized cyclosporine in experimental pulmonary transplantation. *Transplantation* **1992,** 53, (1), 20-5.

Keenan, R. J.; Iacono, A.; Dauber, J. H.; Zeevi, A.; Yousem, S. A.; Ohori, N. P.; Burckart, G. J.; Kawai, A.; Smaldone, G. C.; Griffith, B. P., Treatment of refractory acute allograft rejection with aerosolized cyclosporine in lung transplant recipients. *Journal of Thoracic and Cardiovascular Surgery* **1997,** 113, (2), 335-341.

Keller, M., Innovations and perspectives of metered dose inhalers in pulmonary drug delivery. *International Journal of Pharmaceutics* **1999,** 186, (1), 81-90.

Khlebtsov, B.; Zharov, V.; Melnikov, A.; Tuchin, V.; Khlebtsov, N., Optical amplification of photothermal therapy with gold nanoparticles and nanoclusters. *Nanotechnology* **2006,** 17, (20), 5167-5179.

Kim, T.; Lee, C.-H.; Joo, S.-W.; Lee, K., Kinetics of gold nanoparticle aggregation: Experiments and modeling. *Journal of Colloid and Interface Science* **2008,** 318, 238-243.

Kim, Y.; Atwell, S. H.; Bell, R. G., Determination of water in pressurized pharmaceutical metered dose aerosol products. *Drug Development and Industrial Pharmacy* **1992,** 18, (20), 2185-95.

Kleshchanok, D.; Tuinier, R.; Lang, P. R., Direct measurements of polymer-induced forces. *Journal of Physics: Condensed Matter* **2008,** 20, (7), 073101/1-073101/25.

Kline, S. R.; Kaler, E. W., Aggregation of Colloidal Silica by n-Alkyl Sulfates. *Langmuir* **1996,** 12, 2402-2407.

Klyashchitsky, B. A.; Owen, A. J., Nebulizer-compatible liquid formulations for aerosol pulmonary delivery of hydrophobic drugs: glucocorticoids and cyclosporine. *Journal of Drug Targeting* **1999,** 7, (2), 79-99.

Kooi, M. E.; et al, Accumulation of Ultrasmall Superparamagnetic Particles of Iron Oxide in Human Atherosclerotic Plaques Can Be Detected by In Vivo Magnetic Resonance Imaging. . *Circulation* **2003,** 107, (19), 2453-2458.

Kraft, W. K.; Steiger, B.; Beussink, D.; Quiring, J. N.; Fitzgerald, N.; Greenberg, H. E.; Waldman, S. A., The pharmacokinetics of nebulized nanocrystal budesonide suspension in healthy volunteers. *Journal of Clinical Pharmacology* **2004,** 44, (1), 67-72.

Kreibig, U.; Vollmer, M., *Optical Properties of Metal Clusters* Springer: Berlin, Germany, 1995 Vol. 25.

Kreyling, W. G.; Scheuch, G., *Clearance of Particles Deposited in the Lungs* New York Marcel Dekker Inc: New York, 2000; Vol. 143.

Kumar, S.; Aaron, J.; Sokolov, K., Directional conjugation of antibodies to nanoparticles for synthesis of multiplexed optical contrast agents with both delivery and targeting moieties. *Nature Protocols* **2008,** 3, (2), 314-320.

Kumar, S.; Harrison, N.; Richards-Kortum, R.; Sokolov, K., Plasmonic Nanosensors for Imaging Intracellular Biomarkers in Live Cells. *Nano Letters* **2007,** 7, (5), 1338-1343.

Kunze, J.; Burgess, I.; Nichols, R.; Buess-Herman, C.; Lipkowski, J., Electrochemical evaluation of citrate adsorption on Au(111) and the stability of citrate-reduced gold colloids. *Journal of Electroanalytical Chemistry* **2007,** 599, 147-159.

Kwon, M. J.; Bae, J. H.; Kim, J. J.; Na, K.; Lee, E. S., Long acting porous microparticle for pulmonary protein delivery. *International Journal of Pharmaceutics* **2007,** 333, (1-2), 5-9.

Larson, R. G., *The Structure and Rheology of Complex Fluids*. Oxford University Press Inc.: New York, 1999.

Larson, T. A.; Bankson, J.; Aaron, J.; Sokolov, K., Hybrid plasmonic magnetic nanoparticles as molecular specific agents for MRI/optical imaging and photothermal therapy of cancer cells. *Nanotechnology* **2007,** 18, (32), 325101/1-325101/8.

Lattuada, M.; Hatton, T. A., Preparation and Controlled Self-Assembly of Janus Magnetic Nanoparticles. *Journal of the American Chemical Society* **2007,** 129, (42), 12878-12889.

Lazarides, A. A.; Schatz, G. C., DNA-Linked Metal Nanosphere Materials: Structural Basis for the Optical Properties. *Journal of Physical Chemistry B* **2000,** 104, (3), 460-467.

Lee, S. E.; Liu, G. L.; Kim, F.; Lee, L. P., Remote Optical Switch for Localized and Selective Control of Gene Interference. *Nano Letters* **2009,** 9, (2), 562-570.

Lehnert, B. E.; Morrow, P. E., Association of 59iron oxide with alveolar macrophages during alveolar clearance. *Experimental Lung Research* **1985,** 9, (1-2), 1-16.

Letsou, G. V.; Safi, H. J.; Reardon, M. J.; Ergenoglu, M.; Li, Z.; Klonaris, C. N.; Baldwin, J. C.; Gilbert, B. E.; Waldrep, J. C., Pharmacokinetics of liposomal aerosolized cyclosporine A for pulmonary immunosuppression. *The Annals of thoracic surgery* **1999,** 68, (6), 2044-8.

Lewinski, N.; Colvin, V.; Drezek, R., Cytotoxicity of nanoparticles. *Small* **2008,** 4, (1), 26-49.

Li, H.; Peng, X.; Wu, L.; Jia, M.; Zhu, H., Surface Potential Dependence of the Hamaker Constant. *The Journal of Physical Chemistry C* **2009,** 113, (11), 4419-4425.

Li, J.; He, W.-D.; Sun, X.-L., Preparation of poly(styrene-b-N-isopropylacrylamide) micelles surface-linked with gold nanoparticles and thermo-responsive ultraviolet-visible absorbance. *Journal of Polymer Science, Part A: Polymer Chemistry* **2007,** 45, (22), 5156-5163.

Liao, Y.-H.; Brown, M. B.; Jones, S. A.; Nazir, T.; Martin, G. P., The effects of polyvinyl alcohol on the in vitro stability and delivery of spray-dried protein particles from surfactant-free HFA 134a-based pressurised metered dose inhalers. *International Journal of Pharmaceutics* **2005,** 304, (1-2), 29-39.

Lim, I. I. S.; Ip, W.; Crew, E.; Njoki, P. N.; Mott, D.; Zhong, C.-J.; Pan, Y.; Zhou, S., Homocysteine-mediated reactivity and assembly of gold nanoparticles. *Langmuir* **2007,** 23, (2), 826-833.

Lipinski, C., Poor aqueous solubility - an industry wide problem in drug discovery. *American Pharmaceutical Review* **2002,** 5, 82-85.

Lipinski, C. A., Avoiding investment in doomer drugs, is poor solubility an industry wide problem? *Current Drug Discovery* **2001**, 17-19.

Liu, C.; Wu, J.; Shi, B.; Zhang, Y.; Gao, T.; Pei, Y., Enhancing the Bioavailability of Cyclosporine A Using Solid Dispersion Containing Polyoxyethylene (40) Stearate. *Drug Development and Industrial Pharmacy* **2006,** 32, (1), 115-123.

Liu, F.; Shao, Z.; Kildsig, D. O.; Mitra, A. K., Pulmonary delivery of free and liposomal insulin. *Pharmaceutical Research* **1993,** 10, (2), 228-32.

Liu, Y.; Kathan, K.; Saad, W.; Prud'homme, R. K., Ostwald Ripening of b-Carotene Nanoparticles. *Physical Review Letters* **2007,** 98, (3), 036102/1-036102/4.

Liversidge, E. M.; Liversidge, G. G.; Cooper, E. R., Nanosizing: a formulation approach for poorly-water-soluble compounds. *European Journal of Pharmaceutical Sciences* **2003,** 18, 113-120.

Loo, C.; Lowery, A.; Halas, N.; West, J.; Drezek, R., Immunotargeted Nanoshells for Integrated Cancer Imaging and Therapy. *Nano Letters* **2005,** 5, (4), 709-711.

Lum, H.; Mitzner, W., A species comparison of alveolar size and surface forces. *Journal of applied physiology* **1987,** 62, (5), 1865-71.

Ma, L. L.; Feldman, M. D.; Tam, J. M.; Paranjape, A. S.; Cheruku, K. K.; Larson, T. A.; Tam, J. O.; Ingram, D. R.; Paramita, V.; Villard, J. W.; Clarke, G. D.; Jenkins, J. T.; Asmis, R.; Sokolov, K.; Chandrasekar, B.; Milner, T. E.; Johnston, K. P., Small multifunctional nanoclusters (Nanoroses) for targeted cellular imaging and therapy. *ACS Nano* **Submitted**.

Maa, Y.-F.; Costantino, H. R., Spray freeze-drying of biopharmaceuticals: applications and stability considerations. In *Biotechnology: Pharmaceutical Aspects. 2. Lyophilization of Biopharmaceuticals*, Costantino, H. R.; Pikal, M. J., Eds. American Association of Pharmaceutical Scientists: Arlington, 2004; Vol. 2, pp 519-561.

Maa, Y.-F.; Nguyen, P.-A.; Sweeney, T.; Shire, S. J.; Hsu, C. C., Protein inhalation powders: spray drying vs spray freeze drying. *Pharmaceutical Research* **1999,** 16, (2), 249-254.

Maa, Y.-F.; Prestrelski, S. J., Biopharmaceutical powders: particle formation and formulation considerations. *Current Pharmaceutical Biotechnology* **2000,** 1, (3), 283-302.

Martinet, Y.; Pinkston, P.; Saltini, C.; Spurzem, J.; Mueller-Quernheim, J.; Crystal, R. G., Evaluation of the in vitro and in vivo effects of cyclosporine on the lung T-lymphocyte alveolitis of active pulmonary sarcoidosis. *American Review of Respiratory Disease* **1988,** 138, (5), 1242-8.

Matteucci, M. E.; Brettmann, B. K.; Rogers, T. L.; Elder, E. J.; Williams, R. O.; Johnston, K. P., Design of Potent Amorphous Drug Nanoparticles for Rapid Generation of Highly Supersaturated Media. *Molecular Pharmaceutics* **2007,** 4, (5), 782-793.

Matteucci, M. E.; Crisp, M. T.; Johnston, K. P.; Rogers, T. L.; Hitt, J. E.; Williams, R. O. In *Controlled Precipitation of Naproxen Nanoparticles*, American Association of Pharmaceutical Sciences, Annual Meeting, 2004; 2004.

Matteucci, M. E.; Hotze, M. A.; Johnston, K. P.; Williams, R. O., III, Drug Nanoparticles by Antisolvent Precipitation: Mixing Energy versus Surfactant Stabilization. *Langmuir* **2006,** 22, (21), 8951-8959.

Matteucci, M. E.; Miller, M. A.; Williams, R. O.; Johnston, K. P., Highly Supersaturated Solutions of Amorphous Drugs Approaching Predictions from Configurational Thermodynamic Properties. *Journal of Physical Chemistry B* **2008,** 112, (51), 16675-16681.

Matteucci, M. E.; Paguio, J. C.; Miller, M. A.; Williams, R. O., III; Johnston, K. P., Flocculated Amorphous Nanoparticles for Highly Supersaturated Solutions. *Pharmaceutical Research* **2008,** 25, (11), 2477-2487.

McAllister, S. M.; Alpar, H. O.; Teitelbaum, Z.; Bennett, D. B., Do interactions with phospholipids contribute to the prolonged retention of polypeptides within the lung? *Advanced Drug Delivery Reviews* **1996,** 19, (1), 89-110.

McCabe, W. L.; Smith, J. C.; Harriott, P., *Unit Operations of Chemical Engineering*. 6th ed.; McGraw Hill Inc.: Boston, MA, 2001.

McConville, J. T.; Overhoff, K. A.; Sinswat, P.; Vaughn, J. M.; Frei, B. L.; Burgess, D. S.; Talbert, R. L.; Peters, J. I.; Johnston, K. P.; Williams, R. O., III, Targeted High Lung Concentrations of Itraconazole Using Nebulized Dispersions in a Murine Model. *Pharmaceutical Research* **2006,** 23, (5), 901-911.

McDonald, K. J.; Martin, G. P., Transition to CFC-free metered dose inhalers - into the new millennium. *International Journal of Pharmaceutics* **2000,** 201, (1), 89-107.

McMahon, T. A.; Brain, J. D.; Lemott, S., Species differences in aerosol deposition. *Inhaled Part. 4, Int. Symp., 4th* **1977,** 1, 23-33.

Michael, Y.; Snowden, M. J.; Chowdhry, B. Z.; Ashurst, I. C.; Davies-Cutting, C. J.; Riley, T., Characterisation of the aggregation behavior in a salmeterol and fluticasone propionate inhalation aerosol system. *International Journal of Pharmaceutics* **2001,** 221, (1-2), 165-174.

Miller, F. J.; Mercer, R. R.; Crapo, J. D., Lower respiratory tract structure of laboratory animals and humans: dosimetry implications. *Aerosol Science and Technology* **1993,** 18, (3), 257-71.

Mirkin, C. A.; Letsinger, R. L.; Mucic, R. C.; Storhoff, J. J., A DNA-based method for rationally assembling nanoparticles into macroscopic materials. *Nature (London)* **1996,** 382, (6592), 607-609.

Mitra, R.; Pezron, I.; Li, Y.; Mitra, A. K., Enhanced pulmonary delivery of insulin by lung lavage fluid and phospholipids. *International Journal of Pharmaceutics* **2001,** 217, (25-31).

Mitruka, S. N.; Pham, S. M.; Zeevi, A.; Li, S.; Cai, J.; Burckart, G. J.; Yousem, S. A.; Keenan, R. J.; Griffith, B. P., Aerosol cyclosporine prevents acute allograft rejection in experimental lung transplantation. *Journal of Thoracic and Cardiovascular Surgery* **1998,** 115, (1), 28-37.

Mitruka, S. N.; Won, A.; McCurry, K. R.; Zeevi, A.; McKaveney, T.; Venkataramanan, R.; Iacono, A.; Griffith, B. P.; Burckart, G. J., In the lung aerosol cyclosporine provides a regional concentration advantage over intramuscular cyclosporine. *Journal of heart and lung transplantation : official publication of the International Society for Heart Transplantation* **2000,** 19, (10), 969-75.

Mondain-Monval, O.; Leal-Calderon, F.; Phillip, J.; Bibette, J., Depletion Forces in the Presence of Electrostatic Double Layer Repulsion. *Physical Review Letters* **1995,** 75, 3364-3367.

Moon, S. Y.; Sekino, T.; Kusunose, T.; Tanaka, S.-i., Simple one-step synthesis of water and organic media soluble gold nanoparticles with various shapes and sizes. *Journal of Crystal Growth* **2009,** 311, (3), 651-656.

Muller, R. H.; Bohm, B. H. L. In *Nanosuspensions*, Colloidal Drug Carriers Expert Meeting, Berlin, 1997; Berlin, 1997; pp 149-174.

Muller, R. H.; Jacobs, C.; Kayser, O., Nanosuspensions as particulate drug formulations in therapy. Rationale for development and what we can expect for the future. *Advanced Drug Delivery Reviews* **2001,** 47, (1), 3-19.

Muller, R. H.; Jacobs, C.; Kayser, O., Nanosuspensions as particulate drug formulations in therapy: Rationale for development and what we can expect for the future. *Advanced Drug Delivery Reviews* **2001,** 47, 3-19.

Muller, R. H.; Mader, K.; Gohla, S., Solid lipid nanoparticles (SLN) for controlled drug delivery - a review of the state of the art. *European Journal of Pharmaceutics and Biopharmaceutics* **2000,** 50, (1), 161-177.

Murthy, V. S.; Cha, J. N.; Stucky, G. D.; Wong, M. S., Charge-Driven Flocculation of Poly(L-lysine)-Gold Nanoparticle Assemblies Leading to Hollow Microspheres. *Journal of the American Chemical Society* **2004,** 126, (16), 5292-5299.

Mutch, K. J.; Duijneveldt, J. S. v.; Eastoe, J., Colloid–polymer mixtures in the protein limit. *Soft Matter* **2007,** 3, 155-167.

Mutch, K. J.; Duijneveldt, J. S. v.; Eastoe, J.; Grillo, I.; Heenan, R. K., Small-Angle Neutron Scattering Study of Microemulsion Polymer Mixtures in the Protein Limit. *Langmuir* **2008,** 24, 3053-3060.

Nail, S. L.; Jiang, S.; Chongprasert, S.; Knopp, S. A., Fundamentals of freeze-drying. In *Pharmaceutical Biotechnology. 14. Development and Manufacture of Protein Pharmaceuticals*, Nail, S. L.; Akers, M. J., Eds. Kluwer Academic/Plenum Publishers: New York, 2002; Vol. 14, pp 281-360.

Nguyen, X. C.; Herberger, J. D.; Burke, P. A., Protein powders for encapsulation: a comparison of spray-freeze drying and spray drying of darbepoetin alfa. *Pharmaceutical Research* **2004,** 21, (3), 507-514.

Niven, R. W., *Pharmaceutical Inhalation Aerosol Technology*. Marcel Dekker, Inc.: New York, New York, 1992; Vol. 54, p 340.

Noyes, A. A.; Whitney, W. R., The rate of solution of solid substances in their own solutions. . *Journal of the American Chemical Society* **1897,** 19, 930-934.

Oberdoerster, G., Effects and fate of inhaled ultrafine particles. *ACS Symposium Series* **2005,** 890, (Nanotechnology and the Environment), 37-59.

Ofir, Y.; Samanta, B.; Rotello, V. M., Polymer and biopolymer mediated self-assembly of gold nanoparticles. *Chemical Soceity Reviews* **2008,** 37, (9), 1814-1825.

Oliver, M. J.; McKenzie, L.; Graffiths, W. D.; Morgan, G. R.; O'Kelly, N. In *Initial assessment of a protein formulated in pressurized mdis for pulmonary delivery*, RDD VII, 2000; 2000.

Ostrander, K. D.; Bosch, H. W.; Bondanza, D. M., An in-vitro assessment of a NanoCrystal beclomethasone dipropionate colloidal dispersion via ultrasonic nebulization. *European Journal of Pharmaceutics and Biopharmaceutics* **1999,** 48, (3), 207-215.

Overhoff, K. A.; Engstrom, J. D.; Chen, B.; Scherzer, B. D.; Milner, T. E.; Johnston, K. P.; Williams, R. O., Novel ultra-rapid freezing particle engineering process for enhancement of dissolution rates of poorly water-soluble drugs. *European Journal of Pharmaceutics and Biopharmaceutics* **2007,** 65, (1), 57-67.

Overhoff, K. A.; Moreno, A.; Miller, D. A.; Johnston, K. P.; Williams, R. O., Solid dispersions of itraconazole and enteric polymers made by ultra-rapid freezing. *International Journal of Pharmaceutics* **2007,** 336, (1), 122-132.

Pandey, R.; Khuller, G. K., Antitubercular inhaled therapy: opportunities, progress and challenges. *Journal of Antimicrobial Chemotherapy* **2005,** 55, (4), 430-435.

Patton, J. S., Mechanisms of macromolecule absorption by the lungs. *Advanced Drug Delivery Reviews* **1996,** 19, (1), 3-36.

Patton, J. S., Pulmonary drug delivery comes of age: the outlook for 2005 & beyond. *Drug Delivery Technology* **2005,** 5, (4), 46-49.

Patton, J. S., Unlocking the opportunity of tight glycaemic control: innovative delivery of insulin via the lung. *Diabetes, Obesity and Metabolism* **2005,** 7, (Suppl. 1), S5-S8.

Patton, J. S.; Bukar, J. G.; Eldon, M. A., Clinical pharmacokinetics and pharmacodynamics of inhaled insulin. *Clinical Pharmacokinetics* **2004,** 43, (12), 781-801.

Patton, J. S.; Byron, P. R., Inhaling medicines: delivering drugs to the body through the lungs. *Nature Reviews Drug Discovery* **2007,** 6, (1), 67-74.

Patton, J. S.; C.S. Fishburn; Weers, J. G., The Lungs as a Portal of Entry for Systemic Drug Delivery. *Proceedigns of the American Thoracic Society* **2004,** 1, 338-344.

Peek, L. J.; Roberts, L.; Berkland, C., Poly(d,l-lactide-co-glycolide) Nanoparticle Agglomerates as Carriers in Dry Powder Aerosol Formulation of Proteins. *Langmuir* **2008,** 24, (17), 9775-9783.

Peer, D.; Karp, J. M.; Hong, S.; Farokhzad, O. C.; Margalit, R.; Langer, R., Nanocarriers as an emerging platform for cancer therapy. *Nature Nanotechnology* **2007,** 2, (12), 751-760.

Peeters, J.; Neeskens, P.; Tollenaere, J. P.; Van Remoortere, P.; Brewster, M. E., Characterization of the interaction of 2-hydroxypropyl-beta-cyclodextrin with itraconazole at pH 2, 4 and 7 *Journal of Pharmaceutical Sciences* **2002,** 91, 1414–1422.

Peguin, R. P. S.; da Rocha, S. R. P., Solvent-Solute Interactions in Hydrofluoroalkane Propellants. *J. Phys. Chem. B FIELD Full Journal Title:Journal of Physical Chemistry B* **2008,** 112, (27), 8084-8094.

Peguin, R. P. S.; Selvam, P.; da Rocha, S. R. P., Microscopic and Thermodynamic Properties of the HFA134a-Water Interface: Atomistic Computer Simulations and Tensiometry under Pressure. *Langmuir* **2006,** 22, (21), 8826-8830.

Philipse, A. P., The Random Contact Equation and Its Implications for (Colloidal) Rods in Packings, Suspensions, and Anisotropic Powders. *Langmuir* **1996,** 12, (5), 1127-33.

Philipse, A. P., The Random Contact Equation and Its Implications for (Colloidal) Rods in Packings, Suspensions, and Anisotropic Powders. *Langmuir* **1996,** 12, (24), 5971.

Philipse, A. P.; Wierenga, A. M., On the Density and Structure Formation in Gels and Clusters of Colloidal Rods and Fibers. *Langmuir* **1998,** 14, (1), 49-54.

Pison, U.; Welte, T.; Giersig, M.; Groneberg, D. A., Nanomedicine for respiratory diseases. *European Journal of Pharmacology* **2006,** 533, (1-3), 341-350.

Pissuwan, D.; Valenzuela, S. M.; Killingsworth, M. C.; Xu, X.; Cortie, M. B., Targeted destruction of murine macrophage cells with bioconjugated gold nanorods. *Journal of Nanoparticle Research* **2007,** 9, (6), 1109-1124.

Qu, Y.; Lu, X., Aqueous synthesis of gold nanoparticles and their cytotoxicity in human dermal fibroblasts-fetal. *Biomedical Materials* **2009,** 4, (2), 025007/1-025007/5.

Quinn, E. A.; Forbes, R. T.; Williams, A. C.; Oliver, M. J.; McKenzie, L.; Purewal, T. S., Protein conformational stability in the hydrofluoroalkane propellants tetrafluoroethane and heptafluoropropane analyzed by Fourier transform Raman spectroscopy. *International Journal of Pharmaceutics* **1999,** 186, (1), 31-41.

Rabinow, B. E., Nanosuspensions in drug delivery. *Nature Reviews Drug Discovery* **2004,** 3, (9), 785-796.

Rasenack, N.; Muller, B. W., Dissolution Rate Enhancement by in Situ Micronization of Poorly Water-Soluble Drugs. *Pharmaceutical Research* **2002,** 19, (12), 1894-1900.

Reddy, S. T.; Swartz, M. A.; Hubbell, J. A., Targeting dendritic cells with biomaterials: developing the next generation of vaccines. *Trends in Immunology* **2006,** 27, (12), 573-579.

Riley, T.; Stolnik, S.; Heald, C. R.; Xiong, C. D.; Garnett, M. C.; Illum, L.; Davis, S. S., Physicochemical Evaluation of Nanoparticles Assembled from Poly(lactic acid)-Poly(ethylene glycol) (PLA-PEG) Block Copolymers as Drug Delivery Vehicles. *Langmuir* **2001,** 17, 3168-3174.

Rogers, T. L.; Gillespie, I. B.; Hitt, J. E.; Fransen, K. L.; Crowl, C. A.; Tucker, C. J.; Kupperblatt, G. B.; Becker, J. N.; Wilson, D. L.; Todd, C.; Broomall, C. F.; Evans, J. C.; Elder, E. J., Development and Characterization of a Scalable Controlled Precipitation Process to Enhance the Dissolution of Poorly Water-Soluble Drugs. *Pharmaceutical Research* **2004,** 21, (11), 2048-2057.

Rogers, T. L.; Nelsen, A. C.; Hu, J.; Brown, J. N.; Sarkari, M.; Young, T. J.; Johnston, K. P.; Williams III, R. O., A novel particle engineering technology to enhance dissolution of poorly water soluble drugs: spray-freezing into liquid. *European journal of pharmaceutics and biopharmaceutics* **2002,** 54, (3), 271-280.

Rogers, T. L.; Overhoff, K. A.; Shah, P.; Santiago, P.; Yacaman, M. J.; Johnston, K. P.; Williams III, R. O., Micronized powders of a poorly water soluble drug produced by a spray-freezing into liquid-emulsion process. *European journal of pharmaceutics and biopharmaceutics* **2003,** 55, (2), 161-72.

Rogueda, P., Novel hydrofluoroalkane suspension formulations for respiratory drug delivery. *Expert Opinion on Drug Delivery* **2005,** 2, (4), 625-638.

Rogueda, P. G. A., HPFP, a model propellant for pMDIs. *Drug Development and Industrial Pharmacy* **2003,** 29, (1), 39-49.

Russel, W. B.; Saville, D. A.; Schowalter, W. R., *Colloidal dispersions*. 1989.

Ryoo, W.; Webber, S. E.; Johnston, K. P., Water-in-Carbon Dioxide Microemulsions with Methylated Branched Hydrocarbon Surfactants. *Ind. Eng. Chem. Res.* **2003,** 42, (25), 6348-6358.

Sakagami, M.; Sakon, K.; Kinoshita, W.; Makino, Y., Enhanced pulmonary absorption following aerosol administration of mucoadhesive powder microspheres. *Journal of Controlled Release* **2001,** 77, (1-2), 117-129.

Sakai, T.; Alexandridis, P., Mechanism of Gold Metal Ion Reduction, Nanoparticle Growth and Size Control in Aqueous Amphiphilic Block Copolymer Solutions at Ambient Conditions. *Journal of Physical Chemistry B* **2005,** 109, (16), 7766-7777.

Sakai, T.; Alexandridis, P., Metal nanoparticle synthesis and organization in 1D, 2D and 3D structures formed by amphiphilic block copolymers. *PMSE Preprints* **2005,** 93, 798-799.

Sanvicens, N.; Marco, M. P., Multifunctional nanoparticles – properties and prospects for their use in human medicine *Trends in Biotechnology* **2008,** 26, (8), 425-433.

Sawchuk, R. J.; Cartier, L. L., Liquid-chromatographic determination of cyclosporin A in blood and plasma. *Clinical Chemistry (Washington, DC, United States)* **1981,** 27, (8), 1368-71.

Schanker, L. S.; Mitchell, E. W.; Brown, R. A., Jr., Species comparison of drug absorption from the lung after aerosol inhalation or intratracheal injection. *Drug Metabolism and Disposition* **1986,** 14, (1), 79-88.

Schipper, M. L.; Iyer, G.; Koh , A. L.; Cheng, Z.; Ebenstein, Y.; Aharoni, A.; Keren, S.; Bentolila, L. A.; Li, J. Q.; Rao, J. H.; Chen, X. Y.; Banin, U.; Wu, A. M.; Sinclair, R.; Weiss, S.; Gambhir, S. S., Particle Size, Surface Coating, and PEGylation Influence the Biodistribution of Quantum Dots in Living Mice *Small* **2009** 5 126-134.

Selvakannan, P. R.; Mandal, S.; Phadtare, S.; Pasricha, R.; Sastry, M., Capping of Gold Nanoparticles by the Amino Acid Lysine Renders Them Water-Dispersible. *Langmuir* **2003,** 19, (8), 3545-3549.

Selvam, P.; Chokshi, U.; Gouch, A.; Wu, L.; Porcar, L.; da Rocha, S. R. P., Ethoxylated copolymer surfactants for the HFA134a-water interface: interfacial activity, aggregate microstructure and biomolecule uptake. *Soft Matter FIELD Full Journal Title:Soft Matter* **2008,** 4, (2), 357-366.

Selvam, P.; Peguin, R. P. S.; Chokshi, U.; da Rocha, S. R. P., Surfactant Design for the 1,1,1,2-Tetrafluoroethane-Water Interface: ab initio Calculations and in situ High-Pressure Tensiometry. *Langmuir* **2006,** 22, (21), 8675-8683.

Shah, P. S.; Husain, S.; Johnston, K. P.; Korgel, B. A., Role of Steric Stabilization on the Arrested Growth of Silver Nanocrystals in Supercritical Carbon Dioxide. *Journal of Physical Chemistry B* **2002,** 106, (47), 12178-12185.

Shekunov, B. Y.; Chattopadhyay, P.; Tong, H. H. Y.; Chow, A. H. L., Particle Size Analysis in Pharmaceutics: Principles, Methods and Applications. *Pharmaceutical Research* **2007,** 24, (2), 203-227.

Shoyele, S. A.; Cawthorne, S., Particle engineering techniques for inhaled biopharmaceuticals. *Advanced Drug Delivery Reviews* **2006,** 58, (9-10), 1009-1029.

Shoyele, S. A.; Slowey, A., Prospects of formulating proteins/peptides as aerosols for pulmonary drug delivery. *International Journal of Pharmaceutics* **2006,** 314, (1), 1-8.

Sihvola, A., *Electromagnetic mixing formulas and applications*. 1999; Vol. 47.

Singhal, D.; Curatolo, W., Drug polymorphism and dosage form design: a practical perspective. *Advanced Drug Delivery Reviews* **2004,** 56, (3), 335-347.

Skrabalak, S. E.; Chen, J.; Au, L.; Lu, X.; Li, X.; Xia, Y., Gold nanocages for biomedical applications. *Advanced Materials* **2007,** 19, (20), 3177-3184.

Smith, P. G., Jr.; Ryoo, W.; Johnston, K. P., Electrostatically Stabilized Metal Oxide Particle Dispersions in Carbon Dioxide. *Journal of Physical Chemistry B* **2005,** 109, (43), 20155-20165.

Smith, P. G.; Patel, M. N.; Kim, J.; Milner, T. E.; Johnston, K. P., Effect of Surface Hydrophilicity on Charging Mechanism of Colloids in Low-Permittivity Solvents. *Journal of Physical Chemistry C* **2007,** 111, 840-848.

Smyth, H. D. C., The influence of formulation variables on the performance of alternative propellant-driven metered dose inhalers. *Advanced Drug Delivery Reviews* **2003,** 55, (7), 807-828.

Smyth, H. D. C.; Hickey, A. J.; Evans, R. M., Aerosol generation from propellant-driven metered dose inhalers. In *Inhalation Aerosols: Physical and Biological Basis for Therapy*, Hickey Anthony, J., Ed. 2007; Vol. 221, pp 399-416.

Sokolov, K. V.; Follen, M.; Aaron, J.; Pavlova, I.; Malpica, A.; Lotan, R.; Richards-Kortum, R., Real-time vital optical imaging of precancer using anti-epidermal growth factor receptor antibodies conjugated to gold nanoparticles. *Cancer Research* **2003,** 63, 1999-2004.

Son, Y. J.; McConville, J. T. In *Improvements of an In Vitro Dissolution Test Method For Dry Inhalation Formulations*, American Association of Pharmaceutical Scientists Annual Meeting, Atlanta, GA, 2008; Atlanta, GA, 2008.

Srivastava, S.; Samanta, B.; Arumugam, P.; Han, G.; Rotello, V. M., DNA-mediated assembly of iron platinum (FePt) nanoparticles. *Journal of Materials Chemistry* **2007,** 17, (1), 52-55.

Steckel, H.; Markefka, P.; te Wierik, H.; Kammelar, R., Effect of milling and sieving on functionality of dry powder inhalation products. *International Journal of Pharmaceutics* **2006,** 309, (1-2), 51-59.

Stepkowski, S. M.; Goto, S.; Ito, T.; Reynolds, K.; Didlake, R.; Kim, E. K.; Kahan, B. D., Prolongation of heterotopic heart allograft survival by local delivery of continuous low-dose cyclosporine therapy. *Transplantation* **1989,** 47, (1), 17-23.

Sun, Y.-L.; Chen, Y.-Z.; Wu, R.-J.; Chavali, M.; Huang, Y.-C.; Su, P.-G.; Lin, C.-C., Poly(l-lactide) stabilized gold nanoparticles based QCM sensor for low humidity detection. *Sensors and Actuators B* **2007,** 126, 441-446.

Tadmor, R., The London-van der Waals interaction energy between objects of various geometries. *Journal of Physics: Condensed Matter* **2001,** 13, (9), L195-L202.

Takashima, S., Proton fluctuation in protein. Experimental study of the Kirkwood-Shumaker theory. *Journal of Physical Chemistry* **1965,** 69, (7), 2281-6.

Tam, J.; McConville, J. T.; Williams III, R. O.; Johnston, K. P., Amorphous cyclosporin A nanodispersions for enhanced pulmonary deposition and dissolution. ASAP. *Journal of Pharmaceutical Sciences* **2007**.

Tam, J. M.; McConville, J. T.; Williams, R. O., 3rd; Johnston, K. P., Amorphous cyclosporin nanodispersions for enhanced pulmonary deposition and dissolution. *Journal of pharmaceutical sciences* **2008,** 97, (11), 4915-33.

Tam, J. M.; Tam, J. O.; Murthy, A. K.; Ingram, D. R.; Ma, L. L.; Travis, K. A.; Sokolov, K. V.; Johnston, K. P., Controlled Assembly of Polymer/Inorganic Nanoclusters: A Flexible Platform for the Synthesis of Biodegradable Near-Infrared Absorbing Agents for Imaging and Therapeutic Applications. **In preparation**.

Tandya, A.; Dehghani, F.; Foster, N. R., Micronization of cyclosporine using dense gas techniques. *Journal of Supercritical Fluids* **2006,** 37, (3), 272-278.

Tang, P.; Greenwood, J.; Raper, J. A., A model to describe the settling behavior of fractal aggregates. *Journal of Colloid and Interface Science* **2002,** 247, (1), 210-219.

Tarara, T. E., MIchael S. Hartman, Howard Gill, Characterization of Suspension-Based Metered Dose Inhaler Formulations Composed of Spray-Dried Budesonide Microcrystals Dispersed in HFA-134a. *Pharmaceutical Research* **2004,** 21, (9), 1607-1614.

Taylor, K. M. G.; Taylor, G.; Kellaway, I. W.; Stevens, J., The stability of liposomes to nebulisation. *International Journal of Pharmaceutics* **1990,** 58, (1), 57-61.

Terzano, C., Pressurized Metered Dose Inhalers and Add-on Devices. *Pulmonary Pharmacology & Therapeutics* **2001,** 14, (5), 351-366.

Thomas, K.; Koelwel, C.; Machei, U.; Farber, L.; Gopferich, A., Three generations of cyclosporine a formulations: an in vitro comparison. *Drug development and industrial pharmacy* **2005,** 31, (4-5), 357-66.

Thorsson, L.; Edsbacker, S.; Kallen, A.; Lofdahl, C.-G., Pharmacokinetics and systemic activity of fluticasone via Diskus and pMDI, and of budesonide via Turbuhaler. *British Journal of Clinical Pharmacology* **2001,** 52, (5), 529-538.

Traini, D.; Rogueda, P.; Young, P.; Price, R., Surface Energy and Interparticle Forces Correlations in Model pMDI Formulations. *Pharmaceutical Research* **2005,** 22, (5), 816-825.

Traini, D.; Young, P.; Rogueda, P.; Price, R., The Use of AFM and Surface Energy Measurements to Investigate Drug-Canister Material Interactions in a Model Pressurized Metered Dose Inhaler Formulation. *Aerosol Science and Technology* **2006,** 40, (4), 227-236.

Traini, D.; Young Paul, M.; Rogueda, P.; Price, R., In vitro investigation of drug particulates interactions and aerosol performance of pressurised metered dose inhalers. *Pharmaceutical Research* **2007,** 24, (1), 125-135.

Traini, D.; Young, P. M.; Rogueda, P.; Price, R., In Vitro Investigation of Drug Particulates Interactions and Aerosol Performance of Pressurized Metered Dose Inhalers. *Pharmaceutical Research* **2007,** 24, (1), 125-135.

Troutman, T. S.; Barton, J. K.; Romanowski, M., Biodegradable plasmon resonant nanoshells. *Advanced Materials* **2008,** 20, (13), 2604-2608.

Tsapis, N.; Bennett, D.; Jackson, B.; Weitz, D. A.; Edwards, D. A., Trojan particles: large porous carriers of nanoparticles for drug delivery. *Proceedings of the National Academy of Sciences of the United States of America* **2002,** 99, (19), 12001-12005.

Turkevich, J.; Stevenson, P. C.; Hillier, J., The nucleation and growth processes in the synthesis of colloidal gold. *Discussions of the Faraday Society* **1951,** No. 11, 55-75.

Turkevich, J.; Stevenson, P. C.; Hillier, J., The formation of colloidal gold. *Journal of Physical Chemistry* **1953,** 57, 670-3.

Ulrich, D. R., Chemical processing of ceramics. *Chemical & Engineering News* **1990,** 68, (1), 28-40.

Uzun, O.; Frankamp, B. L.; Sanyal, A.; Rotello, V. M., Recognition-Mediated Assembly of Nanoparticle-Diblock Copolymer Micelles with Controlled Size. *Chemistry of Materials* **2006,** 18, (23), 5404-5409.

Vanbever, R.; Mintzes, J. D.; Wang, J.; Nice, J.; Chen, D.; Batycky, R.; Langer, R.; Edwards, D. A., Formulation and physical characterization of large porous particles for inhalation. *Pharmaceutical Research* **1999,** 16, (11), 1735-1742.

Varun, K.; Robert, K. P. h., Thermodynamic limits on drug loading in nanoparticle cores. *Journal of Pharmaceutical Sciences* **2008,** 97, (11), 4904-4914.

Vasir, J. K.; Labhasetwar, V., Biodegradable nanoparticles for cytosolic delivery of therapeutics. *Advanced Drug Delivery Reviews* **2007,** 59, (8), 718-728.

Vaughn, J. M.; Gao, X.; Yacaman, M.-J.; Johnston, K. P.; Williams, R. O., Comparison of powder produced by evaporative precipitation into aqueous solution (EPAS) and spray freezing into liquid (SFL) technologies using novel Z-contrast STEM and complimentary techniques. *European Journal of Pharmaceutics and Biopharmaceutics* **2005,** 60, (1), 81-89.

Vaughn, J. M.; McConville, J. T.; Burgess, D.; Peters, J. I.; Johnston, K. P.; Talbert, R. L.; Williams, R. O., III, Single dose and multiple dose studies of itraconazole nanoparticles. *European Journal of Pharmaceutics and Biopharmaceutics* **2006,** 63, (2), 95-102.

Vaughn, J. M.; Wiederhold, N. P.; McConville, J. T.; Coalson, J. J.; Talbert, R. L.; Burgess, D. S.; Johnston, K. P.; Williams, R. O.; Peters, J. I., Murine airway histology and intracellular uptake of inhaled amorphous itraconazole. *International Journal of Pharmaceutics* **2007,** 338, (1-2), 219-224.

Venkatraman, S. S., Jie, P. Min, F., Freddy, B.Y.C., Leong-Huat, G., Micelle-like nanoparticles of PLA-PEG-PLA triblock copolymer as chemotherapeutic carrier. *International Journal of Pharmaceutics* **2005,** 298, 219-232.

Vervaet, C.; Byron, P. R., Drug-surfactant-propellant interactions in HFA-formulations. *International Journal of Pharmaceutics* **1999,** 186, (1), 13-30.

Vrij, A., Polymers at Interfaces and the Interactions in Colloidal Dispersions *Pure and Applied Chemistry* **1976,** 48, 471-483

Waldrep, J. C.; Arppe, J.; Jansa, K. A.; Knight, V., High dose cyclosporin A and budesonide-liposome aerosols. *International Journal of Pharmaceutics* **1997,** 152, (1), 27-36.

Waldrep, J. C.; Arppe, J.; Jansa, K. A.; Vidgren, M., Experimental pulmonary delivery of cyclosporin A by liposome aerosol. *International Journal of Pharmaceutics* **1998,** 160, (2), 239-250.

Wang, A. Z.; Bagalkot, V.; Vasilliou, C. C.; Gu, F.; Alexis, F.; Zhang, L.; Shaikh, M.; Yuet, K.; Cima, M. J.; Langer, R.; Kantoff, P. W.; Bander, N. H.; Jon, S.; Farokhzad, O. C., Superparamagnetic iron oxide nanoparticle-aptamer bioconjugates for combined prostate cancer imaging and therapy. *ChemMedChem* **2008,** 3, (9), 1311-1315.

Waters, V.; Sokol, S.; Reddy, B.; Soong, G.; Chun, J.; Prince, A., The effect of cyclosporin A on airway cell proinflammatory signaling and pneumonia. *American Journal of Respiratory Cell and Molecular Biology* **2005,** 33, (2), 138-144.

Watts, A. B.; McConville, J. T.; Robert O. Williams, I., Current Therapies and Technological Advances in Aqueous Aerosol Drug Delivery. *Drug Development and Industrial Pharmacy* **2008,** 34, (9), 913-922.

Webb, S. D.; Cleland, J. L.; Carpenter, J. F.; Randolph, T. W., A new mechanism for decreasing aggregation of recombinant human interferon-g by a surfactant: slowed dissolution of lyophilized formulations in a solution containing 0.03% polysorbate 20. *Journal of Pharmaceutical Sciences* **2002,** 91, (2), 543-558.

Webb, S. D.; Golledge, S. L.; Cleland, J. L.; Carpenter, J. F.; Randolph, T. W., Surface adsorption of recombinant human interferon-γ in lyophilized and spray-lyophilized formulations. *Journal of Pharmaceutical Sciences* **2002,** 91, (6), 1474-1487.

Weers, J. G.; Tarara, T. E.; Dellamary, L. A.; Kabalnov, A.; Schutt, E. G. Stabilized preparations for use in metered dose inhalers. 98-US20615 9916422, 19980929., 1999.

Weissleder, R., A clearer vision for in vivo imaging. *Nature Biotechnology* **2001,** 19, (4), 316-317.

Weissleder, R., Molecular Imaging in Cancer. *Science* **2006,** 312, (5777), 1168-1171.

White, S.; Bennett, D. B.; Cheu, S.; Conley, P. W.; Guzek, D. B.; Gray, S.; Howard, J.; Malcolmson, R.; Parker, J. M.; Roberts, P.; Sadrzadeh, N.; Schumacher, J. D.; Seshadri, S.; Sluggett, G. W.; Stevenson, C. L.; Harper, N. J., EXUBERA: Pharmaceutical Development of a Novel Product for Pulmonary Delivery of Insulin. *Diabetes Technology & Therapeutics* **2005,** 7, (6), 896-906.

Wilcoxon, J. P.; Martin, J. E.; Schaefer, D. W., Aggregation in colloidal gold. *Physical Review A: Atomic, Molecular, and Optical Physics* **1989,** 39, (5), 2675-88.

Williams, R. O., III; Brown, J.; Liu, J., Influence of micronization method on the performance of a suspension triamcinolone acetonide pressurized metered-dose inhaler formulation. *Pharmaceutical Development and Technology* **1999,** 4, (2), 167-179.

Williams, R. O., III; Liu, J., Influence of formulation additives on the vapor pressure of hydrofluoroalkane propellants. *International Journal of Pharmaceutics* **1998,** 166, (1), 99-103.

Williams, R. O., III; Liu, J., Formulation of a protein with propellant HFA 134a for aerosol delivery. *European Journal of Pharmaceutical Sciences* **1999,** 7, (2), 137-144.

Williams, R. O., III; Liu, J.; Koleng, J. J., Influence of metering chamber volume and water level on the emitted dose of a suspension-based pMDI containing propellant 134a. *Pharmaceutical Research* **1997,** 14, (4), 438-443.

Williams, R. O., III; Repka, M.; Liu, J., Influence of propellant composition on drug delivery from a pressurized metered-dose inhaler. *Drug Development and Industrial Pharmacy* **1998,** 24, (8), 763-770.

Williams, R. O., III; Repka, M. A.; Barron, M. K., Application of co-grinding to formulate a model pMDI suspension. *European Journal of Pharmaceutics and Biopharmaceutics* **1999,** 48, (2), 131-140.

Williams, R. O., III, Hie Liu, Formulation of a Protein with Propellant HFA 134a for Aerosol Delivery. *European Journal of Pharmaceutical Sciences* **1998,** 7, 137-144.

Wong, J.; Papadopoulos, P.; Werling, J.; Rebbeck, C.; Doty, M.; Kipp, J.; Neuberger, D. In *Itraconazole Nanosuspension for Intravenous Injection - Determination of the Real Component of Refractive Index Input for Laser Light Diffraction Particle Sizing*, American Association of Pharmaceutical Scientists Annual Meeting, Baltimore, MD, 2004; Baltimore, MD, 2004.

Wu, L.; Peguin, R. P. S.; Selvam, P.; Chokshi, U.; da Rocha, S. R. P., Molecular scale behavior in alternative propellant-based inhaler formulations. In *Inhalation Aerosols: Physical and biological basis for therapy*, Hickey, A. J., Ed. 2007; Vol. 221.

Xia, Y. In *Gold nanocages: A new class of plasmonic nanostructures for biomedical applications*, ACS National Meeting, Boston, MA, United States, August 19-23, 2007 2007; Boston, MA, United States, 2007; pp COLL-528.

Xu, L.; Guo, Y.; Xie, R.; Zhuang, J.; Yang, W.; Li, T., Three-dimensional assembly of Au nanoparticles using dipeptides. *Nanotechnology* **2002,** 13, (6), 725-728.

Yang, W.; Tam, J.; Miller, D. A.; Zhou, J.; McConville, J. T.; Johnston, K. P.; Williams, R. O., High bioavailability from nebulized itraconazole nanoparticle dispersions with biocompatible stabilizers. *International Journal of Pharmaceutics* **2008,** 361, (1-2), 177-188.

Young, T. J.; Mawson, S.; Johnston, K., Rapid Expansion from Supercritical to Aqueous Solution to Produce Submicron Suspensions of Water-Insoluble Drugs. *Biotechnology Progress* **2000,** 16, 402-407.

Young, T. J.; Mawson, S.; Johnston, K. P.; Henriksen, I. B.; Pace, G. W.; Mishra, A. K., Rapid Expansion from Supercritical to Aqueous Solution to Produce Submicron Suspensions of Water-Insoluble Drugs. *Biotechnology Progress* **2000,** 16, (3), 402-407.

Yu, Z.; Garcia, A. S.; Johnston, K. P.; Williams III, R. O., Spray freezing into liquid nitrogen for highly stable protein nanostructured microparticles. *European Journal of Pharmaceutics and Biopharmaceutics* **2004,** 58, (3), 529-537.

Yu, Z.; Johnston, K. P.; Williams III, R. O., Spray freezing into liquid versus spray-freeze drying: Influence of atomization on protein aggregation and biological activity. *European Journal of Pharmaceutical Sciences* **2006,** 27, (1), 9-18.

Yu, Z.; Rogers, T. L.; Hu, J.; Johnston, K. P.; Williams III, R. O., Preparation and characterization of microparticles containing peptide produced by a novel process: spray freezing into liquid. *European journal of pharmaceutics and biopharmaceutics* **2002,** 54, (2), 221-228.

Vita

Jasmine Man-Chi Tam was born in Tempe, Arizona to Gordon and Wendy Tam on February 1st, 1982. After graduating from Gilbert High School (Gilbert, AZ) in 2000, she entered The University of Arizona (Tucson, AZ). While at The University of Arizona, Jasmine conducted undergraduate research with Dr. Reyes Sierra on bioreactive barriers for the containment of heavy metal contamination. She also completed two summer internships at the ExxonMobil refinery in Baytown, Texas. She graduated with a Bachelor of Science degree in Chemical Engineering, *summa cum laude*, in May, 2004 and was named Engineering Woman of the Year. Jasmine enrolled in the Chemical Engineering department at The University of Texas at Austin in August, 2004, to pursue a doctoral degree. Under the guidance of Professor Keith P. Johnston, she earned her Doctor of Philosophy in Chemical Engineering in August 2009.

Permanent address: 541 E. Sagebrush Street, Gilbert, AZ 85296

This dissertation was typed by the author.